City Research Online

City St George's, University of London

Citation: Mandal, J. (2005). Fibre laser development for sensor applications. (Unpublished Doctoral thesis, City, University of London)

This is the accepted version of the paper.

This version of the publication may differ from the final published version. To cite this item please consult the publisher's version.

Permanent repository link: https://openaccess.city.ac.uk/id/eprint/30687/

Copyright and Reuse: Copyright and Moral Rights remain with the author(s) and/or copyright holders. Copies of full items can be used for personal research or study, educational, or not-for-profit purposes without prior permission or charge, unless otherwise indicated, provided that the authors, title and full bibliographic details are credited, a hyperlink and/or URL is given for the original metadata page and the content is not changed in any way. For full details of reuse please refer to City Research Online policy.

City Research Online: http://openaccess.city.ac.uk/ publications@citystgeorges.ac.uk

Fibre laser development for sensor applications

Thesis submitted for the degree of

Doctor of Philosophy

of

City University

School of Engineering and Mathematical Sciences

by

Jharna Mandal

2005

To my parents

Nimai Chandra Mandal

Shova Rani Mandal

Content

List of Tables

List of Figures

Acknowledgements

First of all, I would like to express my deepest gratitude and thank to my supervisors Prof. K.T.V. Grattan, Dr T. Sun and Dr A.T. Augousti for their excellent guidance, supervision and encouragement throughout the work. In particular, Prof. K.T.V. Grattan and Dr T. Sun, for their valuable suggestions and constant observations helped me to move forward to the direction of research and to achieve this goal. I am greatly indebt to them for their patience, help and the experience that I have achieved.

I am pleased to acknowledge the financial support provided by the City University and the FigLeaf IT for my studies. The travel grants which I received from the Worshipful Company of Scientific Instrument Makers, the Tin-plate Workers Alias Wire Workers and the Institute of Physics are strongly appreciated.

I am also pleased to acknowledge the various supports which I received during this work from the University of Nice in France and the Victoria University in Australia.

I am thankful to all my colleagues Venu, Jackson, Dr Suchandan, Dr Shen, Dr Zhao, Dr Xie and many others, at City University for their encouragement and cooperation throughout my studies. I am grateful to Mr Jim Hooker for his technical assistance; Ms Lecha Kowalska, Ms Joan Revelline and Ms Linda Carr for their cooperation during my studies.

I am pleased to thank all my friends, my colleagues in Khulna University in Bangladesh, my parents and my brother, all my cousins and other family members for their encouragement for my studies.

Finally, special thanks to my husband, Dr Manosh Paul, for his love, patience, encouragement and support throughout my studies.

Jharna Mandal
July 2005

Copyright Declaration

The author hereby grants powers of discretion to the City University Librarian to allow this thesis to be copied in whole or in part without further reference to the author. This permission covers only single copies made for study purposes, subject to normal conditions of acknowledgement.

Abstract

This thesis focuses on the development of optical fibre Bragg grating based fibre-lasers for potential temperature sensor applications. The fabrication of both type I and type IIA Bragg gratings in B-Ge co-doped and Ge-doped photosensitive fibres was studied and their long-term temperature sustainability was evaluated. The optimisation of several wavelength-matched normal Bragg grating based fibre lasers was studied for sensor applications. The new sensor approach was developed using a *full-in-fibre* Bragg grating based laser for temperature measurement applications. A chirped fibre grating was used as the second reflector in the laser cavity to achieve temperature tuneable laser action with erbium-doped fibre as the gain medium of the laser. Normal type I or type IIA Bragg gratings were used as the sensing probes of the system, also forming the end reflector in the laser cavity. A special feature was that these gratings were fabricated in various high temperature sustainable photosensitive fibres to enhance the measurement range. The laser-based sensor was also characterised in terms of different values of applied strain to the chirped grating and the performance was compared under both active and passive operating conditions. The laser-based sensor approach was extended for the strain measurement applications when the normal grating was strained. The fabrication of type II chirped gratings was also studied, in order to create better sensor systems.

A detailed investigation into the output characteristics of a uniform wavelength-matched Bragg grating-based fibre laser was evaluated, with each individual Bragg grating acting as the reflector of the laser system, responding to temperature. An analytical model has been created, reflecting the relationship between the grating bandwidth and the temperature, under each of the operational conditions considered. The output characteristics of a very short cavity length fibre laser were analysed when it was tested in an oven. The single point laser-probe approach has been extended for multiplexed sensor applications and simultaneously multi-channel temperature information has been obtained over a wider measurement range. Finally, general conclusions on the work and recommendations for the future research have been made.

List of Publications by the author relevant to the thesis

Journal publications

1. **Jharna Mandal,** Tong Sun, Kenneth T.V. Grattan and Andreas T Augousti, "Fiber laser-based temperature sensor systems using uniform wavelength-matched Bragg grating reflectors", *Sensors and Actuators A*, vol. 120, pp. 451-461, May 2005.
2. **Jharna Mandal,** Yonghang Shen, Suchandan Pal, Tong Sun, Kenneth T.V. Grattan and Andreas T Augousti, "Bragg grating tuned fiber laser system for measurement of wider range temperature and strain", *Optics Communications*, vol. 244, pp. 111-121, January 2005.
3. **Jharna Mandal**, Tong Sun, Kenneth T.V. Grattan, Rui T. Zheng, Nam Q. Ngo and Andreas T Augousti, "A parallel multiplexed temperature sensor system using Bragg grating based fibre lasers", *accepted for publication in IEEE Sensors Journal*, 2005.
4. Suchandan Pal, Yonghong Shen, **Jharna Mandal**, Tong Sun and Kenneth T.V. Grattan, "Simultaneous measurement of strain (to 2000 με) and temperature (to 600 °C) using a combined fluorescence and grating-based technique", *accepted for publication in IEEE Sensors Journal*, 2004.
5. Y H Shen, S Pal, **J Mandal**, T Sun, K T V Grattan, S A Wade, S F Collins, G W Baxter, B Dussardier and G Monnom, "Investigation of the photosensitivity, temperature sustainability and fluorescence characteristics of several Er-doped photosensitive fibers", *Optics Communications*, vol. 237, pp. 301-308, 2004.
6. **Jharna Mandal,** Tong Sun, Kenneth T.V. Grattan, Andreas T Augousti, Scott A Wade, Stephen F Collins, Gregory W Baxter, Bernard Dussardier and Gérard Monnom, "A wide temperature tunable fibre laser using a chirped grating and a type IIA fibre Bragg grating", *Measurement Science and Technology*, vol.15, pp.1113-1119, 2004.

7. **Jharna Mandal**, Suchandan Pal, Tong Sun, Kenneth T.V. Grattan, Andreas T. Augousti and Scott A. Wade, "Bragg grating-based fiber optic laser probe for temperature sensing", *IEEE Photonics Technology Letters*, vol.16, pp. 218-220, January 2004.
8. S Pal, **J Mandal**, T Sun, K T V Grattan, M Fokine, F Carlsson, P Y Fonjallaz, S A Wade and S F Collins, "Characteristics of potential fibre Bragg grating sensor-based devices at elevated temperatures", *Measurement Science and Technology*, vol.14, pp.1131-1136, June 2003.
9. Suchandan Pal, **Jharna Mandal**, Tong Sun and Kenneth T.V. Grattan, "Analysis of thermal decay and prediction of operational lifetime for a type-I boron-germanium codoped fiber Bragg grating", *Applied Optics*, vol. 42, pp. 2188-2197, April 2003.

Conference publications

1. **Jharna Mandal**, Tong Sun, Kenneth T V Grattan, Andreas T Augousti, Scott A Wade, Stephen F Collins, Gregory W Baxter, Bernard Dussardier, Gerard Monnom, Rui T. Zheng and Nam Q. Ngo, "Strain-imposed fibre optic laser-based system for wide range temperature measurement applications", *in Proc. of OptoIreland Conference*, 4-6 April, Dublin, Ireland, 2005.
2. **Jharna Mandal**, Yonghang Shen, Suchandan Pal, Tong Sun, Kenneth T.V. Grattan, Andreas T. Augousti, Rui T. Zheng and Nam Q. Ngo, "Measurement of temperature and strain over a wide range using fibre optic laser-based sensor systems", *in Optics and Photonics Conference* (Photon 04) *Glasgow Caledonian University, Glasgow*, Proc. published by Institute of Physics, UK, pp. 10-11, Sept. 2004.
3. Suchandan Pal, Yonghang Shen, **Jharna Mandal**, Tong Sun, Kenneth T.V. Grattan, S A Wade, S F Collins, G W Baxter, B Dussardier and G Monnom, "Comparison of Sn and Sb-doped specialized fluorescent fibres for grating-based wide range simultaneous strain-temperature measurement applications", *in Optics and Photonics Conference* (Photon 04) *Glasgow Caledonian*

University, Glasgow, Proceedings published by Institute of Physics, UK, pp. 58-59, Sept. 2004.

4. **Jharna Mandal,** Yonghang Shen, Suchandan Pal, Tong Sun, Kenneth T.V. Grattan and Andreas T. Augousti, "Wide range of temperature and strain measurement using Bragg grating based fibre laser approach", *in Proc. of 2nd European Workshop on Optical Fiber Sensors (EWOFS'04)*, pp. 156-159, Santander, Spain, June 2004.
5. Suchandan Pal, Yonghang Shen, **Jharna Mandal**, Tong Sun and Kenneth T. V. Grattan, "Combined fluorescence and grating-based technique for wider range strain-temperature simultaneous measurement using Sb-Er doped fibre", *in Proc. of EWOFS'04*, pp.160-163, Spain, June 2004.
6. Y H Shen, S Pal, **J Mandal**, T Sun, K T V Grattan, B Dussardier, G Monnom, S A Wade, G W Baxter and S F Collins, "Characteristics of some Er^{3+}-doped fibres for Bragg grating applications", *Australian Conf. on Optics, Lasers and Spectroscopy (ACOLS 03)*, December, Melbourne, AU, Abstract 183, 2003.
7. **J Mandal**, S Pal, W Zhao, T Sun, K T V Grattan, and S A Wade, "A novel high temperature sensor based on a compact rare earth fibre laser approach", *in the Tech. Digest of 16th Int. Conf. on Optical Fiber Sensors (OFS-16)*, pp.200-203, Nara, Japan, Oct. 2003.
8. W Zhao, Y H Shen, S Pal, **J Mandal,** T Sun, K T V Grattan, and W D N Pritchard, "Optical fibre systems for measurements of high temperatures", *presented in the Conf.: On-line measurement for quality in the metals industries*, London, UK, Oct. 2003.
9. S. Pal, **J. Mandal**, Y. H. Shen, T. Sun, K. T. V. Grattan and M. Sun, "Photorefractivity of Sb-Er-Ge codoped silica fibre for writing grating with high temperature stability", *presented in the meeting on in-Fibre Gratings and Special Fibres, Photonex03*, Coventry, UK, Oct. 2003.
10. **J Mandal**, S Pal, T Sun, K T V Grattan and A T Augousti, "Optimization of erbium-doped fibre lasers and their sensor applications", *in Proc. of Sensors and their Applications XII Conference*, pp. 271-278, Sept. 2003.
11. T Sun, D I Forsyth, S A Wade S Pal, **J Mandal**, K T V Grattan, W D N Pritchard and G Garnham, "Fibre Bragg grating coupled fluorescent optical

fibre sensors", *presented at 1st Int. Conf. on Optical & Laser Diagnostics*, London, pp.153-158, December 2002.

12. S Pal, **J Mandal**, T Sun, K T V Grattan, M Fokine, F Carlsson and P Y Fonjallaz, "High temperature performance of Bragg grating devices for potential sensor applications", *in Proc. of Advanced Sensors and Instrumentation Systems for Combustion Processes*, held at the Rutherford Conference Centre, London, Oct. 2002.
13. T Sun, S Pal, **J Mandal** and K T V Grattan, "Fibre Bragg grating fabrication using fluoride excimer laser for sensing and communication applications", *in Central Laser Facility, (CLF),* Rutherford Appleton Laboratory, Oxfordshire, pp. 147-149, Annual Report 2001/ 02.
14. S Pal, **J Mandal**, T Sun and K T V Grattan, "High temperature sensor potential of Bragg gratings fabricated in different photosensitive fibres", *in Proc. of the Appl. Optics and Optoelectronics Conference* (Photon 02, Cardiff International Arena, Cardiff), Proceedings published by Institute of Physics, UK, pp. 49-50, September 2002.

Chapter 1

Introduction

1.1. Fibre Bragg grating technology in fibre lasers

The innovation that saw the development of an early fibre laser at the beginning of the 1960s has provided the foundation for the future research and development [Snitzer 1963, Koester and Snitzer 1964] in what remains an active field, spurred on by the development of low loss doped fibre. Such advances in the fabrication of optical glass fibres and opto-electronic components (e.g. couplers) have opened up the possibility of effective signal transmission through the optical medium effectively replacing the then dominant copper cable. The development and the application of optical fibre systems were further advanced by the rapid advances seen in the semiconductor technology – creating new light sources (e.g. laser diodes, light emitting diodes at suitable wavelengths) and photo detectors and suitable optical waveguide technology. Improvements in fibre materials have brought down the transmission losses to a level that is so low that the optical-medium has now become the more important wide-bandwidth (several GHz range) transmission medium.

In addition, the successful incorporation of a range of rare-earth ions into the core of an optical fibre has offered both a low propagation loss and potentially attractive laser properties for telecommunications, sensors and high-resolution spectroscopic applications. The output spectral characteristics of the rare-earth doped fibre used can be varied by changing the doping composition of the host material. In addition, the long lifetime of the metastable state, for example, erbium-doped fibre favours the required high population inversion that can be achieved using the available pump sources [Digonnet 1993].

Fibre Bragg gratings (FBGs) have become important components of a wide range of sensor systems, since their first successful fabrication in the late 1970s and development in the late 1980s, for temperature, strain, chemical sensing and in the aerospace (e.g. parts of airplane wings) and electric power industries, for example [Kersey *et al.* 1997, Rao 1999]. The main advantage of this type of sensor is the use of wavelength-encoded measurement information, thus making the sensor effectively self-referencing. The additional advantages of using FBGs in sensors are their light weight nature, immunity to electromagnetic interference (EMI), stability, high temperature tolerance and the potential for reproducible measurements information. The key issue is the determination of the small, measurand-induced Bragg wavelength shift, using a broadband light-source and an appropriate detection scheme. However, due to the narrow-band nature of the Bragg wavelength, the output power reflected from this type of source is often quite weak, which can lead to a poor signal-to-noise ratio (SNR) in the measurement system, which may limit the number of FBGs that can be interrogated in a distributed sensor scheme.

Another interesting grating structure that has been widely used for dispersion compensation in high-bit rate transmission system is known as the chirped fibre Bragg grating (CFBG) [Othonos and Kalli 1999]. Its monotonically varying period is favoured for several specific telecommunication applications. Recently, this type of device has been reported for passive sensor applications, for example, for strain monitoring applications [Kim *et al.* 2000].

The development of FBGs has enhanced the functionality and potential of optical fibre lasers. The capability to fabricate FBGs directly into rare-earth doped fibres or the integration of gratings into the rare-earth doped fibre with low loss and excellent wavelength selectivity has reinvigorated fiber laser technology. In fibre Bragg grating based fibre lasers, either two wavelength-matched fibre Bragg gratings or one grating combined with a broadband mirror are typically used to provide cavity feedback of the signal in the fibre, together with the active gain medium (rare-earth doped fibre) to create an optical oscillator. An external energy source, i.e. the pump source is required for the gain medium to absorb the pump photons at an appropriate wavelength and

thus to produce the stimulated emission to allow the laser oscillation to occur [Wilson and Hawkes 1987].

In fibre laser-based sensor applications, the changes in the laser wavelength arise from the changes in the Bragg wavelength when any external perturbation, for example, strain or temperature is applied. In a similar way to the fibre Bragg grating sensing scheme, the inherent wavelength-addressing capabilities of Bragg gratings allow the distributed laser-sensors to be created. The main advantage of the fibre laser-based sensors scheme is an increased signal-to-noise ratio (SNR) over a passive FBG sensor scheme. In addition, they provide narrow linewidth signals compared with those reflected from the passive grating element, thus making the device highly sensitive to small perturbations of the measurands. The signal amplification in these sensors is occurring in the optical domain rather than in the electronic domain, for intrinsic fibre laser devices [Kim 1998].

Fibre Bragg grating based fibre-lasers has been extensively used for strain sensing applications [Melle *et al.* 1993, Kersey and Morey 1993] but over a limited range of temperature, typically less than 200 °C [Ball *et al.* 1993, Alavie *et al.* 1993]. A limitation of uniform wavelength-matched Bragg grating based laser sensors is that both the gratings should be in the same measurand-state e.g. both exposed to the temperature or strain to be measured. Bragg grating based optical fibre laser systems has also been used for serial multiplexed sensor applications [Alavie *et al.* 1993] where a common broadband mirror and two FBGs were used to form the laser cavities. Yet the development of a *full-in-fibre* laser-based sensor system, especially for temperature sensing applications remains as an ongoing challenge and the major subject of this work.

1.2. Aims and Objectives of the work

The major objective of this work is to develop fibre Bragg grating based fibre laser sensors for high temperature applications. The achievement of a high signal-to-noise ratio (SNR) is important for remote measurement applications, thus allowing greater measurement resolution and multiple-channel interrogation. The limitation on high

temperature measurements to date has arisen from the lack of the availability of high-temperature sustainable photosensitive fibres in which the gratings are photo-imprinted. Thus the main objectives of this work are summarised as follows:

- A review of the development and the background of fibre laser technology and its potential for sensor application: recognition of the "gap in the market".
- The evaluation of the characteristics of candidate high temperature sustainable optical fibres both commercially available and fabricated through work at partner organisations.
- Fabrication of fibre Bragg gratings into the above fibres and an analysis of their temperature characteristics.
- Creation of a *full-in-fibre* Bragg grating based laser scheme for sensor applications, thus simplifying the alignment and use of the whole sensor system.
- Extension of the temperature measurement range of such a system by employing a high temperature sustainable sensing grating in the system.
- Extension of the sensor system for strain monitoring applications.
- Evaluation of the performance of the uniform wavelength-matched Bragg gratings based laser sensors when each individual Bragg grating, acting as the reflectors of the laser system, responds to temperature.
- Exploration of the optimum laser technology for potential multiplexed sensor applications.
- Publication of relevant results in international literature.

1.3. Structure of the thesis

The research was carried out to meet the above aims and objectives creating new developments in optical fibre laser-based sensor technology.

Following this brief introduction, as Chapter 1, Chapter 2 presents the background to fibre Bragg gratings, their fabrication and the long-term thermal analysis of the gratings created for high temperature use.

Chapter 3 comprises a review of the background to the optical fibre laser technology used and its optimisation for sensor applications, taking into consideration a range of factors, including the reflectivities of the matched-pair FBGs, different types of erbium-doped fibre as the gain medium, fibre length and concentration consideration and the use of different cavity configurations.

Chapter 4 is a detailed review of optical fibre-laser based sensor systems and the theoretical background to the temperature response of the lasers. This chapter introduces a new approach based on a *full-in-fibre* Bragg grating based laser for high temperature sensing applications. The use of a *chirped fibre Bragg grating* (CFBG) as one of the cavity reflectors allows temperature tunable-laser action to be achieved over a wide measurand range. Erbium-doped fibre was used as the gain medium of the laser based on the results obtained from Chapter 3. A normal Bragg grating was used as the wavelength selective and the sensing element of the system and forming the end reflector in the laser cavity. The characteristics of such systems were reversed and analysed.

Chapter 5 discusses the characterisation of a wide temperature tuneable fibre laser using a range of values of applied strain to the chirped grating which forms the second reflector in the laser cavity. The type IIA Bragg grating was used as the sensing element of the system because of its high temperature sustainability, using a similar experimental set-up to that in Chapter 4. The active sensor performance was calibrated using both zero strain and different values of applied strain to the chirped grating when kept at ambient temperature, and the results were compared with the passive operating conditions of the device.

Chapter 6 shows the use of a novel high temperature sustainable type I Bragg grating fabricated in an antimony-germanium (Sb-Ge) co-doped photosensitive fibre. The fabrication of type IIA chirped Bragg gratings in boron-germanium co-doped fibre were achieved for the first time to our knowledge. By incorporating both the gratings in laser configuration, the temperature measured was raised up to 500 °C and the strain monitored up to 1200 με.

Chapter 7 characterises the performance of the uniform wavelength-matched pair of gratings incorporated in a laser for sensor applications with each individual fibre Bragg grating, acting as the reflectors of the laser system, allowing this to respond to temperature. An analytical model has been created for the first time reflecting the relationship between the grating bandwidth and the temperature under each operational condition; and the results obtained have significant implication for the optimum design of this type of fibre laser for temperature measurement applications. The output characteristics of a very short cavity length fibre laser were analysed when it was placed in an oven, simulating its use in temperature measurement.

Chapter 8 extends the single point laser probe approach developed in Chapters 4, 5 and 6 into parallel, multiplexed temperature sensing applications. Multiple laser cavities were formed using a common broadband-chirped grating and several normal fibre Bragg gratings as optical feedback elements were used in conjunction with different lengths of erbium-doped fibres (EDFs) as the independent gain medium of the laser. Another experiment was performed by placing a shared gain medium in front of the splitter and the results obtained showed severe gain-competition across the laser channels. Simultaneous laser oscillation at three different wavelengths was obtained without gain-competition when separate-gain medium was placed across each channel after the splitter and the temperature was measured over the range from room temperature (27 °C) to a maximum of 540 °C when normal fibre Bragg grating was placed in the oven.

Chapter 9 presents a brief concluding discussion of the work and recommendations for future research in this field.

1.4. References

- Alavie, A.T., Karr, S.E., Othonos, A. and Measures, R.M. (1993) A Multiplexed Bragg grating fiber laser sensor system, *IEEE Photon. Technol. Lett.*, vol. 5, pp. 1112-1114.
- Ball, G.A., Morey, W.W. and Cheo, P.K. (1993) Single-and multipoint fiber-laser sensors, *IEEE Photon. Technol. Lett.*, vol. 5, pp. 267-270.
- Digonnet, M.J.F. (1993) *Rare Earth Doped Fiber Lasers and Amplifiers*, Marcel Dekker, New York.
- Kersey, A.D. and Morey, W.W. (1993) Multi-element Bragg-grating based fibre-laser strain-sensor, *Electron. Lett.*, vol. 29, pp. 964-966.
- Kersey, A.D., Davis, M.A., Patrick, H.J., LeBlanc, M., Koo, K.P., Askins, C.G., Putnam, M.A. and Friebele, E.J. (1997) Fiber grating sensors, *IEEE J. Lightwave Technol.*, vol. 15, pp. 1442-1463.
- Kim, S., Kwon, J., Kim, S. and Lee, B. (2000) Temperature-independent strain sensor using a chirped grating partially embedded in a glass tube, *IEEE Photon. Technol. Lett.*, vol.12, pp. 678-680.
- Kim, B.Y. (1998) *Fiber lasers in Optical Sensors*, in *Optical Fiber Sensor Technology*, 1st ed., vol. 2, Grattan, K.T.V. and Meggitt, B.T. Eds., London: Chapman & Hall, pp. 99-115.
- Koester, C.J. and Snitzer, E. (1964) Amplification in a fiber laser, *Appl. Opt.*, vol. 3, pp. 1182-1186.
- Melle, S.M., Alavie, A.T., Karr, S., Coroy, T., Liu, K. and Measures, R.M. (1993) A Bragg grating-tuned fiber laser strain sensor system, *IEEE Photon. Technol. Lett.*, vol. 5, pp. 263-266.
- Othonos, A. and Kalli, K. (1999) *Fiber Bragg Gratings: Fundamentals and Applications in Telecommunications and Sensing*, Artech House, Boston.
- Rao, Y.J. (1999) Recent progress in applications of in-fibre Bragg grating sensors, *Optics and Lasers in Engg.*, vol. 31, pp. 297-324.
- Snitzer, E. (1963) Neodymium glass laser, *Proc. on 3rd Int. Conf. on Solid State Lasers*, Paris, France, pp. 999-1019.
- Wilson, J. and Hawkes, J.F.B. (1987) *Lasers: Principles and Applications*, Prentice Hall International Ltd., UK.

Chapter 2

Fabrication of fibre Bragg gratings and their characterisation for high temperature applications

2.1. Abstract

This Chapter describes the mechanism of fibre photosensitivity (the absorption of ultra violet light in the optical fibre core) and the formation of fibre Bragg gratings. Different techniques have been used to enhance the fibre photosensitivity and to fabricate the fibre Bragg gratings; and these are reviewed. The various properties, which characterise the Bragg gratings used, are studied. The detailed growth behaviour of both type I and type IIA fibre Bragg gratings in B-Ge co-doped and Ge-doped photosensitive fibres was observed. The long-term thermal analysis of these gratings was carried-out involving a series of step-wise incremental temperature changes from 100 °C to a maximum of 750 °C, for more than 48 hours at each temperature before extending the temperature range. The thermal decay of the gratings was analysed in terms of the decay in the reflectivity and the refractive index modulation and their Bragg wavelengths variation with temperature were also studied. Finally the calibration of the grating sensitivity at different temperatures was performed, followed by a presentation of an overall summary of the results of the chapter.

2.2. Introduction

Fibre Bragg gratings (FBGs) have shown themselves to be important components for a range of sensor and telecommunication applications [Othonos and Kalli 1999, Rao 1999]. Highly reflective Bragg gratings are often used as mirrors in fibre laser-based

sensor or communications applications. The advantages of the use of FBGs are their light weight, their immunity to electromagnetic interference (EMI), small-size, higher bandwidth than conventional copper cables, reliability and wavelength-encoded measurement information, thus making the sensor self-referencing and high-temperature tolerant. The photosensitivity of optical fibres allows for the fabrication of Bragg gratings in the optical fibre core. The strength (high or low reflectivity) of these gratings is often determined by the UV-induced refractive index modulation in the fibre core. Hill and co-workers first reported the fabrication of Bragg gratings in germanium-doped optical fibres in 1978. Over the last several years, a number of researchers around the world have investigated the fundamental properties of Bragg gratings, their thermal stability and potential applications. Different techniques have been used to enhance the photosensitivity of germanium-doped and standard telecommunication optical fibres (typical germanium content ~ 3 mol %) to increase the induced refractive index modulation of the desired gratings. The thermal stability of the FBGs is an important feature to be studied before these devices could be used for practical applications. Thermal annealing is used to wipe out the unstable (shadow) portion of the gratings and thus to achieve reproducible performance of the sensors using them, typically up to the annealing temperature. It is important to assess the quality and the durability of gratings fabricated in different photosensitive fibres through temperature trials.

In this chapter, both type I and type IIA Bragg gratings were fabricated in B-Ge co-doped and Ge-doped photosensitive fibres. The growth behaviour of these gratings was observed online through measuring the transmission spectrum profile and the Bragg wavelength shift with UV-exposure time, using an optical spectrum analyser (OSA) and a broadband light source. Long-term thermal testing of these gratings was carried out by placing them in an oven subjected to a series of step-wise incremental temperature variation from 100 °C to a maximum of 750 °C and their performances were monitored at each specific temperature. The thermal characteristics of the gratings were analysed in terms of the decay in reflectivity, the refractive index modulation and their Bragg wavelengths variation with temperature. Finally the thermal sensitivity of these gratings was calibrated.

2.3. Theoretical Background

This section reviews the literature on the formation and the origin of the fibre Bragg gratings in optical fibres are an important feature of the work reported in this thesis.

2.3.1. Photosensitivity and formation of grating

Hill *et al.* [1978] were first to report the fibre photosensitivity in germanium-doped silica fibre. During an experiment to study the nonlinear effects in a specially designed optical fibre, intense visible light at 488 nm wavelength from an Argon ion laser was launched into the core of the fibre. During the exposure, it was observed that the intensity of the light back-reflected from the fibre increased significantly with time and almost all of the incident light back-reflected from the fibre under prolonged exposure. Spectral measurements confirmed that the increase in the reflected light of the fibre was due to a permanent refractive index modulation over the exposed fibre length. The photo-induced refractive index modulation of optical fibres is termed fibre photosensitivity, where the high intensity-points in the input beam alter the refractive index of the photosensitive fibre core permanently. The coherent light propagating in the fibre interferes with a small amount of light back-reflected from the end of the fibre to create a standing wave pattern in the fibre core which creates a photo-induced refractive index grating. As the strength of the grating increases, the intensity of the back-reflected light increases until the reflectivity of the grating reached a saturation point. In this way, a grating with 90 % reflectivity was observed, arising from a weak refractive index modulation in the order of 10^{-5}-10^{-6}. Although the discovery of the photosensitivity in the form of a photo-induced refractive index change emerged to be an ideal mechanism for the fabrication of gratings in optical fibres, unfortunately the so called "Hill gratings" wavelength was limited to the writing light wavelength (488 nm). The wavelength response of the grating was observed to be very small when it was strained.

Meltz *et al.* [1989] first reported the fabrication of fibre Bragg gratings in germanosilicate optical fibres using a holographic exposure arrangements. The Bragg wavelength of the gratings thus created can be varied by varying the incident

wavelength and the angle of the two interfering UV beams, which showed the possibility of grating fabrication in the important telecommunication window, thus eliminates the writing laser wavelength limitation of "Hill gratings". The refractive index modulations achieved was ~ 3×10^{-5}, showing a reflectivity of 50 - 55 %, with Bragg wavelengths of ~ 577 - 591 nm. The magnitude of the refractive index modulation obtained has been shown to depend on several factors, for example, the writing wavelength, the writing beam intensity, total dosage of irradiating light, the composition of the fibre core materials and any pre-processing of the fibre prior to irradiation.

A wide variety of laser sources (continuous wave and pulsed wave) with wavelengths ranging from the visible to the vacuum ultraviolet has been used to create a photo-induced refractive index modulation in the core of optical fibres. The most commonly used, practical light sources are KrF and ArF excimer lasers, operating at the wavelengths of 248 nm and 193 nm, respectively.

2.3.2. Mechanism of Photosensitivity

The photosensitivity that occurred in germanium-doped optical fibre core was believed to originate from germanium-oxygen vacancy defects, such as the twofold coordinate neutral germanium atom: O-Ge-O or Ge_2^0 centre; or Ge-Si or Ge-Ge, the so called "wrong bonds" are responsible for the photo-induced index changes.

2.3.2.1. Origin of defects in germanosilicate glass fibre

Hosono *et al.* [1992] have reported the origin of a 5 eV (~ 240 nm) absorption band in germanosilicate glass due to neutral oxygen monovacancies coordinated by two Ge ions (Ge-Si or Ge-Ge wrong bonds). The optical and the electron paramagnetic resonance (ESR) spectra measurement arising from chemical vapour deposition GeO_2: SiO_2 (germanosilicate) glass samples using a 500 W filtered Hg/Xe lamp irradiation have showed that an absorption band centred at 5 eV is composed of two components. One has an absorption band peak at 5.06 eV with a full-width-half maximum (FWHM) bandwidth of 0.38 eV and the second has an absorption band at 5.16 eV

with a FWHM of 0.48 eV. The UV light irradiation bleached the 5.06 eV band, and generated GeE′ centres. The formation of such GeE′ centres increases in parallel with the bleaching in the intensity of the 5.06 eV band. The shape of the UV bleached band centred at 5.06 eV was found to be Gaussian. The activation energy required for the conversion process was of the order of 10^{-2} eV and a second band at 5.16 eV remains unbleached under UV irradiation, but emits intense luminescence at 3.2 eV (~ 400 nm), along with a weak signal at 4.3 eV (~ 290 nm). This second component has been assigned to Ge^{2+} ions coordinated by two oxygen atoms and having two lone pair electrons (neutral oxygen divacancies). The conversion of neutral oxygen monovacancies (a possible GODC) to GeE′ and the release of an electron have been expressed below [Hosono *et al.* 1992] by:

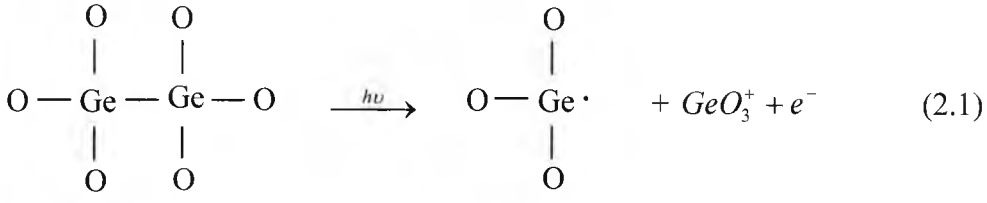

(2.1)

GODC GeE′

where · denotes a nonbonding (unpaired) electron.

Tsai *et al.* [1994] have proposed that a divacancy-type oxygen deficiency centre (ODC) associated with Ge is responsible for the 5.16 eV absorption band in silica and Ge-doped fibres. Two coordinated defects can react with atomic hydrogen (H^0) to form hydrogen-associated paramagnetic centres and the reaction may be expressed as shown below:

$$-\ddot{\mathrm{T}}- + \mathrm{H}^{\circ} \rightarrow =\dot{\mathrm{T}} - \mathrm{H} \qquad (2.2)$$

where T is Si or Ge and · denotes an unpaired electron. When T = Ge, a 11.9 mT (magnetic field) doublet electron spin resonance (ESR) is proposed to exist, making it possible to directly correlate temperature-induced changes in the 5.16 eV band and the corresponding changes in the UV induced, hydrogen-associated paramagnetic defects. For this, the optical absorption coefficients of the 5.16 eV band of Ge-doped samples with different concentrations (100 ppm, 180 ppm) were studied. The 5.16 eV absorption coefficient was found to increase approximately as the square root of the

germanium concentration in silica, which suggests that this band is an oxygen deficiency centre (ODC) divacancy-type defect, associated with Ge [Tsai *et al.* 1994], rather than a two-coordinated Ge ions (Ge^{2+}), as proposed by Hosono *et al.* [1992]. At high temperature during the glass manufacturing process, two germanium oxygen deficiency centres (GODCs) of a Ge divacancy are in thermochemical equilibrium with a GeO_2 in silica and this may be expressed as shown below:

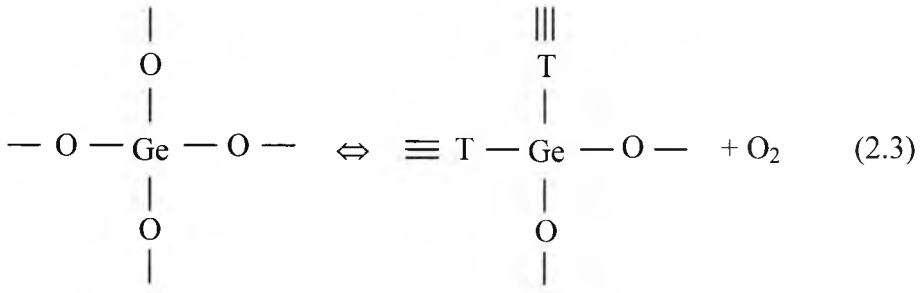

(2.3)

where T is Ge or Si. Since each divacancy defect contains two ODCs, the thermochemical equilibrium constant, k, was defined as follows:

$$k = [ODC]^2 [O_2] / [GeO_2], \qquad (2.4)$$

where [ODC] is the molar concentration of the oxygen deficiency centre (ODC), $[O_2]$ is the partial pressure of O_2 during the glass manufacturing process and $[GeO_2]$ is the molar concentration of GeO_2. From the above equation, it is clear that the square of the ODC concentration is linearly proportional to GeO_2, and therefore, the higher the Ge concentration, the more ODC will be created.

Nishi *et al.* [1995] have reported the comparison between Hg lamp and excimer laser irradiation of vapour-phase axial deposition (VAD) germanosilicate glass samples and showed two photochemical reaction channels. Hg lamp irradiation (~ 16 mW/cm^2 at 4.9 eV) induced GeE′ centres in addition to the bleaching of the absorption band due to oxygen deficient-defects (5 eV band) and the emergence of an intense band near 6.4 eV; this is occurred via a one-photon absorption process. Irradiation with KrF (5.0 eV) and XeCl (4.0 eV) lasers (at power densities of 10 and 90 mJ/cm^2/pulse, respectively) generated two types of paramagnetic defects: electron trapped centres associated with fourfold coordinated Ge ions (so called germanium-electron centres (GEC)), and self trapped hole centres (STH), i.e. bridging oxygen trapping a hole, which occurred via a two-photon absorption process. These photochemical reactions,

through one and two photon absorption processes, proceeded independently in the glass matrix - depending on the power densities of the UV photon irradiation. The formation of GECs was saturated easily with KrF excimer laser irradiation, and finally GECs converted to GeE′ centres under prolonged irradiation. The optical band gap energy (E_g = 7.1 eV) of the germanosilicate glass sample used was lower than twice the photon energies of the KrF and XeCl excimer lasers. The simultaneous formation of GECs and STHs via two-photon absorption process with excimer laser irradiation was expressed through the following reaction [Nishi *et al.* 1995]:

$$\begin{array}{c} | \\ -\mathrm{Ge}- \\ | \end{array} \quad + \quad -\ddot{\mathrm{O}}- \quad \xrightarrow{2h\upsilon} \quad \mathrm{GEC} + \mathrm{STH} \qquad (2.5)$$

Four-fold coordinated — Bridging oxygen

The lone pair electrons on bridging oxygens are excited to the conduction band from the valance band via a two-photon absorption process with excimer laser irradiation; and produced GEC and STH simultaneously. The conversion of the GEC to GeE′ centre may be described using the following reaction:

$$\mathrm{GEC} \rightarrow \mathrm{GeE'} + \mathrm{O\ (nonbridging\ oxygen)} \qquad (2.6)$$

The conversion of the GEC into GeE′ centres was regarded as a structural relaxation of the germanosilicate glass matrix [Nishi *et al.* 1995]. The term GEC centres has been used as abbreviation for Ge(1) or Ge(2) centres depending on the number of the nearest-neighbour Ge ions. The Ge(1) centre is coordinated to four O-Si bonds and the Ge(2) centre is coordinated to three O-Si bonds and to one O-Ge bond, as expressed below [Secats *et al.* 1993]:

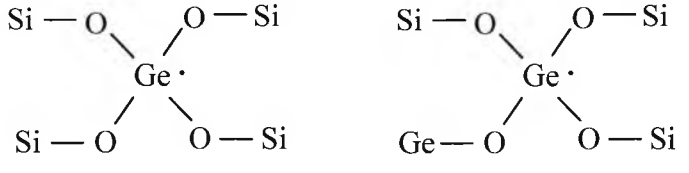

(2.7)

Ge(1) Ge(2)

The Ge(1) or Ge(2) centre can trap an electron to convert it into a $Ge(1)^-$ or $Ge(2)^-$ centre [Sceats *et al.* 1993].

Hosono *et al.* [1996] have reported a detailed relationship between the germanium electron centre (GEC) formation in germanosilicate glasses and the photon energy densities of various excimer lasers. Three different types of excimer laser (ArF: 6.4 eV, KrF: 5.0 eV; XeCl: 4.0 eV) irradiation was used in germanosilicate glasses. The concentration of GEC produced per pulse (N) is plotted in log-log plots as a function of the energy density of the laser light per pulse (I) and the slope for each excimer laser wavelength was found to be ~ 2. For each excimer laser, the GEC conversion is given by: $N = kI^2$, where k represents the apparent formation efficiency and these results have showed that GEC formation occurred via a two-photon absorption process. Although the KrF (photon energy of 5.0 eV) excimer laser wavelength corresponds closely to the absorption band of the pre-existing GODCs (5.06 eV) of germanosilicate glasses, the formation efficiency (k) of the KrF laser light was found to be almost the same as that of the ArF excimer laser light but it was four orders of magnitude lower for the XeCl laser light. This observation showed that germanium electron centres (GECs) are not derived from the originator defects in glass but from the intrinsic structure of the GeO_4 units. Therefore, the defect formation efficiency was reported to be much higher when the two-photon energy (for KrF, ArF lasers) is sufficient to exceed the optical band gap of germanosilicate glasses compared to the two-photon energy (for XeCl laser) that is close to the optical band gap [Hosono *et al.* 1996]. The formation of the GeE′ centres was derived from the oxygen deficiency centres (ODCs) coordinated by 2 Ge ions which occurred by trapping a positive hole (h^+), following a structural relaxation of the GeO_3^* into a planar form and this was expressed through the following reaction [Hosono *et al.* 1996]:

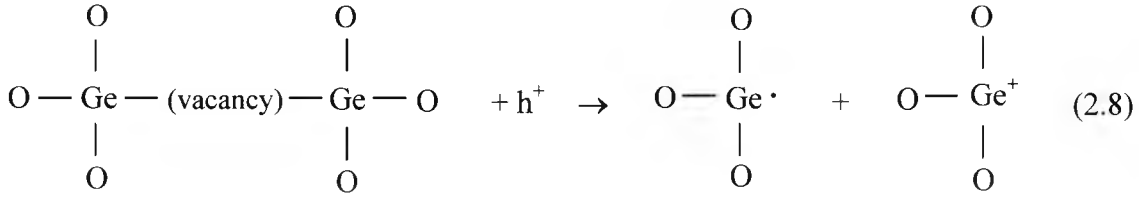

(2.8)

Therefore, no formation of SiE′ (Si-electron trapped) centres was observed in the germanosilicate glasses when irradiated by light from excimer lasers.

2.3.3. Mechanism of photoinduced refractive index change

Two main mechanisms are responsible for the photo-induced refractive index changes in germanium-doped optical fibres. The first is based on the colour-centre related changes in the UV absorption spectrum which gives rise to refractive index changes in the fibre core [Hand and Russell 1990] and the second of these mechanisms is based on the UV light-induced structural changes in the glass matrix which gives rise to refractive index changes in the fibre core [Fiori and Devine 1986; and Russell *et al.* 1991]. The photosensitivity occurring in germanium-doped optical fibre is due to the germanium-oxygen deficiency centres (GODCs), Ge-Si or Ge-Ge (the so called "wrong bonds") which is believed to be responsible for the photo-induced index changes. During the high temperature gas phase oxidation process of the modified chemical vapour deposition (MCVD) technique preform, the Ge^{+4} oxidation state, i.e. GeO_2 converts into the more stable GeO (Ge^{+2}) molecule (and results in an oxygen deficient matrix) at elevated temperatures [Sceats *et al.* 1993]. During the fibre drawing process, this molecule (GeO) can manifest itself in the form of an oxygen vacancy Ge-Si and Ge-Ge "wrong bonds". This oxygen vacancy wrong bond is linked to the absorption band over the wavelength ranges of 240-250 nm.

Hand and Russell [1990] were first to propose the colour-centre model to explain the visible light induced refractive index change in germanosilicate fibres by the bleaching of the absorption band at 240 nm. According to this model, the photo-induced changes in the properties of the glass material originate localised electronic excitations and transition of defects. These colour-centre defects, due to their strong optical absorption of UV light, cause changes in the refractive index of the fibre core. The bleachable "wrong bond" defects (Ge-Si, or Ge-Ge), which absorb the UV light, are formed GeE′ centres and releasing electrons that are free to move through the glass matrix until eventually either recombining with another GeE′ or are trapped at Ge(1) or Ge(2) dopant sites to form $Ge(1)^-$ or $Ge(2)^-$ colour-centres [Russell *et al.* 1991]. Therefore, the refractive index change at a point is related to the number density and orientation of defects in that region and is determined by their electronic absorption spectra. The changes of the refractive index $\Delta n(\lambda')$ are linked to the photo-induced absorption spectrum changes, $\Delta\alpha(\lambda)$, through the Kramers-Kronig (KK)

relationship and the KK relationship may be expressed as shown below [Leconte *et al.* 1997]:

$$\Delta n(\lambda') = \frac{1}{2\pi^2} \int_{\lambda_1}^{\lambda_2} \frac{\Delta\alpha(\lambda)}{1-\left(\frac{\lambda}{\lambda'}\right)^2} d\lambda , \qquad (2.9)$$

where λ_1 and λ_2 are the boundaries of the spectral range within which the absorption changes need to be considered and λ' is the wavelength at which the refractive index changes would be calculated. The above equation is valid for $\lambda' >> \lambda_2 > \lambda_1$. The KK relationship arises from the causality condition for dielectric response (null response before application of a perturbation) and corresponds to that of the index changes produced in the infrared/visible spectral region by the UV/far-UV induced absorption spectrum changes of the glasses.

Several researchers have supported the evidence for colour-centre related changes in the UV absorption spectrum giving rise to refractive index changes in the fibre core [Williams *et al.* 1992, Atkins *et al.* 1993, Leconte *et al.* 1997]. With prolonged UV exposure, the spectrum changes have showed that the defect band at 241 nm is bleached and a broad new absorption band centred at ~ 195 nm appears. It is believed that the growth of the new absorption band centred near 6.35 eV (195 nm) might be responsible for GeE′ centres and the bleaching of the 5.1 eV (242 nm) band corresponds to the GeO band. The refractive index change calculated ($\sim 3 \times 10^{-5}$) from the Bragg gratings is in good agreement with that of the refractive index estimated ($\sim 4.5 \times 10^{-5}$) using the colour-centre model [Atkins *et al.* 1993]. It was also reported that the UV induced index changes are thermally reversible when the sample was heated at 900 °C for 1 hour; and this is consistent with the mechanism of the grating formation where absorption changes play a major role.

Fiori and Devine [1986] have reported that the refractive index changes arise from the UV light-induced structural changes in the glass matrix. The UV laser light irradiation at 248 nm, at intensities well below the breakdown threshold (an accumulated dose of ~ 2000 J/cm^2) creates the linear compaction, leading to the refractive index change, which was found to be thermally reversible. After annealing at 950 °C for 1 hour, the

compaction disappears; and the original sample thickness and the refractive index (before writing) could be retrieved. With continuous exposure of the sample beyond the reversible compaction region, irreversible compaction and etching have occurred, until the 100 nm oxide sample was totally etched for a total accumulated dose of ~17000 J/cm^2. An approximately linear relationship has been obtained for the photo-induced refractive index change as a function of the observed density change of the glass. The linear compaction ($\Delta t/t$) is translated to a volume change ($\Delta V/V$) through the following relationship [Fiori and Devine 1986]:

$$\frac{\Delta V}{V} = \frac{3\left(\frac{\Delta t}{t}\right)}{(1+2\nu)}, \tag{2.10}$$

where ν is the Poisson's ratio. The refractivity (R) was obtained from the Lorentz-Lorenz relationship and this was expressed as below:

$$R = \frac{(n^2-1)}{g(n^2+2)}, \tag{2.11}$$

where g is the specific gravity and n is the refractive index. The refractive index modulation was obtained as below by differentiation of the above Eq. (2.11) and combining Eq. (2.10) [Fiori and Devine 1986]:

$$\Delta n = -\frac{(n^2+2)(n^2-1)}{6n}\left[1-\frac{\Delta R}{R(\Delta V/V)}\right]\frac{\Delta V}{V}, \tag{2.12}$$

For $(V/R)\Delta R/\Delta V<1$, compaction produces an increase in the refractive index as observed by Fiori and Devine [1986]. The first term in the parentheses related to volume changes in the structure and the second term, for the case of SiO_2 is concerned, relates to the volume of the oxygen ion itself.

Limberger *et al.* [1996] have studied the compaction and the photoelastic-induced index changes in fibre Bragg gratings. A strong increase of the tension in the fibre core was observed with the formation of the Bragg grating, in opposition to the result of the stress-relief model [Sceats *et al.* 1993]. This tension increase lowers the refractive index due to the photoelastic effects. On the other hand, compaction of the

core network results in an increased refractive index. The two contributions were evaluated from the axial stress measurements (from the amplitude of the refractive index modulation and from the mean index change of the Bragg gratings). The total Bragg grating index modulation (Δn - superposition of the photoelastic and the compaction contribution) has a positive mean value, and this was explained by a structural modification of the germanosilicate core network. The mean refractive index (Δn_{mean}) was found to be positive since the Bragg wavelength shifts towards the longer wavelength side of the spectrum during the irradiation. The amplitude of the refractive index change due to the photoelasticity was found to be inverted with respect to the compaction-induced index modulation. It was also found that the total Bragg grating index modulation is smaller than the compaction-induced index modulation by 30-35 % due to the photoelastic effect. Thus the refractive index increase was explained in that work from the more positive contribution to the total index change due to the structural modification of the fibre core than the negative index change due to photoelasticity. It was argued that the colour-centre modifications could not account for an index change larger than 2×10^{-4} [Dong *et al.* 1995a], hence, a structural modification leading to the compaction of the glass matrix must be the main contribution (inelastic) to the observed index change [Limberger *et al.* 1996].

Douay *et al.* [1997] have reported a comprehensive study into densification involved in the UV induced photosensitivity of silica glasses and optical fibres. A comparison of densification in hydrogen-loaded and non-hydrogen-loaded preform slices was carried out to determine whether hydrogen involves to the densification process. Densification (permanent displacement) changes the volume of the glass. The photoelastic densification model could account for a large part (40 %) of the refractive index change in non-hydrogen loaded germanosilicate or aluminosilicate preform plates. Though hydrogen loading enhances the UV photosensitivity, no increase in the densification following hydrogen loading was observed in the germanosilicate preform. The refractive index modulation (Δn) in non-hydrogen loaded germanosilicate fibre was found to be thermally reversible, whereas the mean index was not. It is believed that a heating-induced increase in the mean refractive index comes from the thermal compaction of the germanosilicate fibre core and densification accounts for the major part of the UV-induced refractive modulation,

and the thermal reversibility of the refractive index modulation shows that the heating-induced compaction of the fibre core does not prevent further UV-induced densification.

However, it still remains a matter for debate as to how to determine accurately the extent to which each model accounts for the light-induced refractive index changes of the fibre Bragg gratings used in this work.

2.4. Enhancement of photosensitivity

After the discovery of photosensitivity [Hill *et al.* 1978] and the successful fabrication of fibre Bragg gratings in germanosilicate fibres, considerable efforts were taken to understand more fully to increase the photosensitivity of optical fibres. To enhance the photosensitivity of germanosilicate optical fibres, the following techniques were adopted:

2.4.1. Hydrogen loading

Lemaire *et al.* [1993] have reported using high-pressure hydrogen loading technique to enhance the UV photosensitivity of germanosilicate and standard telecommunication fibres. The hydrogen-loading process is carried out by diffusing hydrogen molecules into the fibres at high pressure (~ 20 atm to 750 atm) and low temperature (~ 21 °C to 80 °C). With UV exposure, the dissolved hydrogen molecules react with Si-O-Ge sites in the germanosilicate glass, resulting in the formation of Si-OH absorbing species and germanium-oxygen-deficiency centres which enhances the growth of the 240 nm absorption band, and thus accounting for the enhanced photosensitivity of the optical fibres. Refractive index changes as high as 5.9×10^{-3} have been achieved in standard telecommunication fibres loaded with 3.3 mol % H_2. The main advantage of the hydrogen-loading technique is that it allows strong Bragg gratings to be fabricated in any germanosilicate fibre; in addition in standard telecommunication fibres with a low germanium concentration (~ 3 mol %). The refractive index changes were obtained in the fibre region which was UV irradiated. The unreacted hydrogen in the unexposed UV region of the fibre slowly diffuses out,

thus giving negligible absorption losses at the optical communication windows. Also, the fibre loses its photosensitivity as the hydrogen diffuses out.

2.4.2. Flame Brushing

Flame brushing is another technique used to enhance the photosensitivity in germanosilicate fibre [Bilodeau *et al.* 1993]. Using this technique, the region of the optical fibre to be photosensitised is "brushed" repeatedly using a hydrogen-rich-flame (flamed fuelled with hydrogen) with a small amount of oxygen. The flame temperature reaches as high as 1700 °C and the photo-sensitisation process takes ~ 20 minutes to complete. At high temperature, the hydrogen diffuses quickly into the core of the fibre and reacts with the germanium glass to create germanium-oxygen-deficiency centres which enhance the 240 nm absorption band in the germanium-doped fibre. The flame-brushing technique thus enhances the photosensitivity of the standard telecommunication fibres by a factor greater than 10 and achieves a large refractive index modulation of $>10^{-3}$. Both the enhanced photosensitive techniques (the flame-brushing and the hydrogen-loading) in the germanosilicate glass fibres use hydrogen to react chemically with Ge sites to create the germanium-oxygen-deficiency centres (GODCs) which are responsible for the photosensitivity. UV irradiation bleaches the GODCs band to increase the refractive index modulation of the fibre core. The flame brushing technique is advantageous compared to the hydrogen loading technique because the raised photosensitivity of the fibre is permanent, whereas in hydro-generation techniques the fibre loses its photosensitivity as the hydrogen molecule diffuses out of the fibre core. The disadvantage of this technique is that the high-temperature flame weakens the fibre strength.

2.4.3. Co-doping

Williams *et al.* [1993] have shown that boron co-doping is a technique that enhances the photosensitivity of the germanium-doped fibre. It seems that the addition of boron reduces the refractive index of the fibre core. Camlibel *et al.* [1975] have shown that the boron-doped silica glass results in a lowering of the refractive index value when the glass is quenched (during the fibre drawing process) but during the thermal

annealing, the refractive index increases at temperatures above 350 °C. This lowered value of the refractive index arises due to the build up in the thermo-elastic stresses in the fibre core, causing a large index difference between the boron-containing core and the silica cladding. In tests, UV absorption measurements on fibres in the wavelength ranges between 200 - 300 nm showed only the characteristics of germanium-oxygen-deficiency centre (GODC) absorption band peak at 240 nm [Williams *et al.* 1993]. The boron co-doping did not affect the UV absorption peak at 240 nm, nor the shape of the 240 nm peak; and no other absorption peaks were observed within this wavelength range. The UV absorption measurements suggest that the boron co-doping does not enhance the fibre photosensitivity through the creation of the germanium-oxygen-deficient-centre (GODC), as was reported to be the case with the hydrogen-loading and the flame-brushing techniques. It is believed that the boron co-doping enhances the photosensitivity of the fibre by allowing a photoinduced stress relaxation to occur. In view of the stress-induced refractive index changes reported to occur in boron-doped silica glass fibre [Camlibel *et al.* 1975], it appears that the refractive index increases have occurred through photoinduced stress relaxation initiated by breaking the "wrong bonds" under UV irradiation [Williams *et al.* 1993].

Dong *et al.* [1995b, 1995c] have reported that tin co-doping enhances the photosensitivity of germanium-free phosphosilicate fibres and germanosilicate optical fibres. Photo-induced refractive index changes of the order of 10^{-3} have been obtained in both the silicate optical fibres. Tin co-doping does not introduce significant loss at the telecommunication window of 1550 nm, unlike the boron co-doping. The thermal stability of the tin co-doped gratings was comparable to that of the pure germanosilicate gratings, but this is much more stable compared to the gratings written in boron co-doped germanosilicate fibres [Dong *et al.* 1995c].

2.5. Illustration of uniform fibre Bragg grating

Fibre Bragg grating is considered to be a periodic modulation of the refractive index of a single mode optical fibre core. For uniform fibre Bragg gratings, the phase planes of the grating are perpendicular to the fibre longitudinal axis and with grating planes having constant period, (Λ), are considered to be the main properties of most Bragg

grating structures. A graphical representation of a uniform Bragg grating structure is shown in Fig. 2.1 [Othonos and Kalli 1999]. Broadband light guided along the core of an optical fibre will be scattered by each grating plane.

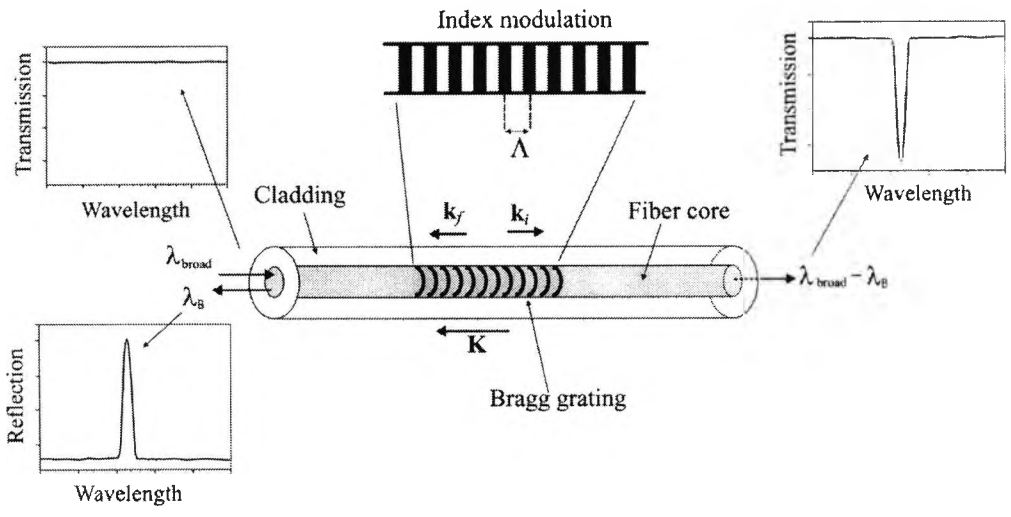

Fig. 2.1: Representation of a uniform fibre Bragg grating with constant amplitude of refractive index modulation and the grating period [Othonos and Kalli 1999].

When the Bragg resonance condition is not satisfied, the reflected light from each of the subsequent grating planes becomes progressively out of phase and will eventually cancel out. Also, light that is not coincident with the Bragg wavelength resonance will experience very weak reflection at each of the grating planes over the length of the grating because of the index mismatch. On the other hand, where the Bragg resonance condition is satisfied, the contributions of reflected-light from each grating plane add constructively in the backward direction to form a back-reflected peak with a centre wavelength defined as the Bragg wavelength. The so called *Bragg grating condition* is the requirement that satisfies both energy and momentum conservations. Energy conservation requires that the frequency of the incident radiation is the same as that of the reflected radiation. Momentum conservation requires that the incident wave vector, $\boldsymbol{k_i}$, plus the grating wave vector, $\boldsymbol{K}$, is equal to the wave vector of the scattered radiation, $\boldsymbol{k_f}$. This relation was expressed as below [Othonos and Kalli 1999]:

$$\boldsymbol{k_i} + \boldsymbol{K} = \boldsymbol{k_f}, \tag{2.13}$$

where the grating vector, $\boldsymbol{K}$, has a direction normal to the grating planes with a

magnitude of $2\pi/\Lambda$, where Λ is the grating pitch as shown in Fig. 2.1. The grating wave vector is equal in magnitude to the incident wave vector but opposite in sign. As a result, the momentum conservation condition becomes:

$$2\left(\frac{2\pi n_{eff}}{\lambda_B}\right)=\frac{2\pi}{\Lambda}, \tag{2.14}$$

Therefore, the first-order Bragg condition can be written as below:

$$\lambda_B = 2n_{eff}\Lambda, \tag{2.15}$$

where the Bragg wavelength, λ_B, is the free space centre wavelength of the input light that will be back-reflected from the Bragg grating and n_{eff} is the effective refractive index of the fibre core at the Bragg wavelength [Othonos and Kalli 1999]. This equation governs the performance of the sensors used in this work.

2.5.1. Parameters of fibre Bragg grating

Based on the coupled mode theory derived by Lam and Garside [1981], and with the (reasonable) assumption that the grating is uniformly formed within the optical fibre core, the refractive index profile along the fibre core region may be expressed as shown below:

$$n(z)=n_0+\Delta n\cos\left(\frac{2\pi z}{\Lambda}\right), \tag{2.16}$$

where n_0 is the average refractive index of the fibre; Δn is the amplitude of the refractive index modulation in the fibre core and z is the distance along the fibre longitudinal mode axis. The reflectivity of a uniform grating with constant amplitude of index modulation and period can be expressed as shown below [Lam and Garside 1981]:

$$R(L,\lambda)=\frac{\Omega^2\sinh^2(SL)}{\Delta k^2\sinh^2(SL)+S^2\cosh^2(SL)}, \tag{2.17}$$

where $R(L,\lambda)$ is the reflectivity of the grating as a function of wavelength, λ and the grating length, L. Ω is the coupling coefficient, $\Delta k = k - (\pi/\Lambda)$ is the detuning wave

vector, $k = 2\pi n_0/\lambda$ is the propagation constant and the parameter S was defined as $S^2 = \Omega^2 - \Delta k^2$. For the sinusoidal variation of index perturbation along the fibre axis (z), the coupling coefficient (Ω) can be expressed as shown below:

$$\Omega = \frac{\pi \Delta n}{\lambda} M_p, \tag{2.18}$$

where M_p is the fraction of the optical fibre mode power coupled to the fibre core and this was approximated to:

$$M_P = 1 - \frac{1}{V^2} \tag{2.19}$$

where V is the normalised frequency of the fibre and can be determined from the cut-off wavelength of the fibre, $\lambda_{cut\text{-}off}$, through the equation below:

$$V = 2.405\left(\frac{\lambda_{cut-off}}{\lambda}\right) \tag{2.20}$$

The above relationship arises from the combination of the following two equations:

$$V = \left(\frac{2\pi}{\lambda}\right) a(NA) \tag{2.21}$$

$$2.405 = \left(\frac{2\pi}{\lambda_{cut-off}}\right) a(NA) \tag{2.22}$$

where a is the fibre core radius, NA is the numerical aperture of the fibre (as given below by:)

$$NA = \left(n_{core}^2 - n_{clad}^2\right)^{1/2} \tag{2.23}$$

where n_{core} and n_{clad} are the refractive indices of the fibre core and cladding respectively.

At the centre of the Bragg wavelength there is no wave vector detuning and $\Delta k = 0$ i.e. $\Omega = S$. Therefore the expression for the reflectivity of the Bragg grating becomes:

$$R(L,\lambda) = \tanh^2(\Omega L), \tag{2.24}$$

Thus, the strength of the reflectivity increases with the increase in both of the photo-induced refractive index modulation and the length of the grating. The approximate full-width-half-maximum (FWHM) bandwidth ($\Delta\lambda$) of a grating may be expressed as shown below [Othonos and Kalli 1999]:

$$\Delta\lambda = \lambda_B S \sqrt{\left(\frac{\Delta n}{2n_0}\right)^2 + \left(\frac{1}{N}\right)^2}, \tag{2.25}$$

where N is the number of the grating planes and the parameter, S, is approximated as 1 for a strong grating (near 100 % reflectivity) and is equal to 0.5 for a weak grating.

Combining Eqs. (2.18) and (2.24), the amplitude of the refractive index modulation (Δn) of a Bragg grating can be written as shown below:

$$\Delta n = \frac{\tanh^{-1}\left(\sqrt{R}\right)}{\pi L M_p}\lambda, \tag{2.26}$$

Therefore, based on Eq. (2.15), the effective refractive index (n_{eff}) of the fibre can be determined as follows:

$$n_{eff} = \frac{\lambda_B}{2\Lambda}, \tag{2.27}$$

2.6. Types of fibre Bragg gratings

Bragg gratings are normally classified into three different classes of photosensitive types: type I, type IIA and type II. Generally, type I Bragg gratings are most commonly observed in the photosensitive fibres available using either continuous wave (CW) or pulsed UV light under moderate intensities. The monotonic increase in the amplitude of the refractive index modulation in the fibre core with UV exposure time defines a type I fibre Bragg grating (FBG) [Othonos and Kalli 1999]. The characteristic behaviour of a Bragg grating (photo-induced refractive index change) is reversible under high temperature excitation. Type I gratings may be erased at

relatively low temperatures which again depends on the compositions of the fibre core materials used and the writing condition.

The growth dynamics of type IIA Bragg gratings are different from those of the type I gratings. Normally fabrication of type IIA Bragg grating is more time consuming (depending on the fibre type and the laser fluence). With continuous UV exposure, the complete or the partial erasure of the type I grating, followed by a new spectral formation occurring defines as type IIA Bragg grating [Othonos and Kalli 1999]. Type IIA gratings are most often observed in high Ge-doped (> 25 mol %) fibre, small core fibres and have often been associated with high internal stresses in the fibres. Thus the refractive index change in a type IIA Bragg grating occurs through compaction of the glass matrix. Though the formation mechanisms of both type I and type IIA Bragg gratings are different, their behaviour when subject to external perturbation is the same for both types of gratings. The Bragg wavelength may shift towards the blue part of the spectrum or show the same trend as that of the initial type I grating formation – this depends of the fibre host materials used.

Type II Bragg gratings are generally formed under very high energy (of 40 mJ or greater, single-pulse 248 nm excimer laser irradiation) achieving a broad spectral (large bandwidth) reflectivity of > 99.8 % [Archambault *et al.* 1993]. Some damage tracks have been found under microscopic observation at the core-cladding interface, which is unique to type II gratings and this suggests a large refractive index change. Also the fact that the damage tracks were localised on one side of the core suggests that most of the UV light has been strongly absorbed on the exposed side of the fibre. Thermal stability tests have shown that the characteristics of the type II grating remain unchanged up to temperatures as high as 800 °C for 24 hours. At 1000 °C, it was found that the grating disappeared after 4 hours; this implies that the localised absorption has been thermally "washed out" [Archambault *et al.* 1993]. Such high temperature sustainable type II gratings may be suitable for sensing applications in hostile environments.

2.7. Techniques involved for fabrication of Bragg Gratings

Fibre Bragg gratings can be fabricated internally or externally, depending on the fabrication techniques used.

2.7.1. Internal writing of Bragg grating

Hill *et al.* [1978] and Kawasaki *et al.* [1978] have demonstrated the internal fabrication technique for Bragg grating reflectors using a single frequency Argon ion laser source operating at 514.5 nm (or 488 nm). The two-photon absorption of the laser light lies in the UV photosensitive range of the Ge-doped optical fibres causes the refractive index changes in the fibre core. A schematic of the experimental set-up for the internal grating fabrication is shown in Fig. 2.2. The laser beam from the Argon ion laser source was launched into the Ge-doped fibre through the 50 x microscopic objective. The 50 % beam splitter shown was used to monitor the back-reflected light from the fibre core during the exposure and the fibre was placed in a quartz tube to avoid thermal effects. The end of the Ge-doped fibre was cleaved at right angles to the fibre axis to provide approximately 4 % Fresnel reflection in the fibre core to build up the initial reflection grating.

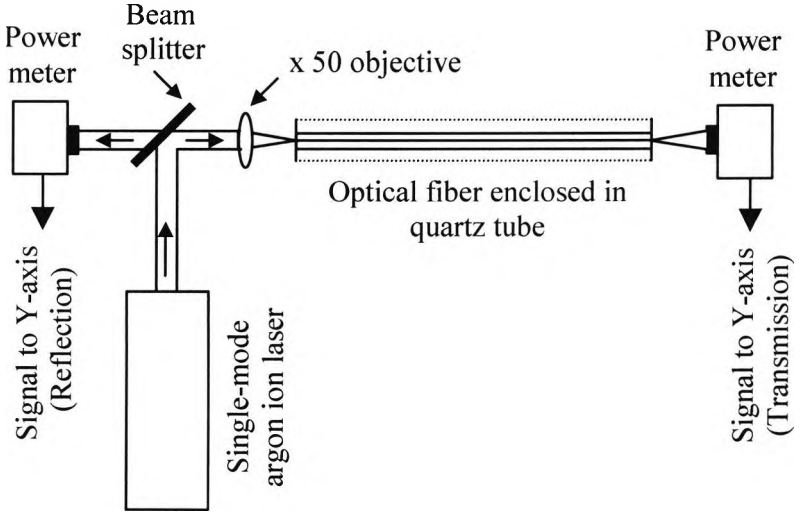

Fig. 2.2: Schematic of the experimental set-up for the internal (self-induced) fabrication of Bragg gratings [Kawasaki *et al.* 1978].

The incident laser light interferes with the Fresnel reflected beam and produces a weak standing wave-pattern in the core of the fibre to induce the grating reflector formation process. The high intensity point alters the index of refraction of the photosensitive fibre core permanently. The build up of the reflection grating was monitored in both the transmission and the reflection modes. The refractive index modulation of the grating reflectors has the same spatial periodicity as that of the interference pattern is formed. The Bragg grating reflectors were formed over 62 cm lengths of the fibre [Kawasaki *et al.* 1978].

2.7.2. External fabrication techniques of Bragg grating

The following techniques are now most commonly used for the external fabrication of Bragg gratings.

2.7.2.1. Interferometer technique

Meltz *et al.* [1989] were first to report the fabrication of fibre Bragg gratings using a two-beam interferometer technique, which is an external writing technique. The schematic of the experimental set-up is shown in Fig. 2.3. In this work, a tuneable excimer pumped dye laser operating in the wavelength range of 486-500 nm is frequency doubled using a frequency-doubling crystal and they provided a UV source at a wavelength of 244 nm, having adequate coherence length from this highly coherent laser source. Thus the UV irradiation lies within the germanium-oxygen-deficient-centre (GODC) defect band. In the figure, the beam splitter is used to divide the UV beam into two-equal intensity beams which are then recombined to produce an interference pattern in the core of the photosensitive fibre, normal to the fibre axis. A pair of cylindrical lenses was used to increase the power density of the beams before interference, following which the interfering beams irradiated the fibre core to create a periodic interference pattern, and thus the refractive index modulation of the fibre core. The resulting focal spot is approximately rectangular shape with 4 mm long by 125 μm wide. The length of the grating was estimated from an inspection of the burn-spot of the rectangular focal beam. The refractive index modulation was estimated to be ~ 3×10^{-5}, with 4.4 mm grating length achieved and a reflectivity of ~

55 %.

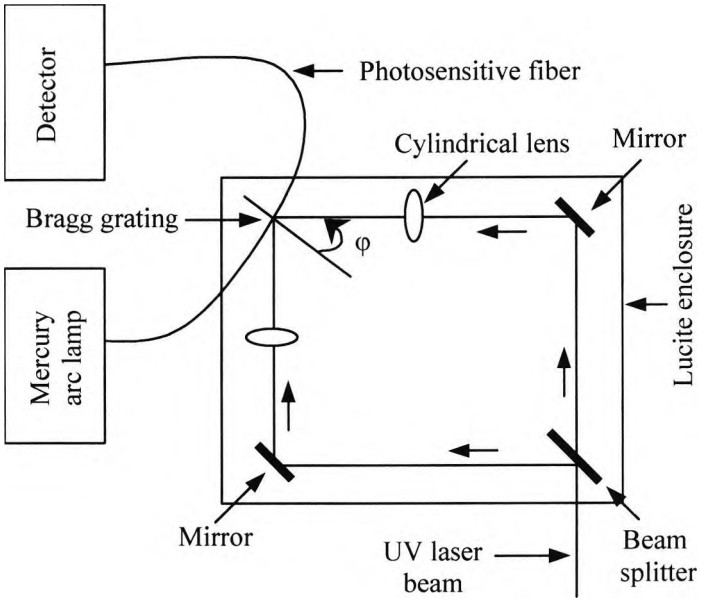

Fig. 2.3: Schematic of the amplitude-splitting interferometer technique used for the fabrication of fibre Bragg gratings [Meltz *et al.* 1989].

The fabrication process is termed the transverse holographic process because the fibre cladding is transparent to the UV light but the fibre core is highly absorbing to the UV light. The Bragg wavelength of the grating can be varied over a wide range by changing the angle (φ) between the two overlapping beams, which will alter the spacing of the interference maxima and thus the period of the gratings. To adjust the Bragg wavelength accurately, the interferometer mirrors need to be controlled precisely. This pioneering work showed the possibility of using the grating based devices in modern telecommunications and sensor systems.

However, in this approach, the UV laser light split into two equal intensity beams after the beam splitter may subsequently recombine after undergoing a different number of reflections from the mirrors, followed by the cylindrical lens used in each optical path. Therefore, the interfering beams may have different orientations, which will result in a low-quality fringe pattern for the laser beams having a low spatial coherence.

Dockney *et al.* [1996] have reported a modified two beam interferometer technique with a phase mask beam splitter and a wavelength tunable UV source for the fabrication of fibre Bragg gratings. The laser wavelength is tunable over the range 240-250 nm with an absolute accuracy of ± 0.02 nm and in this work could deliver energy level up to 75 mW at a repetition rate of 25 Hz. The laser output was diffracted using a phase mask which acts as a beam splitter in the interferometer. The phase mask was designed to have ± 1 order diffraction efficiency of ~ 35 % and the zero-order were nulled to less than 3 %. The first order beams were reflected using two steering mirrors at an angle, θ_m, at a right angle to the phase mask used. The interfering beams were focused through a cylindrical lens into the fibre core to produce an interference fringe pattern, and the schematic of the interferometer configuration used is shown in Fig. 2.4.

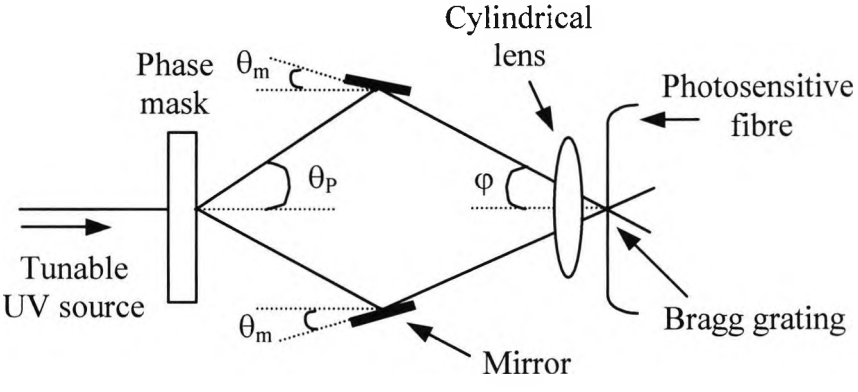

Fig. 2.4: Phase-mask based interferometer configuration for fabrication of Bragg gratings [Dockney *et al.* 1996].

The half-angle of the interfering beams at the fibre, φ, is given by [Dockney *et al.* 1996]:

$$\varphi = \theta_p + 2\theta_m \tag{2.28}$$

where θ_p is the half angle between the diffracted first order beams from the phase mask. When $\theta_m = 0$, the half angle between the diffracted first orders and the interfering beams would be equal, i.e. $\theta_p = \varphi$. For the Bragg grating period, Λ, (which is identical to the interference fringe pattern) depends on both the irradiation

wavelength (λ_w) and the half angle between the overlapping UV beams, φ. Therefore, the period of the grating can be expressed as shown below:

$$\Lambda = \frac{\lambda_w}{2\sin\varphi} \tag{2.29}$$

The Bragg resonance wavelength, λ_B, can be expressed as:

$$\lambda_B = \frac{n_{eff}\lambda_w}{\sin\varphi} \tag{2.30}$$

where n_{eff} is the effective refractive index of the fibre core. From the above equation, it is clear that the Bragg wavelength can be changed either by varying the writing wavelength, λ_w, or φ [Dockney *et al.* 1996]. The advantage of the amplitude-splitting technique is that the Bragg gratings can be written at any desired wavelengths. However, the main disadvantage of this technique is the need to maintain the overlapping of the two interfering beams accurately when the positions of mirrors or the beam splitter are varied during the grating writing.

Eggleton *et al.* [1994] have reported the use of the wave front splitting prism-interferometer technique to holographically fabricate FBGs. A schematic of the experimental set-up is shown in Fig. 2.5. The prism is fabricated from high-homogeneity ultraviolet-grade fused silica which allows good transmission characteristics. The UV writing beam was generated from a frequency doubled dye laser pumped by an excimer laser. The prism design includes the refractive beam expansion to expand the writing beam laterally by refraction at the input face of the prism to increase the exposed fibre length. The expanded beam is spatially bisected by the prism edge X, and one half-beam is spatially reversed by total internal reflection from the prism face, Y. The two-half beams are then combined at the output face of the prism, generating a fringe pattern parallel to the core of the photosensitive fibre used. The alignment of the wave front-splitting interferometer is easier than the amplitude splitting interferometer technique, as the former technique requires fewer optical components. In addition, the interferometer is stable because the path difference is generated within the prism and this remains unaffected by external vibrations.

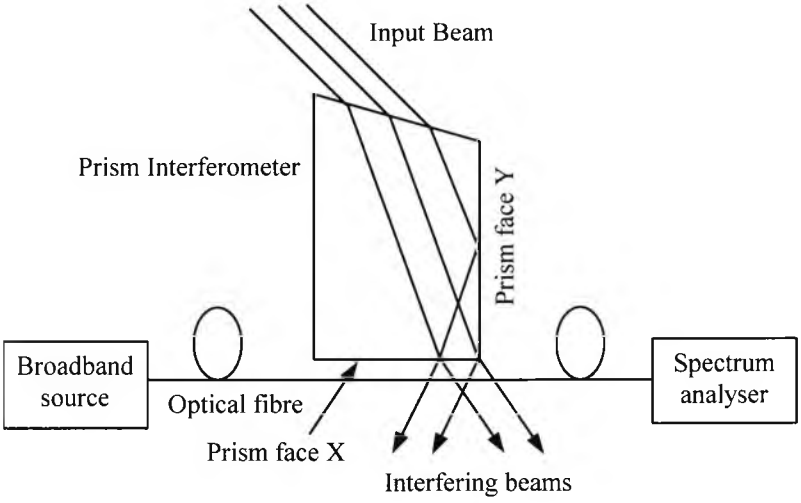

Fig. 2.5: Schematic of prism interferometer technique for fabrication of Bragg gratings [Eggleton *et al.* 1994].

Since the interference pattern is generated by reversing the beam from prism face itself, a UV source with a good spatial coherence is required to create interference with different parts of the beam. By rotating the prism interferometer, the incident angle of the beam can be varied to alter the two beam intersection angle and thus to tune the Bragg wavelength. The disadvantage of the system is that the grating length is limited to half of the writing beam width.

2.7.2.2. Point-by-point fabrication technique

Malo *et al.* [1993] have reported the fabrication of fibre Bragg gratings using a single pulse excimer laser as the UV light source to induce point-by-point individual index modulation (one plane at a time) in the fibre core. The schematic of the experimental set-up is shown in Fig. 2.6. The excimer laser light is passed through a mask containing a slit (width, W = 15 μm). A 15 mm focal lens images the slit on the core of the photosensitive fibre where the long dimension of the image is orientated perpendicular to the fibre core axis. Thus UV irradiation changes the refractive index of the fibre core at one point. The fibre is then translated at a distance, Λ, corresponding to the pitch of the grating, in a direction parallel to the fibre axis, using a precisely controlled translation stage. Again a second portion of the photosensitive

fibre is irradiated. By repeating the irradiation and the translation process of the fibre, a periodic sequence of index perturbation can be created point-by-point in the fibre core to form the desired grating.

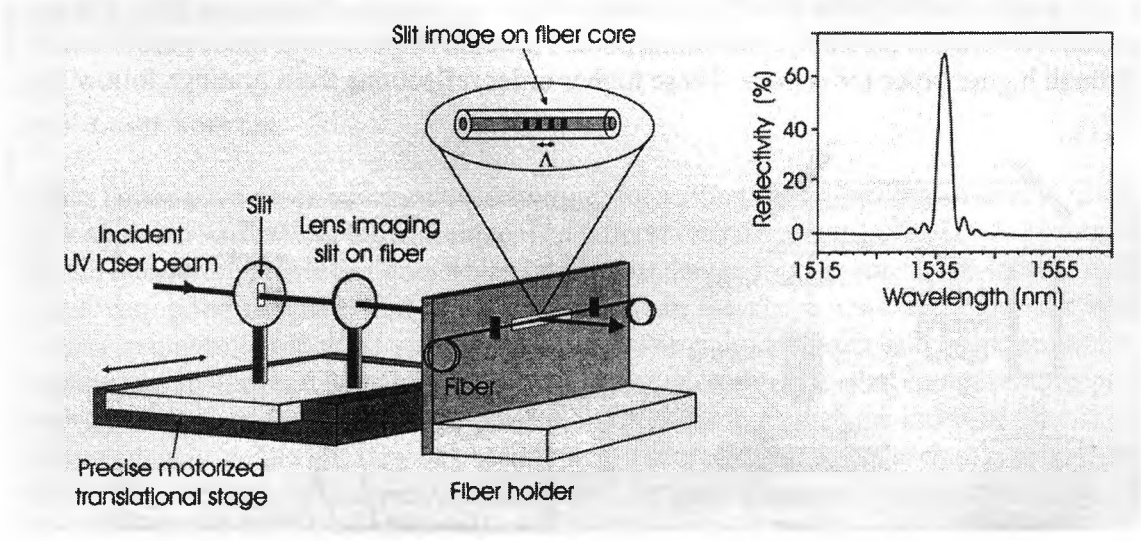

Fig. 2.6: Point-by-point writing technique for the fabrication of fibre Bragg gratings.

The grating formed in this work [Malo *et al.* 1993] had a peak reflectivity of 70 % at a Bragg wavelength of 1536 nm and with a full-width-half-maximum (FWHM) bandwidth of 2.7 nm. The pitch period (Λ) of the grating is 1.59 μm and contains 225 index modulations, therefore, resulting in a grating length of 360 μm. The main advantage of fabricating gratings using this technique is the flexibility, for example, to vary the pitch (Λ) and the length of the gratings. However, the main disadvantages of this technique are that the fabrication process is time consuming and requires precise control of fibre movement in every translation stage during irradiation.

2.7.2.3. Phase-mask technique

Hill *et al.* [1993] and Anderson *et al.* [1993] have demonstrated the fabrication of fibre Bragg gratings using the phase-mask technique. The phase-mask is a diffractive optical element and is manufactured on high optical quality fused silica quartz transparent to the UV laser light. The phase mask can be formed using either holographically or electron-beam lithography technique. The phase mask is produced as a one-dimensional periodic surface relief pattern with a period (Λ_{pm}) imprinted into

the fused silica.

The principle of operation is based on the diffraction of an incident UV beam into several orders, $m = 0, \pm1, \pm2$ ....., as is illustrated schematically in Fig. 2.7.

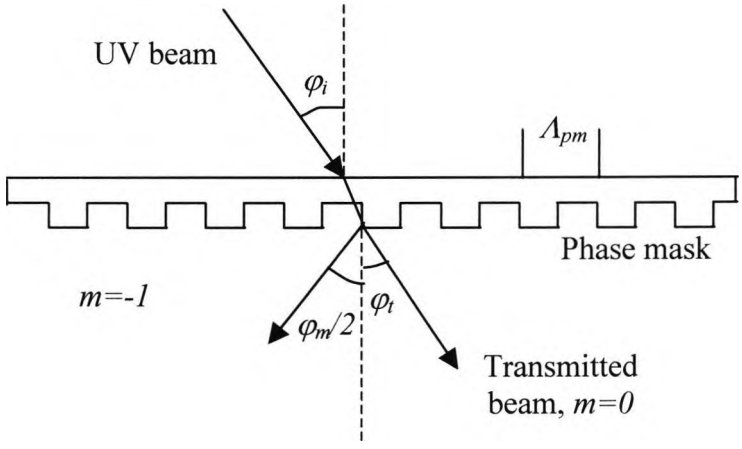

Fig. 2.7: Schematic of the diffraction of an incident beam from a phase-mask [Kashyap 1999].

The incident and diffracted orders satisfy the general diffraction equation derived as below, with the period of the phase-mask being Λ_{pm},

$$\Lambda_{pm} = \frac{m\lambda_{uv}}{\left(\sin\frac{\varphi_m}{2} - \sin\varphi_i\right)} \qquad (2.31)$$

where $\varphi_m/2$ is the angle of the diffracted order, λ_{uv} is the wavelength and φ_i is the angle of the incident UV beam [Kashyap 1999]. When the period of the grating lies between λ_{uv} and $\lambda_{uv}/2$, the incident wave is diffracted into only a single order, $m = -1$ with the rest of the power remaining in the transmitted wave, $m = 0$.

With the UV laser beam at normal incidence, $\varphi_i = 0$, the diffracted radiation is split into $m = 0$ and ±1 orders, and this is shown in Fig. 2.8. The interference pattern at the fibre of two such beams of orders ±1 has a period, Λ, related to the diffraction angle $\varphi_m/2$ by the following equation:

$$\Lambda = \frac{\lambda_{uv}}{2\sin\left(\varphi_m/2\right)} = \frac{\Lambda_{pm}}{2} \tag{2.32}$$

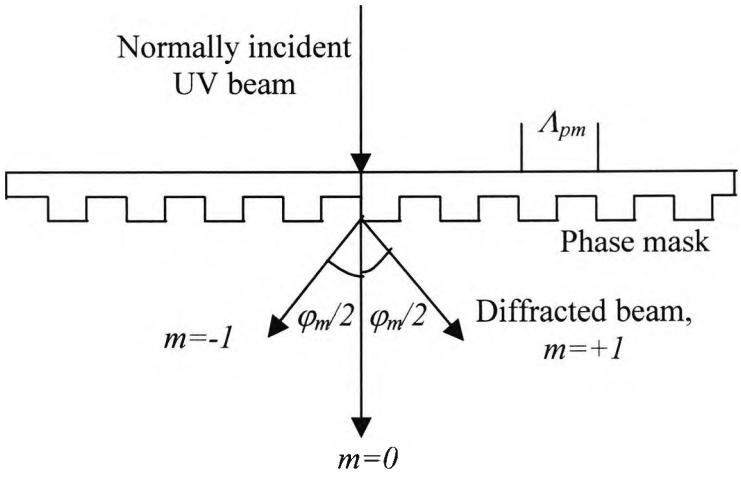

Fig. 2.8: Normally incident UV beam diffracted into two ±1 orders. The remnant radiation exits the phase-mask in the zero-order (m = 0) [Kashyap 1999].

The period, Λ_{pm} of the grating etched in the mask is determined by the Bragg wavelength, λ_B, required for the grating in the photosensitive fibre and using Eqs. (2.15) and (2.32) to arrive at:

$$\Lambda = \frac{N\lambda_B}{2n_{eff}} = \frac{\Lambda_{pm}}{2} \tag{2.33}$$

where $N \geq 1$ is an integer indicating the order of the grating period.

With the UV laser beam at normal incidence was passed through the phase mask to create an interference fringe pattern (Bragg grating pitch) in the photosensitive fibre core placed behind, and in close proximity and parallel to the phase mask used. The interference of the plus and the minus first-order diffracted beams photo-imprint a refractive index modulation in the optical fibre core and thus result in the formation of the gratings. The period of the grating fringe (Λ) is one-half of the period of the phase mask ($\Lambda_{pm}/2$) used.

Hill *et al.* [1993] fabricated Bragg gratings at a Bragg wavelength of 1531 nm wavelength in an Andrew D-type photosensitive fibre using the phase mask technique. The grating had a peak reflectivity of 16 % with a length of 0.95 mm and an estimated refractive index modulation of 2.2×10^{-4}. Anderson *et al.* [1993] fabricated Bragg gratings with a peak reflectivity of 94 % at a Bragg wavelength of 1509 nm in the Ge-doped fibre.

The phase-mask technique for the fabrication of Bragg gratings is independent of the writing laser wavelength, a major advantage over the two-beam interferometer technique. Since the photosensitive fibre is placed directly behind the phase-mask in the near field of the diffractive (plus and minus first-order) beams, the sensitivity to mechanical vibrations (optical beam path length is reduced) is minimised. The use of one optical diffractive element reduces the complexity of the fabrication system and thus makes the device inherently stable for reproducing identical samples. In the work described in this thesis, this approach has been used for Bragg gratings fabrication.

There are other techniques also available for the external fabrication of uniform fibre Bragg gratings: however the most commonly used techniques have been described above. For further details, readers are referred to the work of Othonos and Kalli; 1999.

2.8. Experimental arrangement for fabrication of Bragg gratings

Bragg gratings have been fabricated in this work using the phase-mask technique, as this approach is proven to be flexible and stable to reproduce identical grating samples. The schematic of the experimental set-up used at City University for the fabrication of fibre Bragg gratings is shown in Fig. 2.9. A plano-cylindrical lens (focal length of 20 cm) was used to converge the UV laser beam into a line (rectangular shape, beam length = 6.5 mm) along the core of the photosensitive fibre. KrF excimer laser (detailed specifications are given in Table 2.1) light was passed through a uniform phase mask (pitch period = 1060 nm, dimension = 25 mm × 3 mm, zero-order = 0.94 %, supplied by the O/E Land Inc. Canada) at normal incidence to create an interference pattern in the photosensitive fibre core using the plus and the minus

first-order diffracted beams.

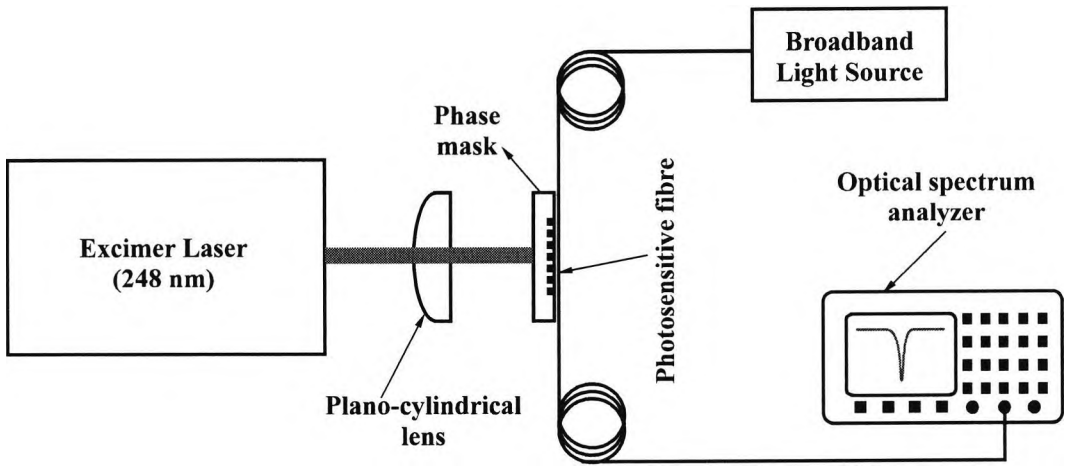

Fig. 2.9: Schematic of the experimental set-up for fabrication of fibre Bragg gratings using the phase-mask technique.

The photosensitive fibre was placed just behind and in close proximity and parallel to the phase mask used, to photo-imprint a refractive index modulation in the fibre core; and thus a Bragg grating was formed. The fibre was connected to a broadband light source and to an Optical Spectrum Analyser (OSA-detailed specifications are given in Table 2.2) to monitor the spectral profile of the grating during fabrication.

Table 2.1: Detailed specifications of the excimer laser used for fabrication of FBGs.

Bragg Star -500	
Laser type	Class IV laser
Laser medium	KrF (Krypton fluoride)
Operating wavelength	248 nm
Pulse Energy	18 mJ (maximum)
Average power	8 W (maximum)
Pulse repetition rate	500 Hz (maximum)
Pulse duration	10 ns (FWHM)
Beam dimensions	3 mm × 6 mm (FWHM)
Cooling	Air cooling

Gas pressure	6500 to 8000 hPa (maximum)
Ambient temperature	15 °C – 32 °C
Maximum on-Time	5 minutes (at a stage)
Duty cycle	> 50 %
Laser emission mode	The continuous mode and the burst mode

Table 2.2: Detailed specifications of the optical spectrum analyser used in this work.

Optical Spectrum Analyser (OSA)	
Model	HP 86140 A Series
Wavelength range (start to stop)	600-1700
Wavelength unit	nm
Resolution bandwidth	Auto
Resolution bandwidth to span ratio	0.01
Medium	Vacuum
Power scale	Manual (Log/Linear)

2.9. Types of photosensitive fibres used for the fabrication of Bragg gratings

Two different types of photosensitive fibres were used during the course of this work (i) B-Ge (boron-germanium) co-doped and (ii) Ge (germanium) -doped fibres for the fabrication of fibre Bragg gratings and detailed specifications are given in Table 2.3.

Table 2.3: Detailed specifications of photosensitive fibres used for the fabrication of Bragg gratings.

Fibre types	Core co-dopant	Mode field diameter (μm)	Numerical aperture (NA)	Cut-off wavelength (μm)	Supplier
PS1250/1500	Boron-germanium co-doped in silica glass host	9.6 μm at 1.550 μm	0.14	1.247	Fibercore Ltd., UK
Redfern GF1 (now Nufern)	Germanium-doped in silica glass host	10.2 μm at 1.550 μm	0.10	1.2	Nufern, Australia

2.9.1. B-Ge co-doped fibre

Fig. 2.10 shows the growth behaviour of B-Ge co-doped fibre Bragg gratings in terms of their reflectivity and the Bragg wavelength variation with UV exposure time, with a typical laser energy of 12 mJ and repetition frequency of 200 Hz. The peak reflectivity of the grating was calculated using the following equation:

$$R = 1 - T_{\min}, \qquad (2.34)$$

where T_{min} is the minimum transmittance of the grating at its Bragg wavelength (λ_B) [Baker *et al.* 1997]. The transmission spectrum profile and the Bragg wavelength variation of the grating with UV-exposure time were monitored online using the OSA. Typically, it was found that the peak reflectivity of the grating reached more than 90% within 3 seconds of UV exposure and finally the type I Bragg grating saturated within 35 seconds of exposure, achieving a peak reflectivity of 99.88 % with a Bragg wavelength of 1535.81 nm. With continuous UV exposure, the growth of the reflectivity stops, then drops to a low level of typically ~ 38 % with the saturation of the type I Bragg grating (within less than 2 minutes), while advancing the formation of type IIA Bragg grating and with that as increased reflectivity of the grating.

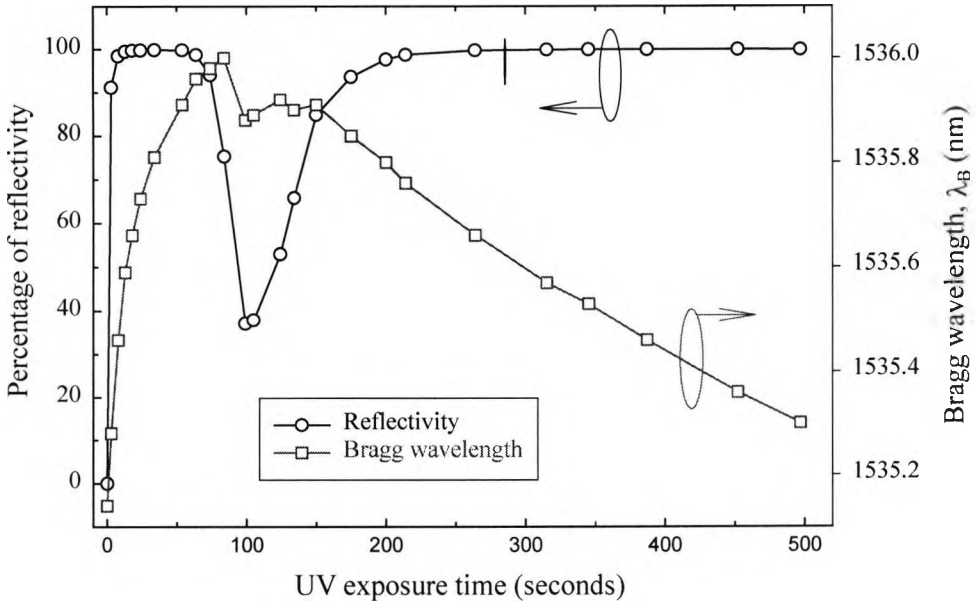

Fig. 2.10: Growth behaviour of the B-Ge co-doped fibre Bragg gratings in terms of their reflectivity and the Bragg wavelength variation with UV exposure time.

The Bragg wavelength moved towards the longer wavelength side of the spectrum during the formation of the type I Bragg grating. During the formation and the saturation of the type IIA Bragg grating, the Bragg wavelength moved towards the shorter wavelength side of the spectrum. The bi-directional shift in the Bragg wavelength (λ_B) of the grating mainly arises from the "opposing" effects of the boron and the germanium co-dopant on the refractive index of the photosensitive fibre. Finally, the type IIA Bragg grating saturates within ~ 9 minutes of the exposure, achieving a peak reflectivity of 99.94 % with a Bragg wavelength of 1535.53 nm. Fig. 2.11 shows the refractive index modulation and the effective refractive index variation of B-Ge co-doped fibre Bragg gratings with UV exposure. The refractive index change in the fibre core mainly arises from the photo-induced bleaching of the defect band peak at 240 nm, and this has been described using the colour-centre mechanism [Hand and Russell 1990] and the densification mechanism [Fiori and Devine 1986]. The start wavelength of the OSA used was 600 nm; therefore, it was not possible to monitor the UV absorption of the photosensitive fibres used in this work.

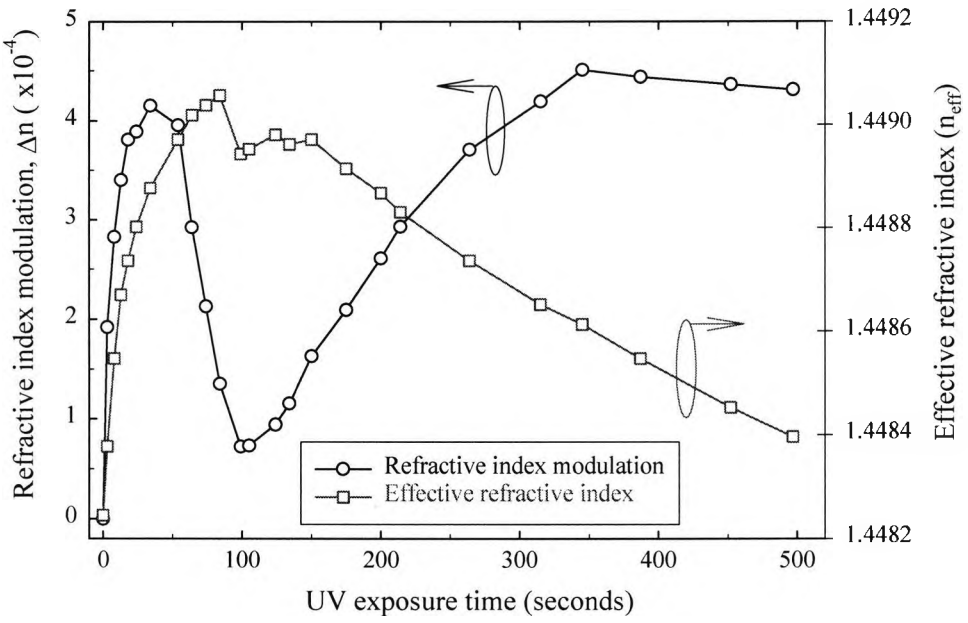

Fig. 2.11: Refractive index modulation and the effective refractive index variation of the B-Ge co-doped fibre Bragg grating with UV exposure time.

The amplitude of the refractive index modulation was calculated from the reflectivity and the length of the grating (6.5 mm) using Eq. (2.26) and the effective refractive index was calculated from the Bragg wavelength shift during the exposure using Eq. (2.27). The length of the grating was measured from the burn-spot of the laser beam after the cylindrical lens and before the phase-mask. The UV laser beam was rectangular in shape with beam length of 6.5 mm. The photo-induced refractive index modulation (Δn) for the B-Ge co-doped type I fibre Bragg grating was estimated to be 4.15×10^{-4} and for the type IIA Bragg grating, 4.52×10^{-4}. The effective refractive index (n_{eff}) was estimated to be 1.4489 and 1.4486 for types I and IIA Bragg gratings respectively. Fig. 2.12 shows the transmission spectra of both types I and IIA Bragg gratings before and after fabrication. The figure clearly shows that the bandwidth of the type I Bragg grating is narrower than that of the type IIA Bragg grating and this arises from the increased induced refractive index modulation of the type IIA grating. The spectrum of the type IIA grating was shifted towards the shorter wavelength side of the spectrum than that of the initial type I grating which arises from the "opposing" effects of the boron and germanium co-dopant, as mentioned earlier. The

characteristics of the fabrication of the Bragg gratings were found to be repeatable for several samples studied.

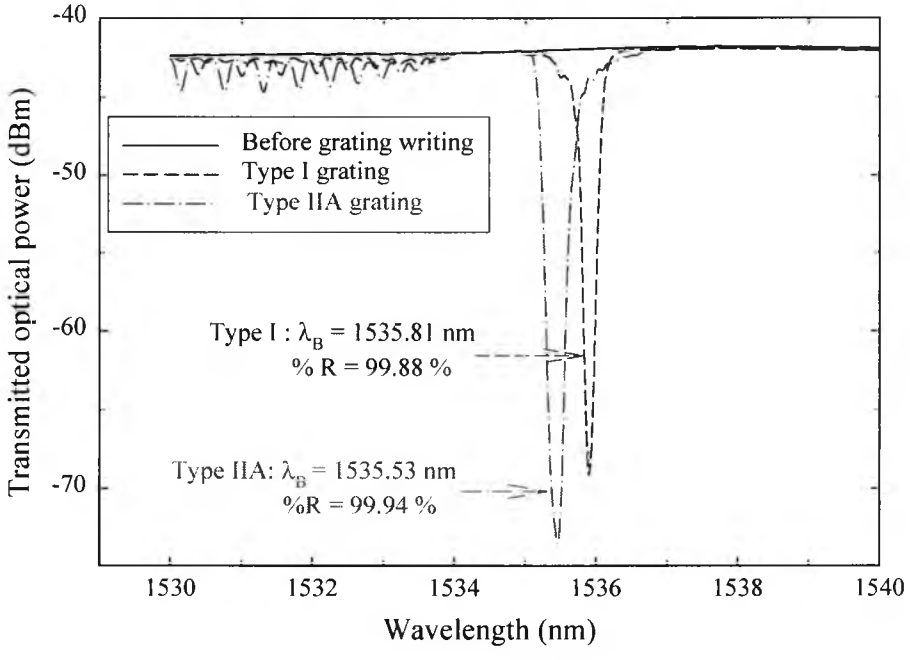

Fig. 2.12: Transmission spectra of the type I and type IIA Bragg gratings in the B-Ge co-doped fibre before and after fabrication.

2.9.2. Ge-doped fibre

Similarly, the formation of both types I and IIA Bragg gratings were monitored in Ge-doped photosensitive fibre, using the same laser energy (12 mJ) and repetition frequency (200 Hz). The growth behaviour of both type I and type IIA Bragg gratings in terms of their reflectivity and the Bragg wavelength variation with UV exposure time are shown in Fig. 2.13. The growth of the reflectivity of both types (types I and IIA) of gratings in the Ge-doped fibre was found to be much slower than those of the B-Ge co-doped fibre using the same writing condition. To achieve a reflectivity of 94.4 % in a type I Bragg grating at a Bragg wavelength of 1534.29 nm took ~ 500 seconds of exposure, whereas a type IIA Bragg grating took ~ 78 minutes of exposure to achieve a peak reflectivity of ~ 97 % with a Bragg wavelength of 1535.28 nm under the same exposure conditions.

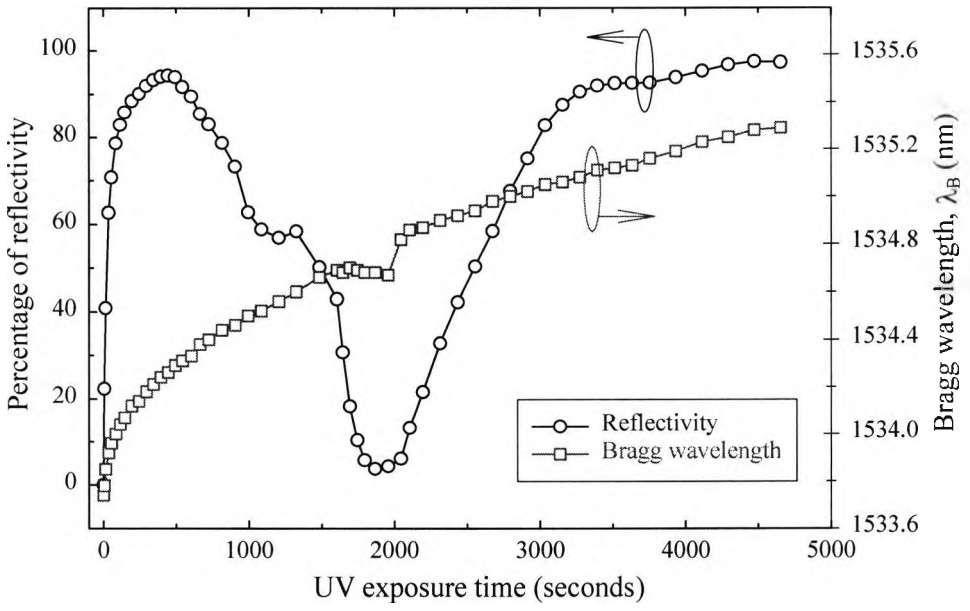

Fig. 2.13: Growth behaviour of the Ge-doped fibre Bragg gratings in terms of their reflectivity and the Bragg wavelength variation with UV exposure time.

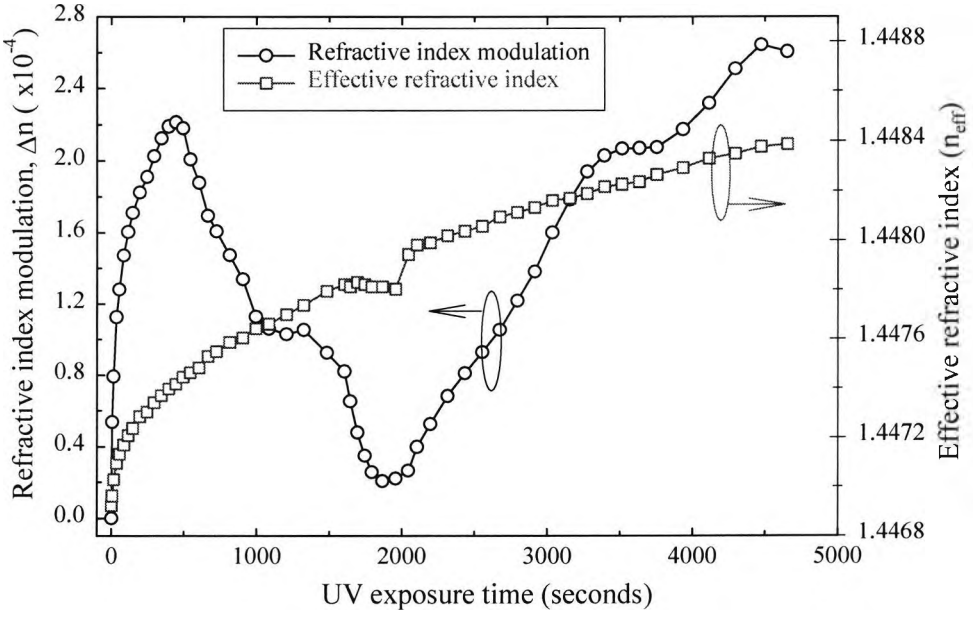

Fig. 2.14: Refractive index modulation and the effective refractive index variation of the Ge-doped fibre Bragg grating with UV exposure time.

The Bragg wavelength (λ_B) of the Ge-doped fibre was always found to shift towards

the longer wavelength side of the spectrum during the formation of both types of gratings. The positive shift in the Bragg wavelength mainly arises from the germanium-dopant in the fibre core, which increases the refractive index of the fibre. Fig. 2.14 shows the refractive index modulation and the effective refractive index of the Ge-doped fibre Bragg gratings with UV exposure time. The amplitudes of the refractive index modulation (Δn) of the Ge-doped types I and IIA gratings were estimated to be 2.21×10^{-4} and 2.64×10^{-4} respectively. The effective refractive index (n_{eff}) of the types I and IIA Bragg gratings were found to be 1.4474 and 1.4484 respectively.

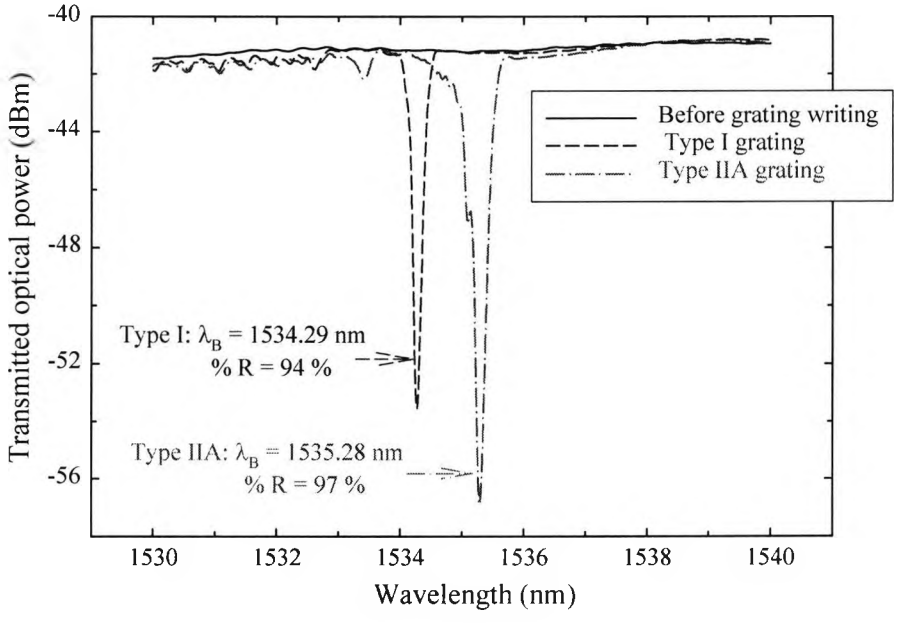

Fig. 2.15: Transmission spectra of both the type I and type IIA Bragg gratings in the Ge-doped fibre before and after fabrication.

Fig. 2.15 shows the transmission spectra of both the types I and IIA Bragg gratings before and after fabrication. The figure clearly shows that the type I Bragg grating is narrower than that of the type IIA grating and the Bragg wavelength of the type IIA grating is on the longer wavelength side of the spectrum.

From the fabrication characteristics of both types (type I and type IIA) gratings, it was found that the B-Ge co-doped fibre is more sensitive to UV-absorption (taking less

than 10 minutes, as discussed, for fabrication of a type IIA grating) compared to those of the Ge-doped fibre, which required ~ 78 minutes of exposure to fabricate the type IIA Bragg grating under the same writing conditions.

2.10. Thermal stability of fibre Bragg gratings

High temperature sustainability of fibre Bragg gratings is important for potential high temperature monitoring applications. As a result, a thermal stability-analysis of these devices is essential. Several groups of researchers have reported the thermal stability of Bragg gratings fabricated in different types of photosensitive fibres [Erdogan *et al.* 1994, Baker *et al.* 1997, Chisholm *et al.* 1998, Brambilla and Rutt 2002, Shen *et al.* 2003, Shen *et al.* 2004, Pal *et al.* 2003a and Pal *et al.* 2004]. According to Erdogan *et al.* [1994], thermal decay involves electrons in the lowest energy trap states returning to their original states under high temperature excitation. The refractive index change is induced by electrons that are excited to the conduction band through UV absorption from the valance band and are then trapped within a broad distribution of energy states lying within the band-gap. The thermal annealing is a process of emptying the traps, which depends on both the temperature of excitation and the depth of the trap state. Erdogan *et al.* [1994] have defined a demarcation energy where the electrons below these energy states have returned to their original state and above this, the trap state is considered too deep to be thermally excited with time. The temperature sustainability of Bragg gratings strongly depends on the host materials used and the UV-exposure time required for their fabrication. Brambilla and Rout [2002] and Pal *et al.* [2004] have showed that the distribution peak energy is the highest for the tin-silicate (3.7 eV) [Brambilla and Rout 2002] and the tin-erbium-germanium-silicate (3.1 eV) [Pal *et al.* 2004], intermediate for the Ge-doped (2.8 eV, 2.6 eV) and the lowest for the B-Ge co-doped (2.1 eV, 2.2 eV) fibre gratings, leading to the tin-doped fibre gratings being the highest and the B-Ge co-doped fibre gratings being the lowest temperature sustaining. B-Ge co-doped fibre gratings, with or without hydrogen-loading, were reported to have a low thermal stability [Baker *et al.* 1997]. The gratings written in specially fabricated antimony-germanium-erbium co-doped [Shen *et al.* 2003], tin-germanosilicate [Dong *et al.* 1995c] and tin-silicate [Brambilla and Rout 2002] fibres could sustain temperatures as high as 800 °C. Most recently, Shen

et al. [2004] have reported that the Bragg gratings written in an antimony-germanium (Sb-Ge) co-doped photosensitive fibre could sustain a temperature as high as 900 °C, with a remaining reflectivity >18 %.

2.11. Experimental arrangement for thermal testing of Bragg gratings

It was seen as necessary as to evaluate the temperature performance of the gratings fabricated, as described above, for their use in potential sensor applications. Type I Bragg gratings in both B-Ge co-doped and Ge-doped photosensitive fibres were fabricated using the same laser energy (12 mJ/pulse) and repetition frequency (200 Hz) prior to their thermal analysis. To do so, all the gratings (both type I and type IIA) fabricated in B-Ge co-doped and Ge-doped fibres were loosely placed in a well-calibrated carbolite oven (MTF 12/38/400) and the schematic of the experimental set-up used is shown in Fig. 2.16. The coating of the fibres (additional sections of single mode fibres were fusion-spliced on both sides of the gratings) were stripped off for around 50 cm in length before they were placed in an oven, to avoid any strain being applied to the fibre at high temperatures.

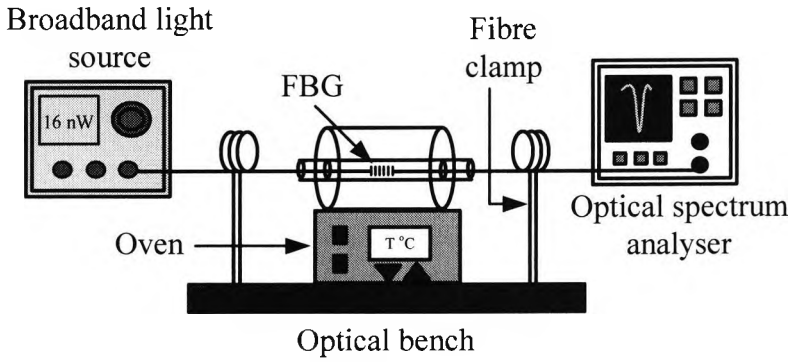

Fig. 2.16: Schematic of the experimental set-up for the thermal testing of fibre Bragg gratings.

Outside the oven, the fibres were fixed on both ends using the fibre-clamps and were connected to a broadband light source and an optical spectrum analyser (OSA) to monitor their on-line performance. During the thermal stability tests of these gratings,

the transmission spectra of the gratings, along with their Bragg wavelengths, were monitored at each temperature.

2.12. Experimental results

2.12.1. Decay in the reflectivity and the refractive index modulation of Bragg gratings

The real-time reflectivities of all the four gratings studied at each temperature were calculated using Eq. (2.34) from the measured transmission spectra of the gratings and the decay of their reflectivities, which are shown in Fig. 2.17.

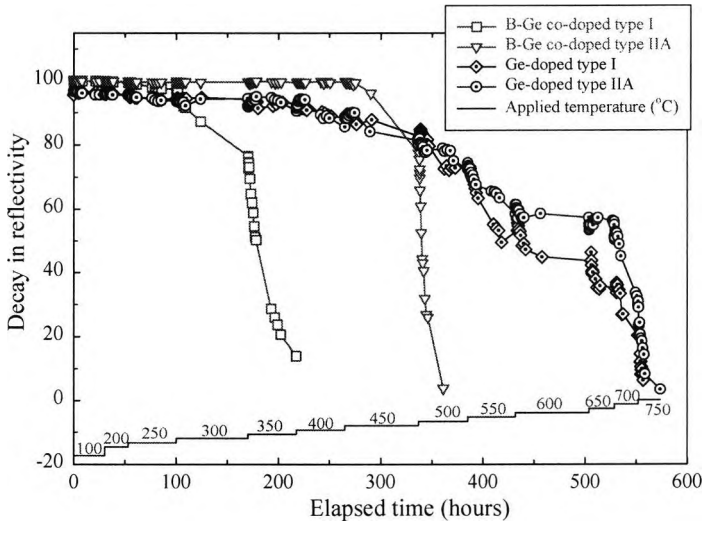

Fig. 2.17: Decay of the reflectivity of both the type I and type IIA Bragg gratings in B-Ge co-doped and Ge-doped fibres with elapsed time at each specific temperature.

These gratings were the B-Ge co-doped and Ge-doped type I and type IIA fibre Bragg gratings, fabricated as discussed in *section 2.9*. The temperature was increased, initially to 100 °C, 200 °C and then in incremental steps of 50 °C up to 750 °C. At each temperature, the gratings were kept for more than 48 hours, before being incremented of the next highest temperature. It was observed that up to a temperature of 200 °C, there was negligible decay in reflectivity for all these gratings. Above 200

°C, a smaller decay in the reflectivity was observed for the B-Ge co-doped type I fibre Bragg gratings, followed by a substantial rapid decay at 300 °C with a remaining reflectivity of ~ 76 % (showing a refractive index modulation of 1.39×10^{-4}). The decay in the reflectivity of Bragg gratings arises from the degradation of the UV-induced refractive index modulation, which is shown in Fig. 2.18.

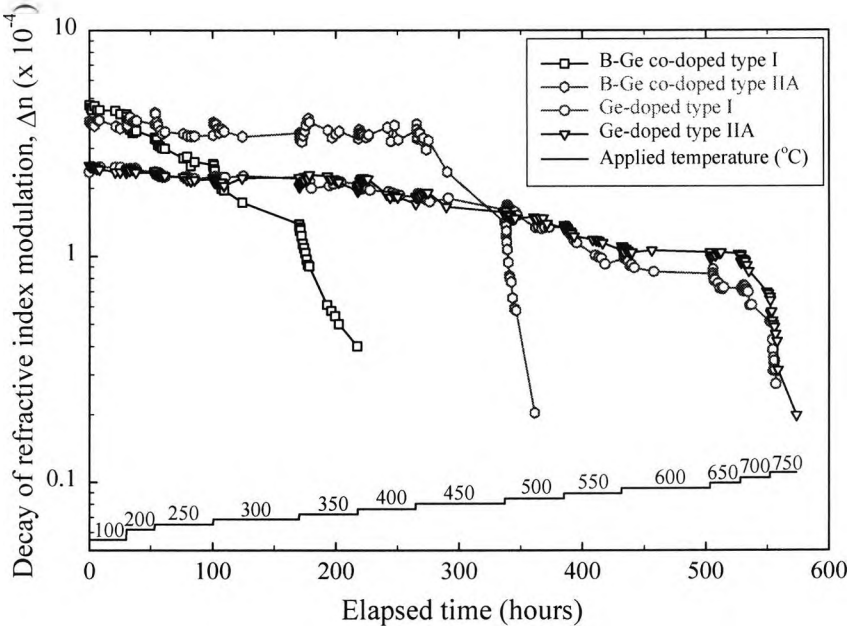

Fig. 2.18: Decay of the amplitude of refractive index modulation of both the type I and type IIA Bragg gratings in B-Ge co-doped and Ge-doped fibres with elapsed time at each specific temperature.

At temperature of 350 °C, the B-Ge co-doped type I grating was completely erased within a few hours. However, the type IIA Bragg grating in the same fibre remained almost unaffected up to a temperature of ~ 400 °C with a reflectivity of > 99 %. At 450 °C, the reflectivity of the grating dropped to ~ 80 % with a refractive index modulation of 2.36×10^{-4}. Increasing the temperature to 500 °C, it was observed that the grating totally "washed out" within ~ 24 hours.

By contrast, a Ge-doped type I Bragg grating can withstand a temperature up to 600 °C with a remaining reflectivity of ~ 44 % after erasure. At a temperature of 700 °C,

the reflectivity has dropped to ~ 15 % with an amplitude of the refractive index modulation of 4.26×10^{-5} and with a small increase in temperature of 50 °C, the grating completely "washed out" within 3 hours. By contrast, the type IIA Bragg grating in the same fibre could sustain a temperature up to 650 °C with a remaining reflectivity of ~ 56 % after erasure [Pal *et al.* 2003b]. At a temperature of 700 °C, the reflectivity dropped to ~ 30 % with a refractive index value of 6.7×10^{-5} and at a temperature of 750 °C, the grating completely "washed out" within ~ 22 hours.

These thermal testing results showed both the type I and type IIA Bragg gratings written in the Ge-doped fibre were found to be more temperature-sustainable, compared to those of the gratings written in the B-Ge co-doped fibre. The decay in the reflectivity of the gratings arises from the decay in the UV-induced refractive index modulation of the fibre core, which is thermally reversible, as reported by Atkins *et al.* [1993]. Although the fabrication of Ge-doped fibre Bragg gratings is much more time-consuming when compared to B-Ge co-doped fibre Bragg gratings, the higher temperature sustainability of these gratings make them suitable for high temperature sensing applications.

2.12.2. Variation of the Bragg wavelengths of Bragg gratings with temperature

Fig. 2.19 shows the variation of the Bragg wavelengths at each specific temperature for B-Ge co-doped and Ge-doped type I fibre Bragg gratings. It was found that the Bragg wavelength, λ_B, shifts towards the longer wavelength side of the spectrum with increase in temperature. However, at each temperature, a small blue shift in the Bragg wavelength was observed with elapsed time. At lower temperatures (up to ~ 200 °C), the decay of the reflectivity of the gratings was negligible and thus less affects on the effective refractive index of the fibre. As a result, the Bragg wavelength stabilised with a relatively shorter annealing time (within ~ 6 hours) at low temperatures. At higher temperatures, however, a relatively longer annealing time (~ 8-10 hours) was taken to reach, asymptotically, the stable point of the Bragg wavelengths. The blue shift in the Bragg wavelength arises from the decay in the UV-induced refractive index modulation of the fibre core at each temperature with time, which indirectly

reduces the effective refractive index of the fibre and thus affects the Bragg wavelength determined [Pal *et al.* 2003b].

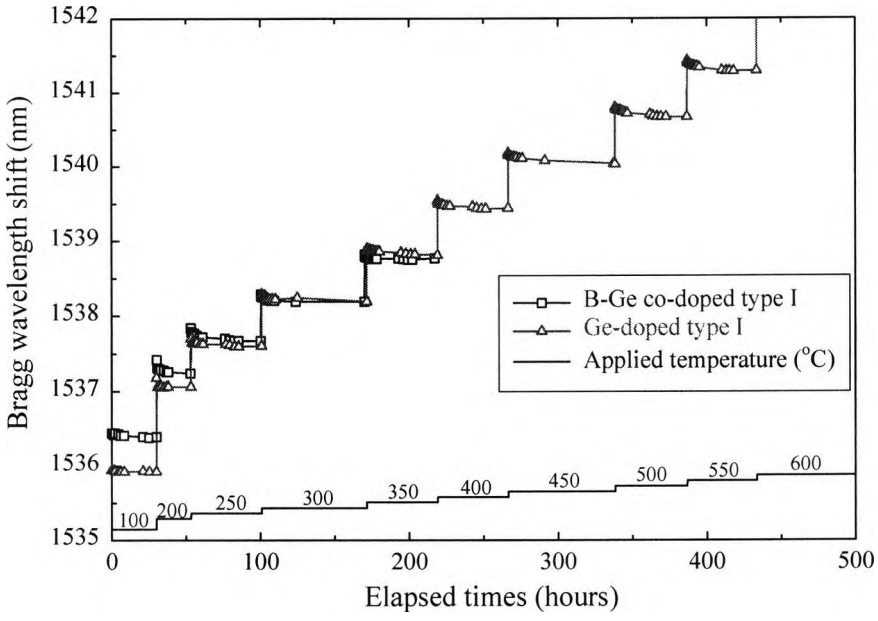

Fig. 2.19: Variation of the Bragg wavelengths at each specific temperature for B-Ge co-doped and Ge-doped type I fibre Bragg gratings with elapsed time.

An exception to this is, the positive shift in the Bragg wavelength which was observed for the B-Ge co-doped type IIA fibre Bragg gratings at particularly higher temperatures (above 350 °C) and this is shown in Fig. 2.20. At lower temperatures, a small blue shift in the Bragg wavelength arises from the degradation of the UV-induced refractive index change where the fibre (containing boron) was not annealed [Camlibel *et al.* 1975]. Above a temperature of 350 °C, the positive shift in the Bragg wavelength occurred when the positive change in the refractive index of the fibre core, due to the annealing of the boron-containing fibre is much larger than the negative change in the refractive index of the fibre core due to the decay of the UV-induced refractive index modulation. High temperature annealing increases the refractive index of the fibre core due to the presence of the boron co-dopant and similar results were reported by Camlibel *et al.* [1975] and Chisholm *et al.* [1998]. For a type I Bragg grating in the same fibre, this effect was not observed, as the gratings could not survive even at temperature up to 400 °C. The positive shift in the B-Ge co-

doped type IIA fibre Bragg gratings needs to be considered for the high temperature sensing applications.

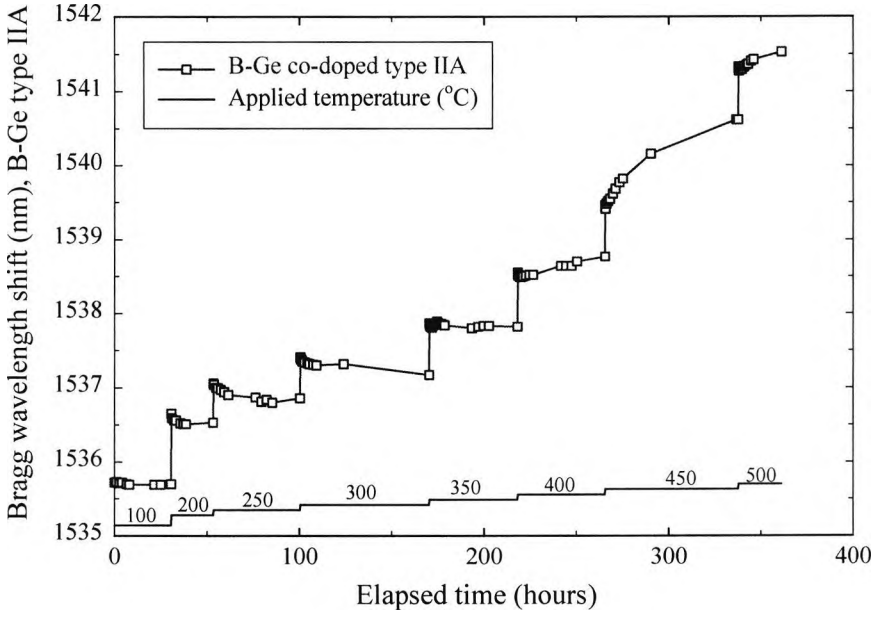

Fig. 2.20: Variation of the Bragg wavelength with elapsed time for the B-Ge co-doped type IIA fibre Bragg grating at each specific temperature.

2.12.3. Calibration of the sensitivity of the Bragg wavelengths of gratings with temperature

Figs. 2.21 and 2.22 show the calibration of the sensitivity of the Bragg wavelengths for both type I and type IIA Bragg gratings in the B-Ge co-doped and Ge-doped fibres respectively with temperature. The Bragg wavelengths plotted were considered at each stable temperature (~ 24 hours) and the thermal sensitivity was calibrated using a linear fit to the experimental data, for simplicity. Following sets of equations can be used to determine the linear sensitivity of the gratings as a function of temperature:

$$\lambda_{B1} = 1535.51 + 0.00882T, \quad \text{B-Ge co-doped type I grating} \qquad (2.35)$$

$$\lambda_{B2} = 1534.45 + 0.01079T, \quad \text{B-Ge co-doped type IIA grating} \qquad (2.36)$$

$$\lambda_{B1} = 1534.57 + 0.01252T, \quad \text{Ge-doped type I grating} \tag{2.37}$$

$$\lambda_{B2} = 1534.51 + 0.01199T, \quad \text{Ge-doped type IIA grating} \tag{2.38}$$

where T is the applied temperature in degree Celsius to the Bragg gratings placed in the oven.

Table 2.4 summarises the detailed results of the thermal sensitivity for both the B-Ge co-doped and the Ge-doped fibre Bragg gratings.

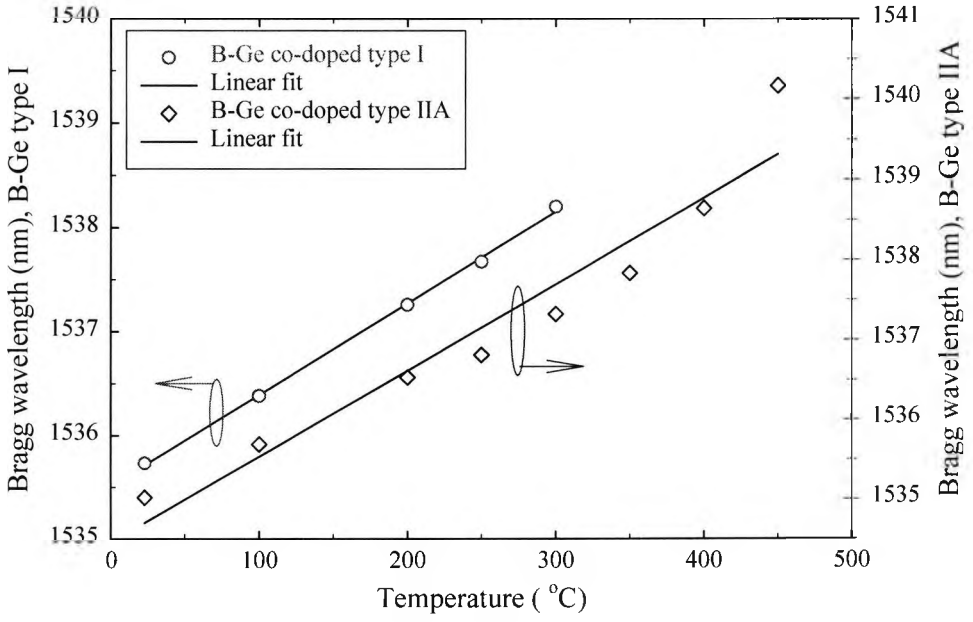

Fig. 2.21: Calibrations of the Bragg wavelengths with temperature for both the type I and type IIA Bragg gratings in the B-Ge co-doped fibre.

B-Ge co-doped fibre Bragg gratings showed a lower thermal sensitivity compared to those of the Ge-doped Bragg gratings but each had a slightly different slope. The sensitivity of the B-Ge co-doped type I Bragg grating was found to be 8.82 pm/°C but with a higher sensitivity of 10.79 pm/°C for the type IIA Bragg gratings (with an increased temperature range of 150 °C). The thermal sensitivity for the type I and type IIA Bragg gratings in Ge-doped fibre was found to be 12.52 pm/°C and 11.99 pm/°C

respectively, over the temperature range from room temperature to 700 °C. However, the thermal sensitivity of these gratings can also be calibrated using the non-linear polynomial regression fitting over the wider temperature range, and this will be considered in Chapters 4 and 8.

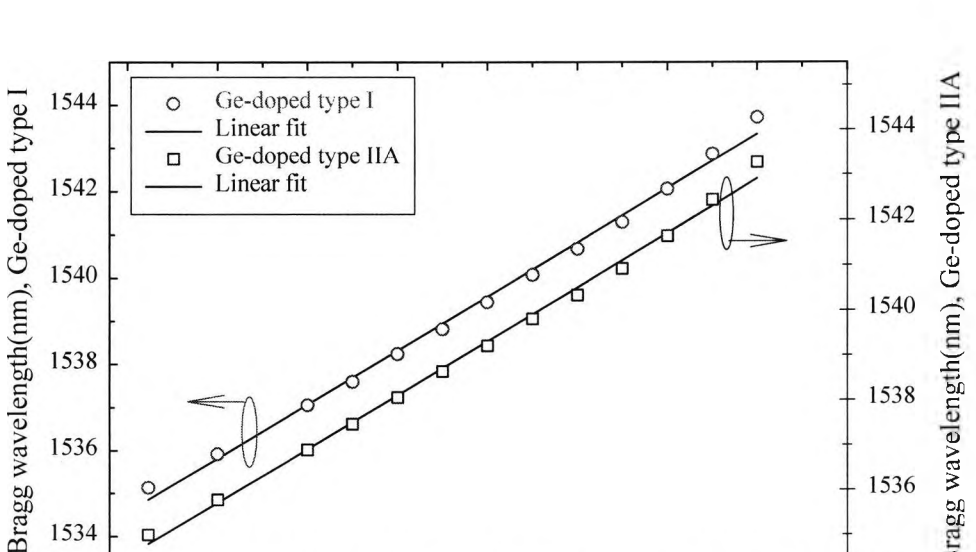

Fig. 2.22: Calibrations of the Bragg wavelengths with temperature for both the type I and type IIA Bragg gratings in the Ge-doped fibre.

Table 2.4: Calibration of the thermal sensitivity of both the type I and type IIA Bragg gratings in B-Ge co-doped and Ge-doped photosensitive fibres.

Types of fibre Bragg gratings (FBGs)	Temperature range (°C)	Thermal sensitivity (pm/°C)	Coefficient of determination (COD)	Standard deviation (SD)
B-Ge co-doped type I	22-300	8.82	0.9988	0.039
B-Ge co-doped type IIA	22-450	10.79	0.9317	0.46
Ge-doped type I	22-700	12.52	0.9956	0.184
Ge-doped type IIA	22-700	11.99	0.9962	0.163

2.13. Summary

This Chapter describes issues surrounding fibre photosensitivity, the possible mechanisms of photo-induced refractive index modulation in the fibre core and the formation of Bragg gratings. Both types I and IIA Bragg gratings in B-Ge co-doped and Ge-doped photosensitive fibres were fabricated using the phase-mask technique. The long-term thermal testing of the gratings fabricated was studied over the temperature range from 100 °C to a maximum of 750 °C. The thermal decay characteristics of these gratings were analysed in terms of the decay in the reflectivity and the refractive index modulation. The Bragg wavelength variations of these gratings were also monitored with increasing temperature. Each type of grating showed a slightly different sensitivity with temperature over the wider range studied.

From the fabrication characteristics of the gratings, it was found that the B-Ge co-doped fibre is more photosensitive when compared to that of the Ge-doped fibre. The fabrication of both types I and IIA gratings in such fibres is less time consuming compared to that of the Ge-doped fibre Bragg gratings using the same writing conditions (laser energy of 12 mJ and repetition frequency of 200 Hz) and thus the writing efficiency is higher for the B-Ge co-doped fibre gratings. However, the long-term thermal testing of these gratings showed that both the type I and type IIA gratings in Ge-doped fibre were able to sustain higher temperatures compared to those of the B-Ge co-doped fibre Bragg gratings. It was found that the B-Ge co-doped type I fibre Bragg grating was completely erased within a few hours at a temperature of 350 °C whereas the dynamic range was increased by 150 °C for the type IIA Bragg gratings in the same fibre. The Ge-doped type I fibre grating can sustain a temperature of up to 600 °C with a remaining reflectivity of ~ 44 % after erasure. The dynamic range for a type IIA Bragg grating in the same fibre was found to be slightly higher and can sustain a temperature of up to 650 °C with a remaining reflectivity of ~ 56 % after erasure. For a B-Ge type IIA fibre Bragg grating, the positive shift in the Bragg wavelength was observed at temperatures above 350 °C. This appears due to annealing effect of the boron-containing fibre which leads to a more positive change in the refractive index of the fibre than the negative change due to the decay of the

UV-induced refractive index modulation. For type I Bragg gratings in the same fibre, no such effects were observed as the grating completely "washed out" at a temperature of 350 °C. The blue shift in the Bragg wavelength arises from the decay of the UV-induced refractive index modulation, which degrades the effective refractive index of the fibre. Thermal testing of these gratings showed that the UV induced refractive index modulation in the fibre core are thermally reversible, but depends on the temperature excitement and the time required to create these gratings. The high temperature sustainability of the Ge-doped fibre gratings arises from the higher energy distribution of the trapped states compared to those of the B-Ge co-doped fibre gratings [Brambilla and Rutt 2002, Pal *et al.* 2004].

This work was important for the optimum selection of fibre Bragg gratings (FBGs) for their characterisation in Bragg grating-based optical fibre laser systems (in Chapter 3) and their sensor applications (in Chapters 4 and 8).

2.14. References

- Archambault, J. -L., Reekie, L. and Russell, P. St. J. (1993) 100 % reflectivity Bragg reflectors produced in optical fibres by single excimer laser pulses, *Electron. Lett.*, vol. 29, pp. 453-455.
- Anderson, D.Z., Mizrahi, V., Erdogan, T. and White, A.E. (1993) Production of in-fibre gratings using a diffractive optical elements, *Electron. Lett.*, vol. 29, pp. 566-568.
- Atkins, R.M., Mizrahi, V. and Erdogan, T. (1993) 248 nm induced vacuum UV spectral changes in optical fibre preform cores: support for the colour centre model of photosensitivity, *Electron. Lett.*, vol. 29, pp. 385-387.
- Baker, S.R., Rourke, H.N., Baker, V. and Goodchild, D. (1997) Thermal decay of fiber Bragg gratings written in boron and germanium codoped silica fiber, *IEEE J. of Lightwave Tech.*, vol. 15, pp. 1470-1476.
- Bilodeau, F., Malo, B., Albert, J., Johnson, D.C., Hill, K.O., Hibino, Y., Abe, M. and Kawachi, M. (1993) Photosensitization of optical fiber and silica-on-silicon/silica waveguides, *Opt. Lett.*, vol. 18, pp. 953-955.
- Brambilla, G. and Rutt, H. (2002) Fiber Bragg gratings with enhanced thermal stability, *Appl. Phys. Lett.*, vol. 80, pp. 3259-3261.
- Camlibel, I., Pinnow, D.A. and Dabby, F.W. (1975) Optical aging characteristics of borosilicate clad fused silica core fiber optical waveguides, *Appl. Phys. Lett.*, vol. 26, pp. 185-187.
- Chisholm, K.E., Sugden, K. and Bennion, I. (1998) Effects of thermal annealing on Bragg fibre gratings in boron/germania co-doped fibre, *J. Phys. D: Appl. Phys.*, vol. 31, pp. 61-64.
- Dockney, M.L., James, S.W. and Tatam, R.P. (1996) Fibre Bragg gratings fabricated using a wavelength tuneable laser source and a phase mask based interferometer, *Meas. Sci. Technol.*, vol. 7, pp. 445-448.
- Dong, L., Archambault, J.L., Reekie, L, Russel, P.St. and Payne, D.N. (1995a) Photoinduced absorption changes in germanosilicate preforms: Evidence for the color-centre model of photosensitivity, *Appl. Opt.*, vol. 34, pp. 3436-3440.
- Dong, L., Cruz, J.L., Tucknott, J.A., Reekie, L, and Payne, D.N. (1995b) Strong photosensitive gratings in tin-doped phosphosilicate optical fibers, *Opt.*

Lett., vol. 20, pp. 1982-1984.

- Dong, L., Cruz, J.L., Reekie, L, Xu, M.G. and Payne, D.N. (1995c) Enhanced photosensitivity in tin-codoped germanosilicate optical fibers, *IEEE Phton. Technol. Lett.*, vol. 7, pp. 1048-1050.
- Douay, M., Xie, W.X., Taunay, T., Bernage, P., Niay, P., Cordier, P., Poumellec, B., Dong, L., Bayon, J.F., Poignant, H. and Delevaque, E. (1997) Densification involved in the UV-based photosensitivity of silica glasses and optical fibers, *IEEE Journal of Lightwave Tech.*, vol. 15, pp. 1329-1342
- Eggleton, B.J., Krug, P.A., Poladian, L., Ahmed, K.A. and Liu, H.F. (1994) Experimental demonstration of compression of dispersed optical pulses by reflection from self-chirped optical fiber Bragg gratings, *Opt. Lett.*, vol. 19, pp. 877-879.
- Erdogan, T., Mizrahi, V., Lemaire, P.J. and Monroe, D. (1994) Decay of ultraviolet-induced fiber Bragg gratings, *J. Appl. Phys.*, vol. 76, pp. 73-80.
- Fiori, C. and Devine, R.A.B. (1986) Evidence for a wide continuum of polymorphs in *a* -SiO_2, *Phy. Rev. B*, vol. 33, pp. 2972-2974.
- Hand, D.P. and Russell, P. St. (1990) Photoinduced refractive index-changes in germanosilicate fibers, *Opt. Lett.*, vol. 15, pp. 102-104.
- Hill, K.O., Malo, B., Bilodeau, F., Johnson, D.C. and Albert, J. (1993) Bragg gratings fabricated in monomode photosensitive optical fiber by UV exposure through a phase mask, *Appl. Phy. Lett.*, vol. 62, pp. 1035-1037.
- Hill, K.O., Fujii, Y., Johnson, D.C. and Kawasaki, B.S. (1978) Photosensitivity in optical fiber waveguides: Application to reflection filter fabrication, *Appl. Phys. Lett.*, vol. 32, pp. 647-649.
- Hosono, H., Kawazoe, H. and Nishii, J. (1996) Defect formation in SiO_2: GeO_2 glasses studied by irradiation with excimer laser light, *Phy. Rev. B*, vol. 53, pp. 11921-11923.
- Hosono, H., Abe, Y., Kinser, D.L., Weeks, R.A., Muta, K. and Kawazoe, H. (1992) Nature and origin of the 5-eV band in SiO_2: GeO_2 glasses, *Phy. Rev. B*, vol. 46, pp. R11 445 - R11 451.
- Kashyap, R. (1999) *Fiber Bragg Gratings, Optics and Photonics Series*, Academic Press, San Diego, California.
- Kawasaki, B.S., Hill, K.O., Johnson, D.C. and Fujii, Y. (1978) Narrow-band

Bragg reflectors in optical fibers, *Opt. Lett.*, vol. 3, pp. 66-68.

- Lam, D.K.W. and Garside, B.K. (1981) Characterisation of single-mode optical fiber filters, *Appl. Opt.*, vol. 20, pp. 440-445.
- Leconte, B., Xie, W.X., Douay, M., Bernage, P., Niay, P., Bayon, J.F., Delevaque, E. and Poignant, H. (1997) Analysis of color-centre-related contribution to Bragg grating formation in Ge:SiO_2 fiber based on a local Kramers-Kronig transformation of excess loss spectra, *Appl. Opt.*, vol. 36, pp. 5923-5930.
- Lemaire, P.J., Atkins, R.M., Mizrahi, V. and Reed, W.A. (1993) High pressure H_2 loading as a technique for achieving ultrahigh UV photosensitivity and thermal sensitivity in GeO_2 doped optical fibres, *Electron. Lett.*, vol. 29, pp. 1191-1193.
- Limberger, H.G., Fonjallaz, P.-Y., Salanthe, R.P. and Cochet, F. (1996) Compaction- and photoelastic-induced index changes in fiber Bragg gratings, *Appl. Phy. Lett.*, vol. 68, pp. 3069-3071.
- Malo, L., Hill, K.O., Bilodeau, F., Johnson, D.C. and Albert, J. (1993) Point-by-point fabrication of micro-Bragg gratings in photosensitive fibre using single excimer pulse refractive index modification techniques, *Electron. Lett.*, vol. 29, pp. 1668-1669.
- Meltz, G., Morey, W.W. and Glenn, W.H. (1989) Formation of Bragg gratings in optical fibers by a transverse holographic method, *Opt. Lett.*, vol. 14, pp. 823-825.
- Nishii, J., Fukumi, K., Yamanaka, H., Kawamura, K., Hosono, H. and Kawazoe, H. (1995) Photochemical reactions in GeO_2-SiO_2 glasses induced by ultraviolet irradiation: comparison between Hg lamp and excimer laser, *Phy. Rev. B*, vol. 52, pp. 1661-1665.
- Othonos, A. and Kalli, K. (1999) *Fiber Bragg Gratings: Fundamentals and Applications in Telecommunications and Sensing*, Artech House, Boston.
- Pal, S., Sun, T., Grattan, K.T.V., Wade, S.A., Collins, S.F., Baxter, G.W., Dussardier, B. and Monnom, G. (2004) Bragg gratings written in Sn-Er-Ge-codoped silica fiber: investigation of photosensitivity, thermal stability, and sensing potential, *J. Opt. Soc. Am. A*, vol. 21, pp. 1503-1511.
- Pal, S., Mandal, J., Sun, T. and Grattan, K.T.V. (2003a) Analysis of thermal

decay and prediction of operational lifetime for a type I boron-germanium codoped fiber Bragg grating, *Appl. Opt.*, vol. 42, pp. 2188-2196.

- Pal, S., Mandal, J., Sun, T., Grattan, K.T.V., Fokine, M., Carlsson, F., Fonjallaz, P.Y., Wade, S.A. and Collins, S.F. (2003b) Characteristics of potential fibre Bragg grating sensor-based devices at elevated temperatures, *Meas. Sci. Technol.*, vol.14, pp.1131-1136.
- Rao, Y.J. (1999) Recent progress in applications of in-fibre Bragg grating sensors, *Optics and Lasers in Engg.*, vol. 31, pp. 297-324.
- Russell, P. St. J., Hand, D.P., Chow, Y.T., Poyntz-Wright, L.J. (1991) Optically-induced creation, transformation and organization of defects and colour-centres in optical fibres, *Int. Workshop on Photoinduced Self-Organization in Optical Fiber*, Qubec City, Qubec, May 10-11, *Proc. SPIE*, vol. 1516, pp. 47-54.
- Secats, M.G., Atkins, G.R. and Poole, S.B. (1993) Photolytic index changes in optical fibers, *Annu. Rev. Mater. Sci.*, vol. 23, pp. 381-410.
- Shen, Y.H., He, J., Sun, T. and Grattan, K.T.V. (2004) High-temperature sustainability of strong fiber Bragg gratings written into Sb-Ge-Codoped photosensitive fiber: decay mechanism involved during annealing, *Opt. Lett.*, vol. 29, pp. 554-556.
- Shen, Y.H., Sun, T., Grattan, K.T.V. and Sun, M. (2003) High photosensitivity Sb/Er/Ge-codoped silica fiber for writing fiber Bragg gratings with strong high temperature sustainability, *Opt. Lett.*, vol. 28, pp. 2025-2027.
- Tsai, T.E., Friebele, E.J., Rajaram, M. and Mukhapadhyay, S. (1994) Structural origin of the 5.16 eV optical absorption band in silica and Ge-doped silica, *App. Phy. Lett.*, vol. 64, pp. 1481-1483.
- Williams, D.L., Davey, S.T., Kashyap, R., Armitage, J.R. and Ainslie, B.J. (1992) Direct observation of UV induced bleaching of 240nm absorption band in photosensitive germanosilicate glass fibres, *Electron. Lett.*, vol. 28, pp. 369-371.
- Williams, D.L., Ainslie, B.J., Armitage, J.R., Kashyap, R. and Campbell, R. (1993) Enhanced UV photosensitivity in boron codoped germanosilicate fibres, *Electron. Lett.*, vol. 29, pp. 45-47.

Chapter 3

Optimisation of wavelength-matched Bragg grating based fibre lasers for sensor applications

3.1. Abstract

This Chapter describes the general principle of the fibre laser with a particular focus on fibre Bragg grating (FBG) based lasers. A brief review of previous laser-based research, the general characteristics of Er^{3+}-doped silica fibres and their potential in fibre lasers is given, including possible pump requirements in fibre lasers and an experimental analysis of several fibre Bragg gratings-based lasers. In this Chapter, experiments were performed using thermally annealed, wavelength-matched Bragg gratings to form the laser cavity feedback enclosing a length of erbium-doped fibre (EDF) as the active gain medium of the laser. An FBG stabilised 1480 nm laser diode (LD) was used as a pump source and an Optical Spectrum Analyser (OSA) employed as the detection scheme. In order to optimise the performance of the Er^{3+}-doped fibre lasers, a range of contributing factors, such as reflectivities of the pairs of FBGs, the dopant levels of different erbium-doped fibres, the pump power effects, the length of the gain medium and different laser cavity configurations were considered. The experimental results obtained were then recorded, evaluated and discussed in detail in this Chapter.

3.2. Introduction

Advances in material science have made possible the doping of a range of rare-earth ions in an optical fibre core, showing both a low propagation loss and attractive laser properties usually designed for telecommunications, sensing, medicine and high resolution spectroscopic applications [Urquhart 1988]. An important property of rare earth doped fibre lasers is that the output spectral characteristics of the laser can be adjusted

by changing the composition of the glass host material. The long lifetime of the metastable state, particularly for Er^{3+} ions, permits the required high population inversion to be achieved using available pump sources under steady-state conditions. All these properties make erbium-doped fibre laser devices successful in telecommunication applications [Miniscalco 1991]. These stable, spectrally narrow linewidth, linear fibre laser sources are the key components to meet the increasing demand for high speed and high-capacity wavelength division multiplexed (WDM) systems for both communications and sensor applications.

In recent years, the expansion in FBG-based technology has further enhanced the functionality of fibre laser technology for many potential applications, especially for sensor use. The ability to integrate fibre Bragg gratings into the rare earth doped fibre with low insertion loss, their immunity to electromagnetic interference (EMI), low polarisation sensitivity, high wavelength selectivity and alignment insensitivity has revolutionised fibre laser technology. FBGs can be fabricated with a desirable reflectivity and appropriate Bragg wavelengths using the phase-mask technique, and thus flexibility are offered to optimise the performance of fibre laser based system for sensor applications.

3.2.1. Brief History of fibre lasers

Snitzer demonstrated the first fibre lasers in 1963 and after that he published the results of amplification using a multi-component glass fibre [Koester and Snitzer 1964]. The neodymium (Nd) glass core (~1m) was pumped by using a flashtube to obtain the amplification and was monitored using a phototube. Typical core and cladding diameters of ~10 μm and 0.75 mm to 1.5 mm respectively were used for the Nd doped glass fibre [Koester and Snitzer 1964]. At that time, the possible use of the fibre lasers was considered for optical information processing. In 1966, Koester observed oscillations in a fibre when the passive fibre core was placed adjacent to a straight flash lamp (pulsed with 2900J), where the cladding of the fibre consisted of Nd-doped glass. Koester was the first to propose the possibility of semiconductor diode pumped operation for such active fibres. Stone and Burrus [1973] reported two types of Nd-doped fused silica fibre lasers with operating wavelengths of ~ 1.06 μm and ~1.08 μm re-

spectively. For the first fibre laser, the active core consisted of Al_2O_3 and Nd_2O_3, co-doped in fused silica (SiO_2), with a SiO_2 cladding. For the second fibre laser, the active core consisted of Nd_2O_3 in fused SiO_2, encircled by a thin sleeve of fused SiO_2 and Nb_2O_5; and finally surrounded by a fused silica jacket. Both the lasers were end-pumped by using a pulsed dye laser (wavelength of 0.590 μm) and an Argon ion laser (wavelength of 0.514 μm) respectively.

From 1975 to 1985, attention was paid to making improvement in the development of fibre laser technologies. Different host materials for the rare earth ions were used to improve the fibre laser technology. Semiconductor lasers with relatively high output power as pump sources and fused and polished couplers to couple the pump power and to extract the laser output were necessary to establish these novel cavity designs for fibre lasers. Over the last few years, several laboratories and research groups across the world have shown their increasing interest in the fibre laser field.

3.2.2. Review of previous laser-based work

Several fibre Bragg grating (FBG)-based laser approaches have been reported over the previous several years using EDF as the active gain medium for the laser due to its potential for communication applications. Reekie *et al.* [1986] were the first to demonstrate a tunable EDF laser using an external grating. Morkel *et al.* [1990] have reported a single frequency EDF-laser in ring configuration operating at ~ 1555 nm with a laser linewidth of ~ 60 kHz. Gilbert [1991] has reported a tunable EDF laser where tuning of the laser wavelength was achieved by tilting the diffraction grating with a piezoelectric transducer (PZT). Cowle *et al.* [1991] have also reported a single frequency fibre loop-laser in a travelling wave configuration and this is shown in Fig. 3.1. Two ends of the coupler were connected with the gain medium (EDF) and a pig-tailed polarisation-independent isolator to form the fibre loop. A mirror or a distributed Bragg reflector (DBR) was used to form the laser cavity. A polarisation controller (PC) was used to adjust the polarisation sensitivity of the DBR. Unidirectional travelling wave operation was achieved using the isolator which eliminates the spatial hole burning effects in the gain medium and thus eliminates multimode operation. Laser oscillation was built with the return of the half signal from the reflectors (mirror or

DBR) to the gain medium through the 50:50 coupler when pumped by using a 980 nm LD. Using a DBR, it was possible to select the laser wavelength more precisely than the mirror.

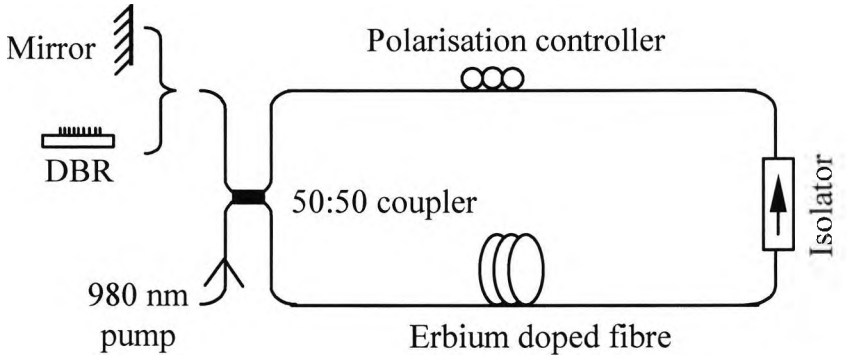

Fig. 3.1: Schematic of the unidirectional fibre loop-laser [Cowle *et al.* 1991].

Ball *et al.* [1991], Ball and Morey [1992] and Zyskind *et al.* [1992] have reported single mode erbium-doped DBR lasers. The intracore Bragg gratings were directly fabricated into the erbium-doped fibre (EDF) with sufficiently high reflectivity to form the feedback, thus avoiding the splice loss in the cavity. In order to obtain single mode laser operation, the length of the EDF should be very short (approximately less than 10 cm) to increase the axial mode spacing, which limits the efficiency of the laser. The output power of a short, single-frequency fibre laser was improved using a master oscillator power amplifier (MOPA) configuration to pump an EDF-amplifier followed by the laser using the residual laser pump power [Mizrahi *et al.*1993, Ball *et al.* 1994].

Kringlebotn *et al.* [1993] have used an erbium-ytterbium (Er:Yb) co-doped fibre as the gain medium of the laser to improve the efficiency of the short cavity laser. For the Er:Yb co-doped fibre, the pump power from a 980 nm source excites the Yb-ions which efficiently transfer their absorbed energy to Er-ions. The Yb ion is a two-fold energy level structure that excludes concentration-quenching and excited state absorption (ESA), also has a very broad absorption (~ 800 to 1064 nm) and emission (~ 970 to 1200 nm) cross-sections. Therefore, an efficient fibre laser could be constructed with a short length of this type of fibres. The slope efficiency of the laser as high as 22

% in a Fabry-Perot cavity laser was reported when pumped by using a 980 nm LD [Kringlebotn *et al.* 1994a].

Kringlebotn *et al.* [1994b] were the first to inscribe UV-induced Bragg gratings directly into the hydrogen loaded Er:Yb co-doped fibre. Thus the distributed feedback (DFB) fibre laser could be constructed without the splicing losses inside the cavity. Single mode DFB laser operation was reported [Asseh *et al.* 1995, Loh and Laming 1995, Sejka *et al.* 1995] by introducing a $\pi/2$ phase shift in the middle of the grating. The phase shift of the grating offers a significant difference in the threshold level between the fundamental mode and the higher order modes of the laser, which is independent of the laser length. The advantage of the DFB laser is the use of a single fibre grating for feedback, which is shown schematically in Fig. 3.2 [Loh *et al.* 1998].

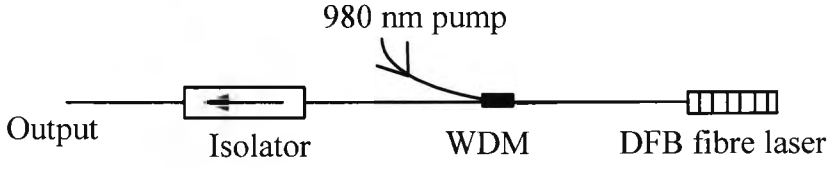

Fig. 3.2: Schematic of the distributed feedback laser configuration [Loh *et al.* 1998].

Dong *et al.* [1997] have reported a simple technique to make the Er:Yb co-doped fibre photosensitive without any modification to the glass host of the fibre core. A highly photosensitive boron-germanium (B-Ge) co-doped cladding was used to encircle the Er:Yb co-doped phosphosilicate fibre core. The highly photosensitive cladding allows the stronger grating to be inscribed directly into the fibre. Fibre lasers (both DBR and DFB lasers) were successfully constructed by writing gratings into the Er:Yb co-doped fibre.

Loh *et al.* [1998] have reported the characteristics of a single frequency grating based fibre laser and this is illustrated in Fig. 3.3. The laser cavity was formed within ~ 1.5 cm length of Er:Yb co-doped fibre using a combination of a Bragg grating and a dielectric (TiO_2/SiO_2) high reflectivity mirror which epoxies on the end of the gain fibre. FBG was directly written into the gain fibre (Er:Yb co-doped), achieving a reflec-

tivity of ~ 98 % at the Bragg wavelength of 1536 nm. The maximum laser output power of 58 mW was reported for 500 mW of the 980 nm pump power.

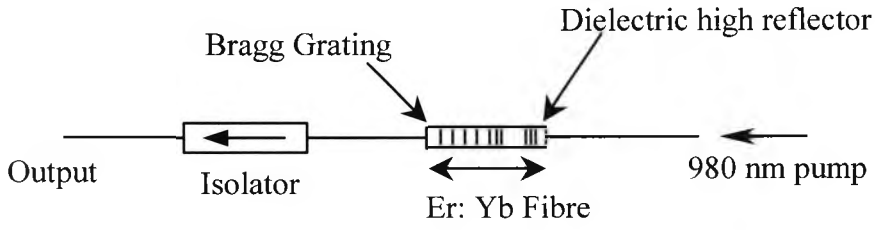

Fig. 3.3: Schematic of Bragg grating based laser configuration [Loh *et al.* 1998].

Park *et al.* [1992] have reported the multiwavelength fibre lasers using both linear and ring cavity configurations and these are shown in Figs. 3.4a and 3.4b respectively. For the linear cavity laser (Fig. 3.4a), the gain module (G) consists of 20 metres EDF to provide the gain of the laser. A fibre pigtailed eight-channel grating WDM having a channel spacing of ~ 4.8 nm and bandwidth of 0.8 nm each was used to configure the multichannel laser system. A fibre loop mirror (FLM) was used to form the variable output couplers to adjust the output coupling loss and hence the gain of each laser channel. The laser output power fluctuations were observed due to the gain competition across each channel. The gain competition arises from the modal instabilities due to spatial hole burning effects, which is caused by the intensity of the standing-wave pattern of longitudinal modes fall within the grating bandwidth of WDM.

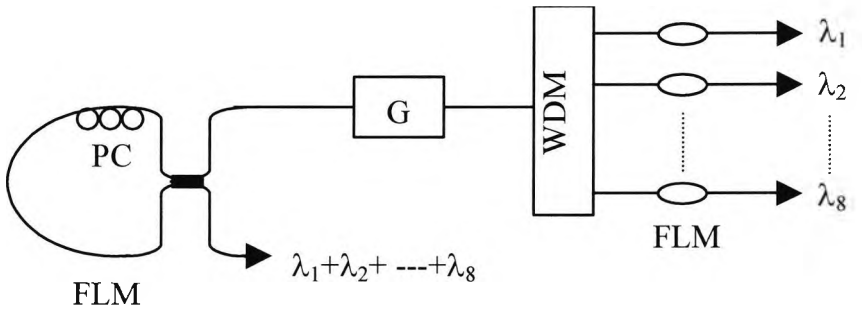

Fig. 3.4a: Multiwavelength linear cavity laser configuration. FLM: fibre loop mirror, PC: polarisation controller, WDM: wavelength division multiplexer and G: gain module [Park *et al.* 1992].

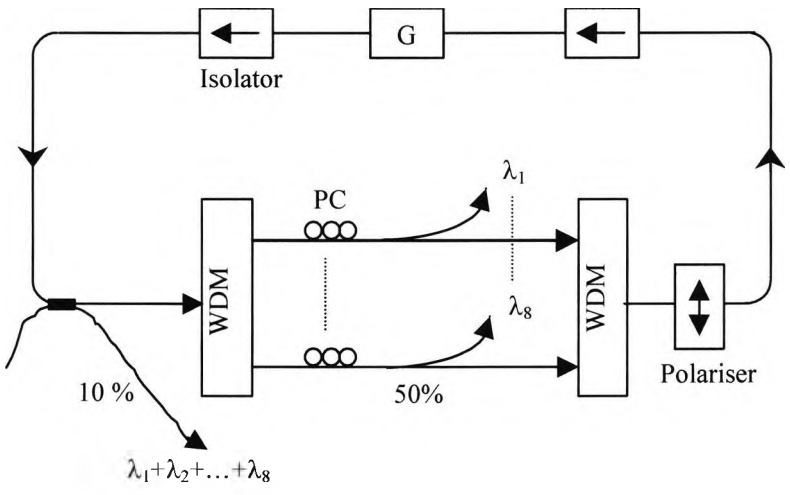

Fig. 3.4b: Multiwavelength ring cavity laser configuration [Park *et al.* 1992].

The output power fluctuations of each channel were improved when the laser was constructed using a ring cavity configuration (Fig. 3.4b) and employing an additional wavelength matched WDM to the first one [Park *et al.* 1992]. A polarisation controller (PC) was used in each channel to provide different cavity losses across the channels and the multiplexed laser outputs at six different channels were obtained using a grating monochromator over the wavelength range from 1528 to 1557 nm.

Chow *et al.* [1996] have reported simultaneous multiwavelength laser operation using in-fibre grating comb filters and this is illustrated in Fig. 3.5. A ring cavity consists of ~ 6 metres alumni-silicate fibre and its unidirectional operation were maintained using an isolator in the gain medium. The gain medium consists of ~ 30 metres EDF and was cooled in liquid nitrogen at 77 K to reduce the homogeneous broadening of the fibre, and thus to reduce the gain cross-saturation between the lasing wavelengths. Two types of in-fibre comb filters were inserted into the ring cavity to obtain multiwavelength laser operations. One filter was a transmissive wide band Fabry-Perot resonator configured using distributed mirrors formed by chirped Bragg gratings fabricated into the photosensitive fibre [Town *et al.* 1995], in series with a 6 nm tuneable filter. The tuneable filter used inside the comb filter to prevent the lasing outside the bandwidth of the chirped grating. The other was a reflective sampled Bragg grating [Eggleton *et al.* 1994]. The reflection spectrum of superstructure Bragg grating con-

sists of a series of uniform spaced peaks at different wavelengths along the length of the fibre.

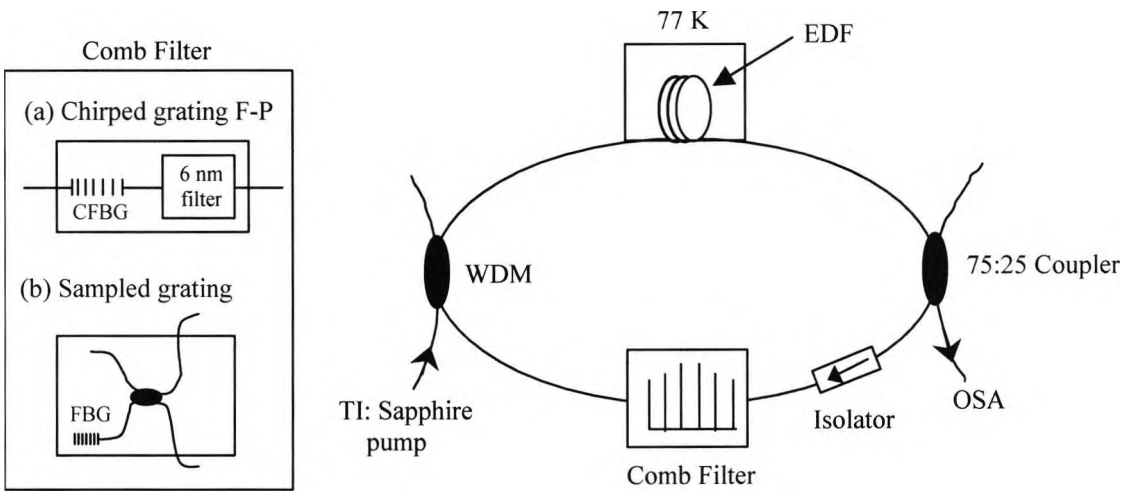

Fig. 3.5: Multiwavelength ring laser configuration showing different grating filters were incorporated into the cavity [Chow *et al.* 1996].

The excimer laser was triggered on and off at regular intervals while the ultraviolet (UV) beam was translated at a uniform velocity along the phase mask used to fabricate the superstructure grating. Multiwavelength laser operation was obtained when the gain medium was pumped with a 300 mW of the 980 nm LD. In both the cases, the laser wavelengths were found to be consistent with comb filter's wavelengths. The overall laser system designs are, however, complex.

Li *et al.* [1997] have reported dual wavelength fibre laser operations in ring cavity configuration. Mao and Lit [2002] have shown multiwavelength fibre laser in cascaded fibre Bragg grating cavities and this is illustrated in Fig. 3.6. A broadband reflection mirror and three FBGs were used to form the multiple laser cavities in serial configuration in conjunction with separate gain medium across each FBG. By adjusting the erbium fibre lengths and the cavity losses (using a variable attenuator), it was possible to obtain three output laser emissions individually, or simultaneously, depending on the pump power. A polarisation controller (PC) was used before the

WDM coupler into the cavity to finally adjust the gain near a specific laser wavelength.

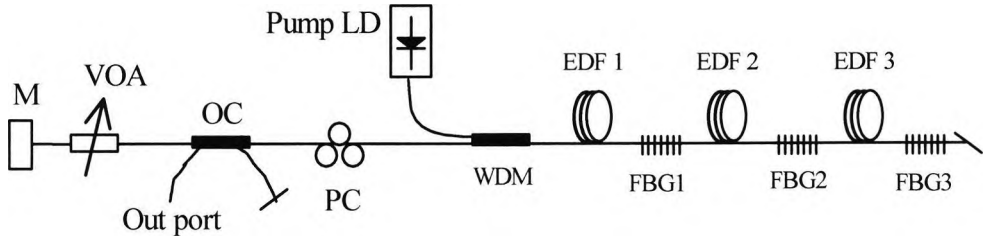

Fig. 3.6: Schematic of multi-wavelength erbium-doped fibre (EDF) laser. M: Broadband mirror, VOA: variable optical attenuator, OC: optical coupler and PC: polarisation controller [Mao and Lit 2002].

Recently Liu *et al.* [2004] have reported single-mode multiwavelength EDF laser in ring configuration and this is shown in Fig. 3.7. The fibre loop mirror (FLM) consists of an optical coupler (OC2) and lengths of unpumped EDF defined as a saturable absorber (SA); and were placed inside the ring cavity to obtain single mode operation of the laser. Two counter-propagating light waves were launched into the loop mirror through optical coupler (OC2) to create spatial hole burning effect into the saturable absorber. This causes slight refractive index change ($\sim 10^{-7}$) in the absorber (SA) and a weak grating (with very narrow reflection bandwidth) was formed, which provides a single-mode laser signal to be obtained. The optical circulator (CL2) was placed in front of the loop mirror to prevent the residual pump signal from the EDF, so that the SA in the loop mirror is unpumped. Polarisation controllers (PCs) were used to control the state of polarisation of light and two circulators were used to obtain unidirectional operation inside the main ring cavity. The gain medium (EDF) was cooled in liquid nitrogen to eliminate the homogeneous broadening effect of the fibre and was pumped by using a 976 nm LD to obtain laser oscillations.

Multiwavelength laser operation was obtained by using either a FBG array or a Lyot-Sagnac filter inside the main ring cavity as the wavelength selector. The Lyot-Sagnac filter consists of a single mode optical coupler (OC) and two lengths of polarisation maintaining fibres (PMFs) with a rotation angle of 52° between two main axes. Using

a Lyot-Sagnac filter as the wavelength selector of the laser, the neighbouring frequency interval ($\Delta\upsilon$) of the laser was obtained by varying the length difference (ΔL_{PM}) between the PMFs, and this was expressed as below [Liu *et al.* 2004]:

$$\Delta\upsilon = \frac{c}{B\Delta L_{PM}}, \tag{3.1}$$

where c is the velocity of light in vacuum and B is the birefringence ($\sim 4\times10^{-4}$) of the polarisation maintaining fibre.

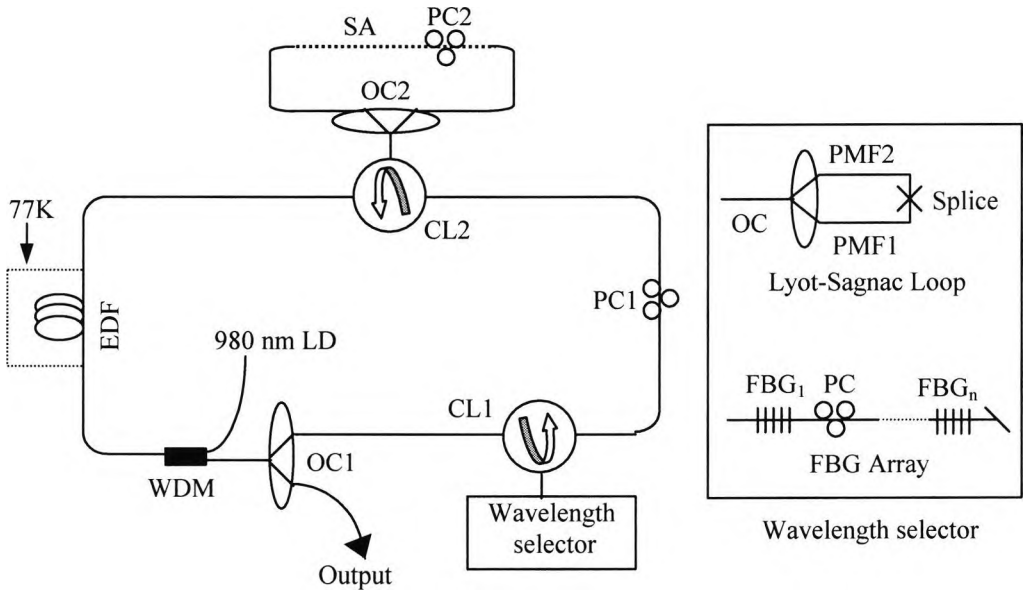

Fig. 3.7: Schematic of the single-mode mutiwavelength fibre laser in ring configuration. PC: polarisation controller, CL: circulator, OC: optical coupler, SA: saturable absorber and PMF: polarisation maintaining fibre [Liu *et al.* 2004].

A review of recent research on laser-based systems shows the potential of various types of laser cavity configurations. The linear laser cavity configuration [Loh *et al.* 1998] system is a simple and effective structure compared, for example, to ring cavity configurations [Liu *et al.* 2004], as the former technique requires fewer optical components which simplify the complete system set-up. As a result, a linear cavity configuration was chosen for the laser systems developed for the work reported in this thesis in order to optimise their performance for sensor applications.

3.3. Rare Earth Ions

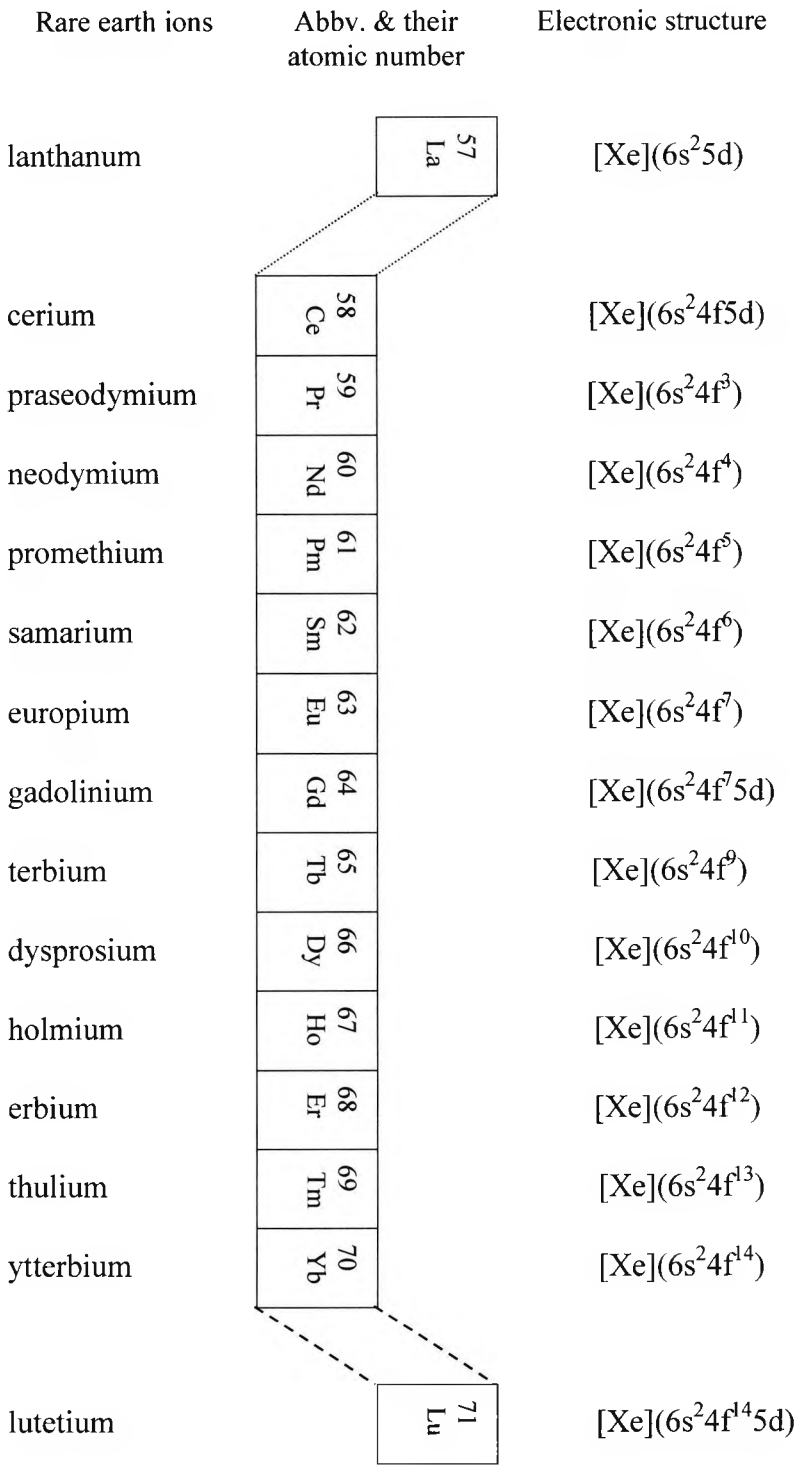

Fig. 3.8: Schematic of the periodic table of the rare earth elements showing their atomic number and electronic configuration [Urquhart 1988].

The rare earths, lanthanides, consist of a set of 15 elements and these are shown schematically in Fig. 3.8. The lanthanides range from lanthanum (La) with an atomic number of 57, and end with lutetium (Lu), with an atomic number 71. All of the rare earth ions have the same outer electronic structure of $5s^2 5p^6([Xe])6s^2$, which are filled shells. [Xe] represents the electronic configuration of Xenon and [Xe] includes the 5s and 5p electrons. Optical absorption and emission spectra are a consequence of transitions between 4f shells. The trivalent (3+) level of ionisation is the most stable for lanthanide ions, and most optical devices use trivalent ions [Urquhart 1988]. However, our main interest is on one particular rare-earth ion, especially erbium (Er^{3+}), having an atomic number of 68.

3.3.1. Energy levels diagram of Er^{3+}-doped fibre

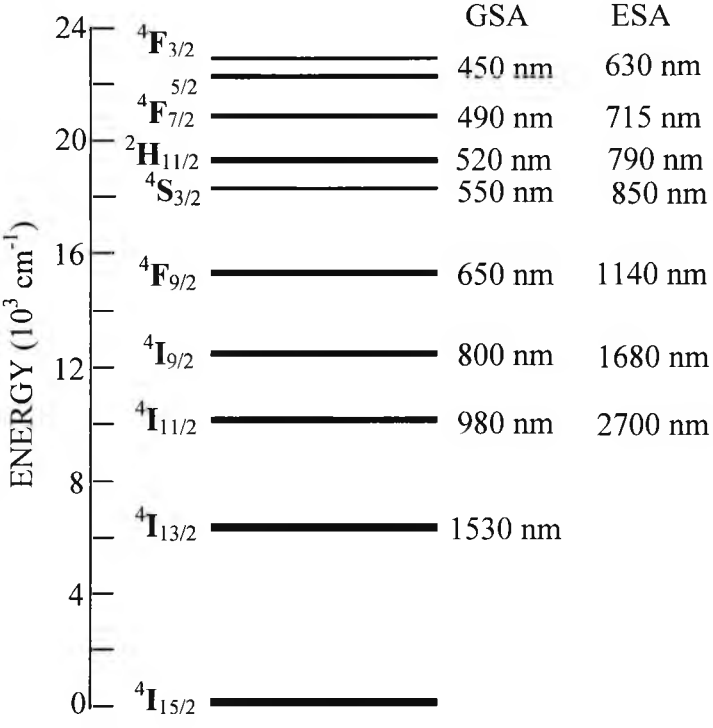

Fig. 3.9: Schematic diagram of energy levels of the erbium-doped fibre. GSA column represents the wavelength of the ground state absorption (GSA) transition *terminating* on the metastable level ($^4I_{13/2}$) and ESA column represents the wavelength of the excited-state absorption (ESA) transition *originating* from the metastable level ($^4I_{13/2}$) [Miniscalco 1991].

Fig. 3.9 shows an energy level diagram of the Er^{3+} ion indicating the energy level up to 24×10^3 cm^{-1}. The metastable state ($^4I_{13/2}$) of Er^{3+} ions has long lifetime (~ 10 ms) and thus produce gain at 1500 nm wavelength range. Any process of removing Er^{3+} ions from this metastable level other than the stimulated emission into the signal mode will necessarily decrease the efficiency of a laser or an amplifier. These processes may take place in any of the following ways. These are discussed in detail elsewhere [Digonnet 1993].

3.3.1.1. Nonradiative Relaxation

One possible mechanism of the nonradiative relaxation to the ground state ($^4I_{15/2}$) is due to the interaction between the electrons and the dynamic lattice. This process normally occurs through multiphonon emission and an approximate exponential dependence on the energy gap to the next lower levels [Layne *et al.* 1977, Layne and Weber 1977]. The occupation numbers of the highest energy modes in each of the glasses are temperature dependent and normally increase with increasing temperature.

3.3.1.2. Excited State Absorption

Excited state absorption (ESA) is also a loss mechanism. This process occurs when there is excitation of an ion into the higher energy levels through the absorption of a pump or a signal photon from the metastable state ($^4I_{13/2}$). Thus ESA depletes the metastable state ($^4I_{13/2}$) and makes insufficient use of the pump power. Even though the ion finally returns to the metastable level, a photon will be lost either converting its energy into heat or through a spontaneous emission at an unwanted wavelength.

3.3.1.3. Cross-Relaxation

The cross-relaxation is a process in which an ion in an excited state transfers parts of its excitation energy to a neighbouring ion. The process involves concentration quenching and co-operative upconversion.

3.3.1.3.1. Cooperative Up-Conversion

The cooperative upconversion process for erbium-doped fibre is shown in Fig. 3.10 [Blixt *et al.* 1991]. Two neighbouring atoms are excited to the metastable or upper laser level ($^4I_{13/2}$) by two photons with a pump wavelength of 1480 nm. One of them (donor) transfers its energy nonradiatively to the other (acceptor), thus promoting the acceptor to the higher energy level $^4I_{9/2}$ while the donor nonradiatively relaxes to the ground state ($^4I_{15/2}$). The acceptor atom relaxes rapidly to the $^4I_{11/2}$ level within a few nanoseconds and then mostly down to the $^4I_{13/2}$ metastable state via multiphonon coupling (4a). Therefore, the net result of the process is the conversion of one excitation ion into heat, thus reduces the efficiencies of the erbium-doped fibre devices.

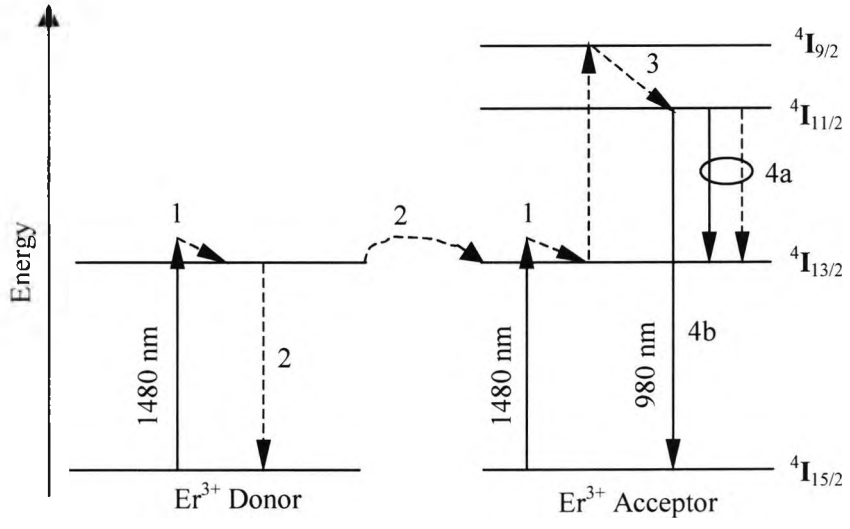

Fig. 3.10: Schematic of upconversion process in erbium-doped fibre. Solid line arrow represents radiative transitions, while dashed line arrow represents nonradiative transitions [Blixt *et al.* 1991].

For 980 nm pump wavelength, hardly one atom out of 10000 relaxes down to the ground state with the emission of a photon (4b), as reported by Blixt *et al.* [1991]. Since cooperative upconversion process requires two interacting ions in the excited state, it will not be significant at low pump power level. At high pump power, the effect is found to be accelerating due to strong interaction between excited ions. For 1480 nm pumping, cooperative up-converted $^4I_{11/2}$ emission at 980 nm wavelength

was reported by Kagi *et al.* [1990] and Blixt *et al.* [1991], due to nonradiative relaxation of the atoms which are promoted to the $^4I_{9/2}$ level. A significant gain difference was reported at high pump powers between the high and the low concentrations of Er^{3+} doped fibre amplifiers.

3.3.1.3.2. Concentration Quenching

The quantum efficiency of an ion was found to decrease with increasing concentration of that ion due to concentration quenching. Energy transfer takes place between two neighbouring ions when they are in close proximity to each other thus resulting in clustering, i.e. local groups of a few ions are very close to each other. Normally, in heavily doped materials, the mean distance between two neighbouring ions is small due to higher ion dopant density, thus leading to possibility of quenching. The process is the loss of excitation and usually shortens the excited or metastable state $^4I_{13/2}$ lifetime [Digonnet 1993].

3.3.2. Solubility of Rare Earth Ions in Silica

To improve the pump-to-signal conversion efficiency of a laser or an amplifier, it is necessary to improve the solubility of rare earth ions in the silica fibre core. Four coordinates Ge do not alter the tetrahedral silica network sufficiently to significantly increase the solubility of rare earth ions, as reported by Ainslie *et al.* [1987]. Er^{3+} should equally be insoluble in silica; the order of magnitude difference in the onset of reported quenching is due to either a stronger interaction between Er^{3+} ions or a greater sensitivity to dissipative processes in amplifier experiments.

The addition of Al (aluminium) has been found to eliminate the clustering problems that may occur in silica glasses [Arai *et al.* 1986]. Arai *et al.* [1986] have reported the role of Al in terms of solution chemistry: Al_2O_3 dissolves well in SiO_2, where Nd_2O_3 dissolves in Al_2O_3 but not in SiO_2, thus Nd_2O_3 is insoluble in SiO_2. The role of Al dopant is integrated into two different local bonding configurations in the SiO_2 network: (i) in a tetrahedral bonding configuration as a network former as $AlO_{4/2}$, and (ii) in an octahedral coordination of oxygen atoms as a network modifier such as $AlO_{6/2}$.

Al ions are fourfold oxygen coordinated as $AlO_{4/2}$ with positively charge compensating ion acts as a hole trap and the $AlO_{6/2}$ configuration acts as an electron trap in silica glass. So $AlO_{4/2}$ and/or $AlO_{6/2}$ form solvation shells to make the rare earth ions (e.g. Nd^{3+}) soluble into the silica glass network [Arai *et al.* 1986].

Power amplifier studies by Laming *et al.* [1991] have shown no significant quenching for Er^{3+} ions concentration of ~1000 ppm in germano-alumino-silicate and alumino-silicate fibres. The modified chemical vapour deposition (MCVD) preform fabrication process depletes rare earth dopant at the centre of the core for Ge and Ge/P-doped silica [Ainslie *et al.* 1988a]. The addition of Al in Ge or P co-doped silica fibres showed to avoid the depletion of the rare earth ions, hence to improve the pump efficiency of the amplifiers. Armitage [1988] has shown to improve the efficiency of the fibre laser amplifier by controlling the radial doping profile of the rare earth ions (i.e. confining the Er^{3+} ions to the centre of the fibre core). This is because for the smaller size of the fibre core, the pump mode size becomes smaller which increases the pump intensity to excite more Er^{3+} ions to the upper laser level.

3.3.3. Absorption and Emission Cross-Sections

For a three level fibre laser system such as Er^{3+}, the absorption and emission cross sections have an important significance in determining the performance of a device [Digonnet 1993]. Since the $^4I_{13/2}$ is the only metastable state for common oxide glasses at room temperature, therefore gain is available at the wavelength of 1500 nm from the $^4I_{13/2} \rightarrow {}^4I_{15/2}$ emission band. The magnitude and the shape of the spectra of the transitions are glass host dependent, and the variation is caused by the difference in the intensities of the ingredient Stark transitions [Duservire and Simpson 1990].

For the investigation of rare earth transitions, it is common to measure one of the cross-section spectra and then calculate the other. However, measuring the absorption cross section is complex, so the stimulated emission cross-section is generally measured for several fibre samples [Duservire and Simpson 1989, Atkins *et al.* 1989, Miniscalco and Quimby 1991]. For the finite linewidth, the relationship between the Einstein's coefficients coupled the integrated cross-sections as follows:

$$g_1 \int v^2 \delta_{12}(v)\, dv = g_2 \int v^2 \delta_{21}(v)\, dv, \qquad (3.2)$$

where δ_{12} and δ_{21} are the absorption and the emission cross-sections between the $^4I_{15/2}$ and $^4I_{13/2}$ manifolds, $g_i = 2j + 1$ are the degeneracy's of the j^{th} levels involved. Two assumptions were made to prove the validity of the above Eq. (3.2): either all the Stark components of the two multiplets must be equally populated, or all the transitions must have the same strength regardless of the compositions involved.

Figs. 3.11a and 3.11b show the Stark level energies of the $^4I_{13/2}$ and the $^4I_{15/2}$ manifolds for the absorption and the fluorescence transitions of the erbium doped aluminosilicate glass fibre. The total Stark splitting of the $^4I_{13/2}$ and the $^4I_{15/2}$ manifolds of the doped fibre were found to be 230 cm^{-1} and 268 cm^{-1} respectively, so the first assumption of Eq. (3.12) is not satisfied at room temperature (kT~ 200 cm^{-1}). Also, the absorption and the emission spectra measurement indicate that the transition strength is quite sensitive to the Stark levels involved for all the glasses at low temperature [Duservire and Simpson 1990].

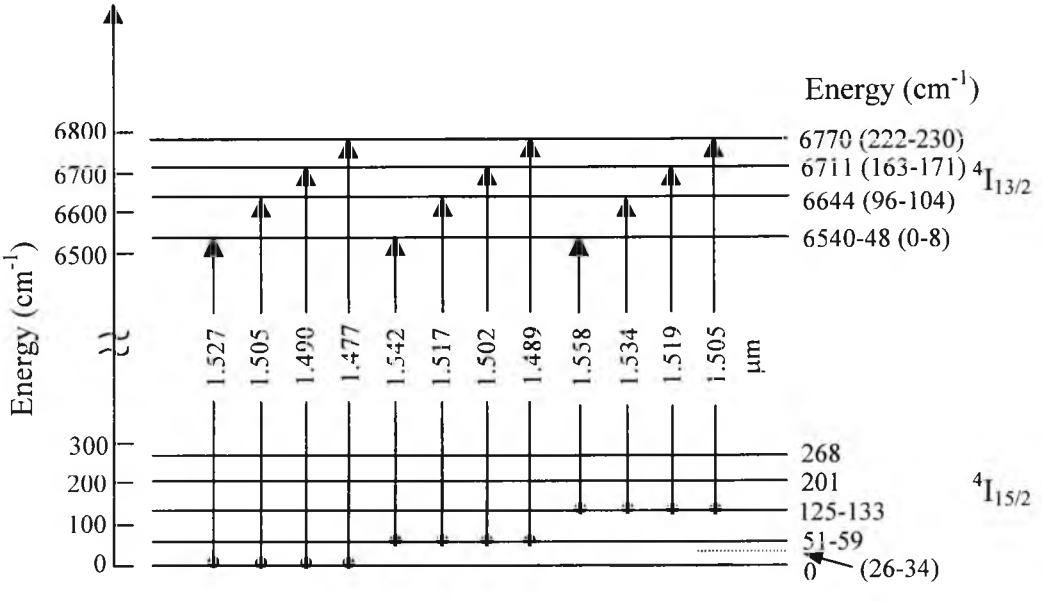

Fig. 3.11a: Evaluation of the Stark level energies of the $^4I_{13/2}$ and the $^4I_{15/2}$ manifolds for the absorption transitions in Er_2O_3-Al_2O_3-GeO_2-Si glass fibre [Duservire and Simpson 1990].

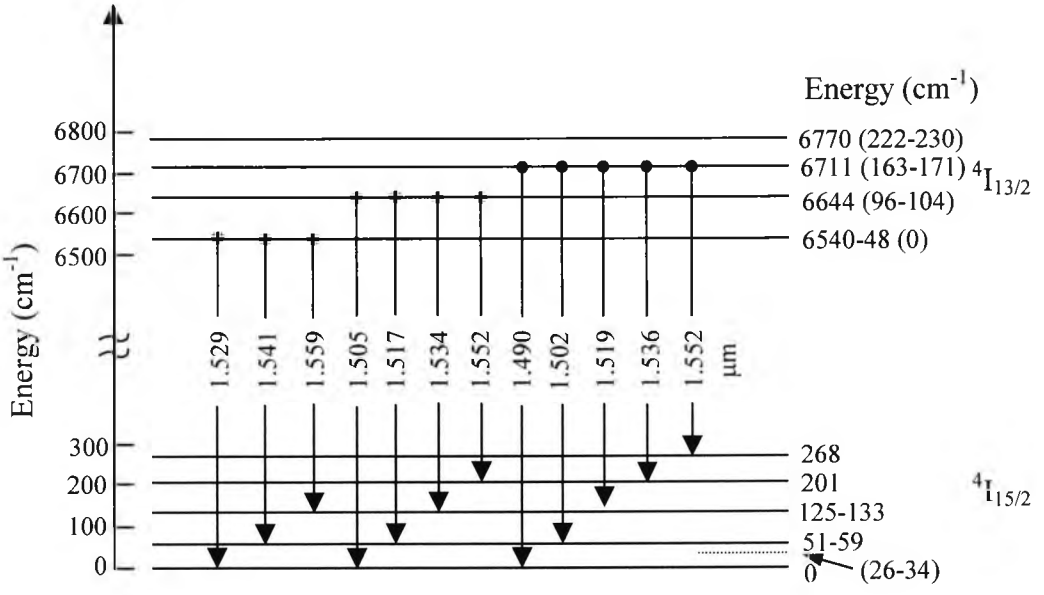

Fig. 3.11b: Evaluation of the Stark level energies of the $^4I_{13/2}$ and the $^4I_{15/2}$ manifolds for the fluorescence transitions in Er_2O_3-Al_2O_3-GeO_2-Si glass fibre [Duservire and Simpson 1990].

The absorption and the emission cross-sections can also be related based on the more general theory of McCumber [McCumber 1964] as follows:

$$\delta_{21}(v) = \delta_{12}(v) e^{(\varepsilon - hv)/kT}, \tag{3.3}$$

where ε is the mean energy transitions to excite Er^{3+} ion from the $^4I_{15/2}$ to the $^4I_{13/2}$ state at temperature T. The only assumption made by McCumber's theory is that the time required to establish a thermal distribution within each manifold be short compared to the lifetime of that manifold. The main disadvantage of the McCumber theory is that ε can only be calculated when the positions of all the Stark levels are known for both the manifolds ($^4I_{15/2}$ and $^4I_{13/2}$ states).

The gain profile of the erbium-doped fibre is determined primarily by the metastable level ($^4I_{13/2}$) and the ground level ($^4I_{15/2}$) of the Er^{3+} ion, themselves comprising several Stark sub-levels which are populated to various degrees depending on the Boltzmann thermal distribution. The fluorescence spectrum of the Er^{3+} doped fibre in this spectral region, in general consists of two wavelength peaks at around 1535 nm and

1552 nm, which vary to a small degree with the hosts material used [Duservire and Simpson 1990].

3.4. Pump Wavelengths

An optically pumped laser, amplifier or super luminescent device needs to be excited by using another optical source which excites the active dopant into one of its absorption bands. Er^{3+}-ions have several absorption bands (centred at the wavelengths of ~ 514, 650, 800, 980 and 1480 nm) from the visible to the infrared region and therefore a variety of pump sources may be used for the excitation of Er^{3+} fluorescence.

3.4.1. 1480 nm pump band

Snitzer *et al.* [1988] first demonstrated that Er^{3+} ions could directly be excited into the $^4I_{13/2}$ metastable level by pumping ~ 1480 nm wavelength. Pumping at wavelength near 1500 nm band is attractive because excited state absorption (ESA) is absent and the mode profiles of the pump and the signal are well matched for the erbium doped fibre amplifier (EDFA). Amplifiers pumped by ~ 1470-1490 nm wavelengths [Atkins *et al.*1989, Duservire 1989, Zyskind *et al.*1989, Shimizu *et al.* 1990] have shown considerable systems performance with excellent results, taking advantage of the available high power InGaAsP 1480 nm laser diodes. Pederson *et al.* [1991] have showed that 1480 nm resonant pumping limits the obtainable population inversion; thus there is some penalty in the signal-to-noise ratio (SNR). Since the ratio of the emission to the absorption cross-section is higher for the signal wavelength at 1551 nm compared to 1532 nm, the quantum conversion efficiency (QEC: the number of signal photons divided by the number of launched pump photons) will be larger at 1551 nm. However, the noise figure for 1480 nm pumping is higher (can be up to 3 dB) than 980 nm pumping, due to the proximity of the pump and the signal wavelength for 1480 nm resonant pumping which lower the average inversion.

Although pumping at the wavelength of 1480 nm superficially involves a two-level system [Becker *et al.* 1999], which is schematically illustrated in Fig. 3.12, it can produce gain because of the shift between the absorption and the emission cross-sections

sections spectra. This offset is an effect of non-uniformly populated Stark levels since kT at room temperature (~200 cm^{-1}) is less than the width of both the $^4I_{13/2}$ metastable and the $^4I_{15/2}$ ground states manifolds (230 - 268 cm^{-1}). From the relationship between the absorption and the emission cross-sections given by Eq. (3.3), the spectral offset increases with decreasing temperature. The $^4I_{15/2} \rightarrow {}^4I_{13/2}$ absorption band is broad [Duservire 1989] and does not vary significantly over this interval, which simplifies the selection of the pump wavelengths and highly multimode pumps will suffice.

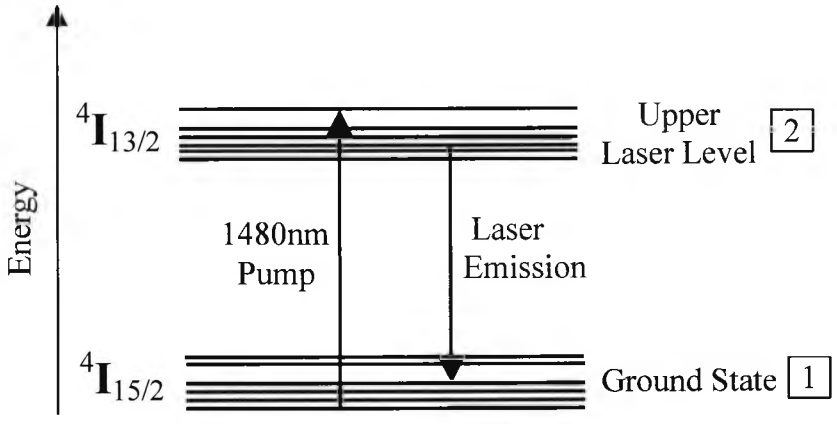

Fig. 3.12: Energy diagram of erbium-doped fibre for 1480 nm pumping [Becker *et al.* 1999].

3.4.1.1. Threshold for 1480 nm pumping

The required pump power for population inversion, $P_{th(inv)}$, and thus to overcome the threshold, $P_{th(power)}$ for lasing can be given by [Becker *et al.* 1999]:

$$P_{th(inv)} = \frac{A_{eff} h\upsilon_p}{\tau_2 \left(\delta_{12}(\upsilon_p) - \delta_{21}(\upsilon_p)\right)}, \tag{3.4}$$

$$P_{th(power)} = \frac{A_{eff} h\upsilon_p}{\tau_2 \left[\delta_{12}(\upsilon_p)\left(\frac{\delta_{21}(\upsilon_s)}{\delta_{12}(\upsilon_s)}\right) - \delta_{21}(\upsilon_p)\right]}, \tag{3.5}$$

where υ_P and υ_s are the photon frequencies at the pump and the signal wavelengths respectively, $\delta_{12}(\upsilon_P)$, $\delta_{21}(\upsilon_P)$, $\delta_{12}(\upsilon_s)$ and $\delta_{21}(\upsilon_s)$ are the pump and the signal absorption

and emission cross-sections respectively, τ_2 is the lifetime of the metastable state ($^4I_{13/2}$), A_{eff} is the effective cross-sectional area of the distributions of erbium ions in the fibre core [Becker *et al.* 1999]. For 1480 nm resonant pumping, $\delta_{12}(\upsilon_s)$ and $\delta_{21}(\upsilon_s)$ can be ignored, and Eqs. (3.4) and (3.5) can be approximated to be the same. Combining Eqs. (3.3) and (3.4), the population inversion, which is effectively equal to the pump threshold power for lasing, is given by:

$$P_{th(inv)} = \frac{A_{eff} h\upsilon_p}{\delta_{12}(\upsilon_p)\tau_2\left[1 - e^{(\varepsilon - h\upsilon)/kT}\right]} = P_{th(power)}, \qquad (3.6)$$

Based on Eqs. (3.5) and (3.6), the optimum conditions for the minimum pump threshold power for lasing involve are to be summarised as below:

- Low emission cross section,
- High absorption cross section,
- Long lifetime of the metastable state,
- Thermal non-equilibrium condition.

3.4.2. 980 nm pump band

The $^4I_{15/2} \rightarrow {}^4I_{11/2}$ transition of Er^{3+} ions corresponds to an absorption band at the ~ 980 nm wavelength which is also attractive for fibre amplifier and laser devices. Amplifiers pumped at this wavelength [Laming and Payne 1990, Laming *et al.* 1991] have also reported excellent performance in terms of gain and efficiency of gain. An amplifier output power of 54 mW was achieved using a fibre length of 31 metres with 100 mW pump power at 978 nm, which shows a pump-to-signal conversion efficiency of 54 % [Laming *et al.* 1991]. This is due to the large absorption cross-section together with the complete absence of the excited state absorption (ESA) at this pump wavelength. A noise figure of ~ 3 dB was reported by [Yamada *et al.* 1990] using the 980 nm pumping and 4.1 dB using the 1480 nm pumping. For 980 nm pumping, erbium-doped fibre operates as a true three level system, which permits nearly complete population inversion to be achieved with relatively low pump power [Laming and Payne 1990]. Becker *et al.* [1990] have used a range of pump sources with their wave-

lengths varying from 960-1000 nm to pump the erbium doped fibre amplifier (EDFA). An amplifier gain of ~ 25 - 28 dB at 1557 nm wavelength was reported with 17 mW of launched pump power using any wavelength pump ranging from 965-985 nm. However, the optimum erbium fibre lengths showed to be different for different pump wavelengths. Using 978 nm pump wavelength and an input signal power of – 40 dBm, with an erbium fibre length of 43 metres, lower threshold and a higher slope efficiency at 1553 nm signal wavelength was reported compared to that at 1533 nm. This can be explained from the fact that the 1553 nm (longer wavelength) transition has less thermal population in its lower state. By contrast, Pederson *et al.* [1991] have reported the quantum conversion efficiency (OEC) is slightly higher at the signal wavelength of ~ 1532 nm compared to that of ~ 1552 nm with 980 nm pumping.

3.4.3. 800 nm pump band

The $^4I_{15/2} \rightarrow {}^4I_{9/2}$ transition of Er^{3+} ions corresponds to an absorption band at the ~ 800 nm wavelength, which requires relatively high pumping power with inexpensive Al-GaAs laser diodes. The $^4I_{9/2}$ level of Er^{3+} is short lived and hence decaying by multiphonon emission. The performance of the 800 nm band is comparatively poor for the 1500 nm devices because the ground state absorption (GSA) transition is weak and also it overlaps with a much stronger $^4I_{13/2}$ excited state absorption (ESA) band. Laming *et al.* [1988] have measured the GSA and ESA spectra for erbium-doped silica fibres with four different core co-dopants (GeO_2, GeO_2/B_2O_3, GeO_2/P_2O_5 and Al_2O_3) over the wavelength ranges from 450-1050 nm. The ESA spectra depend on the core compositions of the fibre and this effect is less significant for P_2O_5 or Al_2O_3 co-doped Er^{3+} fibre for the 515 nm and the 650 nm pump wavelengths because of the reduced pump excited state absorption. The ESA is still the dominant problem for the 488 nm and the 810 nm pump wavelengths.

The available evidence indicates that the 980 and 1480 nm pump wavelengths are the most attractive pump bands for exciting the 1500 nm fibre devices in oxide glasses as these bands are free from ESA, with the 800 nm pump band is a distant third. The 980 nm absorption cross-section is comparable to that at the 1480 nm pumping but about four times greater than that at the 800 nm wavelength [Digonnet 1993].

Based on the previous research work and the characteristics of different pump wavelengths, light from a 1480 nm laser diode was used as the laser excitation scheme because at this wavelength the pump source is free from ESA and also available with relatively higher level of pump power. The integration of FBGs into the rare-earth fibre offers low losses and compatible with optical devices. Erbium-doped fibre was used as the laser gain medium because of its very wide availability at different concentrations of Er^{3+} ions, due to the extensive development of optical fibre lasers and amplifiers for sensor and communications applications. Details of the experimental configuration of the laser used in this work are given below.

3.5. Experimental Set-up

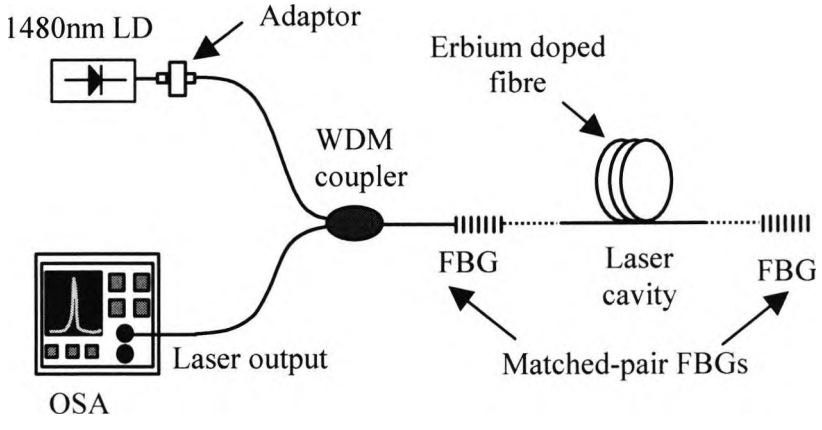

Fig. 3.13: Schematic of a wavelength-matched Bragg grating based erbium-doped fibre laser system. OSA: Optical Spectrum Analyser, WDM: Wavelength Division Multiplexer, LD: Laser Diode.

The schematic of the experimental set-up is shown in Fig. 3.13. An FBG stabilised 1480 nm LD was used as a pump source, connected through an adaptor to one of the input arms of the 1480nm/1550nm wavelength division multiplexed (single mode WDM, isolation (dB): >12, insertion loss (dB): 0.35, supplied by Laser 2000 Ltd., UK) coupler used. Erbium-doped fibre (EDF) was used as the gain medium which was fusion spliced to FBGs at both ends to form the laser cavity feedback. The less

reflective FBG was attached to the output arm of the WDM coupler through a length of Corning single mode fibre (SMF-28) to extract the laser output. Since the pump wavelength (1480 nm) fell outside the Bragg gratings bandwidth, the gratings had no effect on the transmission of pump power into the laser cavity. Two different types of EDFs were used in this work and the details are summarised in Table 3.1.

Table 3.1: Characteristics of erbium-doped fibres used in this work.

Fibre Types	Core compositions and their concentrations	Core Diameter	Numerical aperture (*NA*)	Absorption @1530nm	$\lambda_{cut\text{-}off}$
Fibre 2	Er_2O_3 (650-700 ppm-wt)+GeO_2 (25-28-wt%)+Al_2O_3 (3-wt%) in silica glass host	3.0 μm	0.26	7 dB/m (manufactured) 4.2 dB/m (measured)	1.0 μm
Fibre 1	Er_2O_3 (350-400 ppm-wt)+GeO_2 (25-28-wt%)+Al_2O_3 (3-wt%) in silica glass host	2.3 μm	0.27	4 dB/m (manufactured) 2.8 dB/m (measured)	0.85 μm

In addition, several pairs of different FBGs were tested in this work, where the FBG with high reflectivity (R = 99.9 %) was designed to have higher reflection at the lasing wavelength and the other FBGs with lower reflectivity had showed varying reflectivity from 78 – 95 % to achieve different percentage transmission values at the lasing wavelengths. The laser output spectra were monitored through the other arm of the WDM coupler using an OSA (Model: HP86140A) with a resolution bandwidth (RBW) of 0.2 nm. The insertion loss from the FC/PC connector was around 0.05 dB.

3.5.1. Fabrication of FBGs

Fibre Bragg gratings were fabricated in a boron-germanium (B-Ge) co-doped photosensitive fibres (fibre details are given in Chapter 2) using a KrF excimer laser as UV light source and through the phase-mask technique (details described in Chapter 2).

The energy (varied from 8 to12 mJ) and the frequency (varied from 50 to 200 Hz) of the excimer laser were carefully controlled during the fabrication of several Bragg gratings to achieve desire level of reflectivities. The Bragg wavelengths of the variable reflectivity (78-95 %) of the gratings were closely matched in wavelength terms with the Bragg wavelength of the high reflectivity grating (R = 99.96 %) during their inscription. The Bragg wavelengths of these gratings were achieved at ~1535 nm wavelength and their transmission spectrum were monitored during the fabrication using an OSA. The different parameters of the gratings were calculated using the equations derived in Chapter 2 [Othonos and Kalli 1999] and these values are summarised in Table 3.2.

3.5.1.1. Annealing effect of FBGs

To achieve stable and reproducible performance of the lasers, each of the gratings was annealed at 100 °C for 6 hours using a well-calibrated Carbolite oven (MTF 12/38/400), as these gratings would normally be operated at room temperature. To do so, the gratings were placed loosely in the oven to avoid any axial-strain effects and their characteristics were monitored during the annealing using the OSA.

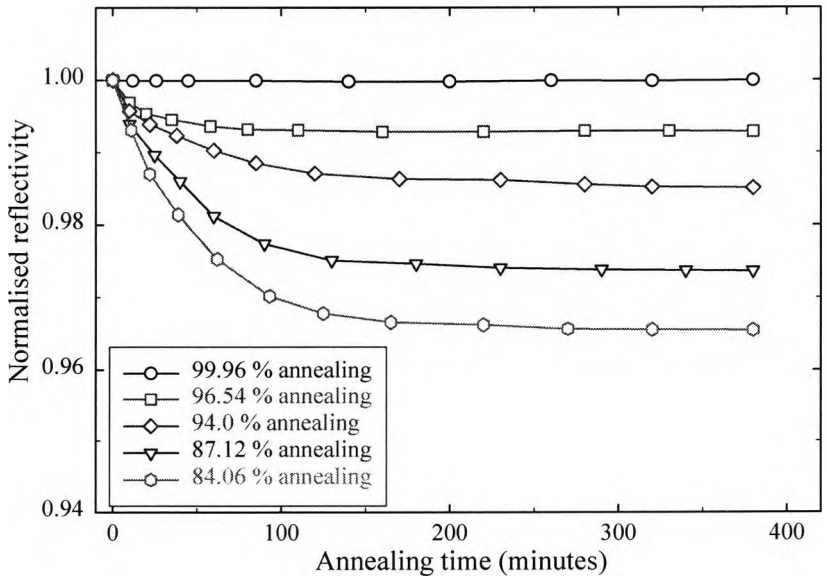

Fig. 3.14: Decay in the reflectivities of the gratings during annealing at a temperature of 100 °C.

During annealing, the decay in the reflectivities of the gratings arises due to the degradation of the UV-induced refractive index (RI) modulation [Chisholm *et al.* 1998 and Pal *et al.* 2003]. These results are shown in Fig. 3.14 where the reflectivities were normalised with respect to their initial reflectivity at temperature of 100 °C. A faster decay in the reflectivities, followed by a substantial slower decay and almost no decay was observed for the last few hours of annealing of these gratings. The highest reflectivity grating (99.96%) showed the least decay in its reflectivity during annealing, which is related to the maximum saturation of the RI modulation during its fabrication compared to the other gratings. The characteristic details of these gratings are given in Table 3.2 before and after the annealing. Further, blue shifts in the Bragg wavelength of all the gratings were observed [Pal *et al.* 2003]. The full-width-half-maximum (FWHM) bandwidth of these gratings were also seen to have decreased along with their decrease in the RI modulation, with a typical example is shown in Fig. 3.15.

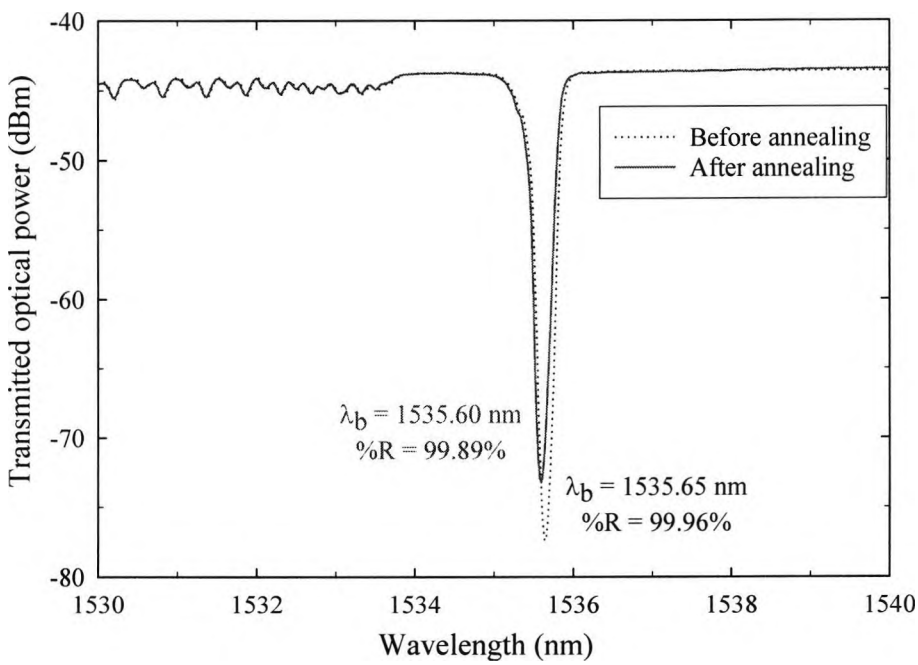

Fig. 3.15: Transmission spectra of the high reflectivity grating (R = 99.9 %) at room temperature before and after annealing.

Although the spectra of the matching pairs of FBGs were changed as well after annealing, the central wavelength still remained matched; this is shown in Fig. 3.16 for the high reflectivity grating (R = 99.9 %) together with a low reflectivity grating (R = 79.6 %).

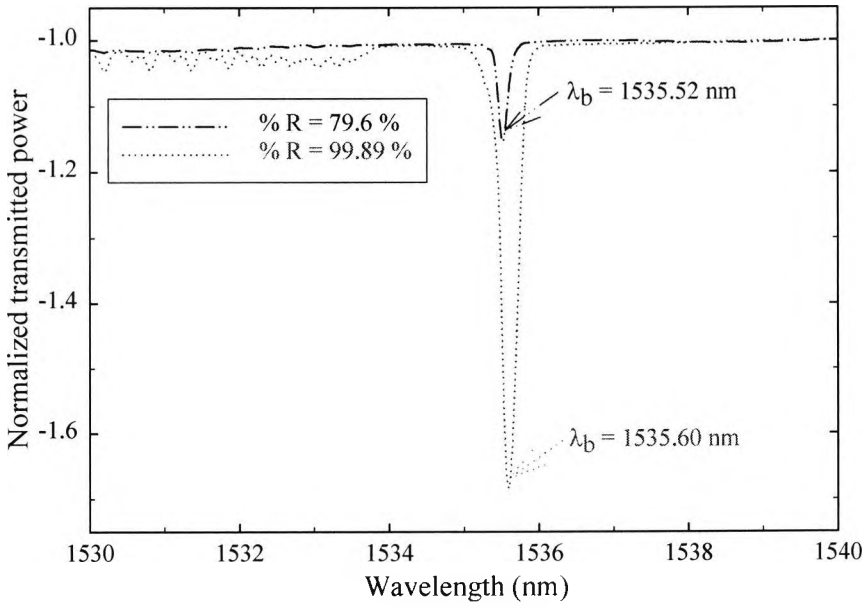

Fig. 3.16: Transmission spectra of the high reflectivity grating (99.9 %) together with a low reflectivity grating (79.6 %) at room temperature after annealing.

Table 3.2: Characteristics of different FBGs used in this work at room temperature before and after annealing.

	Before annealing			After annealing		
Fibre Bragg gratings	Reflectivity (%R)	Bragg wavelength, λ_B (nm)	Refractive index modulation Δn ($\times 10^{-4}$)	Reflectivity (%R)	Bragg wavelength, λ_B (nm)	Refractive index modulation Δn ($\times 10^{-4}$)
FBG 1	99.96 %	1535.65	4.69	99.89 %	1535.60	4.18
FBG 2	96.54 %	1535.64	2.41	95.15 %	1535.57	2.24
FBG 3	94.0 %	1535.71	2.12	91.19 %	1535.65	1.92
FBG 4	87.12 %	1535.64	1.72	84.00 %	1557.57	1.60
FBG 5	84.06 %	1535.63	1.60	79.57 %	1535.52	1.46

3.5.2. Laser Cavity Configuration

3.5.2.1. Wavelength selecting FBGs

As mentioned earlier, in each case, a pair of thermally annealed, fibre Bragg gratings (FBGs) was used to form the laser cavities. Four different types of FBG pairs, termed as Cavity 1, Cavity 2, Cavity 3 and Cavity 4 respectively, were used to optimise the laser cavity configuration. Care had been taken to minimise the splicing loss due to the change of the cavity configuration. Each cavity was characterised in terms of the laser power observed through the less reflective FBG while keeping the highly reflective FBG (R = 99.9%) fixed at the other end of the mirror. Details of laser cavity configurations using different FBG pairs after annealing are summarised in Table 3.3.

Table 3.3: Laser cavity configurations using different FBG pairs after annealing.

Laser Cavities	Reflectivity of the FBG (Variable)	Reflectivity of the FBG (Fixed)	Lasing Wavelength (nm)	At the lasing wavelengths reflectivity's of the FBGs	
				(Variable)	(Fixed)
Cavity 1	95.15 %	99.89 %	1535.56	94.80 %	99.83%
Cavity 2	91.19 %	99.89 %	1535.64	90.52%	99.80%
Cavity 3	84.00%	99.89 %	1535.58	83.91%	99.88%
Cavity 4	79.57 %	99.89 %	1535.50	78.00%	98.00%

3.5.2.2. Choice of gain medium

In this work, two different types of EDFs were used as the gain medium of the laser. For each fibre, the core composition was Er_2O_3+GeO_2+Al_2O_3 in a silica glass host. Al_2O_3 was added to enhance the solubility of the Er^{3+} ions in silica as well as to alleviate any clustering effects that may occur [Digonnet 1993]. Details of the fibre characteristics are shown in Table 3.1 and the length of each fibre was varied from 3 metres to 5 metres, in all the tests carried out, for example, samples 1 – 6, which were tested in this work, are shown in Table 3.4.

Table 3.4: Characteristics of different samples used in this work.

Erbium fibre lengths	Fibre 1 (350-400 ppm of Er^{3+})	Fibre 2 (650-700 ppm of Er^{3+})
3 metres	Sample 1	Sample 4
4 metres	Sample 2	Sample 5
5 metres	Sample 3	Sample 6

3.5.2.2.1. Fluorescence Spectra

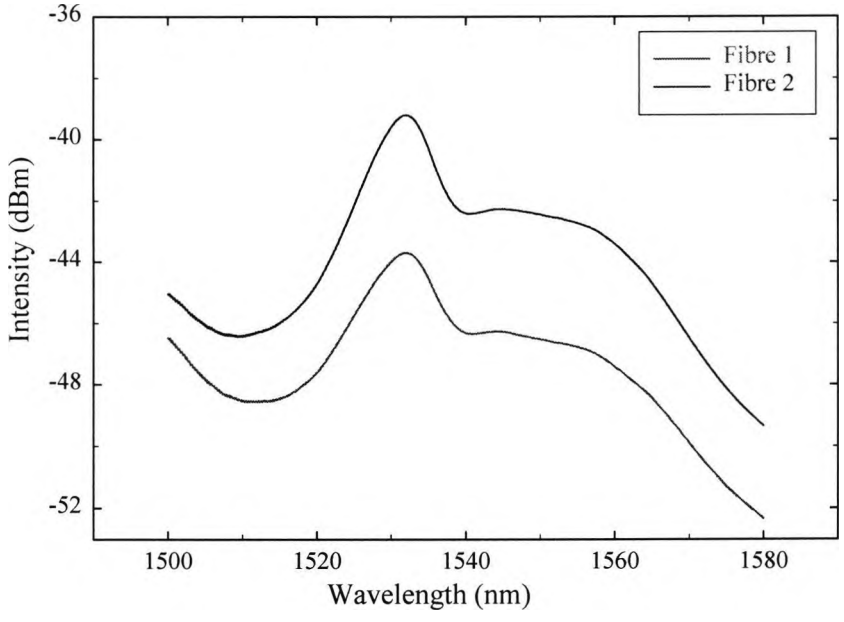

Fig. 3.17: Fluorescence spectra of fibre 1 (350-400 ppm of Er^{3+}) and fibre 2 (650-700 ppm of Er^{3+}) with a fixed pump power of 50 mW of 1480 nm LD.

Fig. 3.17 shows the fluorescence spectra of fibre 1 and fibre 2 respectively for erbium-doped fibre (EDF) length of 2.75 m each with a pump power level of 50 mW. The fluorescence in Er^{3+}-doped silica fibre is due to the decay of electrons from the metastable state ($^4I_{13/2}$) to the ground state ($^4I_{15/2}$) [Ainslie *et al.* 1988b]. This broadband fluorescence spectrum is possible due to the phonon interaction of Stark energy levels in EDF with pump power at room temperature. Chen *et al.* [1994] have reported that the profile of fluorescence spectra closely resemble to that of the emission

cross-sections for the short length (~ order of cm) of the EDF. The peaks at ~ 1535 nm wavelength are relatively sharp compared to those relatively flat gain at ~1551 nm fluorescence spectra of the EDF due to the incomplete population inversion for the 1480 nm pumping used.

3.6. Experimental Results

3.6.1. Laser Threshold Power

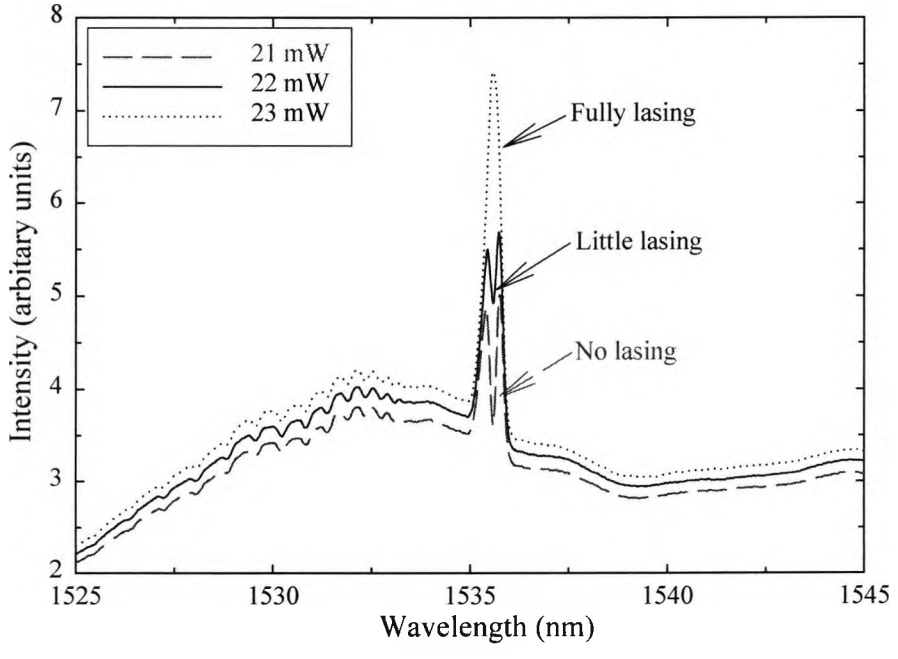

Fig. 3.18: Laser threshold at various pump power for fibre 1(350-400 ppm of Er^{3+}, 3 metres fibre length) and cavity 3 (R = 84 - 99.88 %).

Fig. 3.18 shows the threshold level of the laser for fibre 1 having an Er^{3+} ion concentration of 350 - 400 ppm and for cavity 3 (R = 84 - 99.88 %) at various pump powers of the 1480 nm LD. For a pump power of 21 mW, the spectrum clearly shows that the output was close to the threshold for lasing and with a small increase in the pump power to 23 mW, the lasing effect was observed. With a further increase in the pump power, the output power level of the laser was easily improved.

3.6.2. Effect of erbium-doped fibres on laser performance

The gain characteristics of the laser can be evaluated from the following equations [Shimizu *et al.* 1990]:

$$g(z) = \rho \delta_{21}(\upsilon) \Gamma_s \frac{U}{1+U}, \tag{3.7}$$

and $$U = \frac{P_p(z)}{P_{th(power)}}, \tag{3.8}$$

where $g(z)$ is the gain distribution function along the fibre co-ordinate z, ρ is the erbium concentration, $\delta_{21}(\upsilon)$ is the stimulated emission cross-section of pump wavelength, Γ_s is the overlap factor between the signal mode intensity and the erbium ion distribution in the fibre core with radius (r), $P_p(z)$ is the pump power distribution along the fibre co-ordinate z. The overlap factor (Γ_s) for a step index fibre can be derived from the following equations [Becker *et al.* 1999]:

$$\Gamma_s = 1 - e^{-\frac{r^2}{\omega^2}}, \tag{3.9}$$

$$\omega = \frac{1}{\sqrt{2}}\left(0.65 + \frac{1.619}{V^{1.5}} + \frac{2.879}{V^6}\right), \tag{3.10}$$

and $$V = \frac{2\pi}{\lambda_{cut-off}} \cdot a \cdot (NA), \tag{3.11}$$

where ω is the spot size and NA is the numerical aperture of the fibre.

3.6.2.1. Concentration effect

Based on Eq. (3.7), the presence of a higher concentration of the Er^{3+} ion dopant offers a higher level of gain, which is further confirmed in the results of this work. Fig. 3.19 shows one typical results obtained from samples 1 and 4 (sample 1: fibre 1, 350-400 ppm of Er^{3+}, 3 metre fibre length and sample 4: fibre 2, 650-700 ppm of Er^{3+}, 3 metres fibre length) respectively for cavity 3 (R = 84 - 99.88 %), with a fixed pump power of 100 mW of 1480 nm LD.

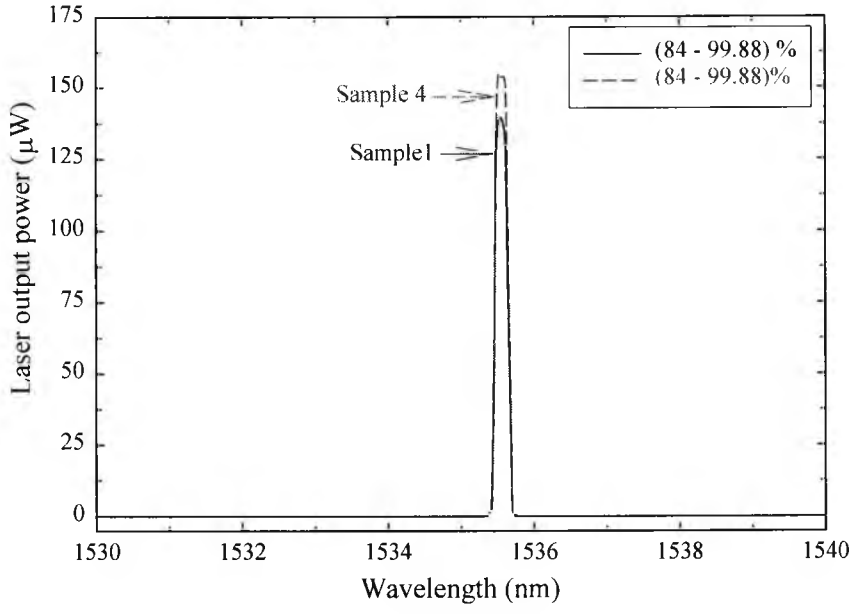

Fig. 3.19: Laser output power as a function of wavelength for sample 1 (fibre 1, 350-400 ppm of Er^{3+}, 3 metres fibre length) and sample 4 (fibre 2, 650-700 ppm of Er^{3+}, 3 metres fibre length) for cavity 3 (R = 84 - 99.88 %) respectively.

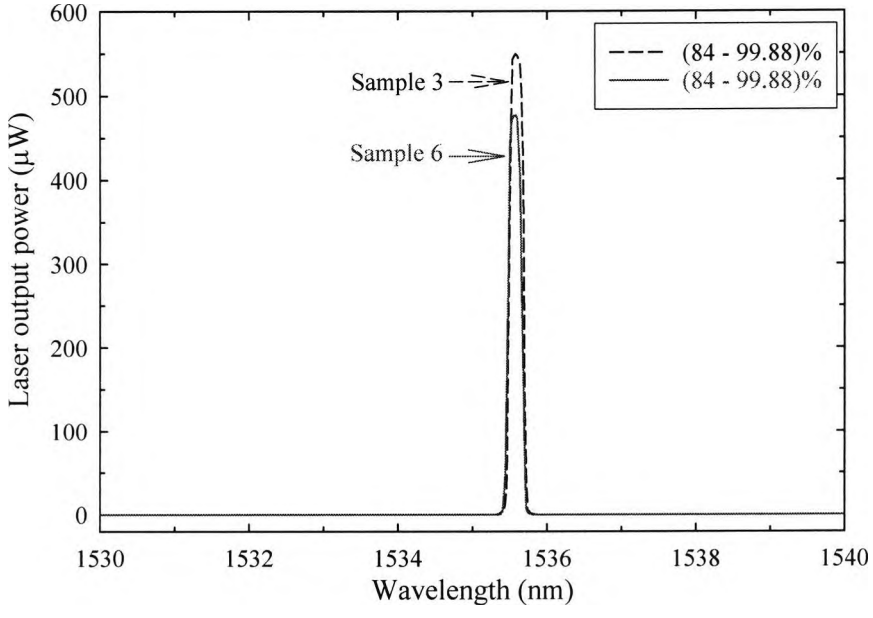

Fig. 3.20: Laser output power as a function of wavelength for sample 3 (fibre 1, 350-400 ppm of Er^{3+}, 5 metres fibre length) and sample 6 (fibre 2, 650-700 ppm of Er^{3+}, 5 metres fibre length) for cavity 3 (R = 84 - 99.88 %) respectively.

However, an exception is shown in Fig. 3.20 from samples 3 and 6 (sample 3: fibre 1, 350-400 ppm of Er^{3+}, 5 metres fibre length and sample 6: fibre 2, 650-700 ppm of Er^{3+}, 5 metres fibre length) respectively for cavity 3 (R = 84 - 99.88 %) with the same level of fixed pump power. A reduction of the gain in the higher concentration of fibre (fibre 2, 650-700 ppm of Er^{3+}) may arise from the cross-relaxation induced up-conversion of Er^{3+} ion with a higher pump power of the 1480 nm pumping, thus lowering the conversion efficiency of the fibre [Kagi *et al.* 1990 and Blixt *et al.* 1991].

3.6.2.2. Pump power effect

The expression for the output power (P_{out}) of a three-level (Er^{3+} fibre) laser system is given by the following equation [Digonnet 1993]:

$$P_{out} = \frac{T_{trans}}{L_R}\frac{h\upsilon_s}{h\upsilon_p}\left(P_{abs(l)} - P_{th(power)}\right), \qquad (3.12)$$

where T_{trans} is the fraction of a circulating power transmitted through the output mirror (or FBG), L_R is the cavity round-trip loss, $P_{abs(l)}$ is the pump power absorption by the fibre of length l, $P_{th(power)}$ is the pump threshold power, $(h\upsilon_s / h\upsilon_p)$ is the conversion efficiency of the fibre.

The expression for the cavity round trip loss was expressed as [Digonnet 1993]:

$$L_R = L_0 - \ln(1 - T_{trans}), \qquad (3.13)$$

where L_0 is the fibre loss including scattering and coupling loss at the fibre-reflectors interface, and the expression $-\ln(1-T_{trans})$ is the transmission loss of the output reflector FBG [Digonnet 1993].

The output power of the laser was found to be linearly proportional to the pump power after lasing occurs and is clearly shown in Figs. 3.21 and 3.22 for samples 3 and 6 (sample 3: fibre 1, 350-400 ppm of Er^{3+}, 5 m fibre length and sample 6: fibre 2, 650-700 ppm of Er^{3+}, 5 m fibre length), with the pump power variations from 18 to 100 mW respectively. Similar results were obtained for other samples tested.

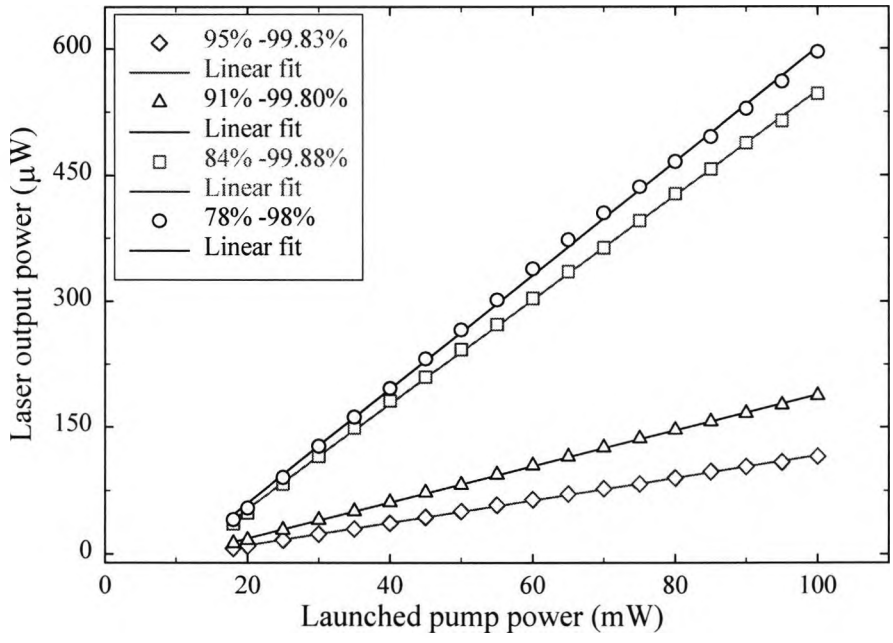

Fig. 3.21: Laser output power as a function of launched pump power for sample 3 (fibre 1, 350-400 ppm of Er^{3+}, 5 metres fibre length).

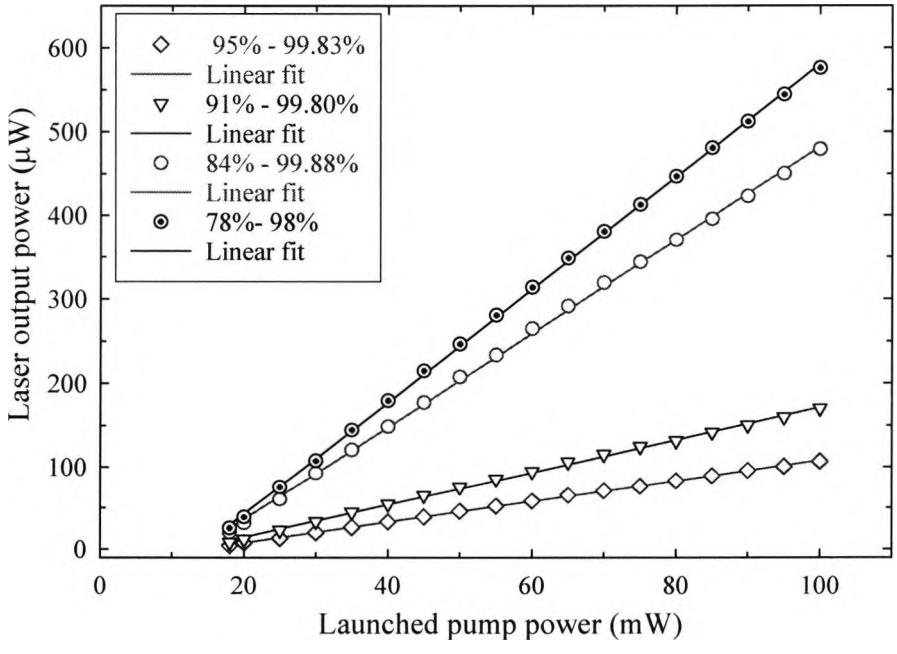

Fig. 3.22: Laser output power as a function of launched pump power for sample 6 (fibre 2, 650-700 ppm of Er^{3+}, 5 metres fibre length).

3.6.2.3. Optical fibre length effect

The output of the fibre laser was monitored under the various conditions mentioned above. Fig. 3.23 shows the laser output power as a function of erbium fibre length varying from 3 to 5 metres for cavity 4 (R = 78 – 98 %) for fibre 1 (350-400 ppm of Er^{3+}) and fibre 2 (650-700 ppm of Er^{3+}) respectively, with a fixed pump power of 100 mW. This figure clearly shows that the maximum laser output power was obtained for the longest length of the fibre, due to its higher absorption of the pump power along the length of the fibre, leading to a higher gain of the laser [Zyskind *et al.* 1989].

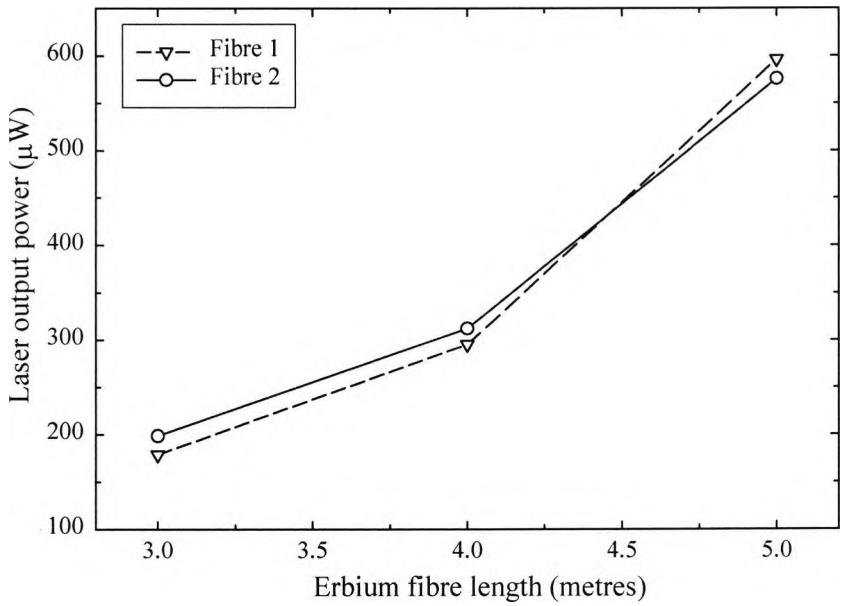

Fig. 3.23: Laser output power as a function of erbium fibre length for cavity 4 (R = 78 – 98 %) for fibre 1 (350-400 ppm of Er^{3+}) and fibre 2 (650-700 ppm of Er^{3+}).

3.6.3. Effect of different cavity configurations on laser performance

Fig. 3.24 shows the laser output power as a function of different cavity configurations with a fixed pump power of 100 mW of 1480 nm LD. From the figure it is clear that the cavity 4 (R = 78 – 98 %) achieved the highest output power, balancing its high

transmission (~ 22 %) of the output power with enough laser gain, this being verified in Eq. (3.12).

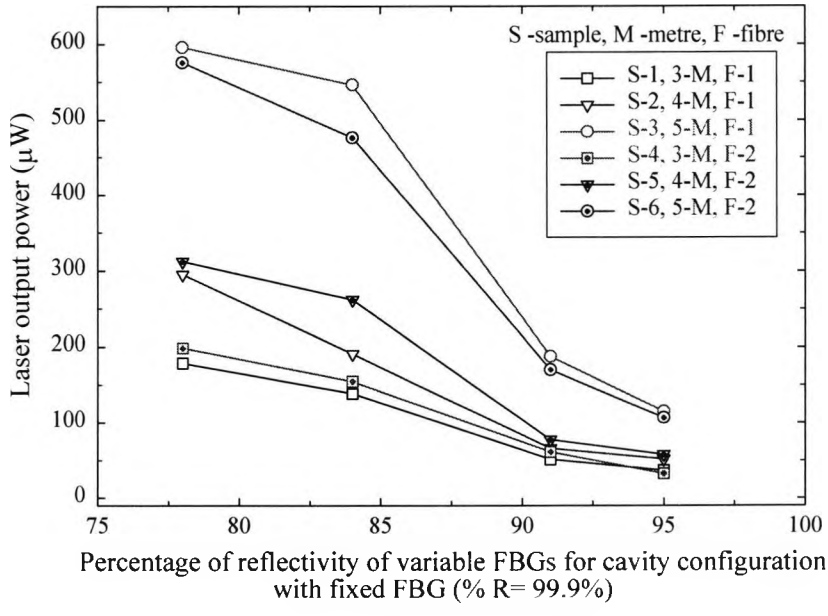

Fig. 3.24: Laser output power as a function of different cavity configurations.

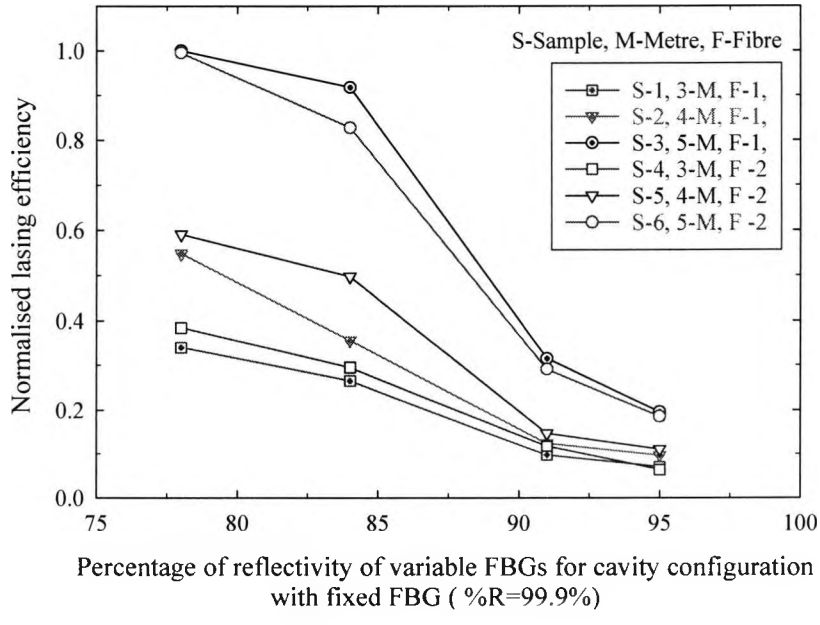

Fig. 3.25: Cross-comparison of the normalised lasing efficiencies as a function of different cavity configurations for fibre 1(350-400 ppm of Er^{3+}) and fibre 2 (650-700 ppm of Er^{3+}).

Fig. 3.25 shows cross-comparison of the normalised lasing efficiencies with respect to different cavity configurations for samples 1 - 6. Lasing efficiencies were calculated from the linear fit to the laser output power, with respect to pump power, for all the cavities and samples quoted. The overall highest efficiency (0.68 %) among the tested samples was obtained by sample 3 (fibre 1, 350-400 ppm of Er^{3+}, 5 metres fibre length) and cavity 4 (R = 78 – 98 %) due to the optimisation of laser output power and the maximum pump efficiency of the fibre, the details of which are listed in Table 3.5. The overall slightly lower efficiency of the laser may arise from the relatively low absorption of the pump power of Er^{3+} doped fibre, various splicing loss associated into the system and also the Fresnel reflection from the bare end of the fibre into the laser cavity. However, it is believed that using index-matching gel at the bare end of the fibre, the Fresnel reflection could be minimised and thus the laser efficiency would be further improved.

Table 3.5: Details of the lasing efficiencies with respect to different cavity configurations and different samples tested for fibre 1 (350-400 ppm of Er^{3+}) and fibre 2 (650-700 ppm of Er^{3+}) respectively.

Lasing Efficiencies (η)									
Fibre 1	**Sample 1**			**Sample 2**			**Sample 3**		
Cavities	(% η)	*COD	*SD	(% η)	COD	SD	(% η)	COD	SD
Cavity 1	0.047	>0.99	0.72	0.066	>0.99	0.62	0.133	>0.99	0.84
Cavity 2	0.066	>0.99	1.00	0.084	>0.99	1.13	0.213	>0.99	0.99
Cavity 3	0.18	>0.99	2.81	0.24	>0.99	2.64	0.62	>0.99	2.94
Cavity 4	0.23	>0.99	3.44	0.37	>0.99	2.94	0.68	>0.99	5.18
Fibre 2	**Sample 4**			**Sample 5**			**Sample 6**		
Cavity 1	0.043	>0.99	0.87	0.075	>0.99	1.35	0.126	>0.99	0.70
Cavity 2	0.080	>0.99	1.58	0.099	>0.99	1.83	0.197	>0.99	1.99
Cavity 3	0.20	>0.99	3.86	0.34	>0.99	4.98	0.56	>0.99	4.20
Cavity 4	0.26	>0.99	4.59	0.40	>0.99	6.52	0.67	>0.99	2.86

* COD - coefficient of determination, * SD-standard deviation

3.6.4. Stability of laser wavelength with cavity variations

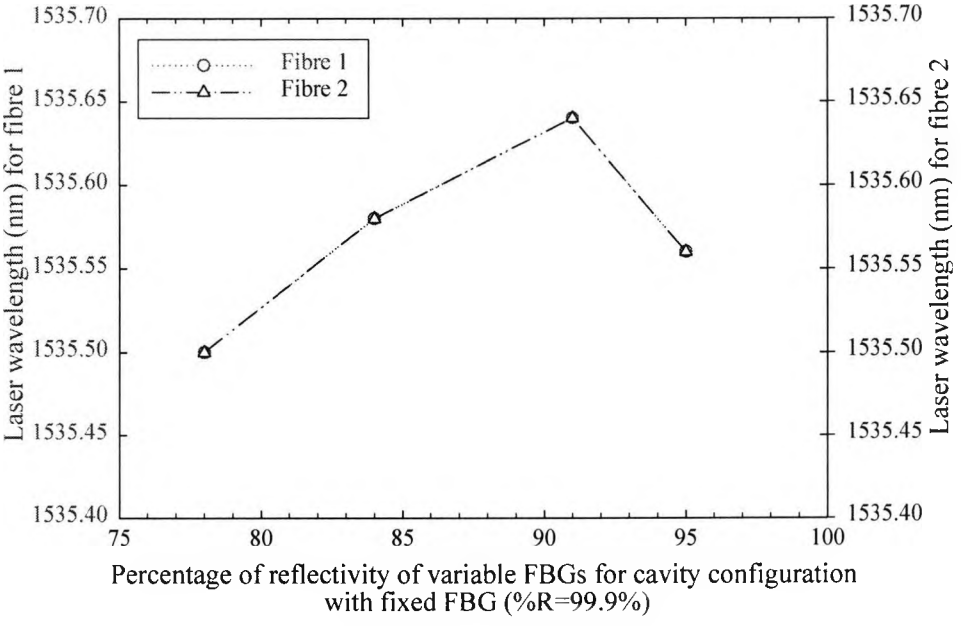

Fig. 3.26: Stability of the laser wavelengths in terms of fibre-to-fibre variation (fibres 1, 2).

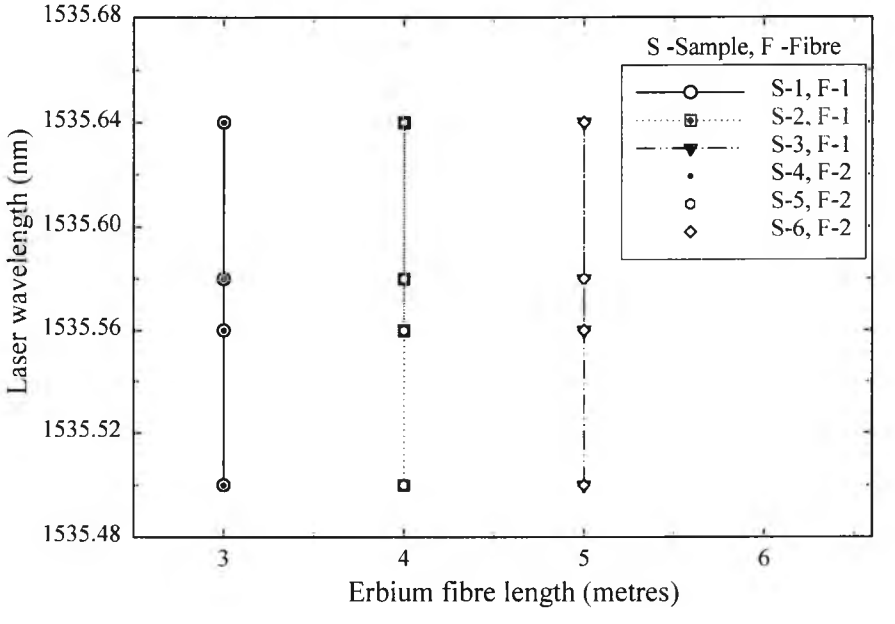

Fig. 3.27: Stability of the laser wavelengths in terms of erbium fibre length variations.

Since the laser cavities were formed using thermally annealed FBGs, the lasing wavelength was selected within the wavelengths associated with these gratings. The lasing wavelengths were found to be consistent with the wavelengths of the less reflective FBGs for all the cavities for the 6 samples tested, owing to its narrower bandwidth than that of the high reflective (R = 99.9 %) grating bandwidth. The outputs of these laser devices were found to be highly stable and repeatable with respect to the variations of fibre-to-fibre (fibres 1, 2) and their length variations, due to the stabilising effects of the FBGs used, which were annealed at a higher temperature than the operating temperatures. These results are shown in Figs. 3.26 and 3.27 respectively at room temperature.

3.7. Summary

An FBG stabilised 1480 nm LD was chosen as a pump source because of the advanced state of InGaAsP laser technology and its availability with high pump power. Erbium doped fibre (EDF) was chosen as the laser gain medium because of its very wide availability at different concentrations of Er^{3+} ions. The signal-to-noise ratio (SNR) of the laser was measured to be ~ 42 dB for cavity 4 (R = 78-98 %) and for sample 1 (fibre 1 with 3 metres fibre length) with a pump power of 75 mW of 1480 nm LD.

Two types of erbium-doped fibres (EDFs) with different Er^{3+} ion concentrations and varying fibre lengths (from 3 to 5 metres) were studied in this work to observe the gain characteristics of the fibre and thus the effect on the laser output power. It was found that the longer length of the fibre offers a higher level of gain due to its high absorption of the pump power along the length of the fibre. This also depends on the concentration of the Er^{3+} ions. The optimised results suggest that with consideration of a longer length of fibre, the lower concentration of Er^{3+} ions is favourable to avoid the cross-relaxation induced up-conversion of Er^{3+} ions at higher pump power. By contrast, for a more compact device, the use of a higher concentration of Er^{3+} ions with shorter lengths is preferable to eliminate the concentration-quenching effects.

The highest output power of the laser was obtained for cavity 4 (R = 78 – 98 %) for both the fibres (fibres 1, 2) tested. Also the highest lasing efficiency was obtained for cavity 4 (R =78 – 98 %) and sample 3 (fibre 1, 350-400 ppm of Er^{3+}, 5 metres fibre length) among the six tested samples. This is due to the maximum conversion efficiency of the fibre 1 over the smaller effective cross-sectional area (A_{eff} = 4.2 μm^2 with fibre core diameter of 2.3 μm) of the fibre core compared to that of the fibre 2 (A_{eff} = 7.1 μm^2 with fibre core diameter of 3 μm).

Thus the characteristics of several different erbium-doped fibre lasers have been evaluated under various conditions mentioned above. The laser output power has been maximised by optimising the gain fibre lengths, the Er^{3+} ion concentrations and the different cavity configurations. The overall performance of these devices was found to be stable and repeatable at the operating temperatures tested, regardless of the difference of the cavity configurations and samples tested, which is one of the most important requirement for sensor and communications applications. The optimised results obtained will be considered for use in active sensor configurations in further work, especially for high temperature sensor developments using erbium-doped fibre as the gain medium. The added advantage of a high signal-to-noise ratio (SNR) and a narrow linewidth of the fibre laser, compared to that of the passive fibre Bragg grating (FBG) sensors, make the laser-devices attractive for a range of applications, for example, in dense multiplexing situations.

3.8. References

- Ainslie, B.J., Craig, S.P. and Davey, S.T. (1987) The fabrication and optical properties of Nd^{3+} in silica-based optical fibres, *Mater. Lett.*, vol.5, pp.143-146.
- Ainslie, B.J., Craig, S.P., Davey, S.T. and Wakefield, B. (1988a) The fabrication, assessment and optical properties of high-concentration Nd^{3+} -and Er^{3+} -doped silica-based fibres, *Mater. Lett.*, vol.6, pp.139-144.
- Ainslie, B.J., Craig, S.P. and Davey, S.T. (1988b) The absorption and fluorescence spectra of rare earth ions in silica-based monomode fiber, *J. Lightwave Technol.*, vol.6, pp.287-293.
- Arai, K., Namikawa, H., Kumata, K., Honda, T., Ishii, Y. and Handa, T. (1986) Aluminium or phosphorus co-doping effects on the fluorescence and structural properties of neodymium-doped silica glass, *J. Appl. Phys.*, vol.59, pp.3430-3436.
- Armitage, J.R. (1988) Three-level fiber laser amplifier: a theoretical model, *Appl. Opt.*, vol.27, pp.4831-4836.
- Asseh, A., Storoy, H., Kringlebotn, J.T., Margulis, W., Sahlgren, B., Stubbe, R. and Edwall, G. (1995) 10-cm Yb^{3+} DFB fibre laser with permanent phase shifted grating, *Electron. Lett.*, vol.31, pp.969-970.
- Atkins, C.G., Massicott, J.F., Armitage, J.R., Wyatt, R., Ainslie, B.J. and Craig-Ryan, S.P. (1989) High gain, broad spectral bandwidth erbium-doped fibre amplifier pumped near 1.5 μm, *Electron. Lett.*, vol.25, pp.910-911.
- Ball, G.A., Morey, W.W. and Glenn, W.H. (1991) Standing-wave monomode erbium fiber laser, *IEEE Photon. Technol. Lett.*, vol.3, pp.613-615.
- Ball, G.A. and Morey, W.W. (1992) Continuously tunable single-mode erbium fiber laser, *Opt. Lett.*, vol.17, pp.420-422.
- Ball, G.A., Holton, C.E., Hull-Allen, G. and Morey, W.W. (1994) 60 mW 1.5μm single-frequency low-noise fiber laser MOPA, *IEEE Photon. Technol. Lett.*, vol.6, pp.192-194.
- Becker, P.C., Lidgard, A., Simpson, J.R. and Olsson, N.A. (1990) Erbium-doped fiber amplifier pumped in the 950-1000 nm region, *IEEE Photon. Technol. Lett.*, vol.2, pp.35-37.

- Becker, P.C., Olsson, N.A. and Simpson, J.R. (1999) *Erbium-Doped Fiber Amplifiers Fundamentals and Technology*, Academic Press, San Diego.
- Blixt, P., Nilsson, J., Carlnas, T. and Jaskorzynska, B. (1991) Concentration-dependent upconversion in Er^{3+}-doped fiber amplifiers: experiments and modelling, *IEEE Trans. Photon. Technol. Lett.*, vol.3, pp.996-998.
- Chen, C.-Y., Wen, S. and Chi, S. (1994) Measuring emission cross-section profile of erbium-doped fibre with low input power, *Electron. Lett.*, vol.30, pp.889-891.
- Chisholm, K.E., Sugden, K. and Bennion, I. (1998) Effects of thermal annealing on Bragg fibre gratings in boron/germania co-doped fibre, *J. Phys. D: Appl. Phys.*, vol.31, pp.61-64.
- Chow, J., Town, G., Eggleton, B., Ibsen, M., Sugden, K. and Bennion, I. (1996) Multiwavelength generation in an erbium-doped fiber laser using in-fiber comb filters, *IEEE Photon. Technol. Lett.*, vol.8, pp.60-62.
- Cowle, G.J., Payne, D.N. and Reid, D. (1991) Single–frequency travelling-wave erbium-doped fibre loop laser, *Electron. Lett.*, vol.27, pp.229-230.
- Digonnet, M.J.F. (1993) *Rare Earth Doped Fiber Lasers and Amplifiers*, M. Dekker, INC. New York.
- Dong, L., Loh, W.H., Caplen, J.E, Minelly, J.D., Hsu, K. and Reekie, L. (1997) Efficient single-frequency fiber lasers with novel photosensitive Er/Yb optical fibers, *Opt. Lett.*, vol.22, pp.694-696.
- Duservire, E. (1989) Analysis of erbium-doped fiber amplifiers pumped in the $^4I_{15/2}$ - $^4I_{13/2}$ band, *IEEE Photon. Technol. Lett.*, vol.1, pp. 293-296.
- Duservire E. and Simpson, J.R. (1989) Amplification of spontaneous emission in erbium-doped single-mode fibers, *J. Lightwave Technol.*, vol.7, pp.835-845.
- Duservire, E. and Simpson, J.R. (1990) Evaluation of $^4I_{15/2}$ and $^4I_{13/2}$ Stark-level energies in erbium-doped aluminisilicate glass fibers, *Opt. Lett.*, vol.15, pp.547-549.
- Eggleton, G.E., Krug, P.A., Poladian, L. and Quellette, F. (1994) Long periodic superstructure Bragg gratings in optical fibres, *Electron. Lett.*, vol.30, pp.1620-1622.
- Gilbert, S.L. (1991) Frequency stabilization of a tunable erbium-doped fibre laser, *Opt. Lett.*, vol.16, pp.150-152.

- Kagi, N., Oyobe, A. and Nakamura, K. (1990) Efficient optical amplifier using a low-concentration erbium-doped fiber, *IEEE Photon. Technol. Lett.*, vol.2, pp.559-561.
- Koester, C.J. and Snitzer, E. (1964) Amplification in a fiber laser, *Appl. Opt.*, vol.3, pp. 1182-1186.
- Koester, C.J. (1966) Laser action by enhanced total internal reflection, *IEEE J. Quantum Electron.*, QE-2, no.9, pp.580-584.
- Kringlebotn, J.T., Morkel, P.R., Reekie, L., Archambault, J.-L. and Payne, D.N. (1993) Efficient diode-pumped single-frequency erbium: ytterbium fiber laser, *IEEE Photon. Technol. Lett.*, vol.5, pp.1162-1164.
- Kringlebotn, J.T., Archambault, J.-L., Reekie, L., Townsend, J.E., Vienne, G.G. and Payne, D.N. (1994a) Highly efficient, low-noise grating-feedback Er^{3+}:Yb^{3+} codoped fibre laser, *Electron. Lett.*, vol.30, pp.972-973.
- Kringlebotn, J.T., Archambault, J.-L., Reekie, L. and Payne, D.N. (1994b) Er^{3+}:Yb^{3+}-codoped fiber distributed-feedback laser, *Opt. Lett.*, vol.19, pp.2101-2103.
- Laming, R.I., Poole, S.B. and Tarbox, E.J. (1988) Pump excited-state absorption in erbium-doped fibers, *Opt. Lett.*, vol. 13, pp. 1084-1086.
- Laming, R.I. and Payne, D.N. (1990) Noise characteristics of Erbium-doped fiber amplifier pumped at 980 nm, *IEEE Photon. Technol. Lett.*, vol.2, pp.418-421.
- Laming, R.I., Townsend, J.E., Payne, D.N., Meli, F., Grasso, G. and Tarbox, E.J. (1991) High-power erbium-doped–fiber amplifiers operating in the saturated regime, *IEEE Photon. Technol. Lett.*, vol.3, pp.253-255.
- Layne, C.B., Lowdermilk, W.H. and Weber, M.J. (1977) Multiphonon relaxation of rare-earth ions in oxide glasses, *Phys. Rev. B*, vol.16, pp.10-20.
- Layne, C.B. and Weber, M.J. (1977) Multiphonon relaxation of rare-earth ions in beryllium-fluoride glass, *Phys. Rev. B*, vol.16, pp.3259-3261.
- Li, S., Ding, H. and Chan, K.T. (1997) Erbium-doped fibre lasers for dual wavelength operation, *Electron. Lett.*, vol.33, pp.52-53.
- Liu, J., Yao, J. and Yeap, T.H. (2004) Single-longitudinal-mode multiwavelength fiber ring laser, *IEEE Photon. Technol. Lett.*, vol.16, pp.1020-1022.

- Loh, W.H. and Laming, R.I. (1995) 1.55 μm phase-shifted distributed feedback fibre laser, *Electron. Lett.*, vol.31, pp.1440-1442.
- Loh, W.H., Samson, B.N., Dong, L., Cowle, G.J. and Hsu, K. (1998) High performance single frequency fiber grating-based erbium: ytterbium-codoped fiber lasers, *J. Lightwave Technol.*, vol.16, pp.114-118.
- Mao, Q. and Lit, J.W.Y. (2002) Switchable multiwavelength erbium-doped fiber laser with cascaded fiber grating cavities, *IEEE Photon. Technol. Lett.*, vol.14, pp.612-614.
- McCumber, D.E. (1964) Theory of phonon-terminated optical masers, *Phys. Rev.*, vol.134, pp. A229-A306.
- Miniscalco, W.J. (1991) Erbium-doped glasses for fibre amplifiers at 1500 nm, *J. Lightwave Technol.*, vol.9, pp.234-250.
- Miniscalco, W.J. and Quimby, R.S. (1991) General procedure for the analysis of Er^{3+} cross sections, *Opt. Lett.*, vol.16, pp.258-260.
- Mizrahi, V., DiGiovanni, D.J., Atkins, R.M., Grubb, S.G., Park, Y.K. and Delavaux, J.M.P. (1993) Stable single-mode erbium fiber-grating laser for digital communication, *J. Lightwave Technol.*, vol.11, pp.2021-2025.
- Morkel, P.R., Cowle, G.J. and Payne, D.N., (1990) Travelling-wave erbium fibre ring laser with 60 kHz linewidth, *Electron. Lett.*, vol.26, pp.632-634.
- Othonos, A. and Kalli, K. (1999) *Fiber Bragg Gratings: Fundamentals and Applications in Telecommunications and Sensing*, Artech House, Boston.
- Pal, S., Mandal, J., Sun, T. and Grattan, K.T.V. (2003) Analysis of thermal decay and prediction of operational lifetime for a type I boron-germanium codoped fiber Bragg grating, *Appl. Opt.*, vol.42, pp.2188-2197.
- Park, N., Dawson, J.W. and Vahala, K.J. (1992) Multiple wavelength operation of an erbium-doped fiber laser, *IEEE Photon. Technol. Lett.*, vol.4, pp.540-541.
- Pedersen, B., Dakss, M.L., Thompson, B.A., Miniscalco, W.J., Wei, T. and Andrews, L.J. (1991) Experimental and theoretical analysis of efficient erbium-doped fiber power amplifiers, *IEEE Trans. Photon. Technol. Lett.*, vol.3, pp.1085-1087.
- Reekie, L., Mears, R.J., Poole, S.B. and Payne, D.N. (1986) Tunable single-mode fiber laser, *J. Lightwave Technol.*, vol. LT-4, pp.956-957.

- Sejka, M., Varming, P., Hubner, J. and Kristensen, M. (1995) Distributed feedback Er^{3+}-doped fibre laser, *Electron. Lett.*, vol.31, pp.1445-1446.
- Shimizu, M., Yamada, M., Horiguchi, M., Takeshita, T. and Okayasu, M. (1990) Erbium- doped fibre amplifiers with an extremely high gain coefficients of 11.0 dB/mW, *Electron. Lett.*, vol.26, pp.1641-1643.
- Snitzer, E. (1963) Neodymium glass laser, *Proc. on 3rd Int. Conf. on Solid State Lasers*, Paris, France, pp.999-1019.
- Snitzer, E., Po, H., Hakimi, F., Tumminelli, R. and McCollum, B.C. (1988) Erbium fiber laser amplifier at 1.55 μm with pump at 1.49 μm and Yb sensitized Er oscillator, *in Proc. of Opt. Fiber Commn. Conf.,* New Orleans, LA, Postdeadline Paper PD2.
- Stone, J. and Burrus, C.A. (1973) Neodymium-doped silica lasers in end-pumped fiber geometry, *Appl. Phys. Lett.*, vol.23, pp.388-389.
- Town, G.E., Sugden, K., Williams, J.A.R., Bennion, I. and Poole, S.B. (1995) Wide-band Fabry-Perot-like filters in optical fiber, *IEEE Photon. Technol. Lett.*, vol.7, pp.78-80.
- Urquhart, P. (1988) Review of rare earth doped fibre lasers and amplifiers, *IEE Proceedings*, vol.135, pp.385-407.
- Yamada M., Shimizu, M., Okayasu, M., Takeshita, T., Horiguchi, M., Tachikawa, Y. and Sugita, E. (1990) Noise characteristics of Er^{3+}-doped fiber amplifiers pumped by 0.98 and 1.48 μm laser diodes, *IEEE Photon. Technol. Lett.*, vol.2, pp.205-207.
- Zyskind, J.L., Giles, C.R., Desurvire, E. and Simpson, J.R. (1989) Optimal pump wavelength in the $^4I_{15/2}$ - $^4I_{13/2}$ absorption band for efficient Er^{3+}-doped fiber amplifiers, *IEEE Photon. Technol. Lett.*, vol.1, pp. 428-430.
- Zyskind, J.L., Mizrahi, V., DiGiovanni, D.J. and Sulhoff, J.W. (1992) Short single frequency erbium-doped fibre laser, *Electron. Lett.*, vol.28, pp.1385-1387.

Chapter 4

Innovative approach to fibre laser-based temperature sensing

4.1. Abstract

The work in this Chapter describes a new approach based on a *full-in-fibre* Bragg grating based fibre-laser system, for the first time in high temperature sensing applications. A brief review of previous laser-based sensor work, especially for temperature sensing applications, is given and the theoretical background to the temperature response of the laser is included. Experimental arrangements used, grating fabrication characteristics and their stabilising effects, the sensing probe configuration and the experimental results obtained are also given. An overall summary of the results is given at the end of the Chapter.

A novel Bragg grating-based fibre optic laser probe was configured for temperature sensing using erbium-doped fibre as the active gain medium and was pumped by using light from a 1480 nm laser diode (LD). The combination of a *chirped* Bragg grating and a normal Bragg grating was used to form the laser cavity feedback. The chirped grating forms the second reflector in the laser cavity to achieve temperature-tuneable laser action over a wide measurement range. The laser probe used a metal sheath to enhance its mechanical strength and contains the normal grating at the sensing point. The normal fibre Bragg grating and the chirped grating were fabricated in the germanium (Ge) -doped and boron-germanium (B-Ge) co-doped photosensitive fibres respectively. The shift in the laser wavelength was monitored in the system using an Optical Spectrum Analyser (OSA) when the probe was temperature-tuned. The temperature sensitivity of the probe was found to be 12.01 pm/°C using a linear fit to the experimental data and was also evaluated using the non-linear polynomial

regressions. The root mean square (RMS) error value of the probe was found to be 3.86 °C with a linear fit and less than 1 °C for the non-linear fitting over the range from room temperature to 300 °C. Response of the laser-based sensor system was also tested by reversing the measurement point in the laser configuration – the chirped grating was kept in the oven and the normal grating at ambient temperature.

4.2. Introduction

Fibre lasers and amplifiers have been widely used in optical fibre communication systems for many years; however, there are fewer approaches reported to using laser-based fibre optic sensors, in spite of the advantages of the use of an amplified measurand-carrying signal in the optical domain, rather than the electronic domain, as is the case with most sensors. Fibre Bragg grating (FBG)-based sensor devices have shown themselves to be important components in a range of sensor applications [Grattan and Meggitt 1998, Kersey *et al.* 1997] over the past several years, because of their mechanical robustness, low loss, immunity to electromagnetic interference, the use of a wavelength-encoded measurement information, and a potential multiplexing capability. The wavelength-encoded measurand information of the sensors has offered a number of distinctive advantages compared to other intensity-based sensing schemes, thus making a self-referencing. In passive FBG-based sensor systems, a spectrally broadband source is required to cover the wavelength range over which the Bragg grating is measurand-tuned. Due to the narrow-band nature of the Bragg wavelength, the output power reflected from this type of source is often quite weak, leading to a poor signal-to-noise ratio (SNR) of the measurement system, especially in noisy environments, thus reducing the potential accuracy available with current detection systems. A laser-based sensor system can, however, provide significant improvements in the SNR and the narrow linewidth of the laser signal allows the detection of much smaller shifts in the laser wavelength, arising as a result of temperature and strain changes, thus making the device highly sensitive to small perturbations of the measurand. The compatibility of fibre Bragg gratings (FBGs) for embedding within composite materials has led to the use of fibre sensor devices in "smart structure" applications.

In this Chapter, a new approach has been developed on fibre Bragg grating based fibre-laser system for high temperature sensing applications for the first time to our knowledge. The normal fibre Bragg grating and the chirped Bragg grating were fabricated in the Ge-doped and the B-Ge co-doped photosensitive fibres respectively, and were used to form the laser cavity feedback. Erbium-doped fibre (EDF) was used as the gain medium of the laser and pumped by using a 1480 nm LD. The approach extends the work discussed in Section 4.3 (up to the maximum of 200 °C) to higher temperatures and uses the single point probe approach, based on near infrared fibre laser, operating over a wide temperature range. The probe contains the normal grating (RB_1) at the sensing point and enrobed by a metal sheath to enhance its mechanical strength. The laser based sensor system replaces the broadband mirror in laser cavity [Alavie *et al.* 1993a, Kersey and Morey 1993a] by using a chirped fibre Bragg grating (CFBG) as the second reflector, thus makes the device *fully-in-fibre* based laser-system for sensor applications and simplifies the alignment of the whole sensor system. The laser-based sensor system also enables remote measurements in electrically or magnetically harsh environments, where high signal-to-noise ratio is required at high temperatures.

4.3. Review of previous laser-based sensor work

In Chapter 3, several different types of laser configurations mainly for communication applications have been reviewed and the laser performance for sensor applications using several wavelength-matched uniform fibre Bragg gratings as optical feedback elements and Er^{3+}-doped fibre as the gain medium of the laser has been optimised. In this Chapter, fibre laser-based devices for potential sensor applications, especially for high temperature sensing applications will be reviewed.

Ball *et al.* [1993a] have reported a simple Bragg grating based laser cavity approach to measure single point strain and multipoint temperatures. Wavelength-matched fibre Bragg gratings (FBGs) pair was created at two ends of the rare-earth doped fibre to form the active sensor which avoids the splicing loss inside the cavity. Thus a short cavity length fibre laser was used to measure the single point strain where the strain values were applied using a piezo-electric translator with a position sensor. To

measure dual-point temperatures, two 25 cm fibre lasers were used with different wavelengths to avoid the grating spectral overlap between the two laser resonators. These two lasers were fabricated at different locations in a rare earth doped fibre. Temperature measurements were performed by winding each fibre laser into a thin copper cylinder which was mounted to a heat plate. Temperature was measured over a range from room temperature to 190 °C, showing a linear thermal sensitivity of 0.011 nm/°C. For multiplexed temperature measurements, independent heat plate was necessary for each of the fibre laser to apply temperature. The laser oscillations were obtained when the gain medium was pumped by using a 980nm LD and the active sensor response was obtained using an appropriate spectrum analyser. The active sensor resolution was limited by the random laser mode hopping and the number of lasing modes presents for both strain and temperature measurements. The limitation of the above laser-based sensors was that both the gratings should be in the same measurand-state.

Ball *et al.* [1993b] have also reported a single frequency polarimetric Bragg grating based fibre laser strain sensor system. Laser cavity was formed using two-intra core fibre Bragg gratings fabricated in highly birefringent fibre to achieve a large separation in the lasing wavelengths. In a birefringent fibre, the Bragg wavelength separation ($\Delta\lambda_B$) between the two birefringent axes is given by:

$$\Delta\lambda_B = \frac{\lambda_B \Delta n_{eff}}{n_{eff}} \tag{4.1}$$

where n_{eff} is the effective refractive index of the fibre core and Δn_{eff} is the fibre birefringence. Highly birefringent fibre will increase the separation of the two eigen polarisation frequencies of the laser because of the spectral location of the two lowest loss lasing modes. The laser oscillates two orthogonal polarisation modes, when optically mixed, generates a single beat frequency that varied at a rate of – 4.1 MHz/milistrain for a linear strain measurements.

A highly photosensitive erbium doped fibre with low birefringence was used to fabricate the gratings. The erbium-doped fibre had an Er^{3+} ion concentration of 600 ppm with germanium and aluminium co-dopant. The fibre birefringence that was due

to both gratings and fibre contributions was measured to be 0.034 nm. The fibre laser was mounted to a linear piezoelectric translation stage (PZT) at two points. The PZT was expanded to measure the variation in beat frequency with applied strain. The resonant wavelengths of the laser are given by the following equations:

$$2n_1 L_C = \left(M + \frac{\phi_1}{\pi} \right) \lambda_{L1}, \tag{4.2}$$

$$2n_2 L_C = \left(N + \frac{\phi_2}{\pi} \right) \lambda_{L2}, \tag{4.3}$$

where L_C is the resonant cavity length, $n_{1,2}$ are the modal refractive indices, M and N are integers, $\phi_{1,2}$ represent the phase shift of the Bragg-grating reflection coefficients of the two orthogonal modes and $\lambda_{1,2}$ are the two lasing wavelengths. The polarisation mode beat frequency is given by the following relationship:

$$\Delta\upsilon = \frac{c}{2n_2 L_C} \left[(M - N) + \frac{(\phi_1 - \phi_2)}{\pi} + M \frac{\delta n}{n_2} \right], \tag{4.4}$$

where δn is the difference between the two modal refractive indices. From the above Eq. (4.4), the polarisation mode beat frequency will depend on the fibre birefringence (δn), the difference in the orders of the longitudinal cavity modes (M-N) and the difference between the phases (ϕ_1-ϕ_2) of the Bragg-grating reflection coefficients of each polarisation mode. Additionally, the grating birefringence and its orientation to the fibre birefringence axes should be known. When strain is applied, the cavity length will increase and this will change the net birefringence because of the core ellipticity and the difference in the elastic properties of the core and the cladding. But the accuracy of the sensor depends on the uncertainties of the parameters and the approximate nature of the computation.

Melle *et al.* [1993] have reported an erbium-doped fibre laser for strain sensor applications. A broadband mirror and a fibre Bragg grating were used to form the laser cavity feedback. The laser wavelength was determined by the Bragg wavelength of the grating, which was remotely located and also used as a strain sensor. The broadband mirror was used to achieve the strain-tuned laser operation without requiring both the reflectors in the same strain state. The broadband mirror was

formed directly on one end surface of a single mode fibre by chemical deposition of silver nitrate and it was fusion spliced to the gain fibre. The Bragg grating was manufactured in Alcatel bend-insensitive low-birefringence fibre with a reflectivity of 86 % at ~ 1550 nm wavelength, at a full-width-half-maximum (FWHM) bandwidth of 0.3 nm. The grating was fusion spliced to the output arm (1500 nm arm) of the coupler, thus contains a WDM coupler within the cavity. The erbium-doped fibre was pumped by using a 980 nm LD through the coupler. The laser light is coupled to a passive wavelength division system (WDS) using a bulk optical spectral filter to detect the output signal from the laser sensor. The Bragg grating was surface-adhered along the centreline of a cantilevered aluminium beam that was loaded in flexure. This allows the grating to be strained in both tension and compression, thus to tune the laser wavelength and with a reported strain sensitivity of 1.20 pm/με.

Kersey and Morey [1993a] have reported Bragg grating based fibre laser systems for strain sensing applications using mode-locked interrogation. Initially an experiment was performed using mode-locked operation of the cavity to selectively address individual FBG elements. The schematic of such system configuration is shown in Fig. 4.1.

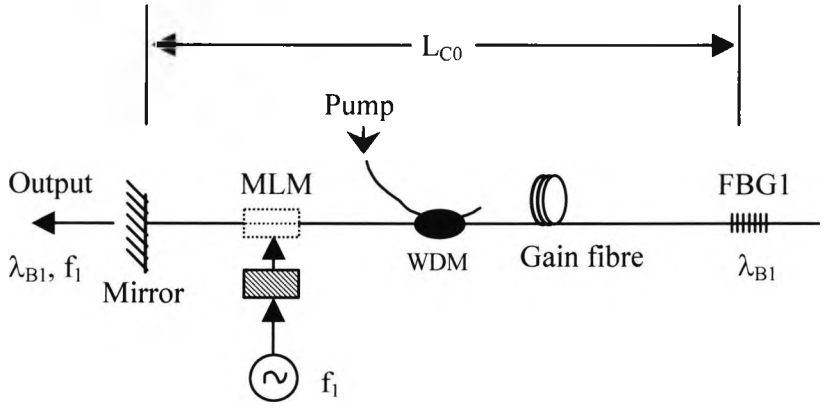

Fig. 4.1: A single Bragg grating based fibre-laser strain sensor system [Kersey and Morey 1993a].

The laser cavity was formed using a single FBG and a partial mirror (used as output port of the laser) and enclosed a gain section of approximately 20 metres length of

commercial erbium-doped fibre amplifier (BT&D, EDFA 3000). The laser output wavelength was consistent with the Bragg wavelength of the grating and thus the laser output is a direct measure of the mechanical perturbation of the FBG. However, the above system design was used to interrogate a single FBG element only.

Mode-locked operation of the system makes the device suitable for addressing a multiplexed FBG elements and the schematic of the system is shown in Fig. 4.2.

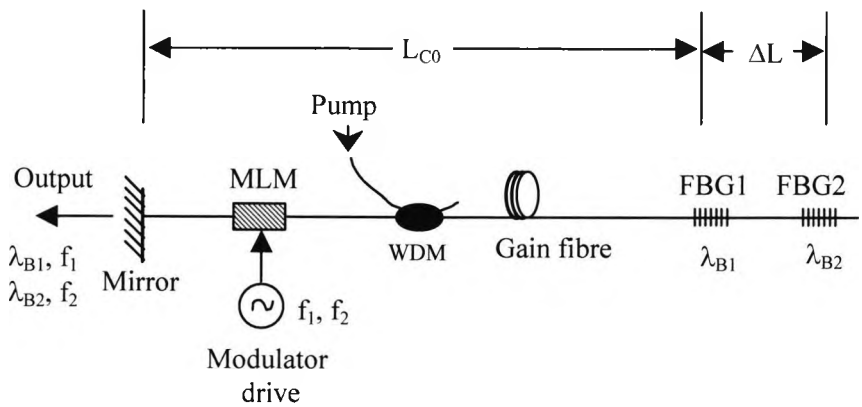

Fig. 4.2: Selectively mode-locked fibre-laser system using two FBG elements [Kersey and Morey 1993a].

The system was mode-locked by including a mode-lock modulator (MLM) driven at a frequency corresponding to a multiple (m) of the cavity mode spacing. Assuming mode locking at the fundamental (m =1) of the cavity spacing, the mode-locked output pulse rate was approximated as below:

$$f_1 = \frac{c}{2nL_{C0}}, \tag{4.5}$$

where L_{C0} is the length of the cavity between the mirror and the FBG1, the laser output consists of a pulse train at frequency (f_1) and wavelength (λ_{B1}) determined by the Bragg grating element. By adding a second FBG (with Bragg wavelength, λ_{B2}) to the system, a pair of cavities are formed but with different cavity lengths. If the spacing between the two FBG elements is ΔL, the cavity was forced to lase in a mode-

locked fashion at either of the two FBG wavelengths by selecting an MLM drive frequency determined by either Eq. (4.5) or Eq. (4.6) expressed below:

$$f_2 = \frac{c}{2n(L_{C0} + \Delta L)}, \tag{4.6}$$

The laser output corresponds to either of the Bragg wavelengths (λ_{B1}) or (λ_{B2}), depends on the drive frequency (f_1) or (f_2) applied to the mode-lock modulator (MLM) respectively. The mode-locker is tuned to a particular cavity; the modulator effectively introduces loss to the other cavity as it is asynchronously driven with respect to the round-trip cavity time. This loss will not allow the other cavity to oscillate, thus allowing the selected cavity for lasing. The number of FBGs that can be interrogated depends on the possible harmonic modes locked within the multiple cavities of the system. For strain measurements, mode-locker was used to select one of the FBGs in the cavity. The FBG was attached to the bottom of a steel plate which was subjected to three-point bending and the strain-induced shift in the laser wavelength was monitored using a detection scheme.

Kersey and Morey [1993b] have also reported multiplexed Bragg gratings based strain sensor in the travelling-wave configuration and the schematic of the experimental set-up is shown in Fig. 4.3.

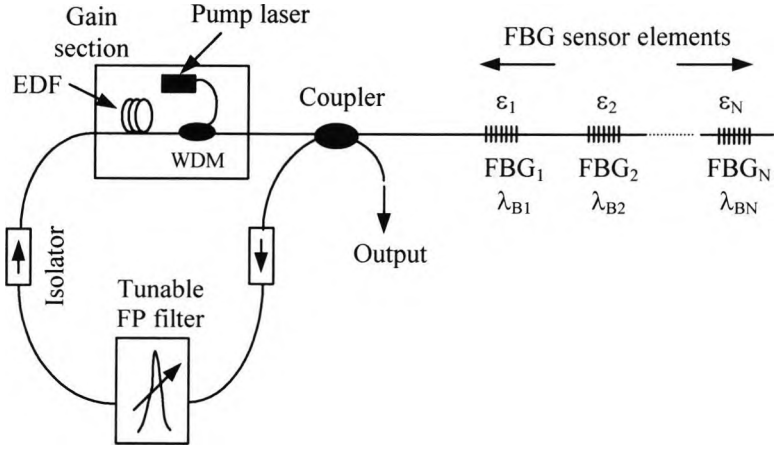

Fig. 4.3: Fibre laser sensor in ring cavity configuration using multiple fibre Bragg grating sensor elements [Kersey and Morey 1993b].

Fibre Bragg gratings were used as the sensing elements and also form one of the cavity elements of the laser. The section containing the erbium-doped fibre (EDF) is a loop reflector which operates in a unidirectional manner through the inclusion of an isolator. A wavelength selective tuneable Fabry-Perot filter was located within the loop reflector, lasing of the system occurs only when the transmission passband of the filter is matched with the wavelength of one of the Bragg grating elements. The laser wavelength was consistent with the Bragg wavelength of one of the FBG elements and is a direct function of the strain applied to the selected Bragg grating. This selective lasing allows each of the FBG sensor elements to be interrogated by assigning each to a particular operational wavelength domain which is non-overlapping, and the operational range of the laser sensor should fall within the gain bandwidth of the erbium-doped fibre used. Therefore tuning the Fabry-Perot filter transmission wavelength over the gain bandwidth allows the sequential addressing of each FBG sensor element and the output was monitored from the fourth port of the fibre coupler using an optical spectrum analyser. The number of sensors could be multiplexed using the system depends on the wavelength spacing of required operational domain (wavelength spacing) of each FBG sensor and the gain bandwidth of the erbium doped fibre used. The potential limitation of the sensor system is that simultaneous responses of the all the sensors cannot be obtained at a time.

Alavie *et al.* [1993a] have reported a multiplexed Bragg grating based fibre laser system to measure both the temperature and the strain. Initially an experiment was performed using a single FBG and a broadband mirror to form the laser cavity feedback and enclosed a length of erbium-doped fibre as the gain medium. The schematic of the experimental set-up is shown in Fig. 4.4 [Alavie *et al.* 1993b]. For a serial multiplexed sensor configuration, a common broadband mirror and two fibre Bragg gratings (FBGs) were used to form the laser cavities in conjunction with erbium doped fibres as the gain media. The homogeneous gain broadening nature of the erbium ion limits the number of lasing modes. To generate multiple lasing lines, a section of erbium-doped fibre was placed between each successive FBGs. Alternatively using a mode-locked arrangement in the laser configuration as reported by Kersey and Morey [1993a], the need for additional gain section between successive FBGs would be eliminated.

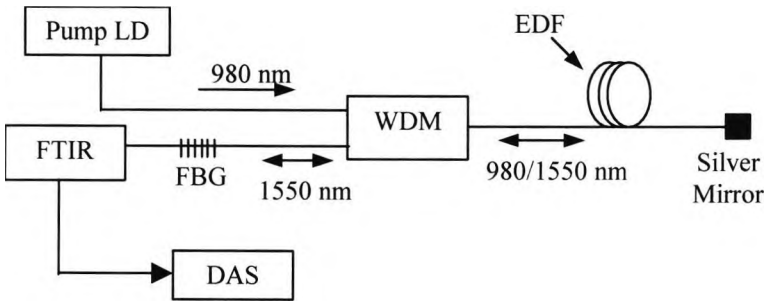

Fig. 4.4: Schematic of the experimental set-up of the laser based sensor system. FTIR: Fourier transforms infrared spectrometer and DAS: Data acquisition system [Alavie *et al.* 1993b].

For temperature measurements, the Bragg grating was immersed in a Pyrex container filled with diffusion pump oil and the container was heated using a temperature-controlled hot plate. The measured temperature range was from 20 to 160 °C, giving a thermal sensitivity of 13.7 pm/°C. For strain measurements, the grating was removed from the oil bath and was fixed to an aluminium cantilever beam using cyanoacrylate adhesive. In the serial multiplexed sensor configuration, gain coupling was observed across the laser channels even when separate gain medium was placed between each successive FBGs [Alavie *et al.* 1993a].

Ball and Morey [1994] have reported a compression-tuned single frequency fibre laser in a master oscillator/power amplifier configuration. The master oscillator/power amplifier (MOPA) design was used to increase the laser output power; hence to improve the laser efficiency. The master oscillator was constructed in a 15 metres length of photosensitive germanosilicate erbium-doped fibre with Er^{3+}-ion dopant concentration of ~ 550 ppm. The laser resonator was formed within 2-cm length of the gain fibre where two uniform fibre Bragg gratings were written directly into the fibre using the holographic exposure arrangements. A 1480 nm laser diode was used as a pump source and the master oscillator was used to absorb the residual pump power of the laser, hence to improve the overall system efficiency. The fibre laser was epoxied using two 128 μm FC ferrules with one end of the laser was mounted to a fixed stage and the other end was mounted to a stepper motor to compress the laser uniformly over 32 nm range. The limitation of the wavelength-matched fibre Bragg grating

based laser sensors is that both the gratings must be in the same measurand state (same temperature or strain).

Koo and Kersey [1995] have reported an interferometric detection scheme to measure strain induced laser wavelength shifts. In a single mode fibre laser, when strain (ε) is applied to the laser cavity of length (L_C) to induce a change in the cavity length (ΔL_C), a frequency shift ($\Delta \upsilon_L$) will be introduced in the laser frequency and was expressed as below:

$$\Delta \upsilon_L = -\frac{\Delta L_C}{L_C} \zeta \upsilon_L = -\varepsilon \zeta \upsilon_L , \tag{4.7}$$

where ζ is a constant (= 0.78) which depends on the photo-elastic properties of the fibre. In the case of a multimode fibre laser, the output of the laser was approximated as below:

$$\Delta \upsilon_L^i = -\frac{\Delta L_C}{L_C} \zeta \upsilon_L^i = -\varepsilon \zeta m_i \upsilon_{FSL} \tag{4.8}$$

where m_i takes an integer value and corresponds to the cavity mode order, and υ_{FSL} is the free spectral range or frequency mode spacing of the laser.

The strain-induced shift in the laser output was detected using a Mach-Zehnder read-out interferometer (MZI), which converts the laser wavelength changes to interferometer phase changes and the schematic of the experimental configuration is shown in Fig. 4.5. The laser cavity feedback was formed using fibre Bragg gratings (FBGs) and enclosed a length of erbium doped fibre as the gain medium. The laser output is coupled to a Mach-Zehnder read-out interferometer (MZI) through the WDM coupler. The interferometer converts the laser wavelength shifts into the interferometer phase shifts. The interferometer phase bias (ϕ_{MZ}) is dependent on the fibre Bragg grating laser sensor output wavelength (or frequency υ_L), and the interferometer optical path difference (OPD) was related using the following equation:

$$\phi_{MZ} = \frac{2\pi n L_{MZ}}{c} \upsilon_L, \tag{4.9}$$

where L_{MZ} is the path difference between the fibre arms of the interferometer and n is the refractive index of the fibre. Cavity strain causes the shift in the laser emission frequency ($\Delta\upsilon_L$), which will modulate the output phase shift of the interferometer, and this was expressed as below:

$$\Delta\phi_{MZ} = \frac{2\pi n L_{MZ}}{c} \Delta\upsilon_L = -\frac{2\pi n L_{MZ}}{c} \varepsilon\zeta\upsilon_L, \tag{4.10}$$

Thus the phase modulation ($\Delta\phi_{MZ}$) of the interferometer is determined by the product of the laser cavity strain (ε) and of the interferometer path imbalance (L_{MZ}). So, the laser cavity strain is a direct function of the MZI optical path difference.

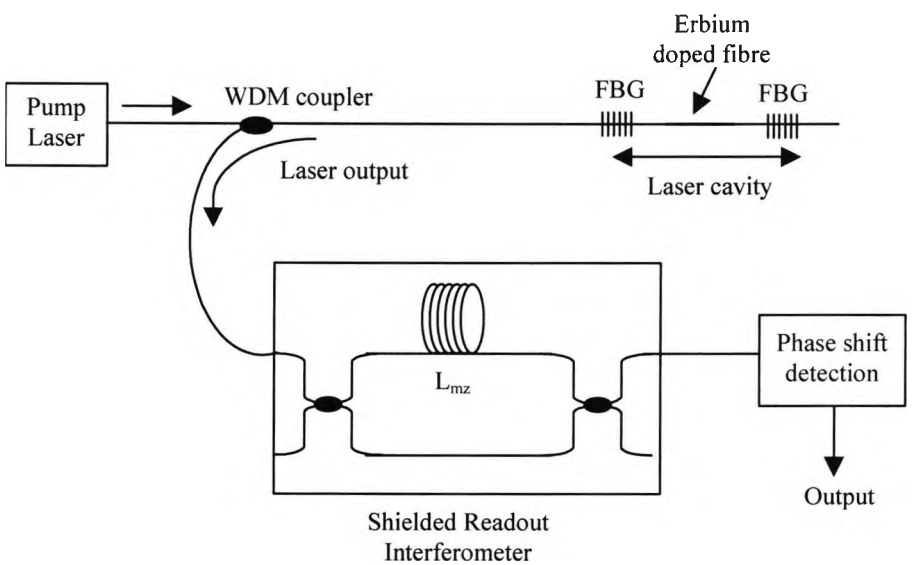

Fig. 4.5: Schematic of a fibre-Bragg grating laser sensor with a Mach-Zehnder read-out interferometer [Koo and Kersey 1995].

For multimode laser output, the interferometer phase bias (ϕ'_{mz}) was modified as below:

$$\phi'_{MZ} = \frac{2\pi n L_{MZ}}{c} \upsilon_L^i = \frac{2\pi n L_{MZ}}{c} m_i \upsilon_{FSL}, \tag{4.11}$$

where the free spectral range of the laser is given by $\upsilon_{FSL} = c/(2nL_C)$ with the round-trip cavity length is $2L_C$. Choosing the interferometer path difference as an integer multiple of the cavity length, i.e. $L_{MZ} = 2gL_C$ where g is an integer, the interferometer bias phases (ϕ_{mz}^{i+1}) for different longitudinal modes were expressed as below:

$$\phi_{MZ}^{i+1} = \phi_{MZ}^{i} + 2g\pi, \tag{4.12}$$

Therefore, the read-out interferometer needs to be biased properly for a multimode laser sensor which allows the read-out interferometer to be locked at quadrature for all lasing modes simultaneously. The strain induced phase shift ($\Delta\phi_{MZ}^{i}$) at the read-out interferometer for the i^{th} lasing mode was expressed as below:

$$\Delta\phi_{MZ}^{i} = \frac{2\pi nL_{MZ}}{c}\Delta\upsilon_{L}^{i} = -\frac{2\pi nL_{MZ}}{c}\varepsilon\zeta\upsilon_{L}^{i}, \tag{4.13}$$

The phase shift induced by each mode depends on the mode frequency of the laser (υ_L^i), is determined by the bandwidth of the Bragg grating.

For strain measurement, the fibre laser cavity was mounted on a piezoelectric fibre stretcher to apply strain and the shift in the laser output was coupled to the read-out interferometer for detection.

Imai *et al.* [1996] have reported an erbium-based temperature sensor system using amplified spontaneous emission (ASE) of fluorescence when excited using 1480 nm pump source, measuring the ratio of the intensities of the fluorescence at two peaks in the spectrum at 1552 nm and 1530 nm. The peak power ratio between the two peaks of the fluorescence spectrum depends on the temperature change. This ratio was found to be a linear function of temperature, over a narrow range of 12 °C to 80 °C and a sensitivity of 0.0085 /°C. However, the total fluorescence power of the erbium-doped fibre was found to decrease with increase in temperature, which is a limiting factor for the signal to noise ratio (SNR) of the system for high temperature sensing application. An average sensitivity of 0.007/°C was reported by Imai and Hokazono [1996] over the temperature range from –50 °C to 90 °C, using the intensity-based temperature-sensing scheme. Zhang *et al.* [1998] have reported detailed investigations of the temperature characterisation of several different concentrations of Er^{3+} doped fibres

(200 ppm, 960 ppm and 4370 ppm of Er^{3+} ions), especially using the thermal sensitivity of the decay time change. A fluorescence probe was constructed with the doped fibres enrobed in a quartz sheath and was placed in an oven for temperature characterisation. The fluorescence lifetime of the Er^{3+}-ion was found to decrease with the increase in temperature when excited using an 810 nm pump source. The fluorescence lifetime was calculated using the following formula [Zhang *et al.* 1998]:

$$\tau = \frac{\int_0^{t_\infty} t \cdot f(t)dt}{\int_0^{t_\infty} f(t)dt}, \quad \text{for } (t_\infty \to \infty) \tag{4.14}$$

where τ is the fluorescence lifetime of erbium doped fibre, $f(t)$ is the fluorescence decay starting from time, $t = 0$ and t_∞ is the observation time of the decay. The decay was found to be more dominant in high temperature region (above 600 °C) and the lifetime decreased from ~ 9 ms to 4.5 ms on average over the range from 0 to 950 °C.

Kim *et al.* [2000] have reported an intensity-based approach for temperature-independent strain measurement using a single chirped grating. One half of the chirped grating (longer reflection part with grating length of 2.5 cm) was embedded in and fixed to a silica glass tube of 2 cm length using epoxy. Therefore, the attached part of the grating was insensitive to the applied strain. To apply strain, the whole length of the chirped grating was attached to the two translation stages using epoxy. The broadband light from an erbium doped fibre amplifier (EDFA) was passed to the chirped grating through a circulator and the reflection spectrum response of the grating was monitored using a photo detector and an optical spectrum analyser. When strain was applied to the sensor, the reflection spectrum of the unattached grating part was found to shift towards longer wavelength side of the spectrum. The 3-dB bandwidth of the overall reflection spectrum was found to decrease as the shorter wavelength reflection spectrum part (unattached grating part) gradually overlaps with the longer wavelength reflection spectrum part (attached grating part which does not respond to strain) with increased strain. The decrease in 3-dB bandwidth causes the decrease of the reflected power from the chirped grating. The maximum range of sensor was limited by the half of the chirped grating's 3-dB bandwidth (with full 3-dB bandwidth of the chirped grating was ~ 2.14 nm) of 1.07 nm, which corresponds to a

strain value of ~ 1000 με. For temperature variation, the reflected power and the bandwidth were found to be unchanged. Due to the larger bandwidth of the chirped grating, the sensor scheme would not be suitable for multiplexing application. However, in intensity-based interrogation scheme, optical intensity variation due to source power fluctuations or bending of the fibre may provide an additional error in the output signal.

Du *et al.* [1999] have reported a fibre Bragg grating Fabry-Perot cavity (GFPC) structure for simultaneous measurement of strain and temperature. The spectrum profile of the grating has two spectral peaks within its main reflection band. The peak power difference along with the shift in their peak wavelengths changes linearly with strain or temperature. Measurement of the peak wavelength shift and the change in the peak power of the reflected light of the sensor were used to determine the temperature and the strain parameters. When the grating and the cavity sections have the same strain and temperature coefficients, the reflection spectrum of the GFPC sensor shifts but its spectrum profile remain unchanged. In that case, temperature and strain parameter cannot be determined simultaneously. For simultaneous measurement of both the parameters, the grating and the cavity sections should have different strain and temperature coefficients. Therefore, the intensity of the two peaks changes periodically with temperature and strain change. Thus by measuring the peak wavelength shifts as well as the intensity change of the two peaks of the grating Fabry-Perot sensor, it was possible to determine both the parameters simultaneously.

For creating the grating Fabry-Perot cavity sensor, an aluminium plate with two parallel slits (2 mm in width separated by 1 mm) was placed between the laser beam and the phase mask. Therefore, two identical gratings of length 2 mm were written at the same time where the gratings position corresponding to the slits. To make the strain and the temperature coefficients of the cavity section different from those of the grating sections, 1 mm long and thin aluminium tube (inside diameter of 0.3 mm and wall thickness of 0.15 mm) was glued into the cavity section. Thus the cavity section is more difficult to stretch at room temperature than the grating section; therefore the strain coefficient of the cavity section will be smaller than that of the grating section. On the other hand, with temperature increases, the cavity section will have larger

temperature coefficients than that of the grating section because of the larger thermal expansion coefficient of aluminium (23.5×10^{-6}/°C) than that of the silica glass fibre (0.5×10^{-6}/°C). The expansion of the aluminium tube with the temperature increase will induce additional strain to the cavity section. Assuming the peak wavelength shifts ($\Delta\lambda_P$) and the changes in the intensity function (ΔM) are linear with the strain and the temperature response; and their changes were expressed as below:

$$\begin{bmatrix}\Delta\lambda_P\\ \Delta M\end{bmatrix}=\begin{bmatrix}A_{1\varepsilon} & A_{1T}\\ A_{2\varepsilon} & A_{2T}\end{bmatrix}\begin{bmatrix}\Delta\varepsilon\\ \Delta T\end{bmatrix}, \tag{4.15}$$

where $\Delta\varepsilon$ and ΔT are the changes in the applied strain and the temperature respectively, $A_{i\varepsilon}$ and A_{iT} are the strain and the temperature coefficients corresponding to the grating and the cavity section (i =1 for grating and i =2 for cavity) respectively. The strain and the temperature can be determined simultaneously by measuring the changes in the peak wavelength shifts and the intensity of the reflection spectrum profile of the sensor and by solving the following linear matrix equation:

$$\begin{bmatrix}\Delta\varepsilon\\ \Delta T\end{bmatrix}=\frac{1}{A_{1\varepsilon}A_{2T}-A_{2\varepsilon}A_{1T}}\begin{bmatrix}A_{2T} & -A_{1T}\\ -A_{2\varepsilon} & A_{1\varepsilon}\end{bmatrix}\begin{bmatrix}\Delta\lambda_P\\ \Delta M\end{bmatrix}, \tag{4.16}$$

So, the strain was measured from 0 to 3000 με and the temperature was measured over the range from 22 to 60 °C with an accuracy of ± 30 με and ± 0.4 °C respectively.

Peng *et al.* [2003] have reported an FBG-based temperature sensor system using a linear cavity fibre laser to measure temperature over the range from 0 °C to 40 °C. One of the cavity mirrors of the laser was the fibre loop mirror and the other was a fibre Bragg grating (FBG1), which acts as the sensing element of the system and enclosed a length of erbium-doped fibre as the gain medium. The laser output was extracted through a 50:50 coupler and was further splitted into the two different couplers (with 50:50 splitting ratio of both the couplers). Two other uniform FBGs (FBG2 and FBG3 respectively) were connected to the two ports of the couplers and their outputs were connected to the detection schemes. The reflected power from one FBG (either FBG2 or FBG3) is used to monitor the temperature variation with reference to the reflected power from the other FBG. The reflected power from both

the gratings (FBG2 or FBG3) was found to be non-linear and decreased rapidly with temperature over a narrow range of 0 °C to 40 °C.

Recently, Lee *et al.* [2004] has reported a Raman fibre laser probe for long-distance remote temperature sensing application where the laser cavities were formed using two uniform FBGs and a common tuneable chirped grating in serial configuration. The Raman pump source consists of four laser diodes operating at 1425 nm, 1435 nm, 1455 nm and 1465 nm, respectively. All the pump wavelengths were combined using a passive combiner and a WDM coupler to have a total pump power of up to 1 W and was launched into the single mode fibre (SMF) through the chirped grating. The temperature performance of the laser was measured over the range from 30 °C to 100 °C, with a reported sensitivity of 7.15 pm/°C.

Several researchers have reported the various laser-based approaches for sensor applications (mainly for strain sensing applications) but as yet little work has been done on developing optical fibre laser-based systems for potential temperature sensing applications and thus remain as an ongoing challenge. It was important to develop a new approach in laser-based sensor work that extends the temperature measurement range from that of the previous laser based work (up to 200 °C maximum) [Ball *et al.* 1993a] to a maximum of 540 °C. The novel fibre-laser based sensor approach was developed using a normal Bragg grating and a chirped grating as optical feedback elements and enclosed a length of erbium-doped fibre as the gain medium [Mandal *et al.* 2004a]. The temperature was measured over the range from room temperature to 300 °C using the normal type I Bragg grating as the active sensor elements and the detail of the sensor configuration will be given in Section 4.5. The laser-based temperature measurement range was further improved by using a type IIA Bragg grating written into the high germanium-erbium (Ge-Er) co-doped photosensitive fibre and this will be described in Chapter 5. Using type IIA Bragg grating in the laser configuration, the temperature was measured over the range from room temperature to 440 °C under zero strain on the chirped grating [Mandal *et al.* 2004b] and up to 500 °C when different strain values were applied to the chirped grating [Mandal *et al.* 2005a]. The high temperature sustainable antimony-germanium (Sb-Ge) co-doped

photosensitive fibre was used to write the normal type I Bragg grating and this was incorporated into the laser-based sensor system to measure the temperature up to 500 °C and also extended the sensor scheme to allow for strain measurement of 0-1200 με [Mandal *et al.* 2005b]. This will be given in detail in Chapter 6. A detailed characterisation of the wavelength-matched normal fibre Bragg gratings-based fibre laser for temperature measurement applications [Mandal *et al.* 2005c] and the comparison of the uniform wavelength-matched laser performances with that of the laser configurations using a normal grating and a chirped grating will be given in Chapter 7. The single cavity (using a normal grating and a chirped grating) laser-based sensor concept was explored for the multiplexed temperature sensor applications. The temperature was measured over the range from room temperature to 540 °C using a multiplexed-laser based sensor concept [Mandal *et al.* 2005d]. This will be given in details in Chapter 8.

The characterisation and the development of Bragg grating-based *full-in-fibre* laser approach were proven to be novel for high temperature sensing applications. Both the high signal-to-noise ratio (SNR) and the narrow linewidth of the laser signal make the active sensor devices especially attractive and also highly sensitive to small perturbations of the measurand in harsh environments, compared to those of the passive FBG sensors, in addition, to all the advantages of the passive sensor schemes. The SNR of the laser depends on the pump power level and the length of the gain medium, thus by increasing the pump power, the laser output power could easily be improved and with that the accuracy of the sensor.

4.4. Theoretical background

The changes in the laser wavelength reflect the changes in the Bragg wavelength of the normal grating, due to the measurand perturbations (arising from the temperature or the strain changes) over the range of the chirped grating which is employed as the second reflector of the laser cavity. The resonance condition for a first-order Bragg grating is given by the following equation [Othonos and Kalli 1999]:

$$\lambda_B = 2n_{eff}\Lambda, \qquad (4.17)$$

where λ_B is the Bragg wavelength, n_{eff} is the effective refractive index of the fibre core and Λ is the grating period. The change in the laser wavelength, $\Delta\lambda_L$, arises mainly from the change in the centre wavelength of the Bragg grating, $\Delta\lambda_B$, with the temperature variation, ΔT and this is expressed as below:

$$\frac{\Delta\lambda_L}{\lambda_L} = func\left(\frac{\Delta\lambda_B}{\lambda_B}\right) = (\alpha + \xi)\Delta T, \tag{4.18}$$

where $\alpha = \frac{1}{\Lambda}\frac{d\Lambda}{dT}$ is the thermal expansion coefficient of the fibre, i.e. the variation in grating period with temperature, (which has a numerical value of $\sim 0.5 \times 10^{-6}/°C$) and $\xi = \frac{1}{n_{eff}}\frac{dn_{eff}}{dT}$ is the thermo-optic coefficient of the fibre i.e. the refractive index variation of the fibre as a function of temperature, having a numerical value in the range in between 8.3 and $9.5 \times 10^{-6}/°C$, at room temperature [Reid and Ozcan 1998].

The temperature dependence of the refractive index can be written as a function of the laser wavelength from the above Eq. (4.18), as shown below:

$$\frac{dn_{eff}}{dT} = n_{eff}\left(\frac{1}{\lambda_L}\frac{\Delta\lambda_L}{\Delta T} - \alpha\right), \tag{4.19}$$

4.5. Experimental Arrangement

4.5.1. Normal grating fabrication

The normal Bragg grating (RB_1) used in this work was written in a commercial germanium (Ge)-doped photosensitive fibre because of the long lifetime and the high stability of gratings written in this fibre at elevated temperatures [Pal *et al.* 2003a]. The Ge-doped (fibre type: GF1) single mode fibre (SMF) had cladding diameter of 125 μm, mode field diameter (MFD) of 10.5 μm @ 1550nm wavelength, cut-off wavelength ($\lambda_{cut\text{-}off}$) of 1.260 μm and was supplied by Nufern, Australia. The normal Bragg grating was fabricated using light from a KrF excimer laser (Braggstar-500 supplied by Tuilaser, AG) as the ultraviolet (UV) source and using the phase mask

technique. The uniform phase mask had its pitch period of 1061 nm, zero-order of 2.21 %, dimension of 10 mm × 5mm and was supplied by Bragg Photonics Inc., Canada. It took nearly 9 minutes of UV exposure with a laser energy of 12 mJ and a repetition frequency of 200 Hz to achieve a reflectivity of ~ 99.9 % at a Bragg wavelength of ~ 1536 nm and with a grating length of 6.5 mm. The transmission spectrum profile of the grating was monitored online using an Optical Spectrum Analyser (OSA - HP86140A) with a resolution bandwidth (RBW) of 0.1 nm. The detail of the growth behaviour of the uniform gratings in this type of fibre was given in Chapter 2. For the grating fabrication, the photosensitive fibre coating was removed using the fibre stripper; and the fibre was cleaned using iso-propyl alcohol (IPA) before the UV exposure.

4.5.2. Annealing of the normal grating

For the analysis of thermal decay of the fibre Bragg gratings, temperature induced irreversible and reversible changes in the Bragg wavelengths of the gratings were observed by Pal *et al.* [2003b] and several other researchers including Hidayat *et al.* [2002]. To ensure the repeatability of the performance of the Bragg grating-based laser probe up to the annealing temperatures, it was important to remove the irreversible changes of the Bragg grating before it could be used for sensor applications. The well-defined annealing process of the grating normally removes the irreversible effects of the grating and thus remains only the reversible changes in the Bragg wavelength, hence to achieve the stable and the repeatable performance from the laser probe. To do this, the normal fibre Bragg grating was placed loosely in a well calibrated tube oven (Carbolite MTF 12/38/400) to avoid any axial strain effects and was annealed at 320 °C for eight hours. Fig. 4.6 shows the transmission spectra of the Bragg grating at room temperature before and after annealing. The grating (RB_I) had a reflectivity of ~ 99.4 % at a Bragg wavelength of 1535.54 nm, which corresponds to a refractive index modulation of ~ 3.30×10^{-4} at room temperature after annealing. The high temperature sustainability of the grating has enabled it to be used as the active element of the sensor head for this work.

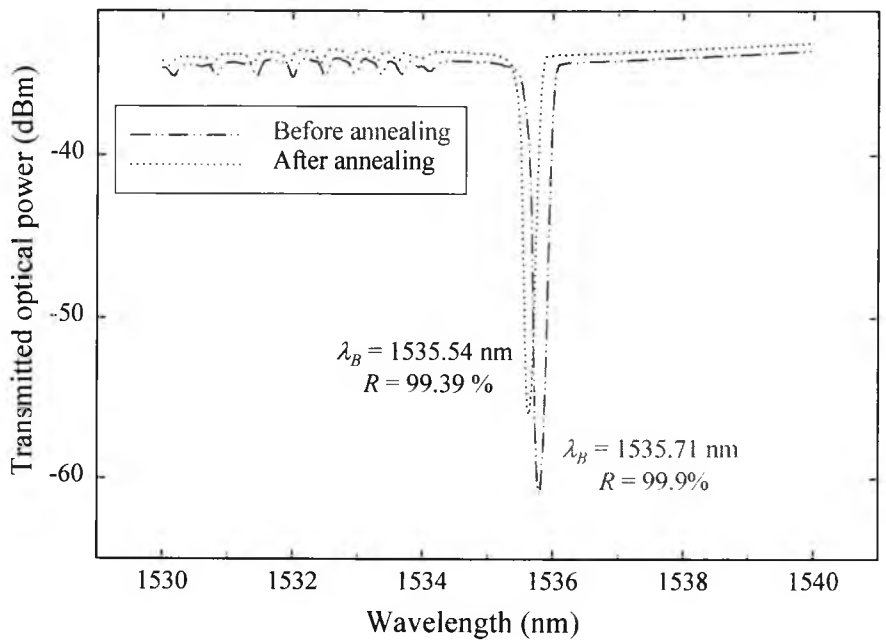

Fig. 4.6: Transmission spectra of the normal Bragg grating at room temperature before and after annealing at 320 °C for 8 hours.

4.5.3. Chirped grating fabrication

The chirped grating (CFBG) used in this work was fabricated in a commercial B-Ge co-doped photosensitive fibre (fibre type: PS 1250/1500, single mode fibre (SMF); cladding diameter: 125 μm, numerical aperture: 0.14, cut-off wavelength: 1.247 μm and was supplied by Fibercore Ltd., UK) using UV light from an excimer laser and employing a chirped phase mask. The chirped phase mask has its centre period: 1060.4 nm, chirp range: 20.7 nm, dimension: 30 mm × 3 mm, zero-order: 0.2 % and was supplied by O/E Land Inc., Canada. It took nearly 17 minutes of UV exposure with a laser energy of 12 mJ and a repetition frequency of 200 Hz to achieve a reflectivity of 75 (± 5) % at centre wavelength of ~ 1537 nm, with a full-width-half-maximum (FWHM) bandwidth of ~ 5.6 nm. The growth behaviour of the chirped grating in this fibre and its principle will be given in detail in Chapter 6. Fig. 4.7 shows the transmission spectra of the chirped grating at room temperature (~ 22 °C) and in a melting ice bath at 0 °C. The spectra were monitored using the OSA with a RBW of 0.2 nm. The chirped grating wavelength shifted ~ 0.2 nm towards the shorter

wavelength side of the spectrum when the grating was inserted in the melting ice bath at 0 °C compared to that at the room temperature (~ 22 °C).

Both the normal and the chirped Bragg gratings were written with the choice of the Bragg wavelength ranges to lie within the well-known fluorescence band of the erbium-doped fibre, to achieve temperature-tuneable laser action, on which the sensor gain depends.

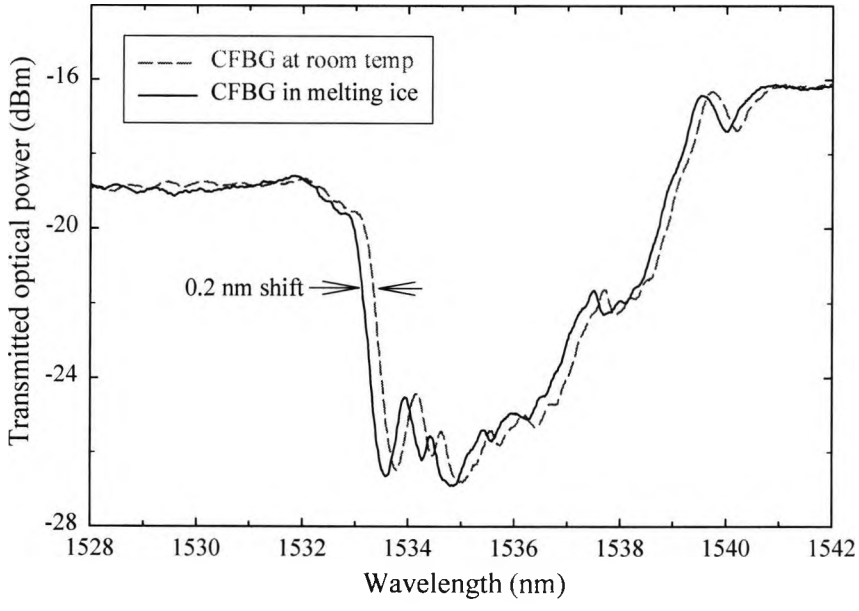

Fig. 4.7: Transmission spectra of the chirped grating at room temperature (~ 22 °C) and in a melting ice bath at 0 °C.

4.5.4. Laser cavity configuration

The schematic of the Bragg grating-based fibre laser sensor system created is shown in Fig. 4.8. The gain medium was a commercial erbium-doped fibre (EDF) with an Er^{3+} ion concentration of 350-400 ppm, in addition with germanium and aluminium oxide co-dopant. Both the Bragg grating reflectors (RB_1 and RB_2) were fusion spliced to the gain-medium to form the resonant laser cavity and the gain medium was externally pumped by using a 1480 nm LD through a 1480/1550 nm wavelength

division multiplexed (WDM) coupler. The laser probe consists of the normal Bragg grating (RB_1) which was placed at the centre of the tube oven and also forms the end reflector into the laser cavity of the sensor. The *chirped* Bragg grating (RB_2) was temperature-stabilised in a melting ice bath at 0 °C and was the second reflector (external to the probe) into the laser cavity to achieve the temperature-tuned measurement. The laser output signal was monitored through the 1550 nm arm of the coupler using an optical spectrum analyser with a RBW of 0.2 nm. The laser cavity length was optimised based on the optimised results obtained in Chapter 3 and as a result was fixed at 5 metres [Mandal *et al.* 2003a].

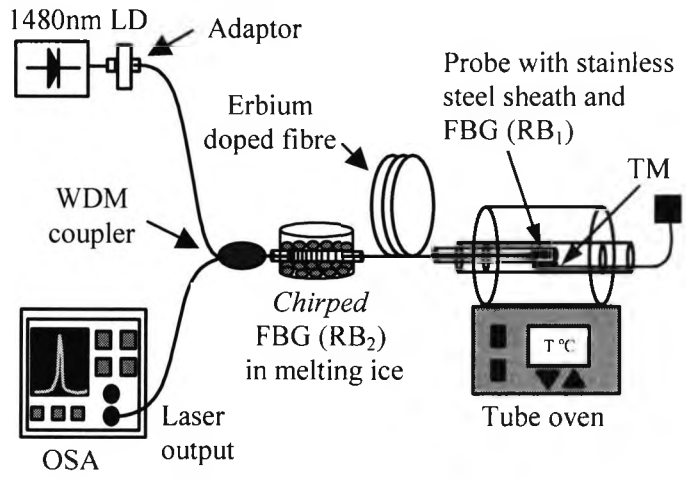

Fig. 4.8: Schematic diagram of a fibre Bragg grating (FBG)-based laser probe sensor system. LD: laser diode; OSA: Optical Spectrum Analyser; TM: Thermocouple meter.

4.5.5. Probe construction

The photograph of the probe is shown in Fig. 4.9, which contains the normal fibre Bragg grating (RB_1) at the left end of the probe. It was constructed with the active part of the probe enrobed in a silica tube (diameter of 750 μm) first and then encircled with a stainless steel metal sheath for additional mechanical strength and hence for the environmental protection.

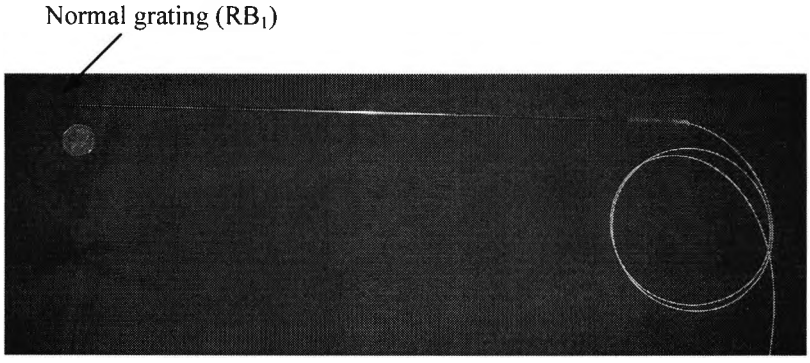

Fig. 4.9: Photograph of the probe containing the normal grating (RB_1) at the left-end.

4.6. Experimental Results

4.6.1. Output spectra of the laser

An investigation to evaluate the performance of the sensor was undertaken by stabilising the temperature of the *chirped* Bragg grating (RB_2) in a melting ice bath at 0 °C and inserting the probe containing the normal Bragg grating (RB_1) in a thermostatically-controlled oven (Carbolite MTF 12/38/400). A K-type thermocouple was held in intimate contact for accurate and continuous comparative monitoring of the oven temperature. In practical applications, the grating could easily be stabilised with a Peltier device at any convenient temperature. The oven temperature was raised from room temperature to 300 °C, with an incremental steps of 20 °C, allowing a settling time of ~ 20 minutes at each temperature. The sensor data were recorded at each temperature after stabilisation using the OSA with a RBW of 0.2 nm. The spectra of the laser output at various temperatures over the range from room temperature to 300 °C are shown in Fig. 4.10. The wavelength of the laser was found to be consistent with the Bragg wavelength of the normal grating (RB_1) owing to its narrower full-width-half maximum (FWHM) bandwidth of the grating (~ 0.21 nm) compared to that of the bandwidth of the chirped grating (~ 5.6 nm). With increasing temperatures, the spectrum of the fibre laser wavelength shifted towards the longer wavelength side of the spectrum with an average signal-to-noise ratio (SNR) of ~ 10 dB.

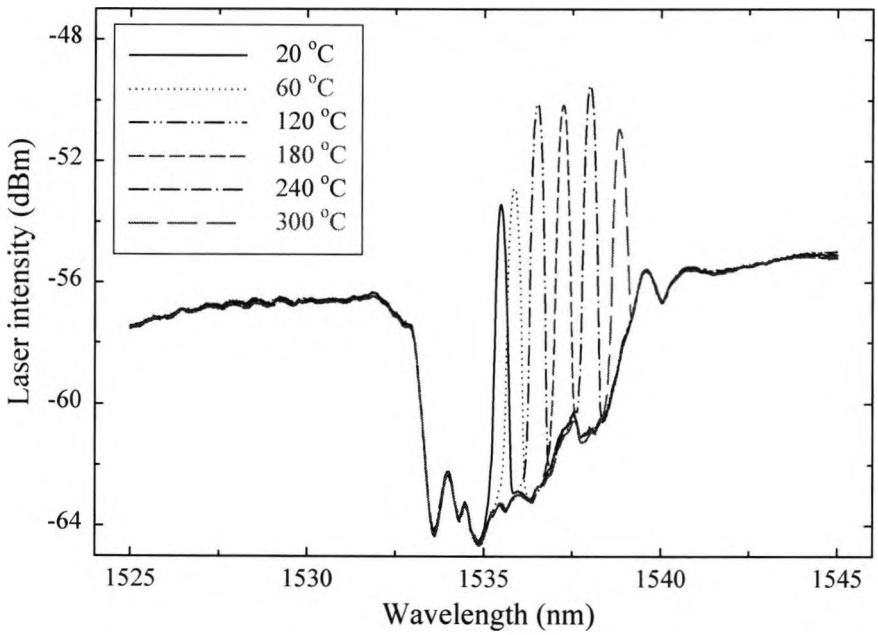

Fig. 4.10: Output spectra of the fibre laser at various probe temperatures over the range from room temperature to 300 °C with a fixed pump power of 21 mW.

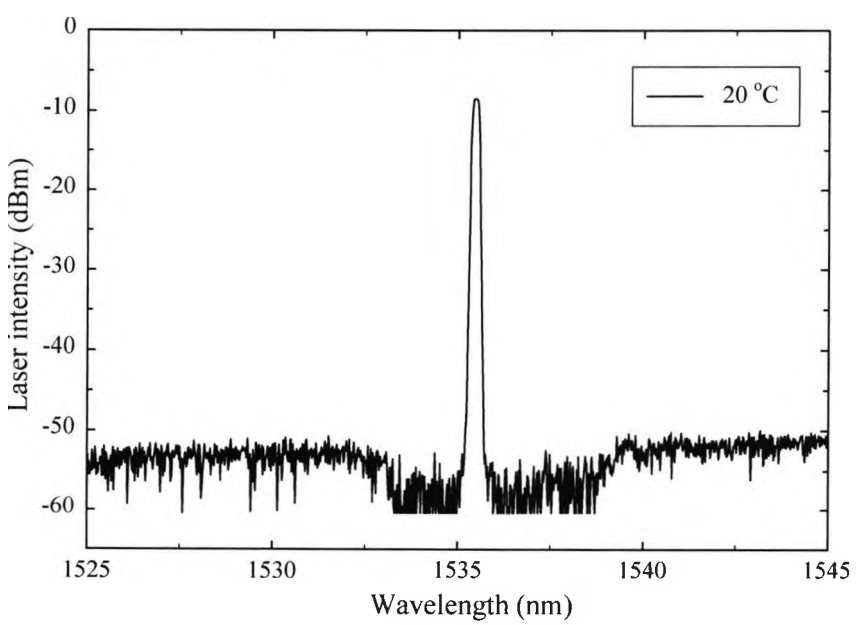

Fig. 4.11: Output spectrum of the fibre laser at room temperature for an optimal pump power of 75 mW.

The shift in the laser wavelength arising from the fractional change in the grating period due to the thermal expansion coefficient ($\delta\Lambda/\delta T$) of the fibre, along with the change in the fibre effective refractive index due to the thermo-optic coefficient effect ($\delta n_{eff}/\delta T$), as is shown in Eq. (4.18).

However, a conventional laser system using two wavelength-matched narrow-band Bragg reflectors could not be used in a similar way, because of the change of the centre wavelength of the one FBG in the probe [Ball *et al.* 1993a; Ball and Morey 1994]. To show clearly that the laser wavelength does shift with temperatures over the broadband range of the *chirped* grating used, the pump power was fixed just above its threshold level at 21 mW. However with a further increase of the pump power, the signal-to-noise ratio (SNR) of the system was easily improved. Fig. 4.11 shows the laser output spectrum at room temperature with a pump power of 75 mW of 1480 nm LD, where the SNR is now approximately 47 dB.

4.6.2. Response of the Probe alone without chirped grating

An experiment was performed to see the response of the probe alone without employing chirped grating in the laser configuration but maintaining the gain fibre length the same as before (at 5 metres). The probe spectra were recorded at different temperatures over the range from room temperature to 300 °C with an incremental steps of 20 °C, as before, using the OSA with a RBW of 0.2 nm. These results are shown in Fig. 4.12 where the signal-to-noise ratio (SNR) of the probe grating was measured to be ~ 3.4 dB, which is much lower than the SNR (~10 dB) of the laser sensor for the same fixed pump power of 21 mW of 1480 nm LD. These results showed that the laser based sensor system offers higher signal-to-noise ratio (SNR) compared to that of the passive FBG sensor, even when the pump power was fixed just above the threshold level of lasing.

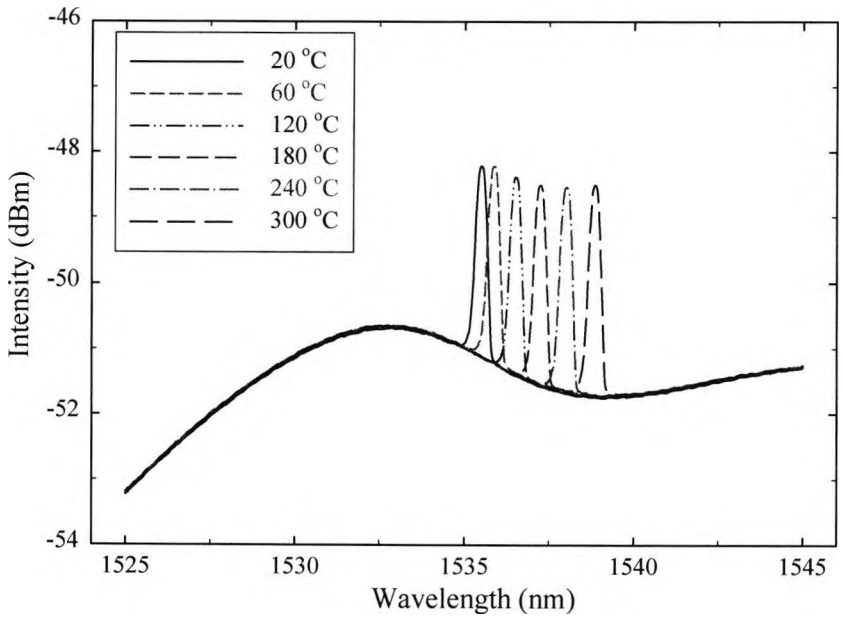

Fig. 4.12: Response of the probe alone without chirped grating in the laser configuration at different temperatures over the range from room temperature to 300 °C with a fixed pump power of 21 mW.

4.6.3. Calibration of the laser probe with temperature

Typical probe calibration curves, showing the laser wavelength (λ_L) change with temperature, using both linear and nonlinear polynomial regression fittings are shown in Figs. 4.13 to 4.15, over the range from room temperature to 300 °C. The measurand is a function of the change in the laser wavelength ($\Delta\lambda_L$), reflecting its thermal response from the changes in the centre wavelength of the *normal* grating reflector RB_1. The laser wavelength (λ_L) as a function of temperature (T) can be calibrated using both linear and nonlinear polynomial regressions to the experimental data obtained over the range from room temperature to 300 °C using the following set of equations. A comparison of the probe calibration results using both linear and nonlinear polynomial regressions is given in Table 4.1.

For a linear fitting:

$$\lambda_L(T) = 1535.133 + 0.01201T, \tag{4.20}$$

where λ_L is the laser wavelength and T is the applied temperature in Degree Celsius to the probe containing normal grating (RB_1).

For a 2nd order polynomial fitting:

$$\lambda_L(T) = 1535.258 + 9.84\times10^{-3}T + 6.763\times10^{-6}T^2, \tag{4.21}$$

For a 3rd order polynomial fitting:

$$\lambda_L(T) = 1535.254 + 9.94\times10^{-3}T + 6.005\times10^{-6}T^2 + 1.569\times10^{-9}T^3, \tag{4.22}$$

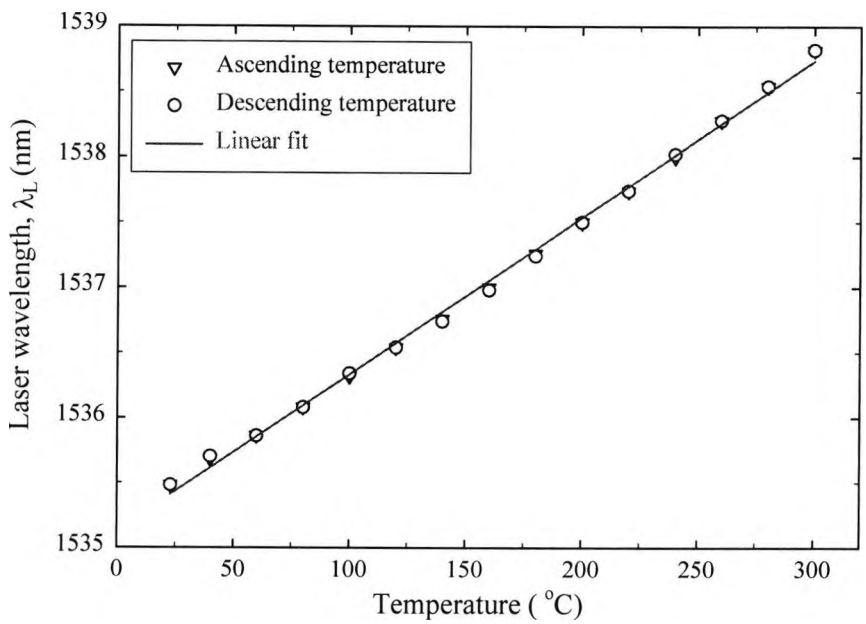

Fig. 4.13: Calibration of the sensor probe with a linear fitting over the range from room temperature to 300 °C.

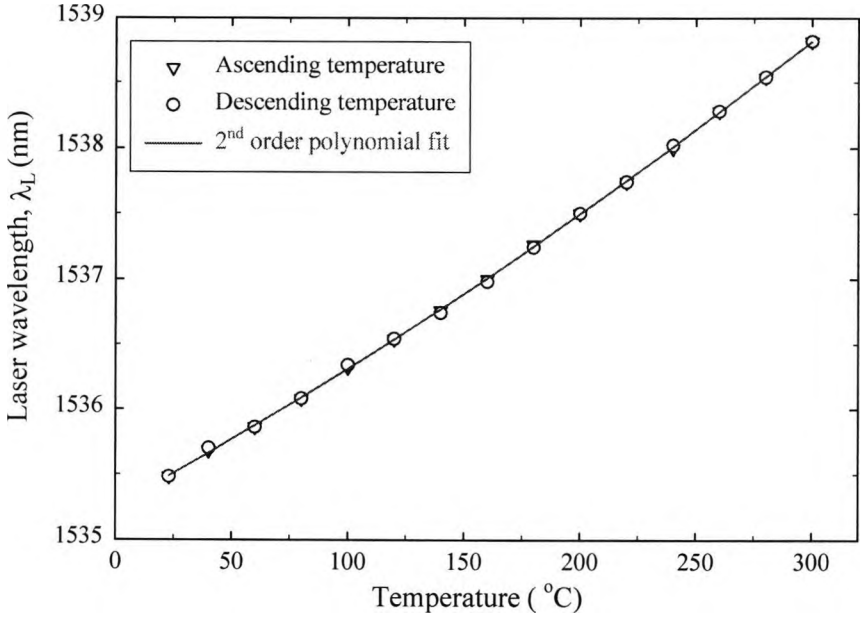

Fig. 4.14: Calibration of the sensor probe with a 2nd order polynomial fitting over the range from room temperature to 300 °C.

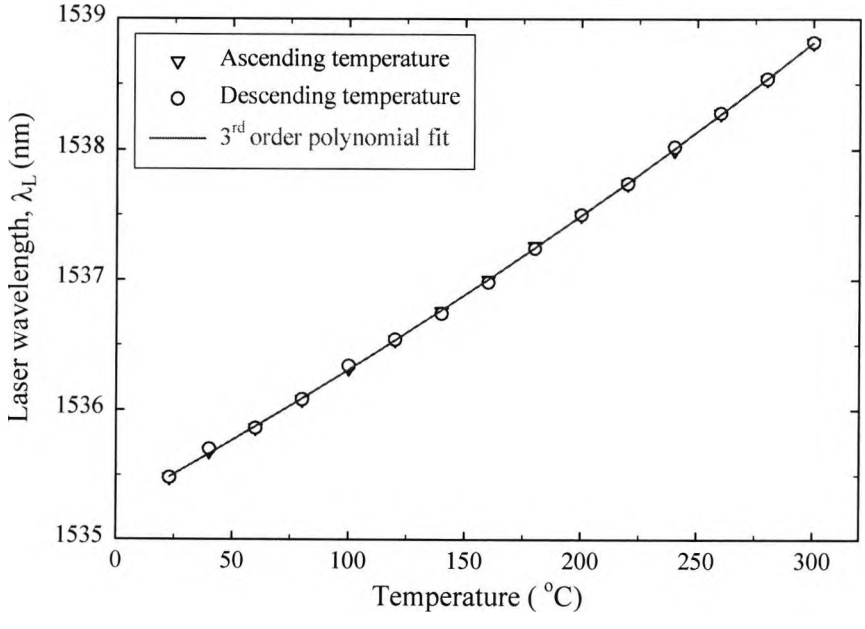

Fig. 4.15: Calibration of the sensor probe with a 3rd order polynomial fitting over the range from room temperature to 300 °C.

Table 4.1: Calibration of the laser probe wavelength using both linear and nonlinear polynomial regressions over the range from room temperature to 300 °C.

Parameters		Linear fitting	2nd order polynomial fitting	3rd order polynomial fitting	Unit used
Temperature range		23 – 300	23 – 300	23 – 300	°C
Sensitivity	23 °C 300 °C	12.01 12.01	9.996 11.87	10.08 11.88	pm/°C
Coefficient of determination (COD)		0.9981	0.99993	0.9993	-
Standard deviation (SD)		0.0434	0.01003	0.0104	-
Root mean square error (RMSE)		0.0464	0.00875	0.00847	nm
RMSE	23 °C 300 °C	3.863 3.863	0.875 0.737	0.843 0.715	°C

Using a nonlinear polynomial regression for the probe calibration showed an improvement in the root mean square (RMS) error of 0.0086 nm in wavelength (on average) (or equivalent to less than 1 °C in temperature) compared to that of the linear fitting with an RMS error of 0.046 nm (or 4 °C) over the range from room temperature to 300 °C. The linear thermal sensitivity of the probe was found to be 12.01 pm/°C and the nonlinear (using a 3rd order polynomial) temperature-dependent sensitivity was found to be 10.08 pm/°C and 11.88 pm/°C at 23 °C and 300 °C respectively. The nonlinear sensitivity at 300 °C is 18 % higher than that of the sensitivity calculated at room temperature (23 °C). The non-linearity in the response of the probe wavelength with temperature variation mainly arises from the non-linear thermo-optic coefficient of the silica glass fibre, as is shown in Eq. (4.18).

For Ge-doped fibre, the thermo-optic coefficient (ξ) was calculated using Eq. (4.19), taking the derivative of Eq. (4.22). As α is much smaller than ξ in Eq. (4.18), it has been assumed that α remains constant, having a value of ~ 0.5×10^{-6}/°C [Reid and

Ozcan 1998] and the thermo-optic coefficient (ξ) was found to vary between 8.911×10^{-6}/°C and 12.42×10^{-6}/°C at 23 °C and 300 °C respectively. The temperature-dependent thermo-optic coefficient ($\frac{dn_{eff}}{dT}$) at 300 °C is 39 % higher than the value calculated at room temperature (23 °C), which supports the existence of a nonlinear thermal sensitivity of the laser calibration.

Ghosh has derived a model of the thermo-optic coefficient as a function of excitonic and isentropic band gaps, and the thermal expansion coefficient of some silicate glasses [Ghosh 1994] as well as standard optical glasses [Ghosh 1995]. The thermo-optic coefficient arises from the contributions of both the electronic transitions and the optical phonons. However, the temperature variation of the excitonic band is the dominant contribution to the thermo-optic coefficient of optical glasses. The thermo-optic coefficient is expressed as below [Ghosh 1995]:

$$2n_{eff}\frac{dn_{eff}}{dT} = \left(n_0^2 - 1\right)\left(-3\alpha R - \frac{1}{E_{eg}}\frac{dE_{eg}}{dT}R^2\right), \tag{4.23}$$

where α is the thermal expansion coefficient of the fibre, n_0 is the low frequency refractive index in the infrared region (IR), E_{eg} is the excitonic band gap and R is the normalised dispersive wavelength which is related to the wavelength, λ, derived using the following relationship:

$$R = \frac{\lambda^2}{\left(\lambda^2 - \lambda_{ig}^2\right)}, \tag{4.24}$$

where λ_{ig}^2 is the wavelength of the isentropic band gap E_{ig}. The value of R is ~ 1 in the infrared region and greater than 1 in the UV region. The isentropic band gap (E_{ig}) is invariant with the variation in temperature. The excitonic band gap (E_{eg}) was found to decrease with the increase in temperature. From Eq. (4.23), it is seen the thermo-optic coefficient ($\frac{dn_{eff}}{dT}$) depends on two factors: the thermal expansion coefficient (α) and the temperature dependence of the excitonic band gap ($\frac{dE_{eg}}{dT}$). The thermal expansion coefficient (α), is generally positive for optical fibre glasses, therefore, the

first term in Eq. (4.23) is negative. In addition, the contribution of the thermal expansion coefficient is relatively small because α is in the order of 10^{-6} /°C. On the other hand, the temperature variation of the excitonic band gap (E_{eg}) is of the order of 10^{-4} eV/°C and is normally negative for the glasses [Matsuoka *et al.* 1991]. As a result, the second term in Eq. (4.23) is positive and larger than the first term, thus resulting in the positive values of the thermo-optic coefficient of fibre glasses. Ghosh [1995] has analysed the refractive index data experimentally and then calculated the temperature dependence of the excitonic band gap ($\frac{dE_{eg}}{dT}$) with temperature as well as the variation of the excitonic band gap E_{eg}, with temperature over the range from 25 °C to 115 °C. It was found that ($\frac{dE_{eg}}{dT}$) is decreasing linearly with increase in temperature and the variation of the excitonic band gap (E_{eg}) with temperature is non-linear; this variation depends on the glass host used.

Flockhart *et al.* [2002] have verified the non-linearity of the Bragg wavelength temperature coefficient over the range from –30 °C to 80 °C based on the model derived by Ghosh [1995], where the non-linearity mainly arises from the non-linear thermo-optic coefficient of the silica glasses. Reid and Ozcan [1998] have reported the temperature dependence of the non-linearity of the Bragg wavelength of fibre Bragg gratings in cryogenic temperature over the range from 4.2 K (for liquid helium) to 350 K. Recently, Pal *et al.* [2004] have showed the non-linearity of the Bragg wavelength shift for both type I and type IIA fibre Bragg gratings over a wide range of temperature from room temperature to 500 °C. Residue in the laser wavelength was calculated from the deviation of the measured wavelength of the probe, and using linear and nonlinear polynomial regressions fit to those data, are shown in Fig. 4.16. The figure clearly shows that the deviation of a linear regression is quite large (in either positive or negative direction) and in parabolic shape compared to those of the nonlinear polynomial regressions. Over the temperature range from 23 °C to 300 °C, both 2nd order and 3rd order polynomial fittings showed a very little difference in the performance of the probe calibration. Therefore, it is better to calibrate the performance of the active sensor probe using a 2nd order polynomial fitting to keep the equation (4.21) length shorter and simpler compared to Eq. (4.22).

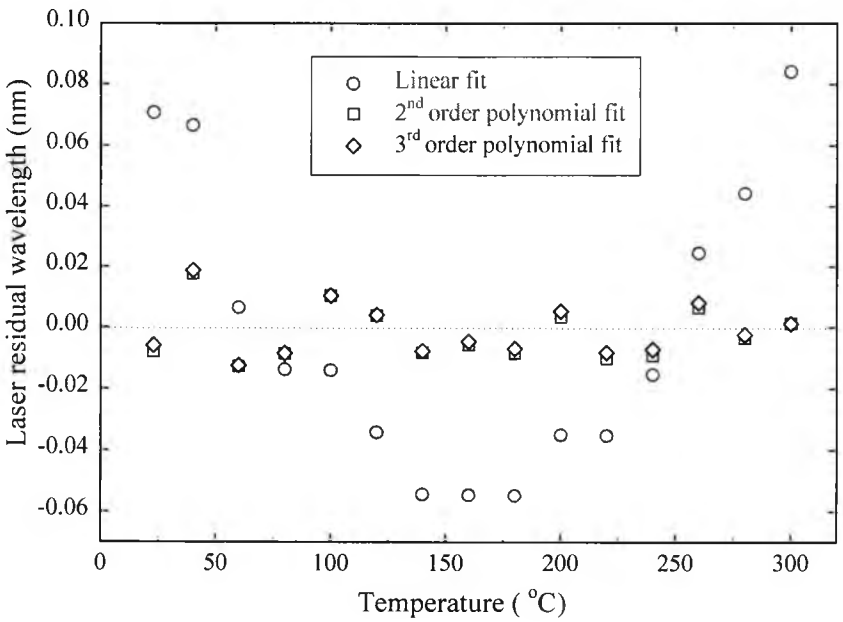

Fig. 4.16: Comparison of the laser residual wavelength with both linear and nonlinear polynomial regressions to the experimental data over the range from room temperature to 300 °C.

The temperature measurement of the probe was limited over the range from room temperature to 300 °C, this mainly arises from the FWHM bandwidth (~ 5.6 nm) of the *chirped* grating RB_2 used, which forms the second reflector into the laser cavity and also from the choice of the Bragg wavelength of the normal grating, RB_1. From the characteristics of both the Bragg gratings and previous work on high temperature grating fabrication [Pal *et al.* 2003a] the upper limit of the measurement range of a system like this is expected to be no higher than 500 °C, in order to allow a realistic lifetime for the probe before the grating "washes out". The sensor could also be adapted for measurements below room temperature using a slightly different wavelength range of the probe grating (RB_1) with appropriate material substrates as was used by Mizunami *et al.* [2001], e.g. employing Teflon, which has a large thermal expansion coefficient, as the bare silica fibre has a negative thermal expansion coefficient (α) below ~150 K [Gupta *et al.* 1996].

The probe calibration was repeated several times with both ascending and descending temperatures to investigate if any hysteresis was present and the probe response was found to be highly repeatable over the entire range of measurements used. The repeatability of the wavelength shift was found to be ± 0.02 nm (or equivalent to ±1.7 °C) from room temperature to 300 °C, with almost no hysteresis being seen. This arises from a combination of the maximum deviation of the sensor data at each temperature over the range from room temperature to 300 °C and considering the linear sensitivity of 12.01 pm/°C; and the resolution bandwidth (of 0.2 nm) of the OSA used. A scanning Fabry-Perot narrow band pass optical filter [Ball and Morey 1994] or Mach-Zehnder read-out interferometer (MZI) [Koo and Kersey 1995] could be used in a practical sensor system to determine the laser wavelength to replace the OSA used in these laboratory experiments.

4.7. Response of the laser system under reverse measurement configuration

The performance of the laser-based sensor system has also been tested by reversing the measurement point in the laser cavity – the *chirped* grating was placed loosely in the oven to avoid any axial strain effects and the normal grating was kept at the ambient temperature. The schematic of such experimental configuration is shown in Fig. 4.17. The gain medium (erbium-doped fibre) and the remaining of the experimental set-up were kept exactly the same as the previous laser configuration, shown in Fig. 4.8. Prior to this experiment, both the normal Bragg grating (GR_1) and the chirped grating (GR_2) were annealed well above their operating temperatures to ensure the stability and the reproducibility of the sensor performance.

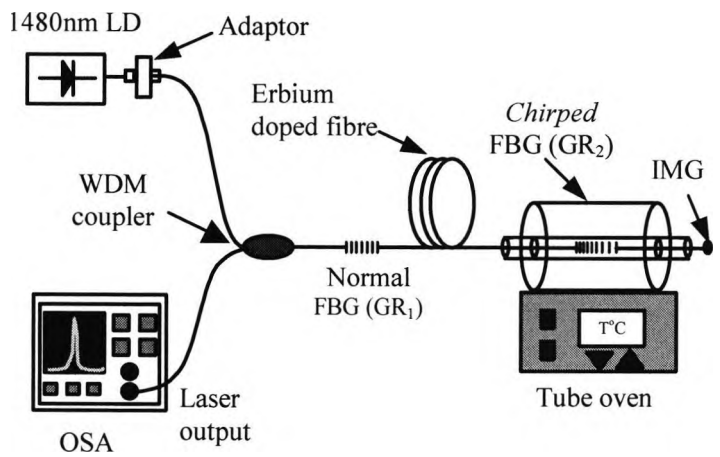

Fig. 4.17: Schematic of the laser based sensor configuration for reverse measurement configuration - chirped grating in oven and the normal grating at ambient temperature; IMG: Index Matching Gel.

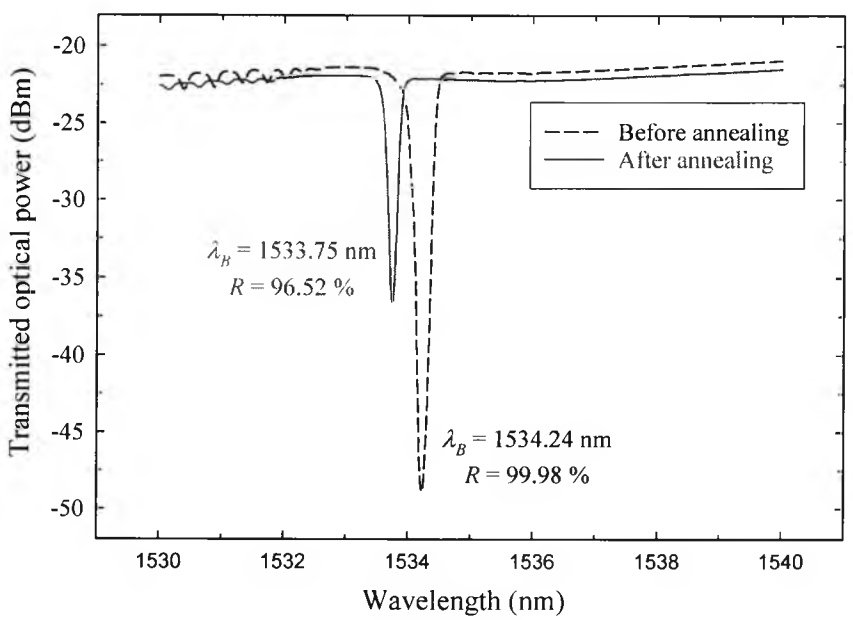

Fig. 4.18: Transmission spectra of the normal Bragg grating (GR_1) at room temperature before and after annealing at 515 °C for 8 hours.

The normal Bragg grating (GR_1) was fabricated in the Ge-doped photosensitive fibre and was annealed at 515 °C for 8 hours. The transmission spectra of the normal

grating (GR_1) at room temperature before and after annealing are shown in Fig. 4.18. The grating was annealed at 515 °C to bring down the reflectivity of the grating from 99.98 % to 96.52 %, as the laser output would be extracted through the normal Bragg grating in this experimental configuration shown in Fig. 4.17. The refractive index modulation of the grating was found to be ~ 2.40×10^{-4}, with a Bragg wavelength of 1533.75 nm after annealing.

The *chirped* grating (GR_2) was fabricated in the boron-germanium (B-Ge) co-doped fibre due to its higher photosensitivity and was annealed at 200 °C for 6 hours, as it would be used as the sensing element for this configuration. The spectra of the chirped grating at room temperature before and after annealing are shown in Fig. 4.19. The reflectivity of chirped grating was measured to be ~ 65 (± 15) % with a bandwidth ~ 5.8 nm at room temperature after annealing.

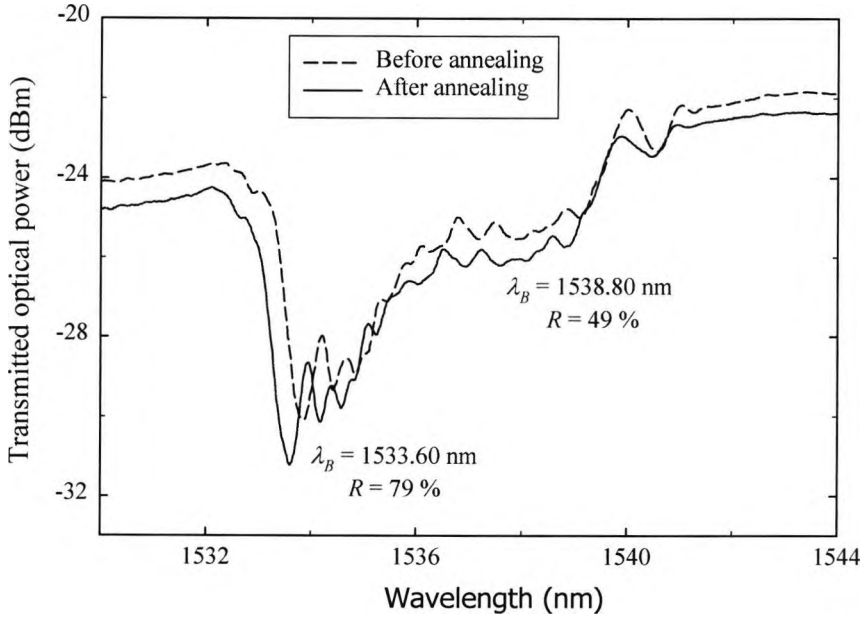

Fig. 4.19: Transmission spectra of the chirped grating (GR_2) at room temperature before and after annealing at 200 °C for 6 hours.

4.7.1. Output spectra

The output of the sensor performance was monitored using the OSA, as before, with a fixed pump power of 21 mW. Under the reverse measurement configuration of the laser, the sensor should not operate and the laser wavelength would not change with temperature, as it would be determined by the normal grating held at room temperature. The oven temperature was raised from room temperature to 170 °C and the output spectrum was monitored using the OSA with a RBW of 0.2 nm. The experimental results for the *chirped* grating in the oven, at room temperature (22 °C) and at 150 °C are shown in Fig. 4.20. The spectra recorded reveal that the laser wavelength is unchanged but the spectrum changes slightly. The system is clearly being influenced by the wavelength matching of the two gratings as the chirped grating is heated. With increasing temperature, the chirped grating spectrum moved towards the longer wavelength side but the Bragg wavelength of the normal grating was found to lie at the edge of the chirped grating along with a decrease in the signal-to-noise ratio (from 9 dB to 3 dB) of the sensor.

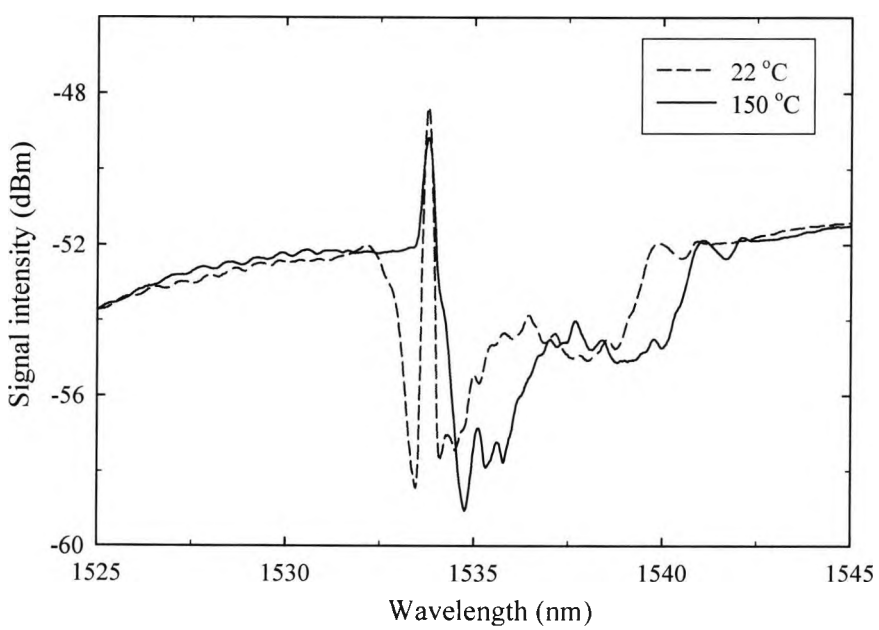

Fig. 4.20: Response of the sensor system at room temperature (22 °C) and at 150 °C for the reverse measurement configuration when the *chirped* grating was placed in the calibration oven.

4.7.2. Response of the signal peak wavelength with temperature

The response of the signal peak wavelength (λ_p) to the temperature changes over the range from room temperature to 170 °C is shown in Fig. 4.21. The expected flat line confirms that the laser *wavelength* is determined only by the wavelength of the normal Bragg grating irrespective of the temperature variation of the *chirped* grating, owing to its much narrower FWHM bandwidth of ~ 0.17 nm compared to that of the *chirped* grating bandwidth of ~ 5.8 nm. This test results confirm that the configuration in Fig. 4.8 operates as a true laser sensor where the laser wavelength is effective as the temperature-dependent measurand as shown in Fig. 4.13. Hence the reverse measurement point approach in the laser configuration is not suitable for sensing applications as the laser signal peak wavelength does not vary with temperature change (Fig. 4.21), and thus the temperature data cannot be obtained using this scheme.

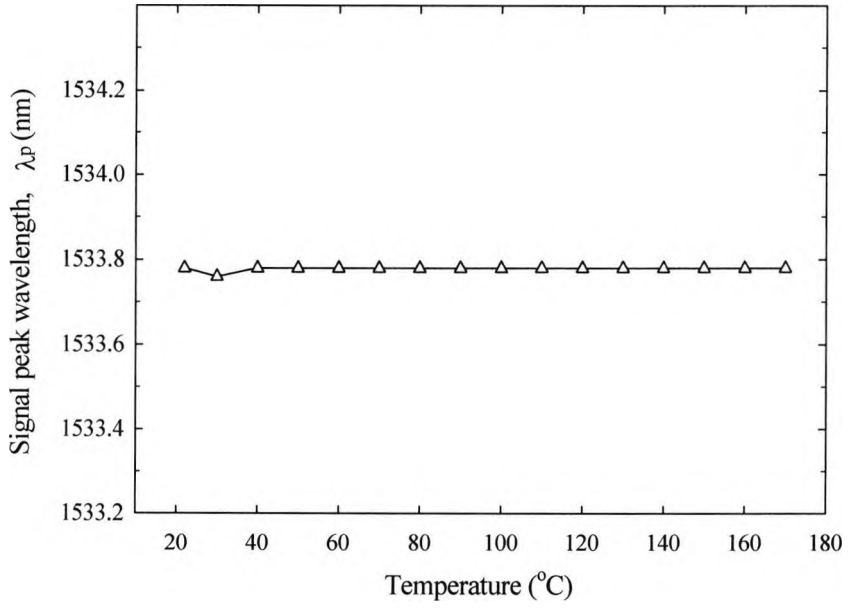

Fig. 4.21: Response of the signal peak wavelength (λ_p) to the temperature changes over the range from room temperature to 170 °C.

4.8. Summary

A simple fibre Bragg grating (FBG)-based laser probe for temperature sensing applications, exploiting the characteristics of both the laser cavity configurations in terms of the output spectra and the wavelength of operation of the laser with different temperatures has been studied. Under the normal cavity configuration of the laser (Fig. 4.8), where the probe containing the normal grating (RB_1) was placed in the high temperature oven and the chirped grating kept in melting ice bath at 0 °C, the sensor works as a true laser based sensor. The reverse measurement configuration of the laser cavity (shown in Fig. 4.17) was used to show that when the *normal* grating (RB_1) was allowed to respond to different temperatures, the device does work as a laser-based sensor and the laser wavelength moved towards the longer wavelength side of the spectrum with increasing temperature. Therefore, the reverse measurement configuration is not suitable for sensor applications; as the laser signal wavelength did not change with temperature variation. The calibration of the probe was performed using both linear and nonlinear polynomial regressions to the measured data. It was found that the nonlinear polynomial shows a better regression and a lesser deviation of the sensor data compared to that of the linear fitting (see Fig. 4.16). The non-linearity in the sensor performance with temperature mainly arises from the nonlinear thermo-optic coefficient of the silica glass fibre. A longer length of the erbium-doped fibre (5 metres) was used as the gain medium of the laser to have relatively higher absorption of the pump power along the fibre length. The laser-based sensor system offers wavelength encoded measurement information along with a better signal-to-noise ratio (SNR) than the fluorescence-based temperature sensing schemes, as reported by several researchers [Zhang *et al.* 1998; Imai and Hokazono 1996].

The new approach to the FBG-based laser probe for high temperature sensing applications was successfully demonstrated for the first time to our knowledge and is convenient, stable and highly repeatable in performance. This arises from the stabilising effect of the grating reflectors (annealing at higher temperature than the operating temperatures) were used to form the laser cavity feedback and also the use of an FBG stabilised 1480 nm pump source. Currently the fabrication of the fibre Bragg gratings required is relatively inexpensive and made easier because of the

availability of different phase-mask technologies. Also with the availability of the high temperature sustaining photosensitive fibres into which the normal Bragg grating was written (the sensor element of the system), this allows the configuration of the novel high temperature sensor system. The use of a *chirped* grating (RB_2) as the second reflector into the laser cavity replaces a broadband mirror, as used by Alavie *et al.* [1993a] and makes the device a *full-in-fibre* laser-based sensor system, thus simplifies the whole system configuration. Employing a chirped grating in the laser configuration allows the achievement of temperature-tuneable laser action over the range from room temperature to 300 °C, without requiring both the gratings to be in the same measurand-state, as reported by Ball *et al.* [1993a]. The novel sensor system was characterised and evaluated using a type IIA Bragg grating as the sensor element of the system and this will be given in the following Chapter (Chapter 5). The practical applications of this device include a range of uses, for example, fire alarm systems as reported by Sun *et al.* [2003], transformer overheating monitoring application [Wickersheim 1991], biomedical applications [Zhang *et al.* 1993] and several other applications where high signal strength is required at elevated temperatures.

4.9. References

- Alavie, A.T., Karr, S.E., Othonos, A. and Measures, R.M. (1993a) A Multiplexed Bragg grating fiber laser sensor system, *IEEE Photon. Technol. Lett.*, vol. 5, pp. 1112-1114.
- Alavie, A.T., Karr, S.E., Othonos, A. and Measures, R.M. (1993b) Fiber laser sensor array, *in Proc. Smart Structures and Materials Conf.*, Albuquerque, NM, SPIE vol. 1918, pp. 308-318.
- Ball, G.A., Morey, W.W. and Cheo, P.K. (1993a) Single-and multipoint fiber-laser sensors, *IEEE Photon. Technol. Lett.*, vol. 5, pp. 267-270.
- Ball, G.A., Meltz, G. and Morey, W.W. (1993b) Polarimetric heterodyning Bragg grating fiber-laser sensor, *Opt. Lett.*, vol. 18, pp. 1976-1978.
- Ball, G.A. and Morey, W.W. (1994) Compression tuned single-frequency Bragg grating fiber laser, *Opt. Lett.*, vol. 19, pp.1979-1981.
- Du, W.C., Tao, X.M., and Tam, H.Y. (1999) Fiber Bragg grating cavity sensor for simultaneous measurement of strain and temperature, *IEEE Photon. Technol. Lett.*, vol. 11, pp. 105-107.
- Flockhart, G.M.H., MacPherson, W.N., Barton, J.S., Jones, J.D.C., Zhang, L. and Bennion, I. (2002) Departure from linearity of fibre Bragg grating temperature coefficients, *in Proc. of 15th Int. Conf. on Optical Fiber Sensors*, Technical Digest, Portland, USA, pp. 75-78.
- Ghosh, G. (1994) Temperature dispersion of refractive indexes in some silicate fiber glasses, *IEEE Photon. Technol. Lett.*, vol. 6, pp. 431- 433.
- Ghosh, G. (1995) Model for the thermo-optic coefficients of some standard optical glasses, *J. Non-Cryst. Solids*, vol. 189, pp. 191-196.
- Grattan, K.T.V. and Meggitt, B.T., Eds., (1998) *Optical Fiber Sensor Technology*, vol. 2, Devices and Technology, Chapman & Hall, London.
- Gupta, S., Mizunami, T., Yamao, T. and Shimomura, T. (1996) Fiber Bragg grating cryogenic temperature sensors, *Appl. Opt.*, vol. 35, pp. 5202-5205.
- Hidayat, A., Wang, Q., Niay, P., Douay, M., Poumellec, B., Kherbouche, F. and Riant, I. (2002) Temperature-induced reversible changes in the spectral characteristics of fiber Bragg gratings, *Appl. Opt.*, vol. 40, pp. 2632-2642.

- Imai, Y., Hokazono, T. and Yoshida, T. (1996) Temperature sensing using 1.54 μm fluorescence in erbium-doped optical fibers, *in Proc. of 11th Int. Conf. Optical Fiber Sensors*, Sapporo, Japan, pp. 268-271.
- Imai, Y. and Hokazono, T. (1996) Fluorescence-based temperature sensing using erbium-doped optical fibers with 1.48 μm pumping, *Opt. Rev.*, vol. 4, pp. 117-120.
- Kersey, A.D. and Morey, W.W. (1993a) Multiplexed Bragg grating fibre-laser strain-sensor system with mode-locked interrogation, *Electron. Lett.,* vol. 29, pp. 112-114.
- Kersey, A.D. and Morey, W.W. (1993b) Multi-element Bragg-grating based fibre-laser strain-sensor, *Electron. Lett.,* vol. 29, pp. 964-966.
- Kersey, A.D., Davis, M.A., Patrick, H.J., LeBlanc, M., Koo, K.P., Askins, C.G., Putnam, M.A. and Friebele, E.J. (1997) Fiber grating sensors, *IEEE J. Lightwave Technol.*, vol.15 pp.1442-1463.
- Kim, S., Kwon, J., Kim, S. and Lee, B. (2000) Temperature-independent strain sensor using a chirped grating partially embedded in a glass tube, *IEEE Photon. Technol. Lett.*, vol.12, pp. 678-680.
- Koo, K.P. and Kersey, A.D. (1995) Bragg grating-based laser sensors systems with interferometric interrogation and wavelength division multiplexing, *J. Lightwave Tech.*, vol.13, pp.1243-1249.
- Lee, J.H., Kim, J., Han, Y.G., Kim, S.H. and Lee, S.B. (2004) Investigation of Raman fiber laser temperature probe based on fiber Bragg gratings for long-distance remote sensing applications, *Opt. Express*, vol. 12, pp. 1747-1752.
- Mandal, J., Pal, S., Sun, T., Grattan, K.T.V. and Augousti, A.T. (2003a) Optimization of erbium-doped fibre lasers and their sensor applications, *in Proc. of XII Conf. on Sensors and their Applications*, Limerick, Ireland, pp. 271-278.
- Mandal, J., Pal, S., Sun, T., Grattan, K.T.V., Augousti, A.T. and Wade, S.A. (2004a) Bragg grating-based fiber-optic laser probe for temperature sensing, *IEEE Photon. Technol. Lett.*, vol. 16, pp. 218-220.
- Mandal, J, Sun, T., Grattan, K.T.V., Augousti, A.T., Wade, S.A., Collins, S.F., Baxter, G.W., Dussardier, B. and Monnom, G. (2004b) A wide temperature tunable fibre laser using a chirped grating and a type IIA fibre Bragg grating, *Meas. Sci. Technol.*, vol. 15, pp. 1113-1119.

- Mandal, J., Sun, T., Grattan, K.T.V., Augousti, A.T., Wade, S.A., Collins, S.F., Baxter, G.W., Dussardier, B., Monnom, G., Zheng, R.T. and Ngo, N.Q. (2005a) Strain-imposed fibre optic laser-based system for wide range temperature measurement applications, *in Proc. in the Conf. on Optical Sensing*, 4-6 April, Dublin, Ireland.
- Mandal, J., Pal, S., Sun, T., Grattan, K.T.V. and Augousti, A.T. (2005b) Bragg grating tuned fiber laser system for measurement of wider range temperature and strain, *Opt. Communs.*, vol. 244, pp. 111-121.
- Mandal, J., Sun, T., Grattan, K.T.V. and Augousti, A.T. (2005c) Fiber laser based temperature sensor systems using wavelength-matched Bragg grating reflectors, *Sensors and Actuators A*, vol. 120, pp.451-461.
- Mandal, J., Sun, T., Grattan, K.T.V., Zheng, R.T., Ngo, N. Q. and Augousti, A.T., (2005d) A parallel multiplexed temperature sensor system using Bragg grating based fibre lasers, accepted for publication in *IEEE Sensors Journal*.
- Matsuoka, J., Kitamura, N., Fujinaga, S., Kitaoka, T., and Yamashita, H. (1991) Temperature dependence of refractive index of SiO_2 glass, *J. Non-Cryst. Solids*, vol. 135, pp. 86-89.
- Melle, S.M., Alavie, A.T., Karr, S., Coroy, T., Liu, K. and Measures, R.M. (1993) A Bragg grating-tuned fiber laser strain sensor system, *IEEE Photon. Technol. Lett.*, vol. 5, pp. 263-266.
- Mizunami, T., Tatehata, H. and Kawashima, H. (2001) High-sensitivity cryogenic fibre-Bragg-grating temperature sensors using Teflon substrates, *Meas. Sci. Technol.*, vol.12, pp. 914-917.
- Othonos, A. and Kalli, K. (1999) *Fiber Bragg Gratings: Fundamentals and Applications in Telecommunications and Sensing*, Artech House, Boston.
- Pal, S., Sun, T., Grattan, K.T.V., Wade, S.A., Collins, S.F., Baxter, G.W., Dussardier, B. and Monnom, G. (2004) Non-linear temperature dependence of Bragg gratings written in different fibres, optimized for sensor applications over a wide range of temperatures, *Sensors and Actuators A*, vol.112, pp. 211-219.
- Pal, S., Mandal, J., Sun, T., Grattan, K.T.V., Fokine, M., Carlsson, F., Fonjallaz, P.Y., Wade, S.A. and Collins, S.F. (2003a) Characteristics of potential fibre Bragg grating sensor-based devices at elevated temperatures, *Meas. Sci. Technol.*, vol. 14, pp. 1131-1136.

- Pal, S., Mandal, J., Sun, T. and Grattan, K.T.V. (2003b) Analysis of thermal decay and prediction of operational lifetime for a type I boron-germanium codoped fiber Bragg grating, *Appl. Opt.*, vol. 42, pp. 2188-2197.
- Peng, P.C., Tseng, H.Y. and Chi, S. (2003) A simple fiber-Bragg-grating sensor system based on a linear-cavity fiber laser, *Microwave and Opt. Tech. Lett.*, vol. 37, pp. 15-17
- Reid, M.B. and Ozcan, M. (1998) Temperature dependence of fiber optic Bragg gratings at low temperatures, *Opt. Eng.*, vol. 37, pp. 237-240.
- Sun, T., Grattan, K.T.V., Sun, W.M., Wade, S.A. and Powell, B.D. (2003) Rare-earth doped optical fiber approach to an alarm system for fire and heat detection, *Rev. Sci. Instrum.*, vol. 74, pp. 250-255.
- Wickersheim, K.A. (1991) Application of fiber optic thermometry to the monitoring of winding temperatures in medium- and large-power transformers, *in Proc. of SPIE,* vol.1584, *Fiber Optic and Laser Sensors IX*, pp.3 -14.
- Zhang, Z.Y., Grattan, K.T.V., Palmer, A.W, Summers, R., Summan, R. and Hughes, S. (1993) Cr:LiSAF fluorescence lifetime based fiber optic thermometer and its applications in clinical RF heat treatment, *in Proc. of SPIE,* vol. 1885, *Biomedical Optics*, pp. 300 -305.
- Zhang, Z.Y., Grattan, K.T.V., Palmer, A.W., Meggitt, B.T. and Sun, T. (1998) Characterization of erbium-doped intrinsic optical fiber sensor probes at high temperatures, *Rev. Sci. Instrum.*, vol. 69, pp. 2924 –2929.

Chapter 5

Characterisation of a wide temperature tuneable fibre laser using a range of values of applied strain to the chirped grating in the laser cavity

5.1. Abstract

In this Chapter, work is reported on several laser-based high temperature sensing applications under conditions of zero strain and of different values of applied strain to the chirped grating which forms the second reflector into the laser cavity. To undertake this study, both normal and chirped gratings were written into a specially fabricated high germanium-erbium (Ge-Er) co-doped photosensitive fibre. The laser-based sensor technique employed the same approach discussed in Chapter 4, but using a type IIA fibre Bragg grating (FBG) as the active sensor element of the system. The fabrication of normal FBGs and chirped fibre Bragg gratings (CFBGs) was studied in this type of fibre. The annealing performance of both the type I and type IIA Bragg gratings was also studied, and the optimum grating sample were chosen for active high temperature sensor applications. The laser cavity feedback was formed using a combination of a CFBG and a type IIA Bragg grating, enclosing a length of erbium-doped fibre (EDF) as the active gain medium. An FBG stabilised 1480 nm laser diode (LD) was employed as the pump source to achieve laser oscillation associated with the Bragg wavelength of the type IIA Bragg grating on the wavelength band around 1550 nm region. The linear thermal sensitivity of the sensor was found to be 13.94 pm / °C with a root mean square error (RMSE) of 8.85 °C, over the temperature range from room temperature to 440 °C. The extended tuneable temperature range of the laser sensor was studied over the range from 70 °C to 500 °C where different values of strain were applied to the chirped grating in the laser cavity. The performance of the sensor was also compared using both the active and the passive operating

conditions of the device. The primary advantage of the active laser-based sensors over the passive optical fibre sensors is the significant improvement in the signal-to-noise ratio (SNR) and a narrow linewidth of the laser signal, making it especially well suited to multiplexing situations. A summary of the results is included at the end of the Chapter.

5.2. Introduction

Fibre Bragg Grating (FBG)-based laser devices have been shown to be important for a range of sensor applications [Kersey and Morey 1993, Mandal *et al.* 2004, Du *et al.* 1999, Kim 1998]. In Chapter 4, a laser based temperature sensor probe has been developed to measure temperature over the range from room temperature to 300 °C. Imai and Hokazono [1997] have developed an erbium-based temperature sensor using excitation at 1480 nm and creating amplified spontaneous emission (ASE) to measure the ratio of the intensities of the fluorescence at two peaks in the spectrum at 1530 nm and 1552 nm. The temperature sensitivity was reported to be 0.007 / °C, on average, over the temperature range from -50 °C to 90 °C. Pal *et al.* [2004] have reported a strain-independent temperature measurement using a combination of both type I and type IIA Bragg gratings written in the high Ge-Er co-doped photosensitive fibre. Both type I and type IIA Bragg gratings have the same strain sensitivity but with different temperature sensitivity shown for each sample. Using the above principle, the temperature was measured from 25 – 300 °C and a strain value of 0 – 500 με with RMS errors of 5.6 °C and 50 με respectively determined. Recently Shen *et al.* [2004] have shown the photosensitivity, temperature-stability and fluorescence characteristics of several erbium-doped photosensitive fibres. Considering three different types of erbium-doped photosensitive fibres such as high germanium-erbium (Ge-Er) co-doped fibre, tin-germanium-erbium (Sn-Ge-Er) co-doped fibre, and antimony-germanium-erbium (Sb-Ge-Er) co-doped fibre samples, the high Ge-Er co-doped fibre showed the highest level of photosensitivity because of the high germanium concentration of the fibre compared to those of the other two samples. From the step-wise thermal characterisation of the three samples, it was found that the Sn-Ge-Er co-doped and the Sb-Ge-Er co-doped fibre samples could sustain higher

temperatures than the high Ge-Er co-doped fibre. This difference in temperature sustainability was attributed to the doping size of the Sb (76 pm in diameter) and of the Sn (71 pm in diameter) ions. The larger doping cation size is believed to be suitable to achieve the high temperature sustainability of the FBGs studied. For the fluorescence characteristics of the three different samples, it was found that the Sb-Ge-Er co-doped fibre (without Al doping) showed the highest level of fluorescence intensity compared to the other two samples.

In this Chapter, a temperature-tuneable fibre laser was developed to measure the temperature over the range from room temperature to 440 °C (zero strain on the chirped grating) and from 70 °C to 500 °C (when 1000 με was applied to the chirped grating). The performance of the sensor was also compared under the active (laser-based) and the passive (non-laser based) operating conditions. Thus the development of the fibre laser-based high temperature sensor system is discussed and the results from several cycles of tests and evaluations are reported.

5.3. Summary of theoretical background

The theoretical background to the use of FBG-based devices has been discussed earlier in Chapter 4 but in summary the change in the laser wavelength ($\Delta\lambda_L$) with temperature arises mainly from the change in the centre wavelength of the Bragg grating ($\Delta\lambda_B$), and this can be expressed through Eq. (5.1) below:

$$\frac{\Delta\lambda_L}{\lambda_L} = func\left(\frac{\Delta\lambda_B}{\lambda_B}\right) = (\alpha + \xi)\Delta T \qquad (5.1)$$

where α is the thermal expansion coefficient of the fibre and ξ is the thermo-optic coefficient of the fibre. As has been seen, for the temperature measurement, the second term in Eq. (5.1) is the dominant factor of the fibre sensor.

In a similar way, the change in the laser wavelength, $\Delta\lambda_L$, with applied strain, ε, can be expressed through Eq. (5.2) below:

$$\frac{\Delta\lambda_L}{\lambda_L} = \left\{1 - \frac{n_{eff}^2}{2}\left[P_{12} - \nu(P_{11} + P_{12})\right]\right\}\varepsilon, \qquad (5.2)$$

where ε is the applied strain to the grating, P_{11} and P_{12} are the strain optic tensor constants, having numerical values of 0.113 and 0.252 respectively, ν is Poisson's ratio, having a numerical value of 0.16 [Othonos 1997]. Using these parameters and the above Eq. (5.2), the numerical value of the photoelastic constant $\left(\frac{n_{eff}^2}{2}\left[P_{12} - \nu(P_{11} + P_{12})\right]\right)$ was found to be ~ 0.21. Therefore, the expected sensitivity at ~1550 nm would produce a 1.2 pm change as a result of applying 1 με to the sensing grating, i.e. the Bragg grating. For high Ge-Er co-doped fibre, the strain optic tensor coefficient, P_{12} was found to be 0.343 for P_{11} = 0.113, ν =0.16, a strain value of ε = 2200 με and n_{eff} = 1.46.

Thus when a temperature change (ΔT) or a strain (ε) is applied to the Bragg gratings in the laser cavity, a shift in the modal frequencies or the wavelengths of the laser output will be observed. In Chapter 4, it was found that the laser wavelength was consistent with the Bragg wavelength of the normal FBG, owing to its narrower bandwidth than that of the chirped grating bandwidth. When different values of strain were applied to the CFBG in the laser cavity, the wavelength of the chirped grating shifted towards longer wavelength side without changing its bandwidth. This allows the achievement of an extended-tuneable-temperature measurement range of the laser-based sensor as the CFBG forms the second reflector into the laser cavity.

5.4. High germanium-erbium co-doped fibres

The high germanium-erbium (Ge-Er) co-doped fibre was specially fabricated at the University of Nice, France, using the modified chemical vapour deposition (MCVD) technique. The fibre (fibre type: A021) had a core diameter of 4.0 μm, cladding diameter of 125 μm, cut-off wavelength ($\lambda_{cut\text{-}off}$) of 1.54 μm, numerical aperture (NA) of 0.297, with a GeO_2 of ~ 20 mole %, Er^{3+} ion of ~ 2700 ppm, in addition to the aluminium oxide (Al_2O_3) co-dopant in the fibre core. The high germanium content

was introduced to the fibre to raise the refractive index of the fibre core and also to enhance the fibre photosensitivity to promote the efficient writing of the desired gratings. The addition of Al_2O_3 enhances the solubility of the Er^{3+}-ion in the centre of the fibre core and also eliminates the concentration quenching effects that may occur. The addition of rare-earth dopant Er^{3+}-ion is used to generate the strong fluorescence from this photosensitive fibre.

5.5. Grating fabrication

5.5.1. Normal type I and type IIA fibre Bragg gratings

Both the type I and type IIA Bragg gratings were fabricated in the high Ge-Er co-doped photosensitive fibre using the same technique as derived in Chapter 2. The specifications of the uniform phase mask used are the same as given in Chapter 4.

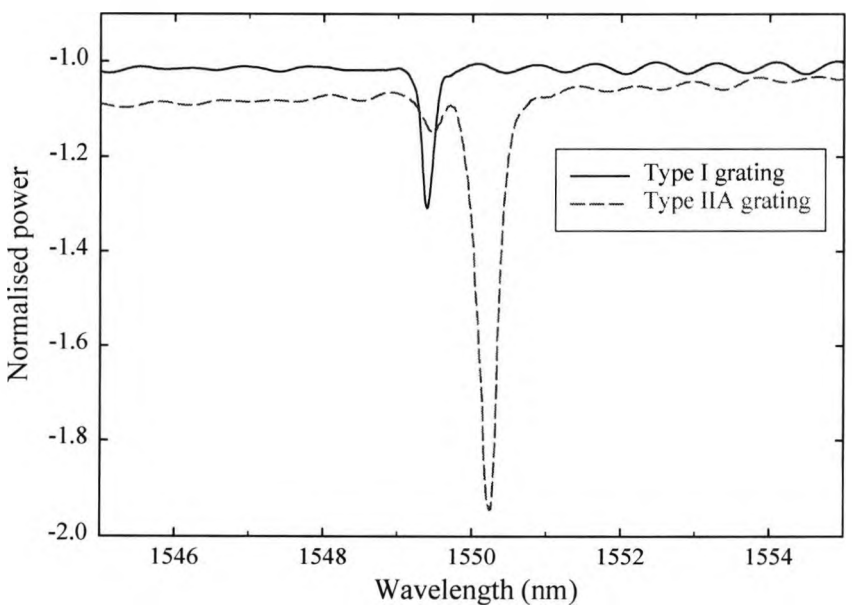

Fig. 5.1: Transmission spectra of type I and type IIA fibre Bragg gratings after saturation of each sample.

The monotonic increase in the refractive index modulation of the grating, and thus the growth of the reflectivity of the grating along with the UV exposure defines a type I Bragg grating [Othonos and Kalli 1999]. The type I FBG was fabricated using laser energy of 12 mJ and a repetition frequency of 200 Hz. The growth of the type I grating saturates within less than 1 minute of exposure, achieving a reflectivity of ~ 96.57 % with a Bragg wavelength of 1549.41 nm, which corresponds to a refractive index modulation of 2.18×10^{-4}. Fig. 5.1 shows the normalised transmission spectra of type I and type IIA Bragg gratings after saturation of each sample.

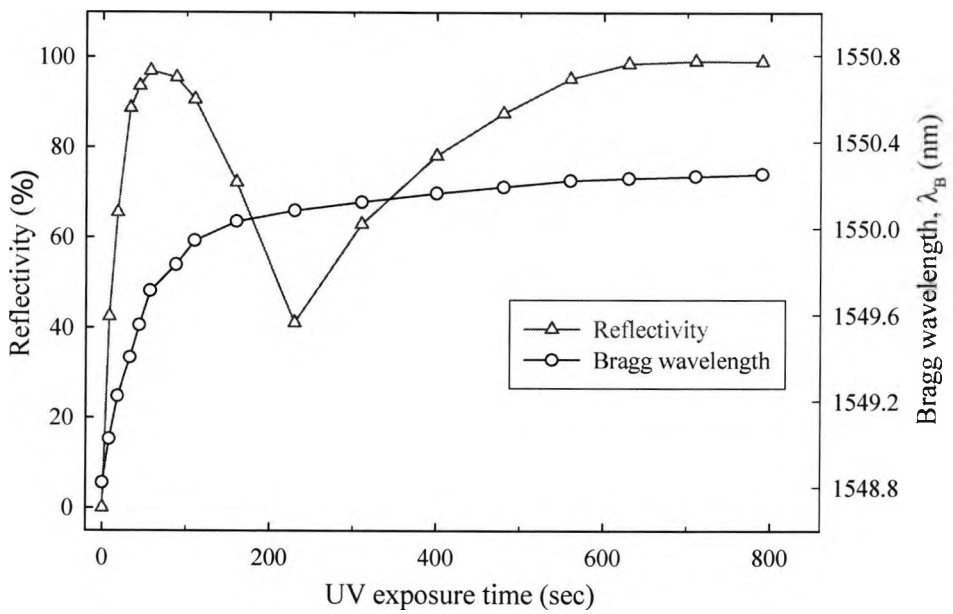

Fig. 5.2: Growth behaviour of the type IIA Bragg grating in terms of its reflectivity and Bragg wavelength variation as a function of UV exposure time.

The type IIA FBG was fabricated with the same level of laser energy (12 mJ) and the frequency (200 Hz). It took nearly 14 minutes of UV exposure to achieve a reflectivity of ~ 99 % at a Bragg wavelength of 1550.24 nm, corresponding to a refractive index modulation of 2.68×10^{-4}. The grating fabrication characteristics were monitored online using an optical spectrum analyser (OSA – HP86140A) and an external broadband light source. Fig. 5.2 shows the growth behaviour of the type IIA

Bragg grating in terms of the change in its reflectivity and the Bragg wavelength as a function of the UV exposure time.

It was found that the growth of the reflectivity stops at a certain level (~ 97 %), then drops to ~ 41 % with the saturation of the type I grating, before the formation of the type IIA grating with continuous UV exposure and with that an increased reflectivity. The Bragg wavelength (λ_B) initially shifts strongly towards the longer wavelength part of the spectrum when the reflectivity increases, however, it shows a very small red shift during the formation (and the saturation) of type IIA Bragg grating, compared to that of the initial type I grating. Further, a larger value of the Bragg wavelength was achieved due to its higher effective refractive index of the fibre core. The refractive index modulation (Δn) of the gratings was calculated using the same equation (2.26), as derived in Chapter 2.

5.5.2. Chirped grating

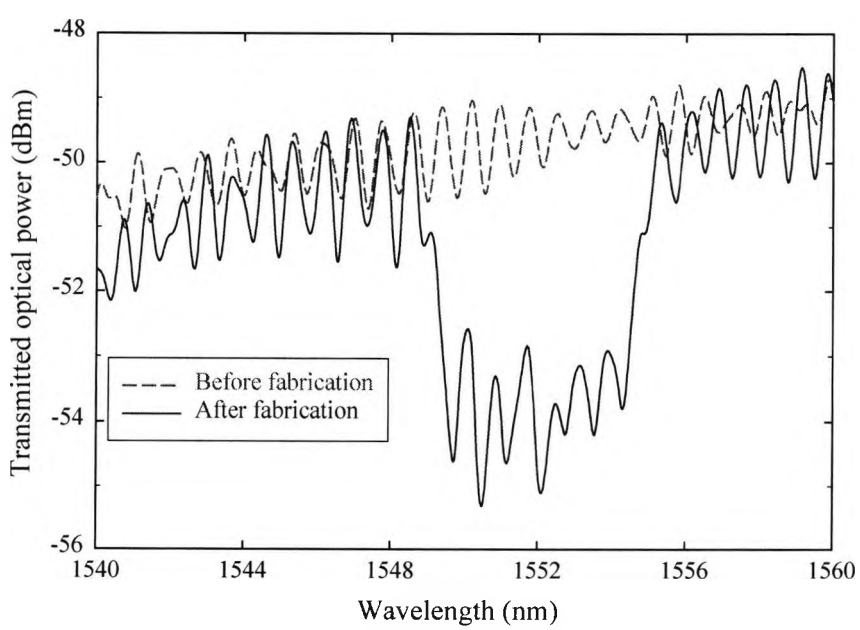

Fig. 5.3: Transmission spectra of the chirped Bragg grating before and after the fabrication.

The chirped grating (CFBG) was also fabricated in the high Ge-Er co-doped photosensitive fibre and using a chirped phase mask (specifications are the same as given in Chapter 4). It took nearly 17 minutes of UV exposure to saturate the sample using the laser energy of 12 mJ and a repetition frequency of 250 Hz. Fig. 5.3 shows the transmission spectra of the grating before and after the fabrication. A maximum reflectivity of ~ 67 (± 3) % was achieved with a centre wavelength of ~ 1552 nm, with a full-width-half-maximum (FWHM) bandwidth of ~ 6 nm. The spectrum of the chirped grating was monitored using an OSA using a resolution bandwidth (RBW) of 0.2 nm.

The wavelengths of both the normal FBG and the CFBG lie within the well-known fluorescence band of the erbium-doped fibre (laser gain medium) to achieve a wide temperature tuneability of the laser sensor.

5.6. Annealing performance of normal Bragg gratings

5.6.1. Annealing results of type I Bragg grating

A similar procedure to that discussed in Chapter 4 was undertaken to anneal the gratings in order to extend the laser-based temperature measurement range. Type I and type IIA Bragg gratings were annealed at 500 °C and 525 °C respectively. During the annealing of type I Bragg grating as shown in Fig. 5.4, by the time the oven temperature reached 500 °C, from room temperature, the grating had already experienced an initial decay of the reflectivity from ~ 96.57 % to 78.50 %. This arises from the degradation of the UV induced refractive index modulation from 2.18×10^{-4} to 1.29×10^{-4}. The faster decay in the reflectivity of the grating was observed for the first few hours of the annealing, followed by a substantial slower decrease in the reflectivity was observed. Finally, after 11 hours of annealing, the reflectivity of type I Bragg grating was found to be still decreasing at much slower trend. The reflectivity of the grating remained to be less than ~ 56 % when the oven was turned off. A blue shift in the Bragg wavelength was observed during annealing which arises from the degradation of the effective refractive index of the fibre core [Pal *et al.* 2003].

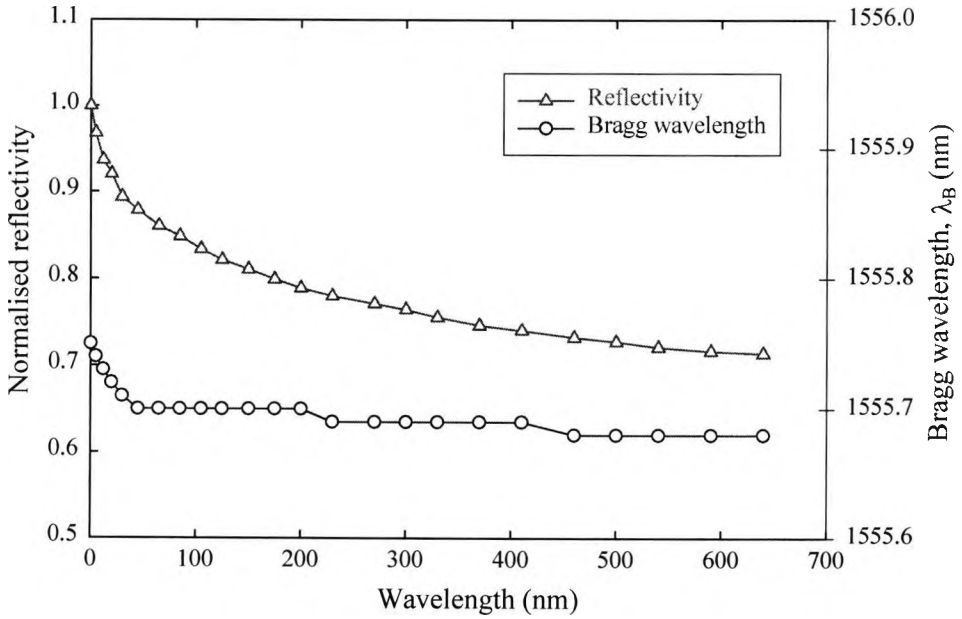

Fig. 5.4: Normalised reflectivity and Bragg wavelength variation of the type I Bragg grating with annealing time at temperature of 500 °C.

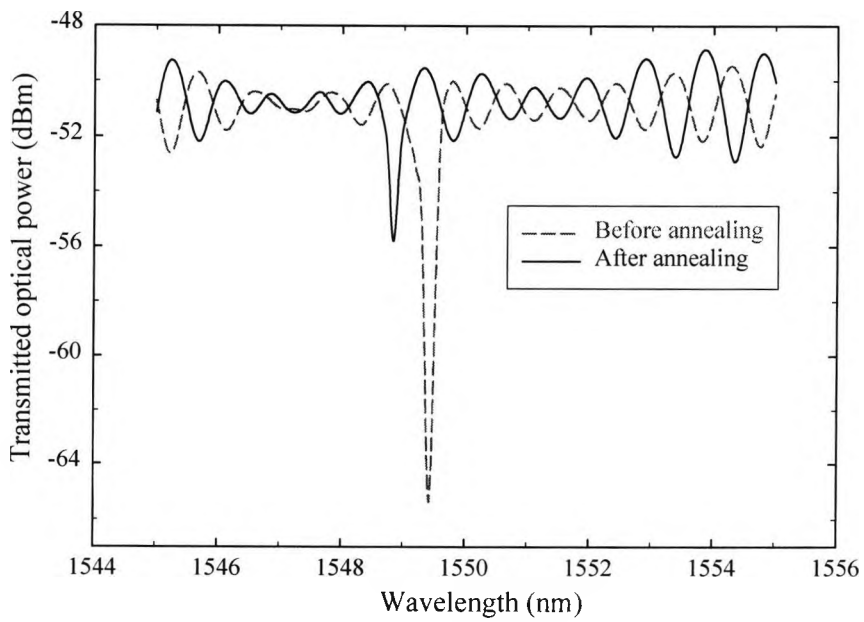

Fig. 5.5: Transmission spectra of the type I Bragg grating at room temperature (~ 26 °C) before and after annealing at temperature of 500 °C for 11 hours.

Fig. 5.5 shows the transmission spectra of the type I Bragg grating at room temperature (~ 26 °C) before and after annealing. The Bragg wavelength of the grating was measured to be 1548.83 nm at room temperature, corresponding to a refractive index modulation of 8.89×10^{-5} and a FWHM bandwidth of 0.16 nm, using an OSA with a RBW of 0.1 nm.

5.6.2. Annealing results of type IIA Bragg grating

In a similar way to that discussed previously, the type IIA Bragg grating was annealed at 525 °C for eleven hours. During the annealing of the type IIA FBG as shown in Fig. 5.6, by the time the oven temperature reached 525 °C (from room temperature) the grating had already experienced an initial decay of reflectivity from ~ 99 % to 96.30 %. This arises from the degradation of the UV induced refractive index modulation from 2.68×10^{-4} to 2.16×10^{-4}. After that, a very small decay in the reflectivity was observed during the first hour of annealing and then almost negligible decay in the reflectivity was seen over the rest of the annealing period. Finally, the type IIA Bragg grating was stabilised with a reflectivity of ~ 95.6 % at a Bragg wavelength of 1556.49 nm, which corresponds to a refractive index modulation of 2.07×10^{-4}. A small blue shift in the Bragg wavelength was observed during the annealing process. Fig. 5.6 shows the normalised reflectivity and the Bragg wavelength variation of the type IIA Bragg grating with annealing time at temperature of 525 °C. The reflectivity of the type IIA Bragg grating was measured (at room temperature after being annealed) to be ~ 95.57 % at a Bragg wavelength of 1549.35 nm, this corresponds to a refractive index modulation of 2.06×10^{-4}. The full-width-half-maximum (FWHM) bandwidth of the grating was measured to be 0.64 nm using an OSA with a RBW of 0.1 nm. Fig. 5.7 shows the transmission spectra of the type IIA Bragg grating at room temperature (~ 26 °C) before and after annealing. The change in the Bragg wavelength (1555.24 nm at the time of fabrication which shows 1555.45 nm before annealing) of the grating arises from the two different OSAs used during the fabrication and the annealing process.

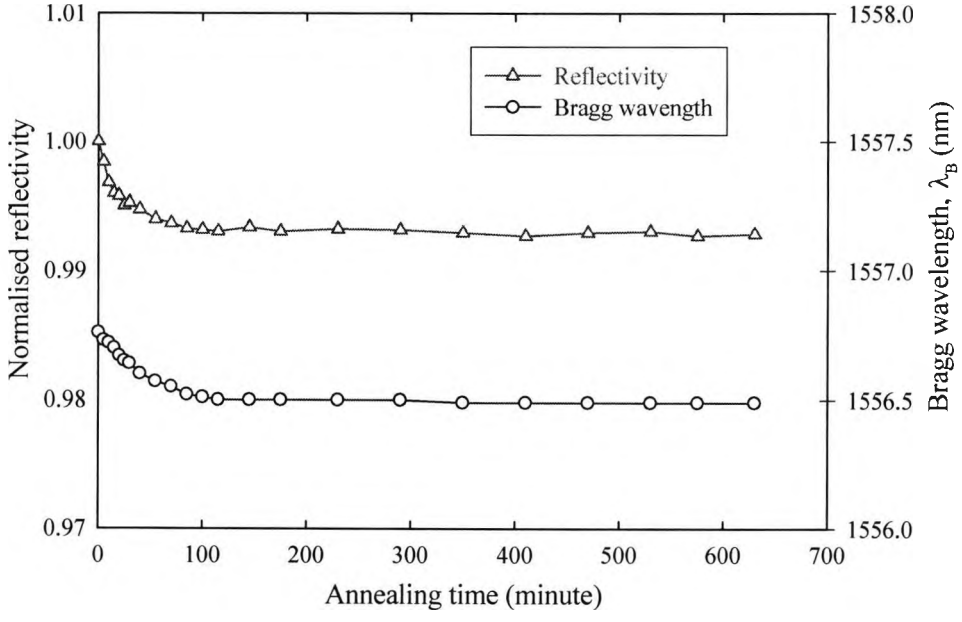

Fig. 5. 6: Normalised reflectivity and Bragg wavelength variation of the type IIA Bragg grating with annealing time at temperature of 525 °C.

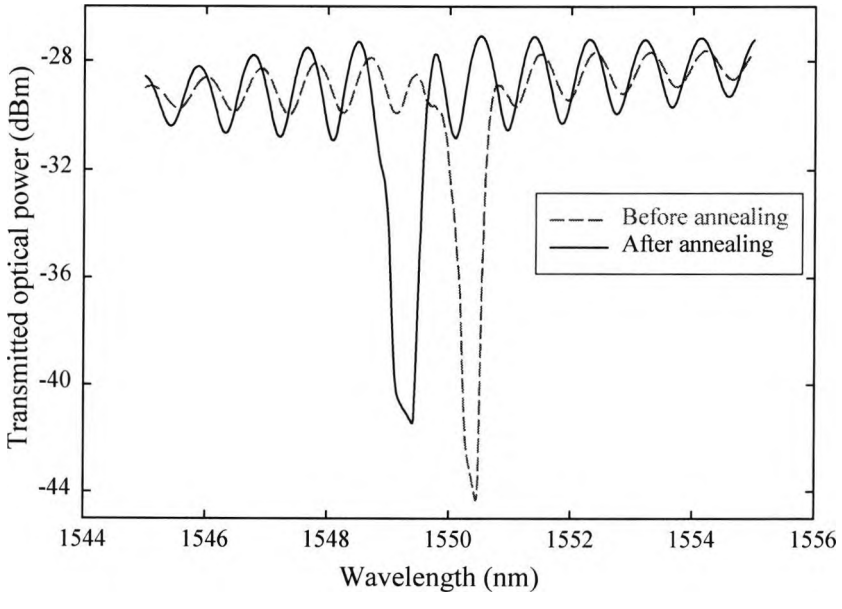

Fig. 5.7: Transmission spectra of the type IIA Bragg grating at room temperature (~ 26 °C) before and after annealing at temperature of 525 °C for 11 hours.

The OSA which does not have built-in-source, shows a wavelength difference of ~ 0.20 nm (lower) than that of the OSA having built-in-source. After fabrication of the gratings, the rest of the experiments were performed using the OSA having built-in-source for wavelength consistency. The chirped grating was annealed at 100 °C for the same period, as the grating was kept at ambient temperature for this application.

5.6.3. Optimum grating selection for active sensor

The above annealing results showed that there is a significant decay in the reflectivity of type I grating (less than 55 %) after being annealed at 500 °C for 11 hours, whereas the type IIA grating had a very high level of reflectivity of ~ 96 % after being annealed at 525 °C for the same period. In the sensor arrangement shown in Fig. 5.8, the normal grating (RB_1) forms the end reflector in the laser cavity. Therefore a relatively high level of reflectivity of the grating is viable to form the laser cavity and thus to minimise the reflection loss from the grating. As a result, a type IIA Bragg grating was chosen for the high temperature measurement applications as the type I grating shows limitation for the same applications.

5.7. Experimental Arrangement

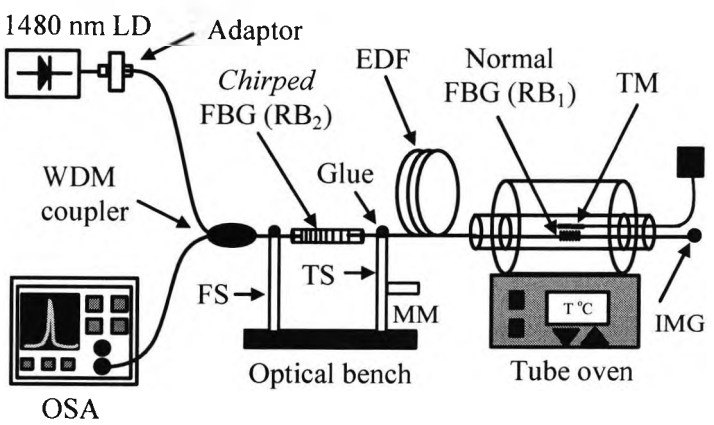

Fig. 5.8. Schematic of the experimental set-up of a fibre laser-based sensor system. LD: laser diode, OSA: optical spectrum analyser, EDF: erbium-doped fibre, FS: fixed stage, TS: translation stage, MM: micrometer, IMG: index matching gel, TM: thermocouple meter.

5.7.1. Laser cavity configuration

The laser cavity, shown in Fig. 5.8, was formed using the combination of a thermally annealed, normal type IIA Bragg grating (RB_1) and a chirped grating (RB_2), fabricated as described above, and enclosed a length of erbium-doped fibre as the laser gain medium. The type IIA FBG forms the end reflector in the laser cavity and also the sensing element of the active sensor. The chirped grating (RB_2) forms the second reflector in the laser cavity and it was kept at ambient temperature. The cavity length was optimised using data obtained from several previous experiments on the cavity length using this type of fibre in Chapter 3 and it was fixed at approximately 5 metres [Mandal *et al.* 2003]. The erbium-doped fibre had an Er^{3+} ion concentration of 350 - 400 ppm, a core diameter of 2.3 μm, a cut-off wavelength ($\lambda_{cut\text{-}off}$) of 0.850 μm (with, in addition, the germanium and aluminium oxide co-dopant), supplied by High Wave Optical Technology, France. To obtain laser oscillation, the gain medium was externally pumped using a 1480 nm LD through a 1480/1550 nm wavelength division multiplexed (WDM) coupler. The output was monitored using the OSA through the other arm of the coupler with a RBW of 0.1 nm, which allows a minimum observable wavelength shift of ± 0.01 nm. Index matching gel (IMG) was used at the bare fibre end to minimise the Fresnel reflection into the laser cavity.

5.8. Experimental results under zero-strain on chirped grating

To monitor the temperature performance of the laser-based sensor, the type IIA Bragg grating (RB_1) was mounted loosely in an oven with a K-type thermocouple in close contact for accurate and continuous comparative monitoring of the temperatures. The oven temperature was raised from room temperature to 480 °C, in an incremental step of 20 °C up to 420 °C, and then in narrower steps to 480 °C; while the laser output spectrum was monitored using the OSA. A settling time of 20 minutes was allowed at each temperature to achieve thermal equilibrium between the grating (RB_1) and the oven before recording the data.

5.8.1. Output spectra

The output spectra of the sensor under zero-strain on the chirped grating, over a range of temperatures from room temperature to 480 °C, are shown in Fig. 5.9 with a fixed pump power of 52 mW of 1480 nm LD.

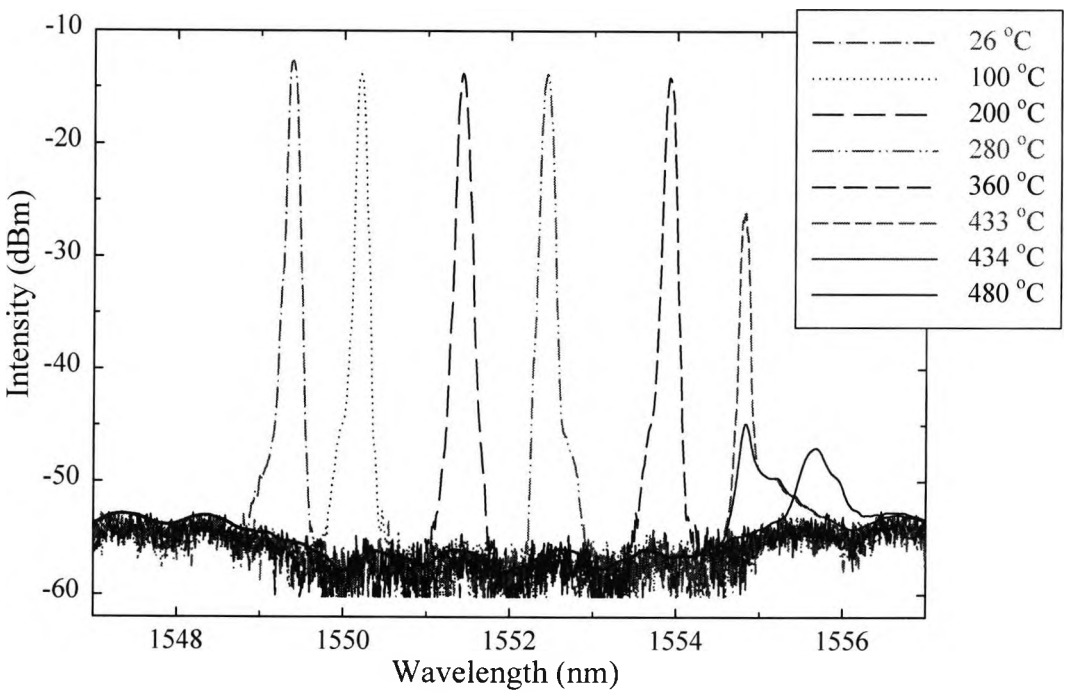

Fig. 5.9: Output spectra of the sensor (zero-strain on chirped grating) with different temperatures from room temperature to 480 °C, with a fixed pump power of 52 mW.

The laser wavelength observed was consistent with the Bragg wavelength of the type IIA Bragg grating, owing to its narrower FWHM bandwidth (~0.64 nm) than that of the bandwidth (~ 5.9 nm) of the chirped grating used. With increasing temperature, the laser wavelength shifted towards the longer wavelength side of the spectrum. This arises from the change in the effective refractive index of the grating due to the thermo-optic coefficient of the fibre along with the fractional change in the grating period due to the thermal expansion coefficient of the fibre, as is seen in Eq. (5.1). A typical signal-to-noise ratio (SNR) of the laser was measured to be approximately 42

dB before the laser action eventually ceases. At 440 °C the laser action totally disappears and the SNR value drops to approximately 7 dB, for the same fixed pump power level of 52 mW, this having been held constant throughout the whole experiment. As discussed, the type IIA Bragg grating had been annealed at 525 °C, (to ensure reproducibility up to this temperature) but the laser action was limited to a more restricted temperature range, and terminated at 440 °C when the chirped grating was left unstrained. The main cause of the upper limit was the fixed FWHM bandwidth (~ 5.9 nm) of the chirped grating RB_2, which formed the second reflector of the laser cavity. However, with the use of a chirped grating having a wider bandwidth or applying strain values to the chirped grating (to shift the chirped wavelength towards the longer side in the spectrum), the laser action could readily be extendable to a temperature of 500 °C, using the present normal grating (RB_1). These results will be given in section 5.9 for uses where different values of strain were applied to the chirped grating.

5.8.2. Intensity and linewidth variation

The intensity and the linewidth variation, with different temperatures from room temperature to 480 °C, are shown in Fig. 5.10 with a fixed pump power of 52 mW. The fluctuation in the laser intensity with temperature mainly arises from the small variations in the reflectivity (67 ± 3)% of the chirped grating (RB_2) used, through which the laser output was extracted, the spatial relationship of the laser to the spectral profile of the Er^{3+}-doped fibre, and the spectrum of the type IIA normal grating used. The metastable level ($^4I_{13/2}$) and the ground level ($^4I_{15/2}$) of the Er^{3+} ion consists of several Stark sub-levels and populated to various degrees depending on the Boltzmann thermal distribution. The fluorescence spectrum, in general, consists of two wavelength peaks at around 1535 nm and 1552 nm, which vary to a small degree with the hosts material used [Duservire and Simpson 1990]. Imai and Hokazono [1997] have reported a typical fluorescence spectrum profile of an erbium-doped fibre showing two peaks at wavelengths of 1530 nm and 1552 nm with 1480 nm pumping, where the peak power on both decreased with increasing temperatures. For this study, the normal type IIA grating (RB_1) was fabricated in Ge-Er co-doped fibre and was

seen to be responding to different temperatures over the fluorescence peak in the 1552 nm range. Also the wider bandwidth (~ 0.64 nm) of the type IIA Bragg grating allows a large number of lasing modes falling within the gain-spectrum, as a result the laser output may sustain a number of modes. All these effects, when combined showed a small impact on the output power of the laser with different applied temperatures.

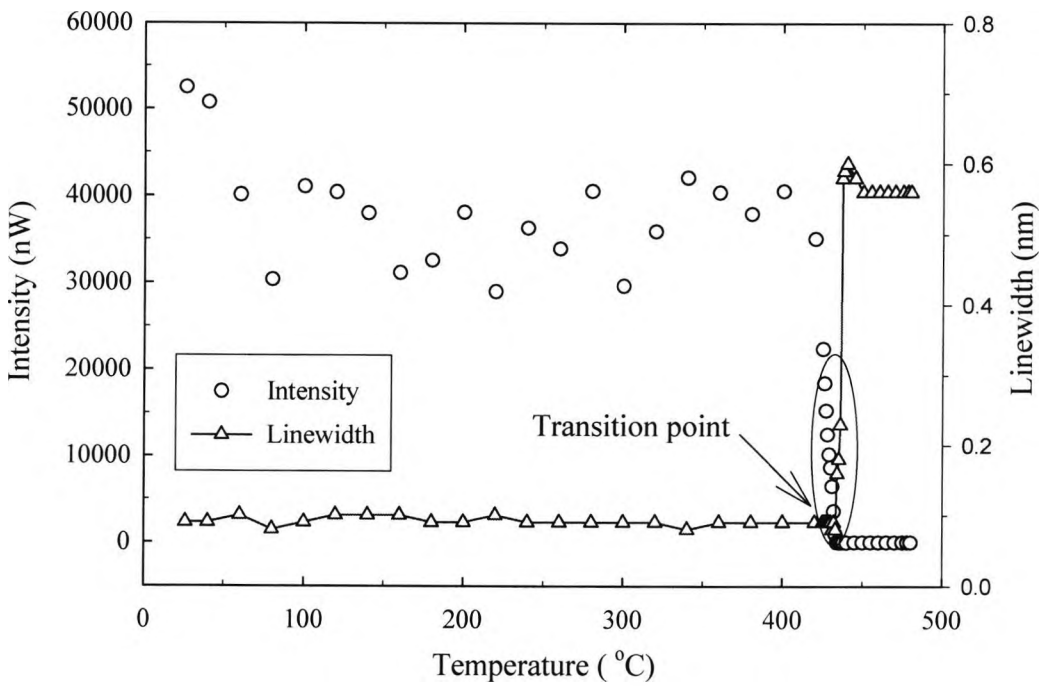

Fig. 5.10: Intensity and linewidth variation of the sensor (zero-strain on chirped grating) with different temperatures from room temperature to 480 °C, with a fixed pump power of 52 mW.

The laser intensity value drops sharply with increasing temperature, beyond a temperature of approximately 425 °C, at which the wavelength of the type IIA Bragg grating was found to be lying at the extreme edge of the chirped grating wavelength width when the chirped grating was left unstrained. Beyond this, a viable laser cavity no longer exists and the laser action was seen to be gradually disappearing. At temperatures beyond 440 °C, the device simply became a passive grating-based sensor with a significantly lower value of the output intensity, which then remained constant up to a temperature of 480 °C, where the linewidth (~ 0.56 nm) of the

passive sensor became much wider than the laser linewidth (~ 0.10 nm) observed before, showing that laser action had ceased. As the measurement was a wavelength-encoded measurement, the relative amplitude fluctuation of the laser does not create a problem for most practical sensor applications.

5.8.3. Calibration of the sensor

The change of the laser wavelength (under zero-strain on the chirped grating) with ascending and descending temperatures is shown in Fig. 5.11 over the range from room temperature to 440 °C.

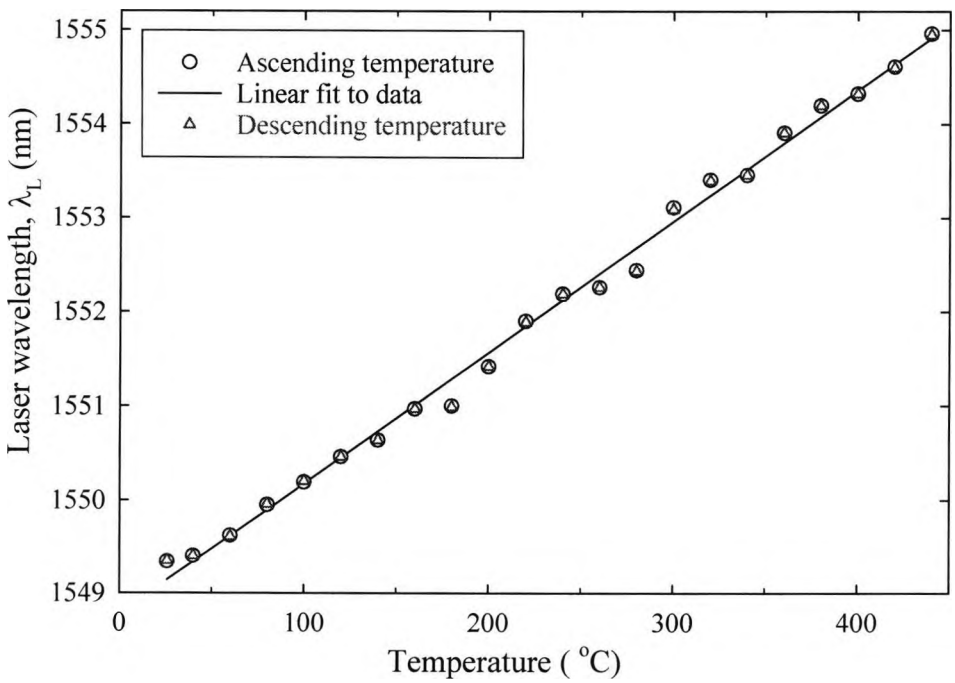

Fig. 5.11: Calibration of the laser sensor (zero-strain on the chirped grating) with ascending and descending temperatures over the range from room temperature to 440 °C.

The thermal sensitivity of the laser wavelength (λ_L) was calculated using both linear and nonlinear polynomial regression fittings to the measured data.

For a linear fitting:

$$\lambda_L(T) = 1548.779 + 0.01394T, \tag{5.3}$$

For a 2nd order polynomial fitting:

$$\lambda_L(T) = 1548.915 + 1.225\times10^{-2}T + 3.659\times10^{-6}T^2, \tag{5.4}$$

For a 3rd order polynomial fitting:

$$\lambda_L(T) = 1549.088 + 8.322\times10^{-3}T + 2.425\times10^{-5}T^2 - 2.962\times10^{-9}T^3, \tag{5.5}$$

where λ_L is the laser wavelength and T is the applied temperature in degrees Celsius of the type IIA Bragg grating – the sensing grating, RB_1. Comparison of the sensor calibration data using both linear and nonlinear polynomial regression fittings are given in Table 5.1.

Table 5.1: Calibration of the laser sensor with zero-strain on the chirped grating over the range from 26 °C to 440 °C.

Parameters		Linear fitting	2nd order polynomial fitting	3rd order polynomial fitting	Unit used
Temperature range		26 – 440	26 – 440	26 – 440	°C
Sensitivity	26 °C 440 °C	13.94 13.94	12.4 13.91	8.93 13.26	pm/°C
Coefficient of determination (COD)		0.9951	0.9959	0.9967	-
Standard deviation (SD)		0.129	0.1204	0.1131	-
Root mean square error (RMSE)		0.123	0.113	0.102	Nm
RMSE	26 °C 440 °C	8.85 8.85	9.08 8.10	11.45 7.73	°C

The linear sensitivity of the laser was found to be 13.94 pm/°C with a root mean square error (RMSE) of 0.123 nm in wavelength or equivalent to 8.85 °C in temperature. The nonlinear (3^{rd} order) polynomial fitting shows almost the same level of RMSE with temperature-dependent sensitivity of 8.93 pm/°C and 13.26 pm/°C at 26 °C and 440 °C respectively.

The laser sensor performance was consistent over several cycles of ascending and descending temperatures, within which the laser wavelength was found to be repeatable to within ± 0.01 nm. The repeatability of the sensor data at each temperature were calculated from the maximum deviation of the sensor data over the ascending and descending temperatures from room temperature to 440 °C using the OSA with a RBW of 0.1 nm. The dominant centre wavelength of the laser was used to measure the sensor wavelength. Negligible hysteresis of the sensor was observed over several repeatable cycles of measurement.

5.9. Experimental results with strain on chirped grating

5.9.1. Effect of strain on the chirped grating

The experimental set-up of the sensor is shown in Fig. 5.8, where both ends of the chirped grating were fixed with adhesive to allow different values of strain to be applied to it. As mentioned earlier, prior to the experiment the chirped grating was annealed at 100 °C for 11 hours to stabilise the grating performance. The strain was applied to the chirped grating (RB_2) by moving the micrometer driven translation stage in steps of 50 μm. The strain-induced effect on the chirped grating was monitored using the OSA with a RBW of 0.1 nm and this is shown in Fig. 5.12, at room temperature, for different applied strain values of 0, 1000 and 2200 με respectively. Any strain applied to an FBG, whether normal or chirped, will change its response by affecting the period of the grating (Λ), coupled with the change in the fibre effective refractive index due to the photoelastic effect, as is seen in Eq. (5.2). A clear shift in the wavelength of the chirped grating was found with different strain values whereas the FWHM bandwidth (~ 5.9 nm) of the grating remains unchanged.

This was investigated as potentially it could be used to extend the operating range of the tuneable laser, but as discussed later, it is not really a practical solution for situations outside the laboratory where a compact laser probe system is required.

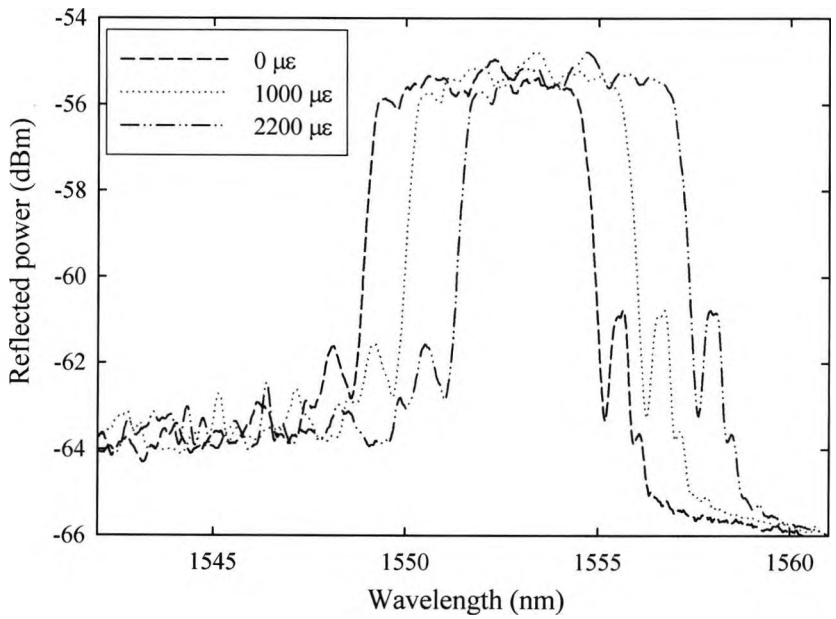

Fig. 5.12: Reflection spectra of the chirped grating at room temperature for different applied strain values of 0, 1000 and 2200 με respectively.

This approach offers one possible way to shift the Bragg wavelength of the chirped grating and thus the laser operational range. When a strain of 1000 με was applied to the chirped grating, the total wavelength shift of the grating was found to be ~ 1.10 nm, with a strain sensitivity of 1.1 pm/με in the 1550 nm band. The 1.10 nm wavelength shift of the chirped grating allows the operational range of the laser sensor to be tuneable between ~ 78 °C and 500 °C (considering the linear thermal sensitivity of the laser of 13.94 pm/ °C) compared with that of the unstrained chirped grating. However with a further increase in the strain value of 2200 με, the wavelength shift of the chirped grating was found to be ~ 2.44 nm, thus potentially shifting the operational range of the laser-based sensor by a further ~ 100 °C. However, such a high value of strain (2200 με), when applied to the chirped grating would lead to a strong possibility of regular breaking of the fibre. Thus for practical applications, this

issue and the fact that the estimated temperature also exceeds the upper limit of the annealing temperature used (~ 525 °C) of the type IIA Bragg grating, limits the use of this technique during normal operational use. Overall, there is little advantage in this approach and the best way to extend the laser operational range is through the use of a broader wavelength chirped grating, which will be investigated in Chapter 6.

5.9.2. Output spectra

Fig. 5.13 shows the output spectra of the sensor at a fixed temperature of 23 °C with different values of applied strain of 0, 550, 600 and 1000 με respectively, with the same fixed pump power of 52 mW. As the wavelength of the normal type IIA Bragg grating was found to be close at the "edge" of the chirped grating under zero strain at this temperature, it requires relatively a small strain value of 600 με to cause the laser action to cease as the cavity resonators conditions are not then met.

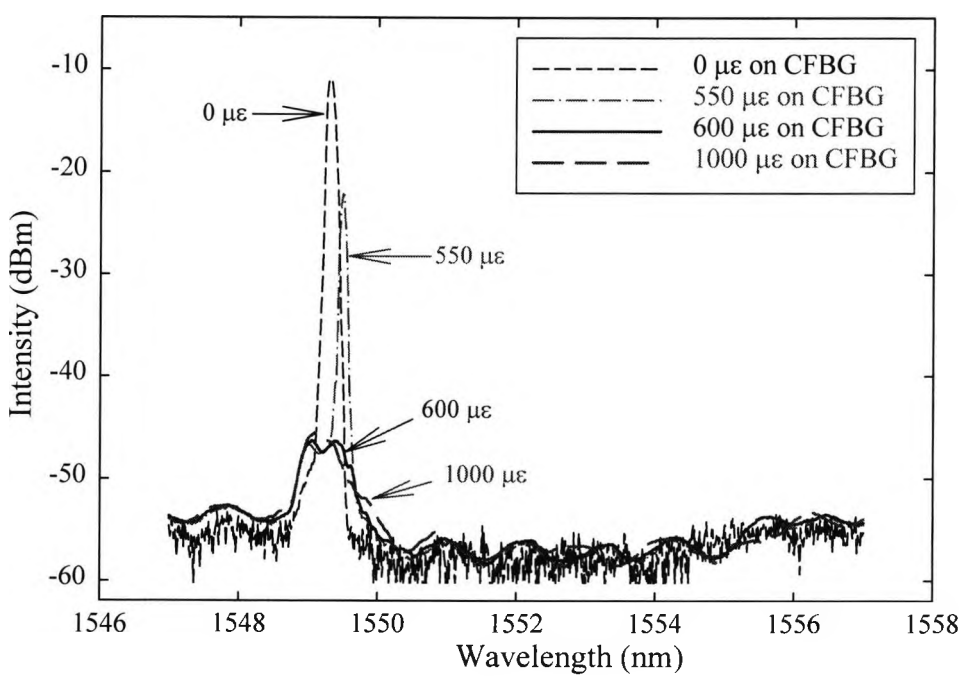

Fig. 5.13: Output spectra of the sensor with different values of applied strain to the chirped grating at a fixed temperature of 23 °C, and with a fixed pump power of 52 mW.

When different strain values were applied to the chirped grating, the spectrum of the chirped grating was seen to shift towards the longer wavelength side with the increased applied strain. However, the wavelength of the type IIA Bragg grating remains the same, and the laser action of the sensor were eventually disappears with increased applied strain. At a strain value of 550 με, the signal to noise ratio (SNR) of the laser drops to ~ 30 dB from that of 41 dB under zero-strain. At a strain value of 600 με, the linewidth of the sensor became significantly larger (~ 0.78 nm) indicating that the laser action ceases with a significant decrease in the SNR value to ~ 6 dB. With further increase in the applied strain value to 1000 με, the wavelength of the type IIA Bragg grating remained unchanged but the spectrum shifted slightly towards the longer wavelength side.

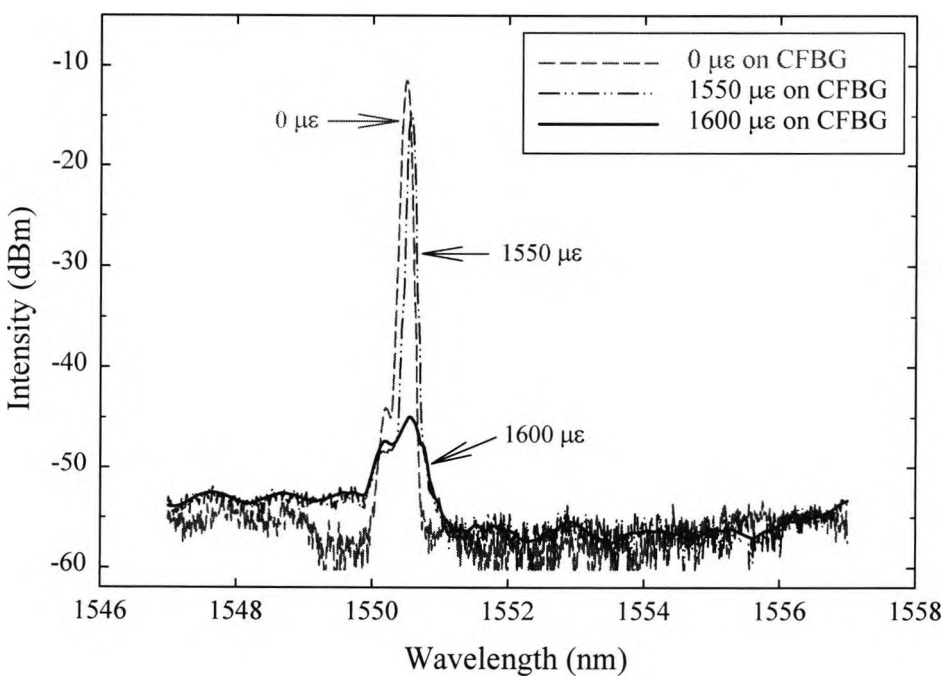

Fig. 5.14: Output spectra of the sensor with different values of applied strain to the chirped grating at a fixed temperature of 120 °C, and with a fixed pump power of 52 mW.

Fig. 5.14 shows the output spectra of the sensor at a fixed temperature of 120 °C with different values of applied strain of 0, 1550 and 1600 με respectively; with the same level of the fixed pump power of 1480 nm LD. At this temperature, the type IIA Bragg grating was found to be around 1.5 nm from the edge of the chirped grating. This situation requires a relatively higher value of strain of 1600 με to allow the laser action to cease totally. At the same time, the linewidth of the sensor became significantly broader to indicate that the laser action ceases with a lower value of SNR as before. This property may be used for switching applications, tailored by the signal intensity requirement.

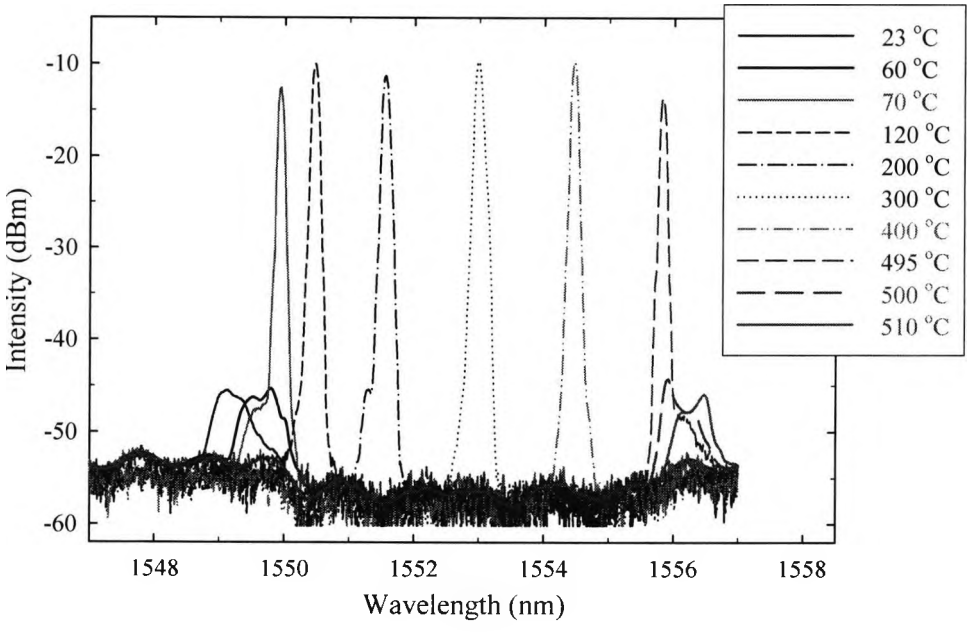

Fig. 5.15: Output spectra of the sensor (with 1000 με on the chirped grating) with different temperatures over the range from 23 °C to 510 °C, with a fixed pump power of 52 mW.

When 1000 με of strain is applied to the chirped grating, the wavelength shift of the grating was found to be 1.10 nm towards the longer wavelength side, which offers an extended tuneable-temperature range of the laser from 78 °C to 500 °C. Fig. 5.15 shows the performance of the sensor with different temperatures from 23 °C to 510 °C under a fixed value of applied strain of 1000 με on the chirped grating. From the

above figure, it is clear that the laser performance was tuneable from 70 °C to 500 °C. Outside this temperature range, the sensor simply became the passive sensor with a significant decrease in the signal-to-noise ratio (SNR) as before and at the same time showing a broadening of the linewidth of the sensor. As the type IIA grating was annealed at 525 °C, the temperature was increased only to 510 °C in this experiment.

5.9.3. Laser intensity and linewidth

Fig. 5.16 shows the intensity and the linewidth variation of the sensor over the range from 23 °C to 510 °C, when the chirped grating was held at ambient temperature under a fixed strain of 1000 με. The significant increase in the output power along with a narrow linewidth in the signal was observed, when the passive sensor turns into an active sensor, at a temperature of 70 °C.

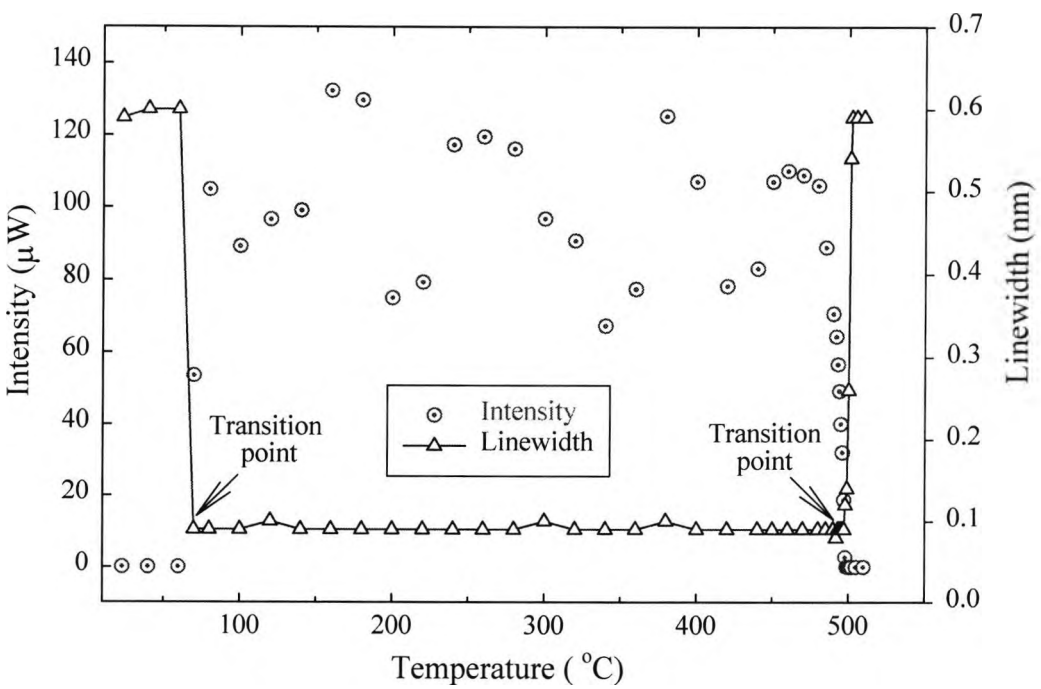

Fig. 5.16: Intensity and linewidth variation of the sensor (with 1000 με on the chirped grating) with different temperatures over the range from 23 °C to 510 °C, with a fixed pump power of 52 mW.

With increasing temperatures from 70 °C to 500 °C, the device acts as an active sensor keeping the narrow linewidth (~ 0.10 nm) of the signal and showing a larger value of the SNR. The fluctuation in the output signal of the laser arises from the same reasons as were described earlier in Section 5.8.2 when the chirped grating was left unstrained. Above the temperature of 500 °C, the significant decrease in the output power along with an increase in the linewidth of the signal was observed for the same fixed pump power of 52 mW, as before, showing that the laser action ceases. The transition points of the sensor were observed to be at 70 °C and at 500 °C, as below and above these temperatures, the sensor simply became the passive sensor with a fixed strain of 1000 με applied to the chirped grating.

5.9.4. Calibration of the sensor

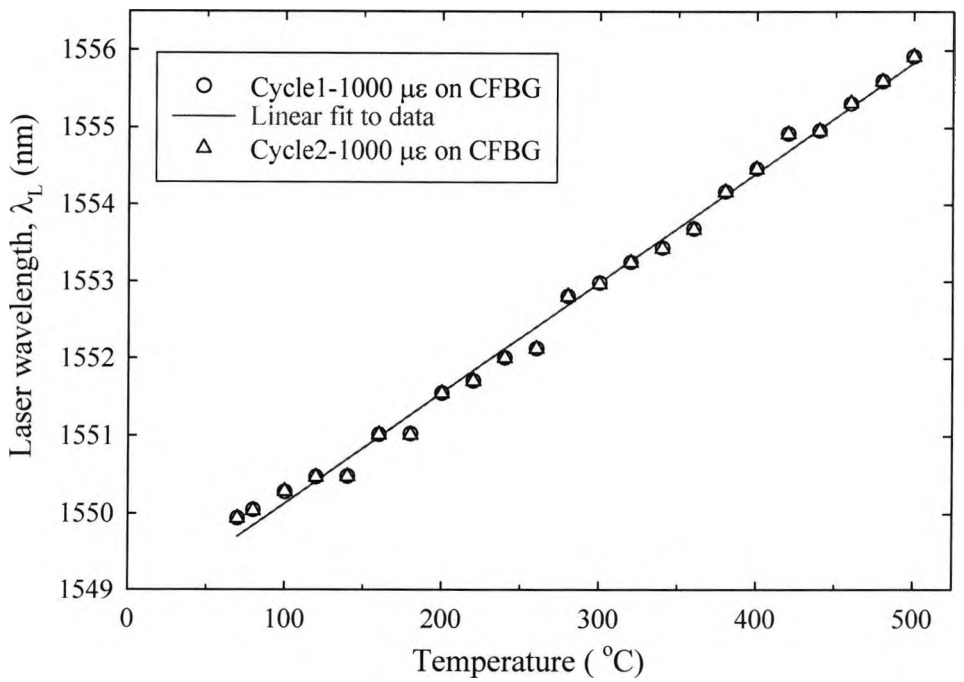

Fig. 5.17: Calibration of the laser sensor (with a fixed strain of 1000 με on the chirped grating) with repeatable cycles of measurement over the range from 70 °C to 500 °C.

The response of the laser wavelength (with fixed strain of 1000 με on the chirped grating) with temperature is shown in Fig. 5.17 over the range from 70°C to 500 °C. The thermal sensitivity of the laser wavelength (λ_L) was calculated using both linear and nonlinear polynomial regressions fitting and detailed results are given in Table 5.2.

For a linear fitting:

$$\lambda_L(T) = 1548.704 + 0.01426T\,, \tag{5.6}$$

Using a 2nd order polynomial fitting:

$$\lambda_L(T) = 1549.037 + 1.123\times10^{-2}T + 5.395\times10^{-6}T^2\,, \tag{5.7}$$

Using a 3rd order polynomial fitting:

$$\lambda_L(T) = 1549.487 + 4.434\times10^{-3}T + 3.297\times10^{-5}T^2 - 3.251\times10^{-8}T^3\,, \tag{5.8}$$

Table 5.2: Calibration of the laser sensor with an applied strain of 1000 με on the chirped grating over the range from 70 °C to 500 °C.

Parameters		Linear fitting	2nd order polynomial fitting	3rd order polynomial fitting	Unit used
Temperature range		70 – 500	70 – 500	70 – 500	°C
Sensitivity	70 °C 500 °C	14.26 14.26	11.61 13.93	6.58 12.79	pm/°C
Coefficient of determination (COD)		0.9944	0.9963	0.9972	-
Standard deviation (SD)		0.1479	0.1228	0.1099	-
Root mean square error (RMSE)		0.141	0.115	0.0999	Nm
RMSE	70 °C 500 °C	9.92 9.92	9.907 8.257	15.177 7.809	°C

The linear thermal sensitivity was found to be 14.26 pm/°C with a root mean square error (RMSE) of 0.141 nm in wavelength, or equivalent to 9.9 °C in temperature. The nonlinear (3^{rd} order) polynomial fitting showed almost the same level of error with temperature dependent sensitivity of 6.58 pm/°C and 12.79 pm/°C at 70 °C and 500 °C respectively. This relatively higher value in RMSEs arises from the wider bandwidth (~ 0.64 nm) of the normal type IIA Bragg grating (RB_1) used – the sensing element of the sensor. However, the error in the measurement could be reduced further using a type IIA Bragg grating with a narrower linewidth (the reflectivity of the grating would not be fully saturated during the fabrication) than that of the present grating used.

5.10. Summary

A simple but effective technique using a laser-based sensor configuration has shown a wider temperature measurement capability over the range from room temperature to 500 °C (maximum), when different strain values were applied to the chirped grating. A type IIA Bragg grating was chosen as the sensing element because of its high temperature sustainability (the reflectivity remained at ~ 96 %) after annealing at 525 °C, whereas the type I Bragg grating showed a significant decay in its reflectivity (<55 %) after annealing at 500 °C for the same period. As a result, the type I Bragg grating showed a significant limitation for high temperature laser-based sensor applications.

With the optimum choice of the Bragg wavelength of the type IIA Bragg grating (RB_1), the temperature measurement range of the laser was extended (from that reported in Chapter 4) to 440 °C employing almost the same FWHM bandwidth (< 6 nm) of the chirped grating (RB_2) as the second reflectors in the laser cavity. An extended tuneable laser based sensor performance was studied over the range from 70 °C to 500 °C, when a fixed strain value of 1000 με was applied to the chirped grating, which was kept at an ambient temperature.

The performance of the active sensor was compared with that of a passive sensor system under the same experimental conditions. The laser-based approach offers, through the optical configuration in the system, all the normal advantages of the use of FBGs in sensor applications, with the very significant benefit, in addition, of a higher signal-to-noise ratio (SNR). Two gratings are required in the active device compared to that of one grating in the passive device. Currently, the fabrication costs of gratings are relatively low. The only additional cost is the pump source, which is required to excite the Er^{3+}-ion into the upper laser level. Any fluorescence-based sensor devices require external pump source to generate the fluorescence from the rare-earth dopant, as is used by Imai and Hokazono [1997]. However, the narrower bandwidth of the laser-based sensor system potentially enhances the multiplexing capability of the system. A greater number of Bragg gratings could be used over the wider 'chirp' of the grating in the laser configuration compared to that of the passive configuration. Thus, this is an *alternative* sensor strategy, which will complement the use of the passive FBG approach, especially when high signal levels are required.

Also with a sufficient length of high Ge-Er co-doped fibre, the laser can be configured in a single piece of fibre utilising the fluorescence property of the Er^{3+}-ion as the gain medium and the fibre Bragg gratings (FBGs) as cavity feedback elements. This also avoids the additional splicing loss between the FBGs and the gain medium. In this way, the modal mismatching of the fibre core can be eliminated, which will reduce the overall system loss.

The highly repeatable performance of the laser was achieved due to the stabilising effect of both the gratings and the stable pump source used. The linear sensitivity of the laser was found to be ~ 14.1 pm/°C, on average, with a RMSE of 9.4 °C, over the wider measurement range from room temperature to 500 °C (maximum). Also, talking about the thermal non-linearity for the sensor calibration, the RMSE was found to be almost in the same range as that of the linear calibration. So to simplify the signal-processing unit of the system, it is easier to calibrate the sensitivity of the laser using a simple linear fitting. This relatively larger error in the system mainly arises from the wider bandwidth (~ 0.64 nm) of the type IIA Bragg grating used as the sensing element of the system. On the other hand, the use of a narrower bandwidth

(~ 0.21 nm) type I Bragg grating as the sensing element of the laser system showed an improvement in the error analysis with the nonlinear regression fitting compared to that of the linear fitting, over the range from room temperature to 300 °C, as shown in Chapter 4.

The characteristics of the sensor were studied in terms of its wavelength response, the signal intensity and the linewidth variation, further exploiting the characteristics with temperature beyond the point where the laser performance ceases totally. The extended tuneable operational range of the laser was also studied by applying a high level of strain to the chirped grating in the laser configuration. The sensor system thus created is repeatable in its wavelength performance, and relatively inexpensive to fabricate. The error value of the active sensor device could be further improved by reducing the bandwidth of the type IIA Bragg grating (RB_1), as discussed earlier, which will select the laser wavelength more precisely. The practical applications of these devices include temperature monitoring in composites and various industrial applications involving fire alarm systems, aero-engine temperature studies; laser-based devices could be applied to any of these fields, as reviewed by a number of authors, e.g. Grattan and Sun [2002].

5.11. References

- Du, W.C., Tao, X.M., and Tam, H.Y. (1999) Fiber Bragg grating cavity sensor for simultaneous measurement of strain and temperature, *IEEE Photon. Technol. Lett.*, vol. 11, pp. 105-107.
- Duservire, E. and Simpson, J.R. (1990) Evaluation of $^4I_{15/2}$ and $^4I_{13/2}$ Stark-level energies in erbium-doped aluminisilicate glass fibers, *Opt. Lett.*, vol. 15, pp. 547-549.
- Grattan, K.T.V. and Sun, T. (2002) Optical-fiber sensors: temperature and pressure sensors, *MRS Bull.*, vol. 27, pp. 389 – 395.
- Imai, Y. and Hokazono, T. (1997) Fluorescence-based temperature sensing using erbium-doped optical fibers with 1.48 μm pumping, *Opt. Rev.*, vol. 4, pp. 117-120.
- Kersey, A.D. and Morey, W.W. (1993) Multiplexed Bragg grating fibre-laser strain-sensor system with mode-locked interrogation, *Electron. Lett.*, vol.29, pp.112-114.
- Kim, B.Y. (1998) *Fiber lasers in optical sensors, in Optical Fiber Sensor Technology*, vol.2, Grattan, K.T.V. and Meggitt, B.T., Eds. London: Chapman & Hall, pp. 99-115.
- Mandal, J., Pal, S., Sun, T., Grattan, K.T.V., Augousti, A.T. and Wade, S.A. (2004) Bragg grating-based fiber-optic laser probe for temperature sensing, *IEEE Photon. Technol. Lett.*, vol. 16, pp. 218-220.
- Mandal, J., Pal, S., Sun, T., Grattan, K.T.V. and Augousti, A.T. (2003) Optimization of erbium-doped fibre lasers and their sensor applications, *in Proc. Sensors and their Applications XII Conf.* (Institute of Physics Publishing Ltd), Limerick, Ireland, pp.271-278.
- Othonos, A. (1997) Fiber Bragg Gratings, *Rev. Sci. Instrum.*, vol. 68, pp. 4309 - 4341.
- Othonos, A. and Kalli, K. (1999) *Fiber Bragg Gratings: Fundamentals and Applications in Telecommunications and Sensing*, Artech House, Boston.
- Pal, S., Sun, T., Grattan, K.T.V., Wade, S.A., Collins, S.F., Baxter, G.W., Dussardier, B. and Monnom, G. (2004) Strain-independent temperature

measurement using a type-I and type-IIA optical fiber-Bragg grating combination, *Rev. Sci. Instrum.*, vol. 75, pp.1327-1331.

- Pal, S., Mandal, J., Sun, T., Grattan, K.T.V., Fokine, M., Carlsson, F., Fonjallaz, P.Y., Wade, S.A. and Collins, S.F. (2003) Characteristics of potential fibre Bragg grating sensor-based devices at elevated temperatures, *Meas. Sci. Technol.*, vol.14, pp.1131-1136.
- Shen, Y.H., Pal, S., Mandal, J., Sun, T., Grattan, K.T.V., Wade, S.A., Collins, S.F., Baxter, G.W., Dussardier, B. and Monnom, G. (2004) Investigation of the photosensitivity, temperature sustainability and fluorescence characteristics of several Er-doped photosensitive fibers, *Opt. Communs.*, vol. 237, pp. 301-308.

Chapter 6

Novel antimony-germanium (Sb-Ge) co-doped photosensitive fibre for high temperature and strain measurements using a fibre laser-based approach

6.1. Abstract

The work in this Chapter reports a Bragg grating based fibre laser approach to the measurement of high temperature and strain using a high reflectivity grating fabricated into a novel antimony-germanium (Sb-Ge) co-doped photosensitive fibre for sensor applications. This high temperature sustainable Sb-Ge co-doped fibre was specially fabricated in China. A normal type I Bragg grating and a chirped grating were used as the optical feedback elements and enclosed erbium (Er^{3+}) -doped fibre as the active gain medium of the laser. The type IIA chirped grating was fabricated into the boron-germanium (B-Ge) co-doped photosensitive fibre. The normal type I Bragg grating had its reflectivity of 92.6 % after being annealed at 525 °C for 11 hours. Therefore, it was used as the active element of the sensor head, in so doing forming the end reflector into the laser cavity of the system. The shift in the laser wavelength was monitored in such a system when the normal Bragg grating was temperature or strain-tuned. The resulting temperature was measured from room temperature to 500 °C and strain values of 0 to 1200 με using the laser-based system. The root mean square (RMS) error values of the active sensor system were found to be 2.6 °C and 28.3 με over the above measured ranges of temperature and strain respectively.

6.2. Introduction

Several laser-based approaches have been reported to measure strain and temperature, for example, using a mode-locked interrogation technique in the laser cavity for strain measurement [Kersey and Morey 1993], a laser-based sensor system for temperature measurement using a combination of a normal grating (type I or type IIA) and a chirped grating to form the laser cavity [Mandal *et al.* 2004a; 2004b], or using multiple Bragg gratings in a laser configuration to measure strain and temperature [Alavie *et al.* 1993]. However, in most of the laser-based sensor schemes proposed in the literature, the temperature range has normally been limited up to ~ 300 °C (and more recently 440 °C) [Mandal *et al.* 2004b]. This mainly arises from the limitations of the availability of the high temperature sustainable photosensitive fibres in which to fabricate the normal fibre Bragg gratings (FBGs) and also from the narrow bandwidth of the chirped grating used as one of the cavity reflectors, to achieve tunable laser action [Mandal *et al.* 2004b].

Recently, a system for simultaneous measurement of temperature and strain was reported [Pal *et al.* 2004a; 2004b] using the combination of fluorescence and a grating based technique over the wider range of temperature from room temperature to 600 °C and strain values of 0-2000 με. The specially fabricated antimony-erbium-germanium (Sb-Er-Ge) co-doped silica fibre had GeO_2 ~ 15 wt. %, SbO_2 of ~ 5000 ppm and ErO_2 of 500 ppm. The fluorescence was generated from the Er^{3+}-ions dopant into the fibre core and a normal Bragg grating was written into a 10 cm length of the Sb-Er-Ge fibre. The Bragg wavelength of the grating is a function of both the temperature and the strain variations. The amplified spontaneous emission (ASE) fluorescence intensity occurring at two peaks around the wavelengths of 1535 nm and 1552 nm, which are insensitive to strain variation but temperature-dependent. For the measurement of both parameters, the sample was placed in an oven with both ends of it was fixed to two-micrometer driven stages (with one end being fixed and the other end is variable). The ASE power of the sample was generated using a 980 nm pump source and the output was measured using the Optical Spectrum Analyser (OSA). The intensities of two peaks at 1535 nm and 1552 nm were observed at different

temperatures to estimate the fluorescence-peak-power-ratio (FPPR) for the temperature determination. The fluorescence peak wavelengths were found to be unchanged with the temperature variations but the fluorescence peak power ratio (1535nm/1552nm) was found to decrease continuously with the increase in temperature. This again limits the signal strength for high temperature sensing applications. A shift of the "dip" in the fluorescence spectrum due to the Bragg wavelength was observed with temperature variations, thus the temperature-induced shift in the Bragg wavelength could be calibrated. This temperature-induced shift in the Bragg wavelength could be subtracted from the overall Bragg wavelength shift to find the strain-induced wavelength shift in the sensor-system.

In this Chapter, a Bragg grating-based fibre laser sensor system was developed to measure independently both a wider range of temperature from room temperature to 500 °C and strain values from 0-1200 με, respectively. The laser based sensor system employs a similar approach to previous work [in Chapters 4, 5] to form the laser cavity but incorporating a novel high temperature sustaining normal type I Bragg grating (RB_1) as the sensor head in the system to measure the temperature as high as 500 °C. Also the active sensor approach was extended for strain measurement applications. Thus, the normal grating was measurand-tuned for the determination of both the above parameters. The type IIA chirped grating (RB_2) with a broader bandwidth (~10.80 nm) was used to form the second reflector in the laser cavity to achieve the tuneable laser action over the wider measurand range.

6.3. Theoretical Background

The cavity resonance condition of a laser-based system is defined as below [Wilson and Hawkes 1987]:

$$\lambda_L = \frac{2nL_c}{m}, \tag{6.1}$$

where λ_L is the resonant laser wavelength, n is the refractive index of the gain medium, L_c is the laser cavity length and m is a positive integer. For an Er^{3+} fibre length of ~ 96 cm, the cavity mode spacing was determined to be 108 MHz (with n =

1.45 for silica fibre). Therefore, many longitudinal modes of the laser are possible within the resonant cavity, but only those longitudinal modes having sufficient gain will oscillate.

The changes in the laser cavity length (ΔL_c) with the changes in the resonant laser wavelength ($\Delta\lambda_L$), with temperature or strain can be expressed as below:

$$\Delta L_c = \frac{m\Delta\lambda_L}{2n}, \tag{6.2}$$

The changes in the laser wavelength reflect the changes in the Bragg wavelength of the normal grating, due to the measurand perturbations (arising from temperature or strain changes) over the range of the chirped grating, which is employed as the second reflector in the laser cavity.

6.4. Detail of Sb-Ge co-doped fibres

The novel Antimony-Germanium (Sb-Ge) co-doped silica fibre used was specially fabricated in China, using a modified chemical vapour deposition (MCVD) technique. The fibre consists of GeO_2 ~ 12 wt. % and SbO_2 of ~ 5000 ppm in a silica glass host. The single mode fibre (SMF) had a cladding diameter of 125 μm, core diameter of 5 μm, numerical aperture (*NA*) of 0.18 and cut-off wavelength of 1.2 μm. The Sb^{3+} ion was introduced into the fibre core because of its large cation size (76 pm) to obtain the high temperature sustainability of the gratings written into these types of fibres, at elevated temperatures [Shen *et al.* 2004]. The germanium-oxide (GeO_2) was included in the fibre to raise the refractive index of the fibre core and also to enhance the photosensitivity of the fibre for efficient inscription of the desired gratings.

6.5. Grating Fabrication

6.5.1. Normal Grating

The normal grating was fabricated in an Sb-Ge co-doped fibre using a KrF excimer laser as the ultra violet (UV) source with a laser energy of 12 mJ and repetition

frequency of 200 Hz, and using a uniform phase mask technique (details are given Chapter 4). It took nearly 19 minutes of exposure to achieve a maximum reflectivity of ~ 99.20 % with a Bragg wavelength of 1536.62 nm, with grating length of ~ 6.5 mm and a refractive index (RI) modulation of 3.26×10^{-4}. The growth behaviour of the normal type I Bragg grating in terms of its reflectivity and Bragg wavelength variation with UV exposure time is shown in Fig. 6.1.

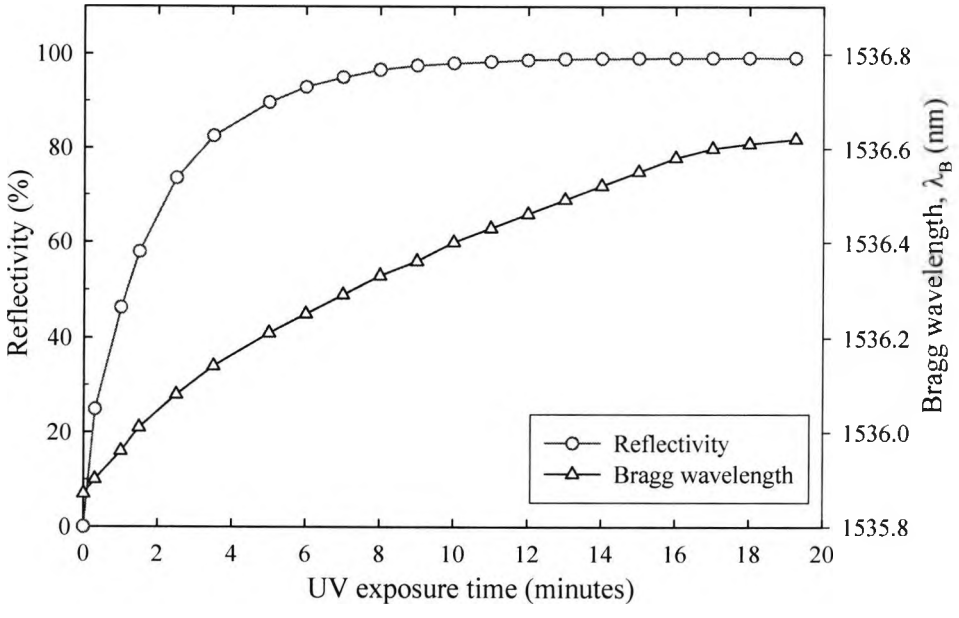

Fig. 6.1: Growth behaviour of the normal type I grating in terms of its reflectivity and Bragg wavelength variation as a function of UV exposure time.

The figure clearly shows that the initial growth of the reflectivity of the grating was much faster (within 5 minutes of exposure the grating achieved reflectivity of ~ 90 %), followed by a substantial and slower increase in the reflectivity values and finally reaching saturation. After saturation, when the sample was over exposed for 1 more minute, there was a very little decrease in its reflectivity (from 99.22 % to 99.20 %) was observed, showing that the grating had finally saturated. The Bragg wavelength was always observed to shift towards the red side of the spectrum with almost linear growth and finally it is stabilised, with its reflectivity. The transmission spectrum of the grating was monitored online during the fabrication using an Optical Spectrum

Analyser (OSA, model: HP86140A). Fig. 6.2 shows the growth of the refractive index modulation and the effective refractive index of the grating with UV exposure time. Initially the value of the refractive index modulation increases almost linearly, along with a faster increase in the reflectivity, followed by a relatively slower trend where the grating growth was slower. Finally saturation was observed, achieved with a maximum refractive index modulation of 3.26×10^{-4}, corresponding to a reflectivity of 99.20 %. The effective refractive index of the fibre grows almost linearly with the same trend as that of the Bragg wavelength, and then is stabilised achieving a value of 1.4483.

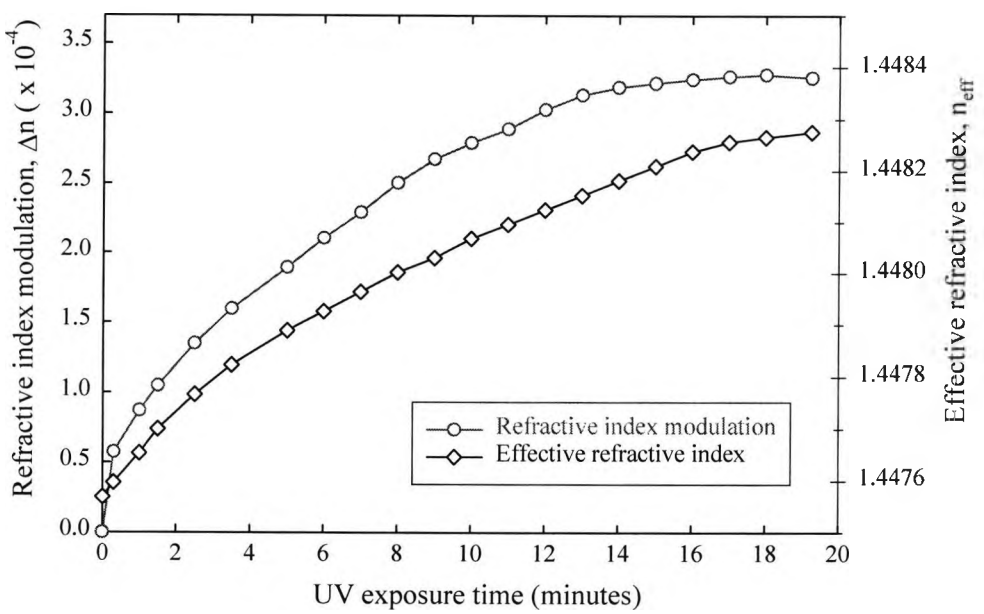

Fig. 6.2: Growth of the refractive index modulation and the effective refractive index of the normal type I Bragg grating as a function of UV exposure time.

6.5.2. Chirped Grating

The wavelength of the chirped fibre Bragg grating (CFBG) was expressed as below [Othonos and Kalli 1999]:

$$\lambda_B(z) = 2n_{eff}(z)\Lambda(z), \tag{6.3}$$

where $\lambda_B(z)$ is the chirped grating wavelength which is a function of both period of the grating, $\Lambda(z)$, and the refractive index of the fibre core, $n_{eff}(z)$ along the fibre axis, z. The chirped grating can be fabricated by axially varying either $\Lambda(z)$ or $n_{eff}(z)$.

For a linearly chirped grating and using a chirped phase mask, the variation in the grating period is linear with the fibre axis, z, along with the constant refractive index of the fibre core, $n_{eff}(z)$. The chirped grating period, $\Lambda(z)$ can be expressed as below:

$$\Lambda(z) = \Lambda_0 + \Lambda_n(z), \tag{6.4}$$

where Λ_0 is the starting period of the grating and Λ_n is the linear slope (change) along the length of the grating. The bandwidth of the chirped grating, $\Delta\lambda_{CBW}$, can be expressed as below [Kashyap 1999]:

$$\begin{aligned} \Delta\lambda_{CBW} &= 2n_{eff}\left(\Lambda_{long} - \Lambda_{short}\right), \\ &= 2n_{eff}\Delta\Lambda_{chirp} \end{aligned} \tag{6.5}$$

where Λ_{long} and Λ_{short} are the long (end) period and the short (start) period of the chirped grating which is shown schematically in Fig. 6.3 [Kashyap 1999].

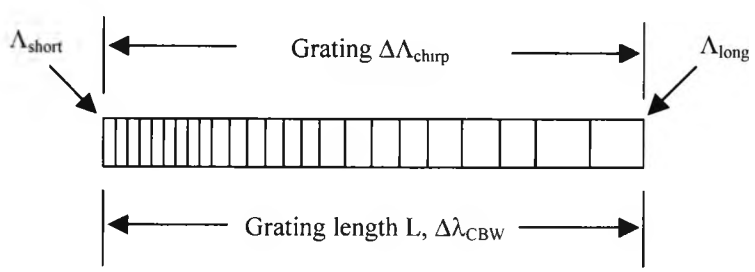

Fig. 6.3: Schematic of the chirped grating to show the long and the short period, and the bandwidth of the grating.

The reflection from a CFBG is a function of wavelength and therefore, the light entering into a longer wavelength chirped grating (increasing in period from the input end) suffers a delay ι on reflection which is approximately given as [Kashyap 1999]:

$$\iota(\lambda) = \frac{(\lambda_0 - \lambda)}{(\Delta\lambda_{chirp})}\frac{2L}{v_g}, \quad \text{for } 2n_{eff}\Lambda_{short} < \lambda < 2n_{eff}\Lambda_{long} \tag{6.6}$$

where λ_0 is the centre of the Bragg wavelength of the chirped grating, L is the chirped grating length, and v_g is the average group velocity of light into the fibre. The effect of the chirped grating is that it disperses light by introducing a maximum delay of $2L/v_g$ between the shortest and longest reflected wavelengths of the grating. This property is used to compensate for chromatic dispersion-induced broadening in optical fibre transmission systems. At 1550 nm wavelength, the group delay t in reflection is ~ 10 ns/m. Therefore, a grating of 1 m long with a bandwidth of 1 nm will have a dispersion of 10 ns/nm [Kashyap 1999].

Several approaches have been reported for the fabrication of chirped fibre Bragg gratings (CFBGs). Byron *et al.* [1993] have fabricated a CFBG that uses tapering of the length of a photosensitive fibre and a holographic exposure arrangement. For this technique to form the chirped grating, the variation in the fibre effective refractive index was created along the length of the tapered fibre. However, this method is limited by the high precision tapering capability to reproduce more than one sample. Sugden *et al.* [1994] have adopted mechanical deformation techniques to bend the photosensitive fibre, but using the same holographic exposure arrangement. Thus, the CFBG was formed by varying the grating period continuously along the length of the curved photosensitive fibre. With increasing curvature angle of the fibre, it was found that the reflectivity of the grating decreases but the full width at half maximum (FWHM) bandwidth increases. Hill and Eggleton [1994] have reported the dynamic strain gradient technique to produce a tuneable chirp with increasing spectral width, where the reflectivity of the grating was found to decrease from 95 % to 50 % with increasing fibre tension from 0 to 4.5 N. For this experiment, the uniform grating was bonded to a base with the help of adhesive and the tension was applied on one side of the grating only. Therefore, the spatial period of the grating changes along the length of the fibre according to the strain gradient and the Bragg wavelength shifts. The grating chirp is an automatic consequence of the strain gradient, which is the magnitude of the non-uniform tension drop across the grating. Therefore, the limitation in all the above techniques is the reproducibility of more than one grating with identical characteristics.

Kashyap *et al.* [1994] have used the linear and the quadratic step-chirp phase mask to produce several chirped gratings with different bandwidths. A schematic of the step-chirped grating is shown in Fig. 6.4 [Kashyap 1997].

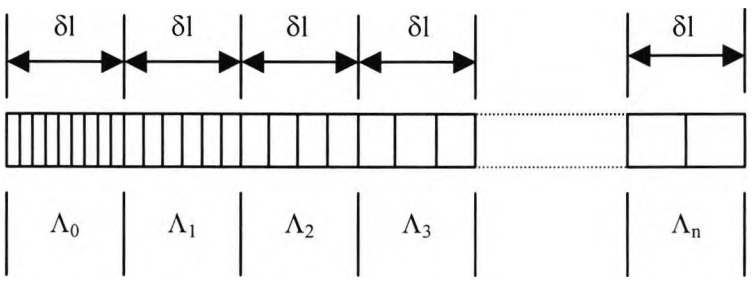

Fig. 6.4: Schematic diagram of a step chirped grating showing N number of sections with equal length of each section, δl, with a different period of Λ_n [Kashyap 1997].

The chirped grating consists of total N sections with each section having an equal length, δl, and the total length of the grating is L. The length of each section, δl, was defined as follows [Kashyap 1997]:

$$\delta l = \frac{L}{N}, \tag{6.7}$$

The total chirp, $\Delta\lambda$ is defined as follows [Kashyap 1997]:

$$\Delta\lambda = N\delta\Lambda, \tag{6.8}$$

The number of steps, $\delta\Lambda = (\Lambda_2 - \Lambda_1)$ is the difference between the grating periods.

Farries *et al.* [1994] have reported the fabrication of a chirped grating with a very broad reflection bandwidth (44 nm) with reflectivities of over 90 %, using hydrogen loaded boron-doped optical fibre, and the holographic exposure arrangements. Also a 2 nm wide transmission band pass filter was created within the broadband (44 nm) reflection spectrum of the chirped grating by placing an amplitude mask at the centre of the grating during exposure. Byron and Rourke [1995] have used a uniform period phase mask to produce a chirped grating using "stretch-and-write techniques". The hydrogen loaded boron-germanium (B-Ge) co-doped fibre was clamped using two towers, one of which was mounted on a motorised stage to apply strain to the fibre.

The laser beam was deflected through 90° using a mirror mounted on a motorised stage which allows the beam to be scanned horizontally. To produce a chirped grating, initially a grating was written at a given fibre strain, then the strain on the fibre was either increased or decreased. The writing beam was moved along to create the second grating section exactly adjacent to the first and the exposure was repeated. The bandwidth of the chirped grating was limited by the length of the phase mask and the maximum strain to which the photosensitive fibre can be subjected. The phase mask techniques offer the flexibility to produce more readily what are essentially identical characteristics for the gratings and also to reduce the system complexity for the fabrication.

The chirped grating (CFBG) used in this work was fabricated in a commercial B-Ge co-doped photosensitive fibre using UV light from an excimer laser and employing a chirped phase mask (specifications are given in Chapter 4). The beam size of the laser was fixed at 6.5 mm. The excimer laser energy of 12 mJ and the repetition frequency of 200 Hz were used to fabricate the chirped grating, where the transmission spectrum profile was monitored online using the OSA, with a resolution bandwidth (RBW) of 0.2 nm. Fig. 6.5 shows the growth behaviour of the chirped grating spectra with different UV exposure times. Interestingly, the growth behaviour of the chirped grating was found to be similar to that of the normal type IIA Bragg grating in the B-Ge co-doped fibre [Sun *et al.* 2001/2002]. The formation of the type I and type IIA chirped gratings can be explained from the two types of photosensitive effects involved in the highly germanium-doped fibre during the long exposure of UV irradiation [Riant and Haller 1997]. The formation of the type IIA grating was found only in highly stress, smaller core diameter fibres. The formation of the type IIA grating was not observed in hydrogen-loaded fibres, which shows that the hydrogen loading treatment modifies the chemical or the physical properties of the fibre, thus preventing the formation of type IIA grating.

In this work, initially the spectrum of the chirped grating grows faster, along with a positive increase in the refractive index modulation and the Bragg wavelength increases, this being defined as a type I chirped fibre Bragg grating (CFBG) within ~ 90 seconds of the UV exposure. An average reflectivity of ~ 40 % was achieved with

a spectral width of around ~ 5 nm and then it saturates, with the saturation of the refractive index modulation. With continuous exposure, the spectrum of the type I chirped grating was found to erase almost totally (showing the maximum transmission of the optical power) with a maximum decrease in the refractive index modulation, with only two distinct dips at wavelengths of 1535.40 nm and 1541.66 nm respectively, showing an average reflectivity of ~ 20 (±1) %, after a further ~ 170 seconds of exposure while at the same time advancing the formation of a new type of grating (defined as a type IIA grating).

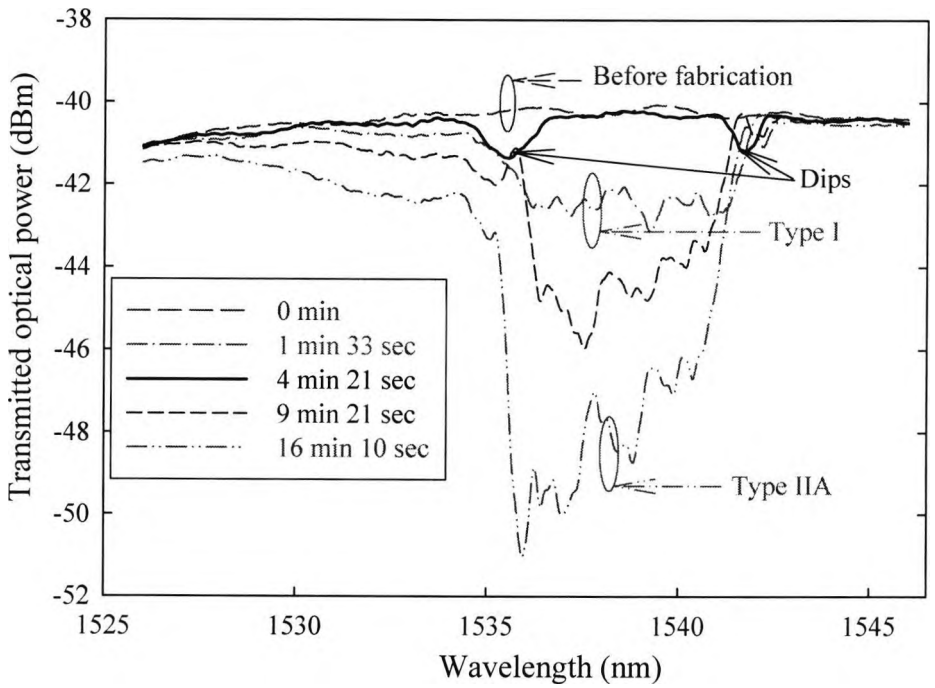

Fig. 6.5: Growth behaviour of the chirped grating spectra with different UV exposure times with laser energy of 12 mJ and repetition frequency of 200 Hz.

With further illumination, the transmission power loss (equivalent to the reflectivity) of the new chirped grating increases with again an increase in the refractive index modulation and it finally saturates achieving a maximum reflectivity of ~ 80 (± 8) % with a spectral width of ~ 6 nm, which requires a total UV exposure of ~ 16 minutes. The 2nd saturated spectrum of the CFBG results in a type IIA chirped grating. The type IIA CFBG offers both higher values of reflectivity and a wider bandwidth

compared to that of the initial type I chirped grating, which is a function of the induced refractive index modulation. During the formation of this type IIA CFBG, the wavelength shifts toward the shorter wavelength side of the spectrum compared to that of the initial type I chirped grating formation. The blue shift in the wavelength can readily be explained from the opposing effects of the boron and germanium co-dopant in the refractive index value of the fibre core. The phenomenon of both type I and type IIA chirped Bragg grating formation was found to be repeatable for one fixed alignment position of the chirped phase mask used for several samples, under the same UV exposure conditions, in the same photosensitive fibre. The formation of type IIA CFBG was observed for the first time, to our knowledge. It is believed that with better alignment of the chirped phase mask, the irregularities of the shape of the chirped grating spectrum can be reduced but the resulting grating was adequate for the laser experiments carried out.

The maximum spectral width of the chirped grating obtained was ~ 6 nm when the fibre was exposed at one fixed position of the chirped phase mask used. For a grating length of 6.5 mm and bandwidth of ~ 6 nm, the chirp rate is 0.923 nm/mm. For the present experiments, two different type IIA chirped gratings were fabricated into the B-Ge co-doped fibre using the same exposure conditions, but with different positions of the chirp phase mask, for wavelengths ranging from ~ 1535 nm to 1545 nm, achieving a wavelength overlap factor of ~ 1 nm, with a bandwidth of ~ 6 nm each, and their transmission spectra are shown in Fig. 6.6. A higher bandwidth of the chirped grating could be achieved through the full scanning of the chirped phase mask, as used by Byron and Rourke [1995].

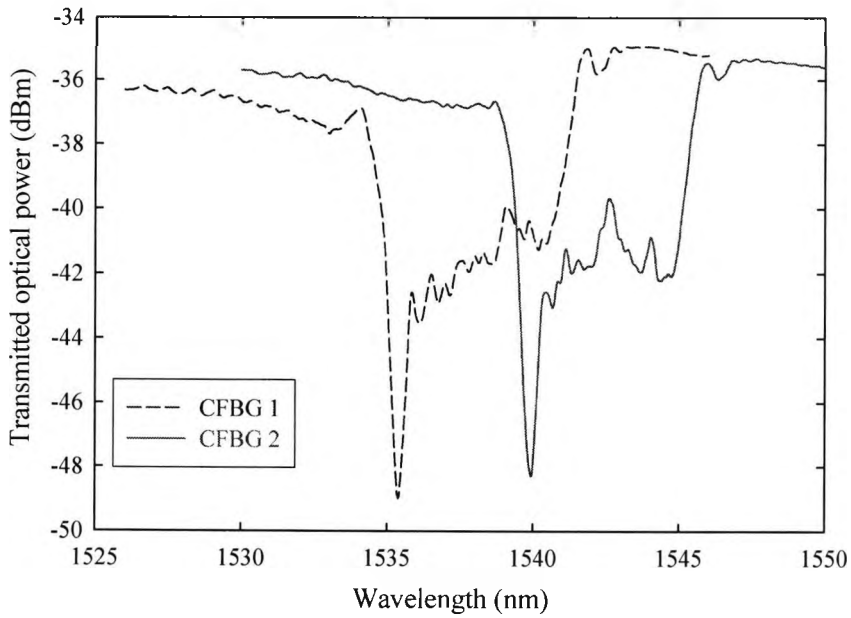

Fig. 6.6: Transmission spectra of the two different chirped gratings with wavelength ranging from ~ 1535 nm to 1545 nm with a wavelength overlap factor of ~ 1 nm.

6.6. Annealing of the normal grating

The normal type I Bragg grating was annealed at 525 °C for 11 hours to enhance the stability and the wavelength reproducibility of the grating, as it would be used as the sensing element of the system. The annealing temperature was chosen based on the data obtained from the previous long-term thermal testing of these types of gratings, as shown in Fig. 6.7 [Shen *et al.* 2004]. The gratings written in the Sb-Ge co-doped fibre (laser energy of 12 mJ and repetition frequency of 200 Hz and 300 Hz respectively) showed a better thermal stability compared to that of the grating written in the tin (Sn)-doped fibre, using the same level of the laser energy but with a frequency of 300 Hz, over the temperature range form room temperature to 950 °C. For the present experiments, a normal type I grating was fabricated using laser energy of 12 mJ and frequency of 200 Hz. To achieve a reflectivity of ~ 94 %, the annealing temperature was chosen to be 525 °C so that the temperature could be measured as high as up to 500 °C with better reproducibility of the sensor.

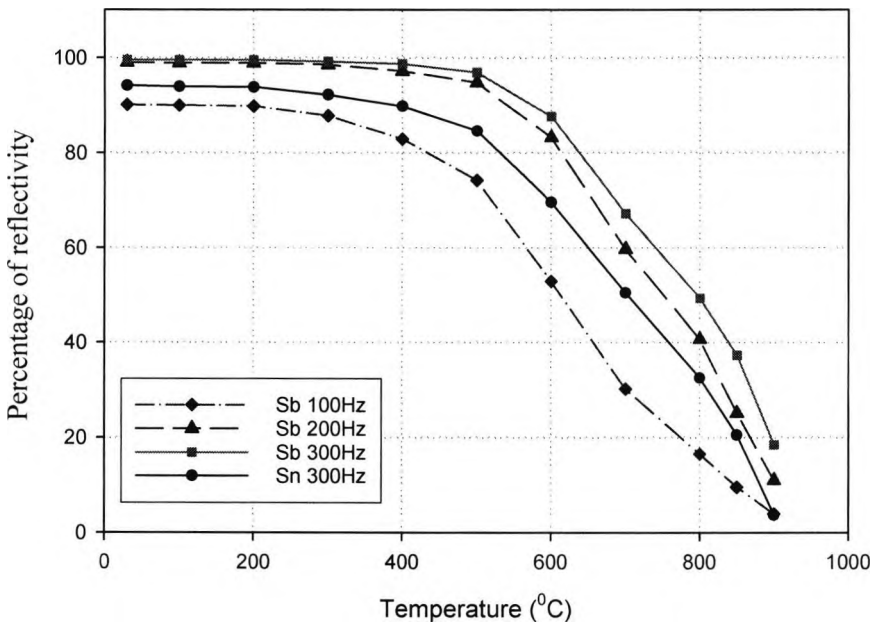

Fig. 6.7: Decay in the reflectivities of the Bragg gratings written in Sb-Ge co-doped and Sn-doped silica fibres with temperature over the range from room temperature to 950 °C [Shen *et al.* 2004].

To anneal the normal type I Bragg grating, it was placed loosely in a well-calibrated tube oven (Carbolite, MTF 12/38/400). During the annealing of the type I Bragg grating, it took nearly an hour to set the oven temperature at 525 °C from room temperature (~22 °C). As a result, the grating had already experienced an initial decay of the reflectivity from 99.2 % to 96.86 % arising from the degradation of the UV induced refractive index (RI) modulation from 3.26×10^{-4} to 2.56×10^{-4}. The decay in the RI modulation and the effective RI change of the grating during the annealing process is shown in Fig. 6.8. A faster decay in the reflectivity was observed for the first few hours, followed by a substantially slower decay, and almost no decay was observed for the last ~ 3 hours of annealing. Finally the reflectivity of the grating stabilised at 92.61 %, along with the stabilisation of the RI modulation of the grating at 2.09×10^{-4}. Additionally, a blue shift in the Bragg wavelength was observed [Pal *et al.* 2003] and it took ~ 6 - 7 hours to reach the asymptotic point of the stable value of the Bragg wavelength and finally it stabilised at a wavelength of 1543.07 nm, along with the stabilisation of the effective refractive index of the grating at 1.4544.

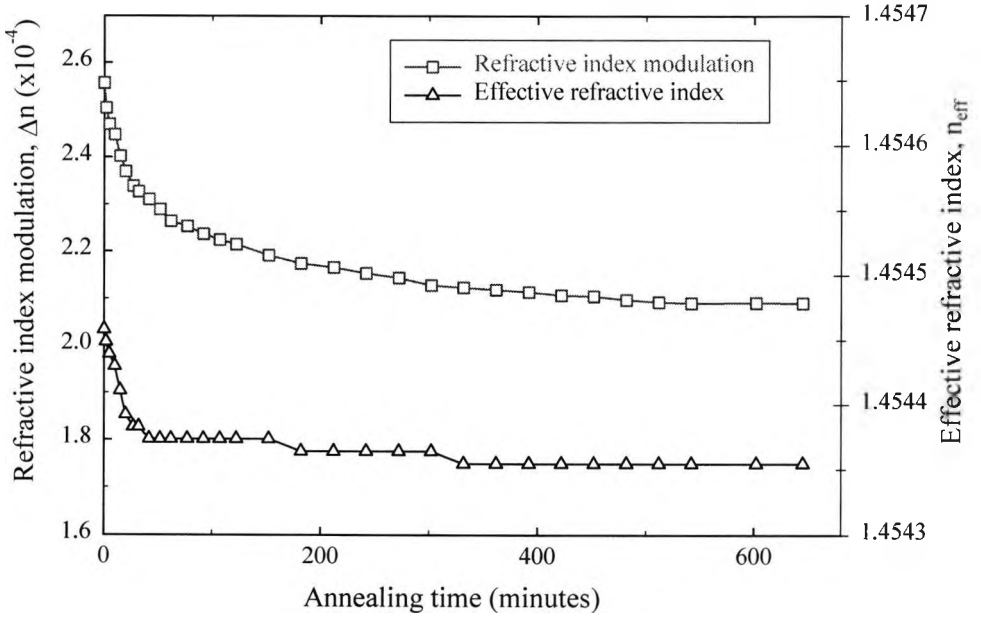

Fig. 6.8: Decay in the refractive index modulation and the effective refractive index of the normal type I Bragg grating with annealing time at temperature of 525 °C.

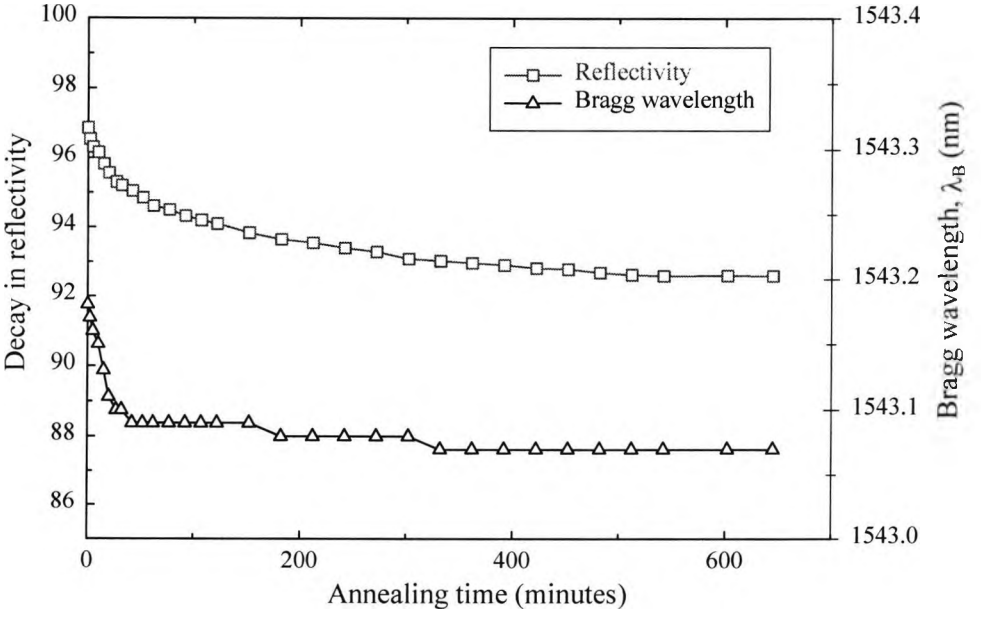

Fig. 6.9: Decay in the reflectivity and the Bragg wavelength change of the normal type I Bragg grating with annealing time at temperature of 525 °C.

Fig. 6.9 shows the decay in the reflectivity and the Bragg wavelength change during the annealing process at temperature of 525 °C. Fig. 6.9 clearly shows that the shift in the Bragg wavelength follows closely the same decay trend of the effective refractive index of the grating, as was shown in Fig. 6.8. Fig. 6.10 shows the reflection spectra of the normal type I Bragg grating both at room temperature (~ 24 °C) before and after annealing. The reflectivity was measured (after annealing) to be ~ 92.6 % with a full width at half maximum (FWHM) bandwidth of 0.23 nm at Bragg wavelength of 1536.35 nm (using the OSA with a RBW of 0.1 nm).

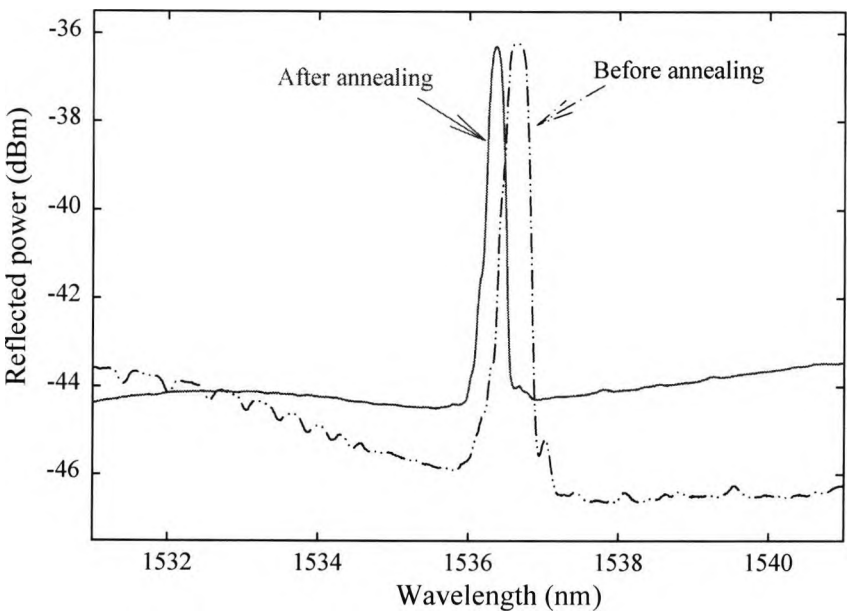

Fig. 6.10: Reflection spectra of the normal grating at room temperature (~ 24 °C) before and after annealing.

6.7. Enhancement of the chirped grating bandwidth

To enhance the total spectral width of the chirped Bragg grating, and hence to extend the active sensor measurement range, two individual type IIA chirped Bragg grating samples (shown in Fig. 6.6) were fusion-spliced together after annealing. Both the samples were annealed at 100 °C for the 11 hours, as the chirped grating would normally be used at room temperature. Fig. 6.11 shows the reflection spectra of the

chirped grating at room temperature (before and after annealing) and inset is shown the transmission spectrum of the grating after annealing. The reflectivity value was measured to be ~ 75 ± 10 %, with a FWHM bandwidth of ~ 10.80 nm, centred at ~ 1540 nm at room temperature after annealing.

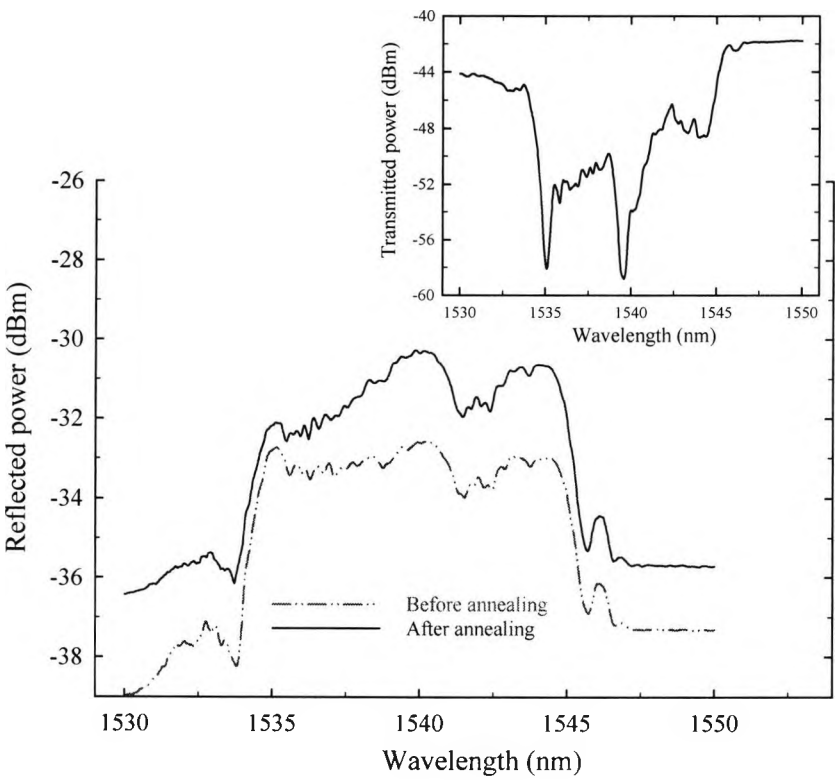

Fig. 6.11: Reflection spectra of the chirped grating at room temperature (~ 22 °C) before and after annealing (after the two samples were fusion-spliced together where the individual spectrum was shown in Fig. 6.6). Inset shows the transmission spectrum after annealing.

6.8. Experimental Arrangement

6.8.1. Laser Cavity Configuration

A thermally annealed normal type I Bragg grating (RB_1) and a chirped Bragg grating (RB_2), fabricated as described above, were fusion spliced to a commercial erbium

(Er^{3+})-doped fibre which formed the laser active medium and the experimental set-up is shown in Fig. 6.12. The Er^{3+}-doped fibre had an Er^{3+}-ion concentration of ~ 3000 ppm, a core diameter of 3.4 μm, a numerical aperture of 0.18, and a cut-off wavelength of 0.895 μm (with, in addition, germanium and aluminium oxide co-dopant), supplied by Moritex Europe Ltd., Sweden.

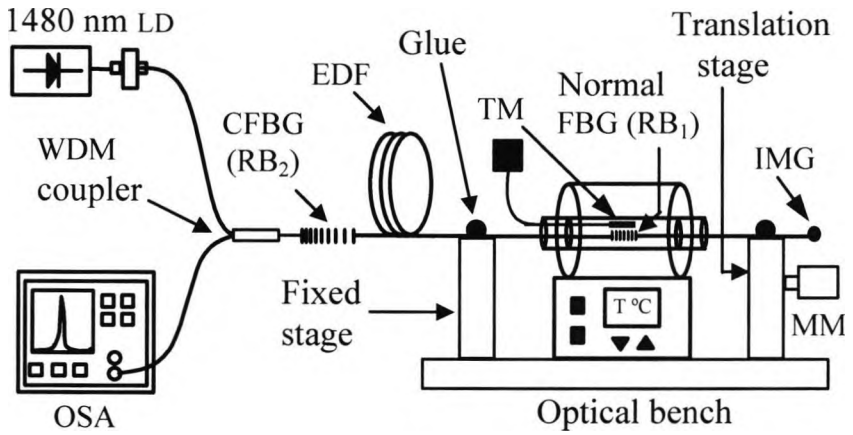

Fig. 6.12: Schematic diagram of a fibre Bragg grating-based laser system for temperature and strain measurements. CFBG: chirped fibre Bragg grating; EDF: erbium-doped fibre; TM: thermocouple metre; MM: micrometer, IMG: index matching gel.

The addition of Al_2O_3 enhances the ability of the Er^{3+} ion to dissolve in the centre of the fibre core, hence to improve the pump power efficiency of the laser and also to reduce any quenching effects that may occur [Digonnet 1993]. The sensing grating (RB_1) was placed in the centre of the tube oven with both ends of the grating fixed (with adhesive) to two-micrometer stages (with one end being fixed and the other end is variable) under zero axial strain to avoid the strain effect for temperature measurements. The chirped grating (RB_2) was kept at ambient temperature. To obtain laser oscillation, the gain medium was optically pumped by using light from a 1480 nm FBG stabilised laser diode (LD), through a 1480/1550 nm wavelength division multiplexed (WDM) coupler and the output was monitored using the OSA. Index matching gel (IMG) was used at the remote end of the normal grating to minimise the Fresnel reflection into the laser cavity.

6.9. Experimental results

6.9.1. Temperature Measurements

The following steps were undertaken to evaluate the temperature effect on the sensor performance.

6.9.1.1. Output spectra

Fig. 6.13 shows the output spectra of the laser operating at different temperatures, over the range from room temperature (~ 22 °C) to 500 °C, with a fixed pump power of 60 mW of 1480 nm. The laser wavelength measured was found to be consistent with the Bragg wavelength of the normal type I Bragg grating, owing to its spectral width being much narrower (~ 0.23 nm) than that of the chirped grating bandwidth (~10.80 nm). With increasing temperature, the laser wavelength shifted towards the longer wavelength side of the spectrum arising from the fractional change in the fibre-grating period due to the thermal expansion coefficient, along with the change in the fibre effective refractive index due to the thermo-optic coefficient effect.

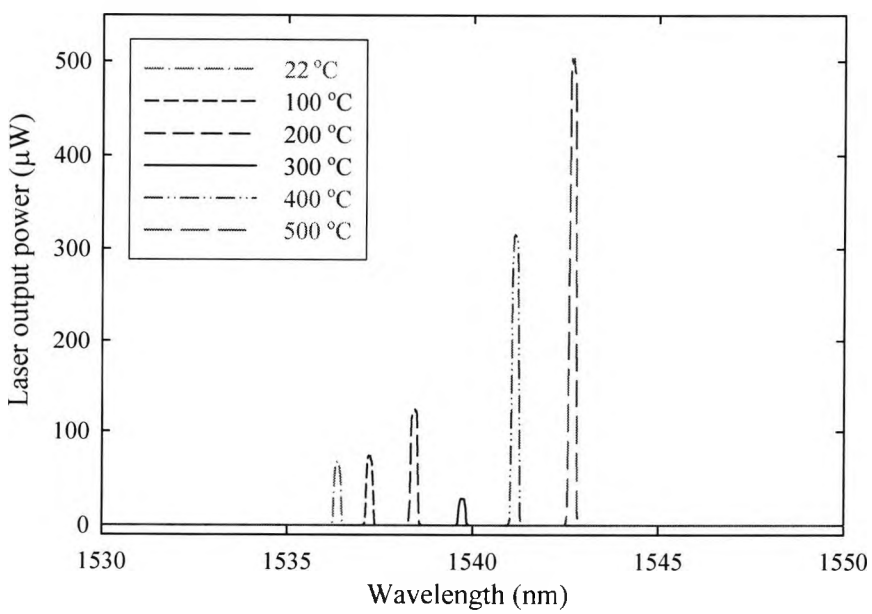

Fig. 6.13: Output spectra of the laser with different temperatures over the range from room temperature (~ 22 °C) to 500 °C with a fixed pump power of 60 mW.

6.9.1.2. Intensity and linewidth variation

The intensity and the linewidth variation of the laser at different temperatures over the range from room temperature to 500 °C are shown in Fig. 6.14, operating with a fixed pump power of 60 mW. At a temperature of 300 °C, the output power of the laser was found to decrease to a level of ~ 30 μW at a wavelength of ~ 1539.73 nm with the same fixed pump power of 60 mW. This arises because both the metastable level ($^4I_{13/2}$) and the ground level ($^4I_{15/2}$) of the Er^{3+} ions consist of several Stark sub-levels populated to various degrees depending on the Boltzmann thermal distribution and their fluorescence spectra, in general, comprise two peaks at the wavelengths of ~ 1535 nm and 1552 nm, this varying to a small degree with host materials used [Desurvire and Simpson 1990, Becker *et al.* 1997].

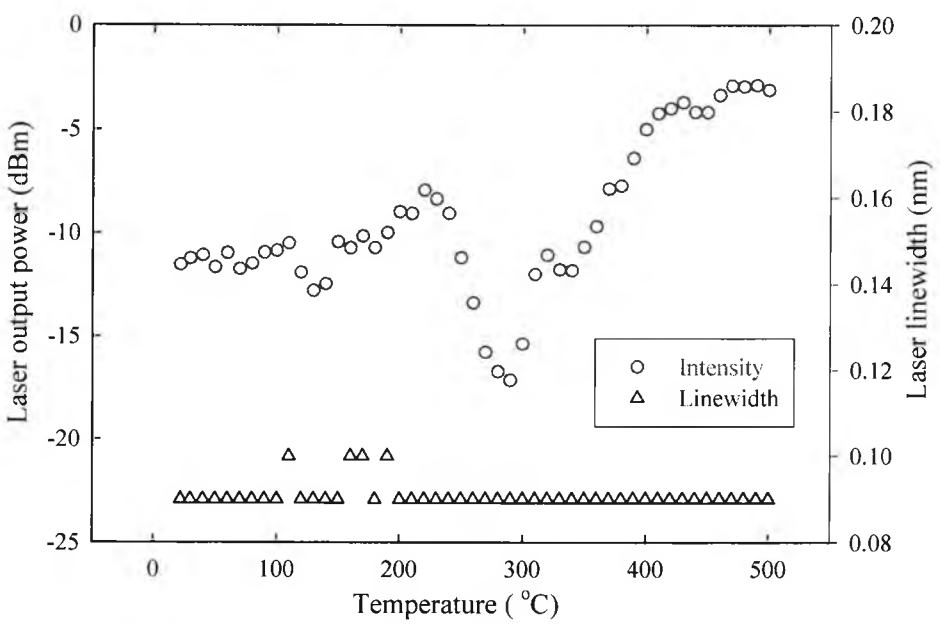

Fig. 6.14: Output power and the linewidth variation of the laser with different temperatures over the range from room temperature to 500 °C with a fixed pump power of 60 mW.

The variation in the output power of the laser was also attributed to the reflectivity variations of the chirped grating spectrum and its spatial relationship to the spectral

profile of the Er^{3+}-doped fibre used as the gain medium of the laser, over a wide range of temperatures, with a typical laser linewidth value of ~ 0.09 nm, or 11.4 GHz. The reflectivity of the chirped grating was much higher around the 1540 nm wavelength (Fig. 6.11), as this allows less output power transmission of the laser because the output was extracted through the chirped grating, which is shown in Fig. 6.12. Above the 1540 nm wavelength range, the output power of the laser again increases where the reflectivity of the chirped grating was found to be lower. However, by using a "smoother" spectrum of the chirped grating it is expected that the output power variations of the laser would be more readily minimised and this effect will be considered in more detail in Chapter 8. As the measurement was a wavelength-encoded measurement, the relative amplitude fluctuations do not represent a major problem for several practical applications.

6.9.1.3. Sensor Calibration with 10 °C Temperature change

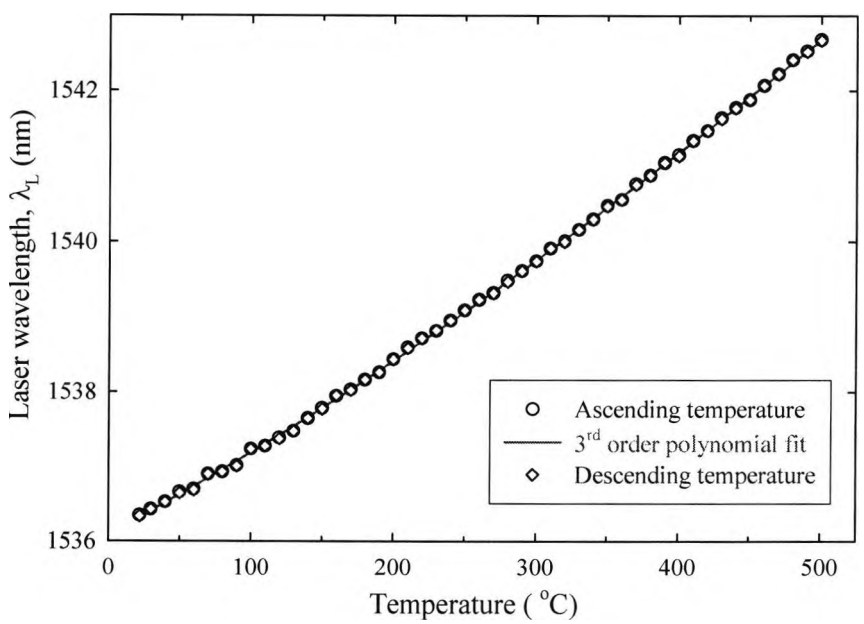

Fig. 6.15: Calibration of the laser wavelength with ascending and descending temperatures over the range from room temperature to 500 °C.

During the temperature calibration of the sensor system, a K-type thermocouple was held in intimate contact with the normal grating (RB_1) for accurate and continuous comparative monitoring of the oven temperature. The temperature was raised from room temperature to 500 °C, in incremental steps of 10 °C, allowing a settling time of ~ 15 minutes at each temperature to achieve the thermal equilibrium between the oven temperature and the sensing grating, before recording the data using the OSA. The change in the laser wavelength with ascending and descending temperatures over the range from room temperature to 500 °C is shown in Fig. 6.15. The calibration of the laser wavelength (λ_L) as a function of temperature (T) was calculated using both linear and nonlinear polynomial regressions fitting.

For a linear fitting:

$$\lambda_L(T) = 1535.82 + 0.01338T \tag{6.9}$$

Using a 2nd order polynomial fitting:

$$\lambda_L(T) = 1536.06 + 1.08\times10^{-2}T + 4.94\times10^{-6}T^2 \tag{6.10}$$

Using a 3rd order polynomial fitting:

$$\lambda_L(T) = 1536.10 + 1.01\times10^{-2}T + 8.43\times10^{-6}T^2 - 4.47\times10^{-9}T^3 \tag{6.11}$$

where T is the applied temperature in degrees Celsius of the sensing grating, RB_1. Comparison of the sensor calibration results using both linear and nonlinear polynomial regressions fitting are given in Table 6.1.

With a linear fitting to the experimental data, the temperature sensitivity was found to be 13.38 pm/°C, with a root mean square error (RMSE) value of 0.093 nm in wavelength, which is equivalent to 6.9 °C in temperature over the range from room temperature to 500 °C. However, taking into consideration of a non-linear (3rd order) polynomial fitting, the temperature-dependent sensitivity was found to be 10.24 pm/ °C and 13.16 pm/ °C at 22 °C and 500 °C, where the sensitivity at 500 °C was found to be 29 % higher than at room temperature. Also with the non-linear fitting, the

RMSE value was found to be 0.028 nm, which is equivalent to less than 3 °C (on average). This shows an improvement in the error calibration compared to that of 6.9 °C with a linear fitting over the wider measurement range mentioned above. The non-linearity in the thermal sensitivity of the sensor arises from the non-linear thermo-optic coefficient (ξ) of the silica glass, as was derived by Ghosh [1995].

For Sb-Ge co-doped fibre, the temperature dependent thermo-optic coefficient (ξ) was found to lie in the range between 9.14×10^{-6}/°C to 13.53×10^{-6}/°C at the temperature extremes of 22 °C and 500 °C respectively, for a constant thermal expansion coefficient (α) of 0.5×10^{-6}/°C and $n_{eff} = 1.4483$. The parameter was calculated using the same equation, (4.19) (as derived in Chapter 4) and taking the derivative of equation (6.11). The calculated room temperature thermo-optic coefficient (ξ) value 9.14×10^{-6}/°C of the Sb-Ge co-doped fibre agrees well the published value 9×10^{-6}/°C of the thermo-optic coefficient for the germanium doped silica fibre, as quoted by Reid and Ozcan [1998].

Table 6.1: Calibration of the laser sensor using both linear and nonlinear polynomial regressions fitting over the range from 22 °C to 500 °C.

Parameters		Linear fitting	2nd order polynomial fitting	3rd order polynomial fitting	Unit used
Temperature range		22 – 500	22 – 500	22 – 500	Deg C
Sensitivity	22 °C	13.38	10.92	10.24	pm/°C
	500 °C	13.38	13.28	13.16	
Coefficient of determination (COD)		0.9976	0.99976	0.99979	-
Standard deviation (SD)		0.095	0.030	0.028	-
Root mean square error (RMSE)		0.093	0.029	0.027	nm
RMSE	22 °C	6.93	2.66	2.64	°C
	500 °C	6.93	2.18	2.05	

6.9.1.4. Sensor Calibration with 1 °C Temperature change

Fig. 6.16 shows the shift in the laser wavelength with temperature change in 1 °C steps over the range from room temperature to 150 °C. The temperature was increased in a very narrow step to see the discontinuity in the laser wavelengths, due to its mode changing effect. The sensor wavelength was found to be particularly stable when both the resonant wavelength and the Bragg wavelength of the FBG matched exactly, at the gain peak of the laser. Alternatively, it can be seen from the figure that whenever there is a mismatch in the resonant wavelength and the Bragg wavelength of the FBG, a discontinuity occurs. This was not clearly observable when the sensor performance was studied with a 10 °C change in temperature (Fig. 6.15). However, dominant central wavelength of the laser was used to identify the sensor wavelength.

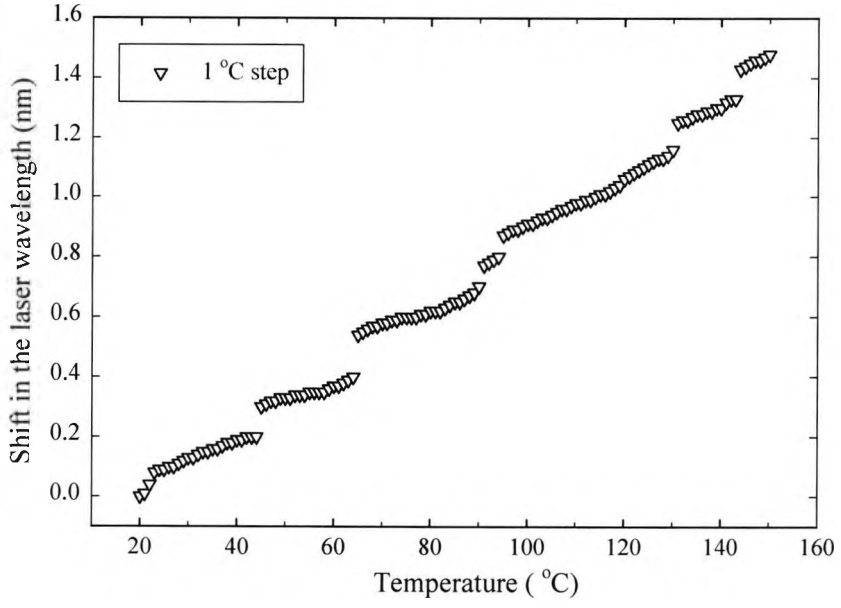

Fig. 6.16: Shift in the laser wavelength in 1 °C temperature change over the range from room temperature to 150 °C.

6.9.2. Strain Measurements

For strain measurements, the following steps were undertaken to observe the strain-induced effect on the sensor performance.

6.9.2.1. Output spectra

For different strain measurements, the oven temperature was fixed at 22 °C while the chirped grating was kept at ambient temperature, for the same fixed pump power of 60 mW. The strain was applied to the normal grating (RB_1) by moving the translation stage with a micrometer in steps of 50 μm, and the strain-induced laser wavelength shift was monitored using the OSA (with a RBW of 0.1 nm), over an applied strain value of 0 - 1200 με. The strain value was applied up to 1200 με to avoid any damage to the fibre as the sensing grating (RB_1) had been annealed at 525 °C for 11 hours prior to the experiment.

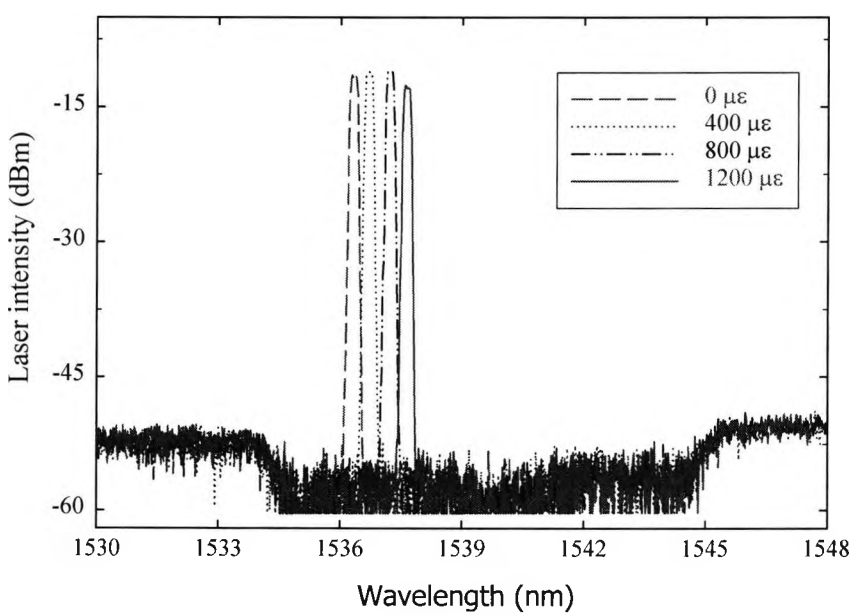

Fig. 6.17: Output spectra of the laser with different strain values of 0 to 1200 με with a fixed pump power of 60 mW.

However, Chen *et al.* [2004] have reported simultaneous strain and temperature measurements using a fibre Bragg grating inscribed in a high birefringence fibre over a slightly wider strain range (0 to 1300 με) but a more limited temperature range (–50 °C to 80 °C). The response of the laser output to different values of applied strain is shown in Fig. 6.17. The laser wavelength shifted towards the longer wavelength side of the spectrum because of the fractional change in the grating period, which is coupled with the change in the fibre effective refractive index due to the photo-elastic effect with increased applied strain, as described in Chapter 5. The wide "dip" over the wavelength range from ~ 1534 nm to 1545 nm in the fluorescence spectrum of the Er^{3+}-doped fibre arises from the reflection characteristic of the chirped grating. A high signal-to-noise ratio (SNR) of the laser signal (~ 41 dB) at these spectral "dips" can easily be seen from the figure when the normal grating (RB_1) was measurand-tuned. A poor SNR is observed beyond the tuneable laser wavelength range, outside the FWHM bandwidth (~ 10.80 nm) of the chirped grating. Similar characteristics were observed with the temperature measurement results obtained in Chapters 4 and 5.

6.9.2.2. Sensor Calibration with Strain

The change in the laser wavelength with both increasing and decreasing values of strain in the range 0 - 1200 με is shown in Fig. 6.18, where the laser wavelength, λ_L as a function of strain (ε) can be expressed through the equation below:

$$\lambda_L(\varepsilon) = 1536.28 + 1.11 \times 10^{-3} \varepsilon \qquad (6.12)$$

where ε is the applied strain (in microstrain) to the sensing grating, RB_1. The sensitivity was calculated using a linear fit to the experimental data, with a coefficient of determination (COD) of > 0.9969 and standard deviation (SD) of 0.0326. The sensitivity was found to be 1.11 pm/με with an RMSE of 28.3 με.

For Sb-Ge co-doped fibre, the strain-optic tensor coefficient, P_{12} was found to be 0.35 for a strain value of ε =1200 με, P_{11} = 0.113, Poissson's ratio, ν =0.16 and n_{eff} = 1.4483. This value was calculated using the Eq. (5.2), as derived in Chapter 5.

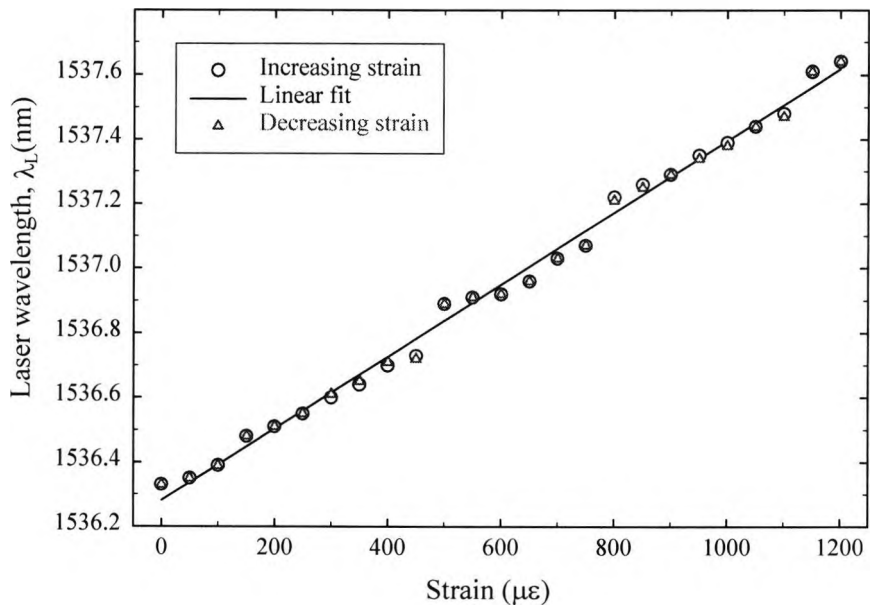

Fig. 6.18: Calibration of the laser wavelength with both increasing and decreasing values of strain over the range from 0 - 1200 με.

For both temperature and strain measurements, the entire measurement cycles were repeated using both ascending and descending values, as a result of which the response of the active-sensor was found to be repeatable to within ± 0.01 nm (using the OSA with a RBW of 0.1 nm), with almost negligible hysteresis being observed.

6.9.3. Effect on laser cavity length with resonant laser wavelength changes

The changes in the laser wavelength ($\Delta\lambda_L$) that were observed reflect the changes in the Bragg wavelength of the normal grating RB_1, arising from the measurand perturbations (due to the temperature or strain changes), over the range of the chirped grating used as one of the reflectors in the laser cavity. The change in the laser cavity length (ΔL_C) with the changes in the resonant laser wavelength with temperature or strain is shown in Eq. (6.2). Considering a linear thermal sensitivity of 13.38 pm/ °C, the maximum error value of the system was found to be 116×10^{-3} nm (in wavelength),

equivalent to 8.7 °C (in temperature) at 270 °C over the measured range from 22 °C to 500 °C. The error value depends on the measurand range, the sensitivity of the system, the bandwidth of the chirped grating and the resolution of the detection system. Assuming the fundamental mode of the laser (i.e. $m = 1$) and $n = 1.45$ for silica fibre, the maximum change in the laser cavity length was found to be 40×10^{-3} nm using the maximum error value reported, this being derived using Eq. (6.2) and leading to a maximum error value of 3 °C in the system.

Similarly for the strain measurements, the maximum error value was found to be 50.5 $\times 10^{-3}$ nm, equivalent to 45.5 με at a strain value of 450 με, with a linear sensitivity of 1.11 pm/ με over the range of 0 to 1200 με. For the fundamental mode of the laser, the maximum change in the laser cavity length was found to be 17.4×10^{-3} nm using Eq. (6.2), which may cause a maximum strain error value of 15.7 με in the system.

6.10. Summary

Frequently type I Bragg gratings written into highly photosensitive B-Ge co-doped fibre using the same writing conditions (laser energy of 12 mJ and frequency of 200 Hz) have been found to be readily "washed out" at temperatures of 350 °C [Pal *et al.* 2003], within a few hours, which implies that there are very significant limitations for their use in active sensor applications. Similarly, type I Bragg gratings written into the high germanium-erbium co-doped fibre also showed significant decay in their reflectivity values when annealed at 500 °C for ~ 11 hours (the reflectivity fell to less than 55 % after annealing). For type IIA Bragg gratings written into the same fibre showed a much better temperature sustainability, when annealed at 525 °C for the same period (the reflectivity remained as high as ~ 96 % after annealing). When the type IIA Bragg grating was used for laser-based high temperature measurements, the larger value of the reflection spectral width (~ 0.64 nm) of the grating leads to a higher error value of ~ 8.9 °C in the detection system over the temperature range from room temperature to 440 °C, as discussed in Chapter 5.

In this Chapter, the formation of the type IIA chirped fibre Bragg grating (CFBG) in the B-Ge co-doped fibre has been reported for the first time to our knowledge, with the similar growth behaviour to that of the uniform type IIA Bragg grating in the fibre. The formation phenomenon of both types I and IIA CFBGs was found to be repeatable for one fixed alignment position of the chirped phase mask used for several samples. The bandwidth of the chirped grating was enhanced by fusion-splicing two different type IIA chirped Bragg gratings with their wavelength overlap factor of 1 nm over the wavelength ranging from ~ 1535 nm to 1545 nm. The wider FWHM bandwidth (10.80 nm) of the chirped grating was used as the second reflector into the laser cavity to achieve both the wide measurement range of temperature and strain.

A normal type I Bragg grating was written into an Sb-Ge co-doped fibre because of its ability to operate reliably at the high temperature as high as 500 °C. The grating written in the Sb-Ge co-doped fibre showed a higher level of photosensitivity compared to that of the Sn-doped fibre, as reported by Shen *et al.* [2004]. The fabrication of type I Bragg grating written into the Sb-Ge co-doped fibre takes ~ 19 minutes of exposure to create compared to that of the type IIA Bragg grating (~ 14 minutes) written into the high Ge-Er^{3+} co-doped fibre, to achieve almost the same level of reflectivity of ~ 99 % using the same writing conditions. For the present active sensor system, the linear thermal sensitivity of the Sb-Ge co-doped fibre was found to be 13.38 pm/ °C that is almost in the same range as compared to that of the sensitivity of 13.94 pm/ °C in the high Ge-Er^{3+} co-doped fibre. In addition, an improvement in the root mean square error (RMSE) values (of 6.9 °C for a linear fitting and less than 3 °C for the polynomial fittings) was obtained over the wider measurement range from room temperature to 500 °C compared to that an RMSE value of 8.9 °C over the range from room temperature to 440 °C (in Chapter 5).

The precision of the laser-based sensor system in the tests carried out and reported has been limited by the random laser mode hopping observed in the central wavelength of the laser. For a laser linewidth of 0.09 nm (measured using the OSA with a RBW of 0.1 nm) and with a cavity length of ~ 96 cm, the laser is supporting many tens of longitudinal modes, therefore the laser output is significantly multi-moded. As a result

the laser appears to be hopping between several modes, this creating a small impact on the laser wavelength and the output intensity, and contributing to the error in the measurand. However, the effect on the laser wavelength is seen more clearly in the strain measurements, because of the smaller wavelength changes (~ 1.11 pm/με) that occur over the total measurand range used compared to that of the temperature measurements (~13.38 pm/°C). A similar effect was observed when the temperature was changed in a very narrow step of 1 °C over the range from room temperature to 150 °C. In this measurement, the dominant central wavelength of the laser was used to determine the sensor wavelength, using the OSA, with as before, a RBW of 0.1 nm. However, the sensor was found to be particularly stable when both the resonant wavelength and the Bragg wavelength of the FBG matched exactly, at the gain peak of the laser. By reducing the cavity length, the axial mode spacing of the laser could be further increased to maintain the laser oscillation on a single longitudinal mode over the measurement range considered and thus the mode hopping effects could be fully eliminated, as reported by Ball and Morey [1994]. As the erbium-doped fibre has relatively low pump absorption per unit length of fibre, to maintain the laser oscillation in a single longitudinal mode limits the laser efficiency. One possible way to improve the single frequency sensor output by using a master oscillator power amplifier (MOPA) configuration to pump an additional gain section (erbium-doped fibre) external to the fibre laser using the residual fibre laser pump power [Ball *et al.* 1994], which again results in a more complex the overall system design.

The key achievement was a novel active sensor system using type I Bragg grating written into high temperature sustainable Sb-Ge co-doped fibre being developed to operate over a wider range and the results were evaluated using several repeatable cycles of measurement. The temperature was monitored over the range from room temperature to 500 °C and strain values of 0 - 1200 με while at the same time achieving acceptable measurement errors of less than 3 °C (using the nonlinear fittings) and 28.3 με respectively over the above measured ranges of both the parameters. The high signal-to-noise ratio (SNR) and the narrow linewidth in the laser signal make the active sensor device suitable for a range of measurement situations, including use under harsh environmental applications.

6.11. References

- Alavie, A.T., Karr, S.E., Othonos, A. and Measures, R.M. (1993) A Multiplexed Bragg grating fiber laser sensor system, *IEEE Photon. Technol. Lett.*, vol.5, pp.1112-1114.
- Ball, G.A. and Morey, W.W. (1994) Compression tuned single-frequency Bragg grating fiber laser, *Opt. Lett.*, vol. 19, pp.1979-1981.
- Ball, G.A., Holton, C.E., Hull-Allen, G. and Morey, W.W. (1994) 60 mW 1.5μm single-frequency low-noise fiber laser MOPA, *IEEE Photon. Technol. Lett.*, vol. 6, pp.192-194.
- Becker, P.C., Olsson, N.A. and Simpson, J.R. (1997) *Erbium-Doped Fiber Amplifiers: Fundamentals and Technology*, Academic Press, San Diego USA.
- Byron, K.C. and Rourke, H.N. (1995) Fabrication of chirped fibre gratings by novel stretch and write technique, *Electron. Lett.*, vol. 31, pp. 60-61.
- Byron, K.C., Sugden, K., Bricheno, T. and Bennion, I. (1993) Fabrication of chirped Bragg gratings in photosensitive fibre, *Electron. Lett.*, vol. 29, pp. 1659-1660.
- Chen, G. Liu, L., Jia, H., Yu, J., Xu, L. and Wang, W., (2004) Simultaneous strain and temperature measurements with fiber Bragg grating written in novel Hi-Bi optical fiber, *IEEE Photon. Technol. Lett.*, vol .16, pp. 221 –223.
- Desurvire, E. and Simpson, J.R. (1990) Evaluation of $^4I_{15/2}$ and $^4I_{13/2}$ Stark-level energies in erbium-doped aluminosilicate glass fibers, *Opt. Lett.*, vol.15, pp. 547-549.
- Digonnet, M.J.F. (1993), *Rare Earth Doped Fiber Lasers and Amplifiers*, Marcel Dekker, New York.
- Farries, M.C., Sugden, K., Reid, D.C.J., Bennion, I., Molony, A. and Goodwin, M.J. (1994) Very broad reflection bandwidth (44 nm) chirped fibre gratings and narrow bandpass filters produced by the use of an amplitude mask, *Electron. Lett.*, vol. 30, pp. 891-892.
- Ghosh, G. (1995) Model for the thermo-optic coefficients of some standard optical glasses, *J. Non-Cryst. Solids*, vol. 189, pp. 191-196.
- Hill, P.C. and Eggleton, B.J. (1994) Strain gradient chirp of fibre Bragg gratings, *Electron. Lett.*, vol. 30, pp.1172-1174.

- Kashyap, R., McKee, P.F., Campbell, R.J. and Williams, D.L. (1994) Novel method of producing all fibre photoinduced chirped gratings, *Electron. Lett.*, vol. 30, pp. 996-998.
- Kashyap, R. (1999) *Fiber Bragg gratings*, Academic Press, San Diego.
- Kashyap, R. (1997) Design of step-chirped fibre Bragg gratings, *Opt. Commun.*, vol. 136, pp. 461-469.
- Kersey, A.D. and Morey, W.W. (1993) Multiplexed Bragg grating fibre-laser strain-sensor system with mode-locked interrogation, *Electron. Lett.*, vol.29, pp.112-114.
- Mandal, J., Pal, S., Sun, T., Grattan, K.T.V., Augousti, A.T. and Wade, S.A. (2004a) Bragg grating-based fiber-optic laser probe for temperature sensing, *IEEE Photon. Technol. Lett.*, vol. 16, pp. 218-220.
- Mandal, J, Sun, T., Grattan, K.T.V., Augousti, A.T., Wade, S.A., Collins, S.F., Baxter, G.W., Dussardier, B. and Monnom, G. (2004b) A wide temperature tunable fibre laser using a chirped grating and a type IIA fibre Bragg grating, *Meas. Sci. Technol.*, vol. 15, pp. 1113-1119.
- Othonos, A. and Kalli, K. (1999) *Fiber Bragg Gratings: Fundamentals and Applications in Telecommunications and Sensing*, Artech House, Boston.
- Pal, S., Shen, Y.H., Mandal, J., Sun, T. and Grattan, K.T.V. (2004a) Combined fluorescence and grating-based technique for wider range strain-temperature simultaneous measurement using Sb-Er doped fibre, *in Proc. of 2nd European Workshop on Optical Fiber Sensors* (EWOFS'04), Santander, Spain, pp.160-163.
- Pal, S., Shen, Y.H., Mandal, J., Sun, T. and Grattan, K.T.V. (2004b) Simultaneous measurement of strain (to 2000 με) and temperature (to 600 °C) using a combined fluorescence and grating-based technique, accepted in *IEEE Sensors Journal*.
- Pal, S., Mandal, J., Sun, T., Grattan, K.T.V., Fokine, M., Carlsson, F., Fonjallaz, P.Y., Wade, S.A. and Collins, S.F. (2003) Characteristics of potential fibre Bragg grating sensor-based devices at elevated temperatures, *Meas. Sci. Technol.*, vol.14, pp.1131-1136.

- Riant, I. and Haller, F. (1997) Study of the photosensitivity at 193 nm and comparison with photosensitivity at 240 nm influence of fiber tension: type IIa aging, *IEEE J. Lightwave Technol.*, vol. 15, pp. 1464-1469.
- Shen, Y.H., He, J., Sun, T. and Grattan, K.T.V. (2004) High-temperature sustainability of strong fiber Bragg gratings written into Sb-Ge-Codoped photosensitive fiber: decay mechanism involved during annealing, *Opt. Lett.*, vol. 29, pp. 554-556.
- Sugden, K., Bennion, I., Molony, A. and Copner, N.J. (1994) Chirped gratings produced in photosensitive optical fibres by fibre deformation during exposure, *Electron. Lett.*, vol. 30, pp. 440-442.
- Sun, T., Pal, S., Mandal, J. and Grattan, K.T.V. (Annual Report 2001/2002) Fibre Bragg grating fabrication using fluoride excimer laser for sensing and communication applications, *Central Laser Facility (CLF)*, Rutherford Appleton Laboratory, pp. 147-149.
- Reid, M.B. and Ozcan, M. (1998) Temperature dependence of fiber optic Bragg gratings at low temperatures, *Opt. Eng.*, vol. 37, pp. 237-240.
- Wilson, J. and Hawkes, J.F.B. (1987) *Lasers: Principles and Applications*, Prentice Hall International Ltd, UK, pp.1-34.

Chapter 7

Characterisation of uniform wavelength-matched fibre Bragg grating-based fibre lasers for temperature sensor systems

7.1. Abstract

In this Chapter, a detailed investigation is reported into the output characteristics of a uniform wavelength-matched fibre Bragg grating-based fibre laser configuration, forming the basis of a sensor system. The performance was evaluated in terms of its wavelength, signal intensity, linewidth and the output spectrum when each individual fibre Bragg grating, each acting as the reflector of the laser system, has been allowed to respond to temperature changes. An analytical model has been created for the first time reflecting the relationship between the grating bandwidth and the temperature under each operational condition; and the results obtained have significant implication for the optimum design of this type of fibre laser, particularly for temperature sensor applications. Additional experiments were performed into the output characteristics of a fibre laser created with a very short cavity length, placed in an oven for temperature measurement. A brief summary of the overall results and their comparisons are given at the end of the Chapter.

7.2. Introduction

Several uniform wavelength-matched Bragg grating-based laser approaches have been reported, especially for applications where both the gratings have been held at a uniform temperature, or in a constant strain or compression state [Ball and Morey 1992, Ball *et al.* 1993; Ball and Morey 1994]. An optical fibre laser-based sensor system has been developed to operate over a wide range of temperature from room

temperature to 500 °C (maximum) and the detailed results and their working principles were given in the Chapters 4, 5 and 6. The laser cavity was formed using the combination of a chirped grating and a normal (type I or type IIA) fibre Bragg grating. The normal Bragg grating was measurand-tuned (acting as the sensor probe) and combined with a chirped grating as the other reflector used to achieve the tuneable laser action over the range required from the measurement.

In this Chapter, a detailed investigation has been carried out into the output characteristics of a fibre laser as the basis of a sensor system utilising the characteristics of wavelength, signal intensity, linewidth and the output spectrum when each individual Bragg grating is allowed to respond to temperature in a wavelength-matched normal Bragg grating based laser configuration. A close relationship between the grating bandwidth and the temperature has been obtained under several conditions evaluated. The results obtained have significant implication for the optimum design of this type of fibre laser, particularly for sensor applications. In a further experiment, the output characteristics of a fibre laser were studied when the full length of a short cavity laser was used as the sensor probe and placed in an oven, to evaluate its use for compact practical sensor applications.

7.3. Matched-pair grating fabrication

For the fibre laser, the matched-pair of fibre Bragg gratings was fabricated in boron-germanium (B-Ge) co-doped fibre (fibre details of are in Table 7.1) using a KrF excimer laser as UV source and a phase mask technique, as described in previous Chapters. The energy (8 to 12 mJ) and the frequency (100 to 200 Hz) of the excimer laser were carefully controlled during the inscription of the gratings to achieve a wavelength-matched Bragg grating pair with the desired level of reflectivity, with a Bragg wavelength of around 1535 nm. A grating, having a reflectivity of < 90 % is defined as a low reflectivity grating (LR_1) in this system: conversely a reflectivity of just less than 100 % (~ 99.96 %) is defined as high reflectivity grating (HR_1). It took less than one minute (~ 55 sec) of UV exposure to achieve a reflectivity of 99.96 % using the laser energy of 12 mJ and a repetition frequency of 200 Hz. The reflectivity of the low reflective grating was targeted to be ~ 87 %, which from previous

experiments recorded in Chapter 3 was found suitable, to extract a satisfactory level of laser output while balancing the cavity losses. In addition, the Bragg wavelength of this grating (LR_1) was clearly matched in wavelength terms with the Bragg wavelength of the high reflectivity grating (HR_1), this being done during their inscription.

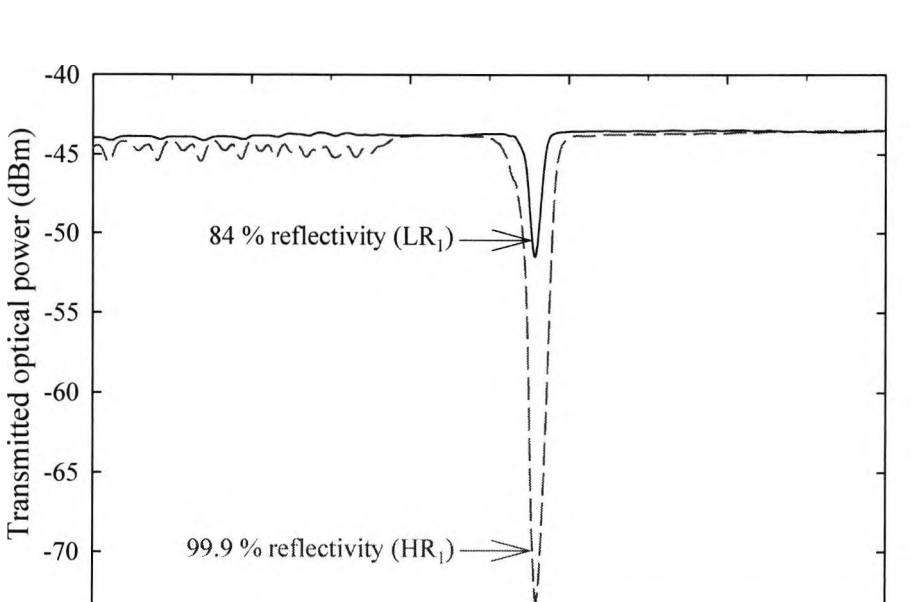

Fig. 7.1: Transmission spectra of the high reflective grating (HR_1) and the low reflective grating (LR_1) at room temperature after annealing.

These gratings had previously been thermally annealed at 100 °C for 6 hours (to ensure stable operation for sensor applications) and details of the annealing results were given in Chapter 3. The reflectivity was calculated from the minimum transmittance power at the Bragg wavelength of the grating and was found to be ~ 84 % for the low reflectivity gratings (LR_1) and ~ 99.9 % for the high reflectivity grating (HR_1), at room temperature after annealing and their transmission spectra are shown in Fig. 7.1. The figure clearly shows that both gratings were centrally matched at a Bragg wavelength of ~ 1535.60 nm. The full-width-half-maximum (FWHM) bandwidths of the gratings were measured to be $\Delta\lambda_{LR}$ = 0.22 nm for LR_1 and $\Delta\lambda_{HR}$ =

0.46 nm for HR_1 respectively, using the Optical Spectrum Analyser (OSA) with a resolution bandwidth (RBW) of 0.1 nm.

7.4. Experimental Arrangement

The system used in this work, to enable an investigation of the effect of the measurand-tuned fibre Bragg grating (FBG) characteristics on the fibre laser, is shown in Fig. 7.2.

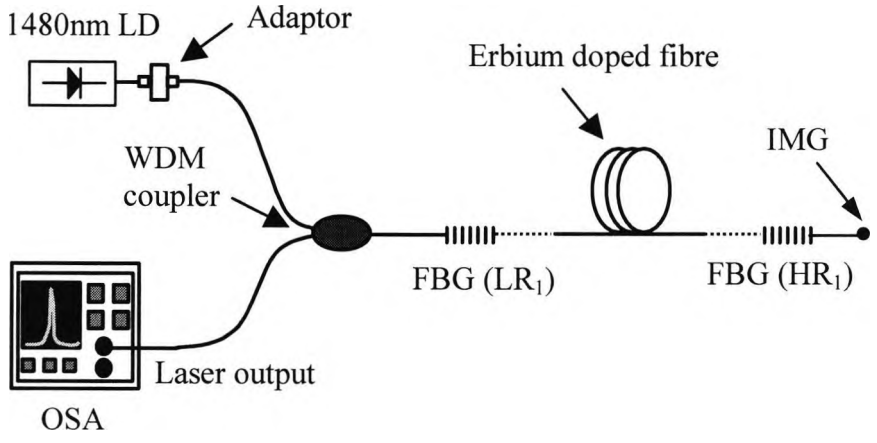

Fig. 7.2: Experimental set-up of the wavelength-matched fibre Bragg gratings-based laser system. FBG: fibre Bragg grating (LR_1: Low reflectivity grating, HR_1: High reflectivity grating), OSA: Optical Spectrum Analyser; IMG: index-matching gel.

7.4.1. Laser cavity configuration

The laser cavity feedback was formed using a simple wavelength-matched normal Bragg grating pair shown in Fig. 7.1, which were fusion spliced to a length of Er^{3+} doped fibre (EDF 510) as the gain medium. The length of the gain medium was fixed at ~ 5 metres based on the optimised results obtained in Chapter 3 and the erbium-fibre details are given in Table 7.1. The low reflectivity grating (LR_1) was fusion spliced to the output arm of the 1480/1550 nm wavelength division multiplexed (WDM) coupler through a length of Corning SMF-28 optical fibre. The gain medium was optically pumped using a 1480 nm FBG stabilised laser diode (LD) through the

input arm of the coupler; and the laser output was monitored through the other arm of the coupler using the OSA. For Er^{3+} fibre of length ~ 5 metres, the cavity mode spacing was found to be 21 MHz or 0.16 pm (with n = 1.45 for silica fibre). As a result, many longitudinal modes of the laser are possible within the resonant cavity, but only those longitudinal modes having sufficient gain will oscillate.

Table 7.1: Detailed specifications of different fibres used in this work.

Fibre type	Core composition	Core diameter (μm)	Numerical aperture	Cut-off wavelength (μm)	Supplier
Photosensitive fibre: PS 1250/1500	B-Ge	4.8	0.14	1.247	Fibercore Ltd., UK
EDF 510: Er^{3+} fibre of length 5m	Er_2O_3 (350-400 ppm)+Ge_2O_3+Al_2O_3	2.3	0.27	0.850	HighWave Optical Tech., France
Er 123: Er^{3+} fibre of length 5.9 cm	Er_2O_3 (5000 ppm)+Ge_2O_3+Al_2O_3	3.3	0.16	0.887	Moritex Europe Ltd., Sweden

7.5. Experimental results

As discussed above, the fibre laser was created as the active element of a temperature sensing system. Two steps were taken to monitor the temperature effect on the laser system when each individual *Bragg grating reflector* in the laser cavity was heated, while keeping the length of the gain medium constant and the pump power fixed at 16 mW throughout the experiments carried out.

With system 1 the laser output was characterised when the *low reflectivity grating (LR_1)* alone was allowed to respond to temperature changes. To do so, this low reflectivity grating (LR_1) was placed in the centre of the oven and the high reflectivity grating (HR_1) was kept at ambient temperature.

With system 2 the laser output was characterised when the *high reflectivity grating (HR_1)* alone was heated. For this, the high reflectivity grating (HR_1) was placed in the centre of the oven, while the low reflectivity grating (LR_1) was kept at ambient temperature.

In both cases, the laser output was extracted through the low reflectivity grating (LR_1), and monitored using the OSA, while the high reflectivity grating (HR_1) was maintained as the end cavity reflector to achieve a higher gain cavity operating at the lasing wavelength. Index matching gel was used at the bare end of the fibre to minimise the Fresnel reflection into the laser cavity.

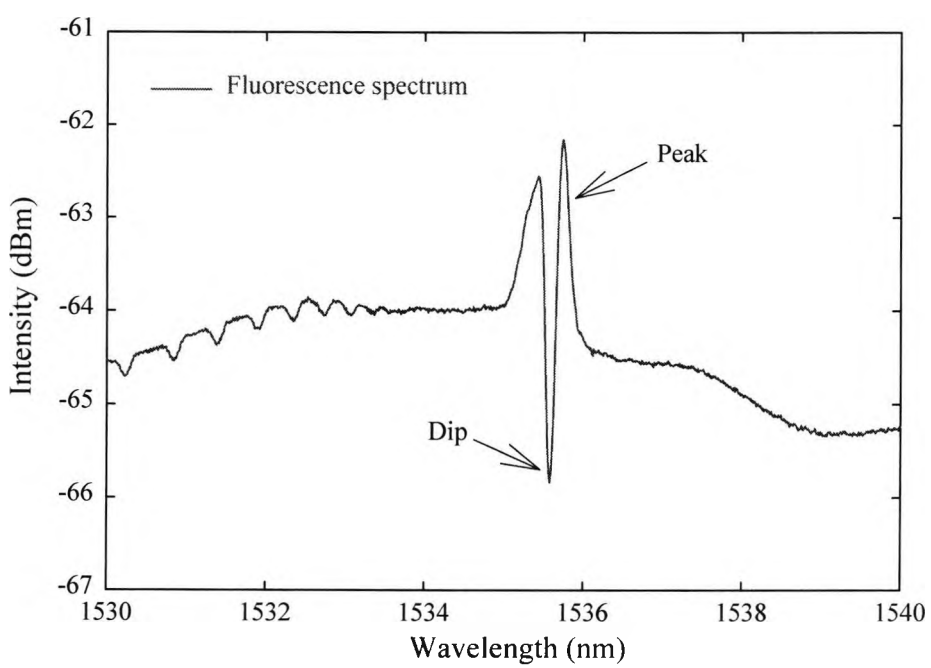

Fig. 7.3: Fluorescence spectrum showing the clear transmission dip and the reflection peak before lasing occurred.

Fig. 7.3 shows the fluorescence spectrum before lasing occurred. The clear "dip" in the centre of the reflection peak in the fluorescence signal shows the reflection at the Bragg wavelength due to the low reflectivity grating (LR_1) and the reflection "peak"

arising from the high reflectivity grating (HR_1), which forms the end cavity reflector of the laser. Thus when any external perturbation (in this case temperature) is applied to one of the gratings, this results in a mismatch of the Bragg wavelength of the matched-pair gratings in the laser cavity and, as a result, a separation of the transmission dip and the reflection peak in the spectrum occurred, thus affecting the cavity resonant wavelength.

7.5.1. Low reflectivity grating (LR_1 - reflectivity of 84 %) in oven

To monitor the temperature effects on the low reflectivity grating (LR_1) in the laser cavity, this grating (LR_1) was placed loosely in the centre of the oven (Carbolite: MTF 12/38/400) to avoid any longitudinal strain effects while the high reflectivity grating (HR_1) was kept at ambient temperature. The oven temperature was raised from room temperature to 95 °C, allowing a settling time of ~ 10 minutes at each temperature to achieve a thermal equilibrium between the grating and the oven temperature, before recording the data using the OSA (with a RBW of 0.1nm, which corresponds to a minimum observable wavelength shift of ± 0.01 nm).

7.5.1.1. Wavelength response of the sensor

The response of the laser wavelength with temperature is shown in Fig. 7.4. This was found to be linear over the narrow range of temperature from room temperature (~ 22 °C) to 55 °C. The sensitivity (S_{LT}) was calculated using a linear fit to the experimental data, with a coefficient of determination (COD) > 0.998 and a standard deviation (SD) of 0.0058, and the sensitivity was found to be 6.67 pm/ °C. The laser wavelength, λ_L, as a function of temperature, T can be expressed through Eq. (7.1) below:

$$\lambda_L(T) = 1535.43 + 6.67 \times 10^{-3} T, \qquad (7.1)$$

where T is the temperature applied (in °C) to the low reflectivity grating (LR_1).

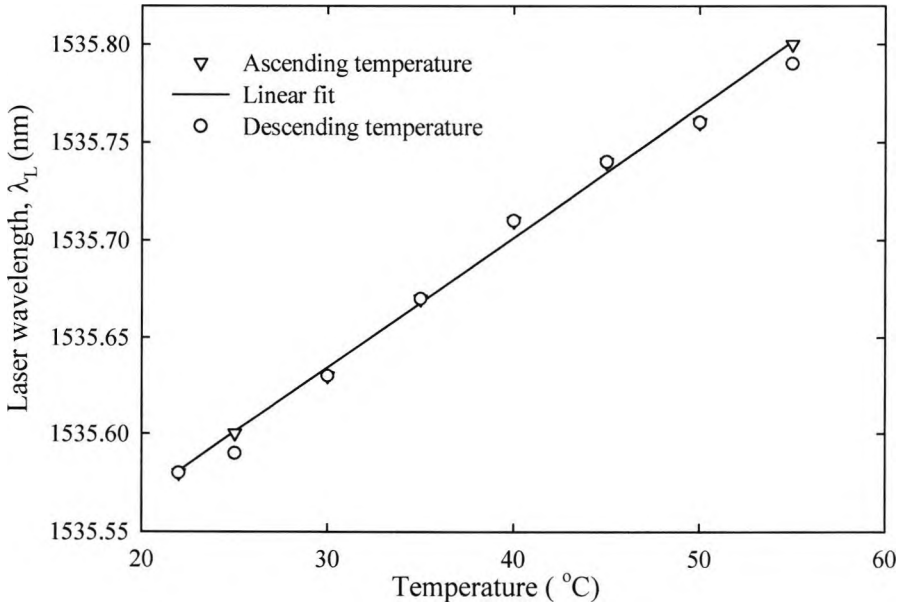

Fig. 7.4: Response of the laser wavelength with temperature from room temperature to 55 °C when the low reflectivity (LR_1) grating was placed in the oven.

7.5.1.2 Grating bandwidth-effects on laser performance

When a low reflectivity grating (LR_1) alone is placed in oven, the linear operational range of the laser can be expressed through Eq. (7.2) below, with the assumption that both central-wavelengths of the gratings are matched at room temperature after annealing:

$$LRT_{linear} = T_{room} + \frac{\frac{1}{2}\Delta\lambda_{HR}}{S_{LT}}, \tag{7.2}$$

where T_{room} is the room temperature, S_{LT} is the linear thermal sensitivity of the laser. Using Eq. (7.2), the linear operational range of the laser (LRT_{linear}) is from room temperature (~ 22 °C) to 56 °C. The experimental data shown in Fig. 7.4 clearly show the linear operational range of the laser from 22 °C to 55 °C, which agrees well with the temperature predicted using Eq. (7.2), when the low reflectivity grating, LR_1, was placed in oven.

The unstable operational range of the laser may be expressed through Eq. (7.3) below:

$$LRT_{unstable} = \frac{\frac{1}{4}\Delta\lambda_{HR} + \frac{1}{2}\Delta\lambda_{LR}}{S_{LT}}, \tag{7.3}$$

Using Eq. (7.3), the unstable operational range ($LRT_{unstable}$) of the laser would be ~ 34 °C.

Therefore, the maximum temperature for lasing, including both the linear and the unstable operational range expressed by Eqs. (7.2) and (7.3), can be summarised through Eq. (7.4) below:

$$LRT_{total} = T_{room} + \frac{\frac{3}{4}\Delta\lambda_{HR} + \frac{1}{2}\Delta\lambda_{LR}}{S_{LT}}, \tag{7.4}$$

where LRT_{total} is the temperature at which the laser action will cease when the low reflectivity grating alone will be heated above room temperature. Using Eq. (7.4) and considering the linear sensitivity of the laser of 6.67 pm/ °C, the rise above room temperature that is required to quench the laser action totally is ~ 68 °C.

Fig. 7.5 shows the response of the laser-based system over the temperature range from 22 °C to 95 °C, exploring this beyond a temperature of ~ 55 °C. From 56 to 62 °C, the laser wavelength did show negligible response to the temperature change. It is believed that the laser retains its fundamental lasing mode before the Bragg wavelengths of the matched-pair gratings start to become mismatched. Over the temperature range from 63 to 88 °C, the transmission dip and the reflection peak in the laser signal were quite unstable, this mainly arising from the edge-matching of the two matched-pair gratings in the laser cavity, which causes the laser oscillation to be unstable, leading to laser mode hopping. At a temperature of 90 °C (± 1 °C), the complete separation of the transmission dip and the reflection peak was observed and this agrees quite well with the prediction of the temperature at which this would be expected to occur using Eq. (7.4). This small uncertainty (± 1 °C) may arise from the lack of "smoothness" of the grating spectrum used. With a further increase in temperature, the transmission dip kept varying towards the longer side of the spectrum

but the reflection peak was found to remain constant as the high reflectivity grating (HR_1) was kept at ambient temperature.

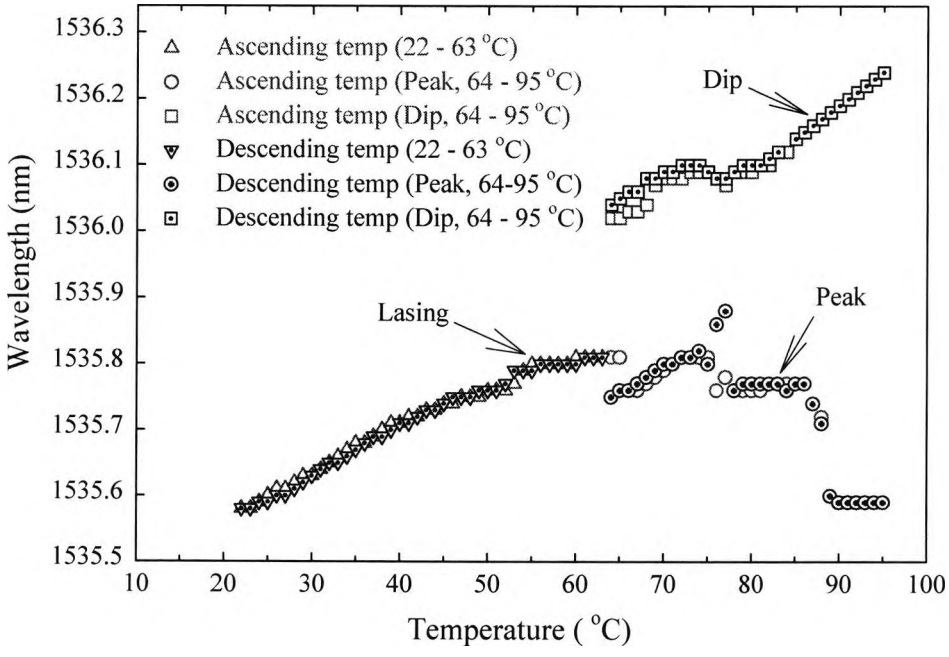

Fig. 7.5: Wavelength response of the laser based system with temperature from 22 °C to 95 °C when the low reflectivity grating (LR_1) was placed in the oven and the high reflectivity grating (HR_1) was kept at ambient temperature.

The experiments were repeated using several cycles of both ascending and descending temperature, where the grating wavelength response was found to be repeatable within ± 0.01 nm, as measured using the OSA.

7.5.1.3. Laser-mode hopping

For a fibre Bragg grating based laser system, both the resonant laser wavelength and the peak gain wavelength (Bragg wavelength of the fibre grating) depends on temperature. When they differ, the emission wavelength would suddenly jump to the neighbouring mode, the effect is termed mode hopping. The laser oscillation takes

place at the Bragg wavelength of the grating, when the gain medium is externally pumped to overcome the cavity losses and the cavity resonance condition is satisfied:

$$\lambda_L = \frac{2nL_c}{m}, \tag{7.5}$$

where λ_L is the resonant laser wavelength, n is the refractive index of the gain medium, L_C is the laser cavity length and m is a positive integer [Wilson and Hawkes 1987]. Each value of m (which satisfies the resonance condition) is a longitudinal mode of the cavity. The cavity mode spacing or the free spectral range (FSR) of the laser is the difference between each longitudinal mode and this is expressed as below:

$$\Delta\lambda_{FSR} = \frac{\lambda_L^2}{2nLc}, \tag{7.6}$$

The change in the laser cavity length, ΔL_C arises from the resonant laser wavelength changes, $\Delta\lambda_L$, can be expressed as below:

$$\Delta L_C = \frac{m\Delta\lambda_L}{2n}, \tag{7.7}$$

In FBG-based laser sensor applications, the change in the laser wavelength, $\Delta\lambda_L$ arises from the resonance condition change of the Bragg wavelength ($\Delta\lambda_B$) of the grating, for example, with temperature change, ΔT and this can be expressed through the equation below:

$$\frac{\Delta\lambda_L}{\lambda_L} = func\left(\frac{\Delta\lambda_B}{\lambda_B}\right) = (\alpha + \xi)\Delta T, \tag{7.8}$$

where $\alpha = \frac{1}{\Lambda}\frac{\delta\Lambda}{\delta T}$ is the thermal expansion coefficient and $\xi = \frac{1}{n_{eff}}\frac{\delta n_{eff}}{\delta T}$ is the thermo-optic coefficient of the fibre. One possible way to reduce the discontinuity in the laser wavelength due to mode hopping is to increase the laser cavity length so that the spacing between the two longitudinal modes will be less, as seen in Eq. (7.6).

A typical example of the laser mode hopping which occurs with ascending temperature is shown in Fig. 7.6, at a temperature of 77 °C. The figure clearly shows that the laser was hopping between several longitudinal modes arising from the

unstable resonant condition in the laser cavity. This mainly arose from the edge matching of the Bragg wavelengths of the gratings in the laser configuration, before the gratings were totally separated, and will result in an error in the temperature measurement using the calibration against the laser wavelength.

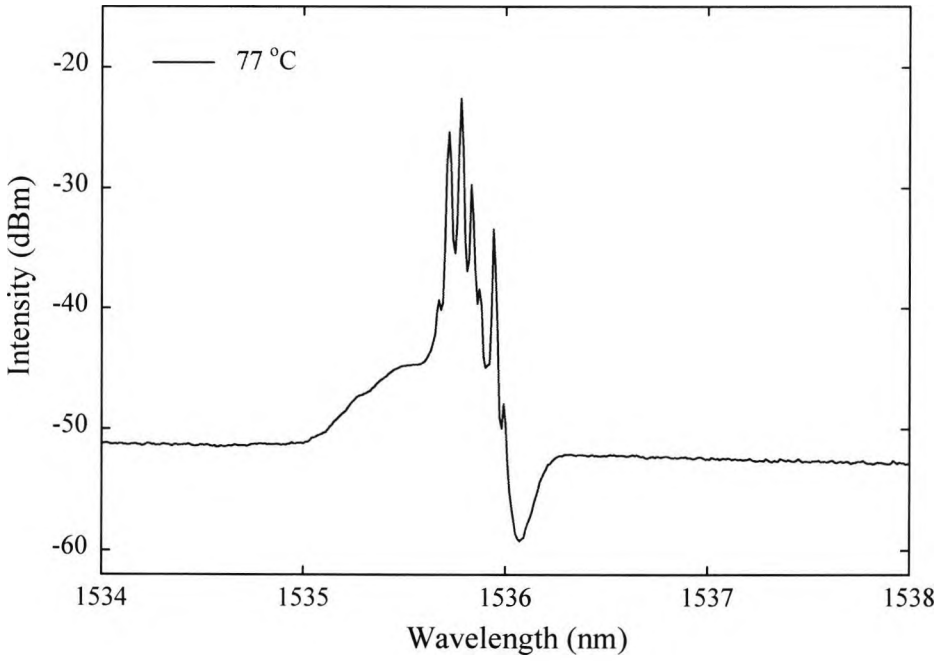

Fig. 7.6: Laser mode hopping with ascending temperature at 77 °C when the low reflectivity grating (LR_1) was placed in the oven.

7.5.1.4. Laser intensity and linewidth variation

The intensity and the linewidth variation of the laser-based sensor system with temperature are shown in Fig. 7.7 with a fixed pump power of 16 mW. The sinusoidal variation in the laser intensity, over the temperature range from 22 °C to 55 °C, appears to be directly related to the intensity distribution profile of the longitudinal modes along the fibre, as shown by Kim *et al.* [1996], which is expressed below as:

$$I(z) = 4I_m \sin^2(\beta_m z), \tag{7.9}$$

where $I(z)$ is the intensity distribution profile of the m^{th} longitudinal mode, I_m is intensity of the light travelling in one direction in the cavity, β_m is the wave number of the m^{th} mode and z is the distance along the fibre from one of the mirrors. This might also be related to the sinusoidal index variation profile of the Bragg grating along the fibre axis [Limberger *et al.* 1996] as the thermal response of the laser arises from the dominant contribution of the effective refractive index change with temperature variation of the silica fibre.

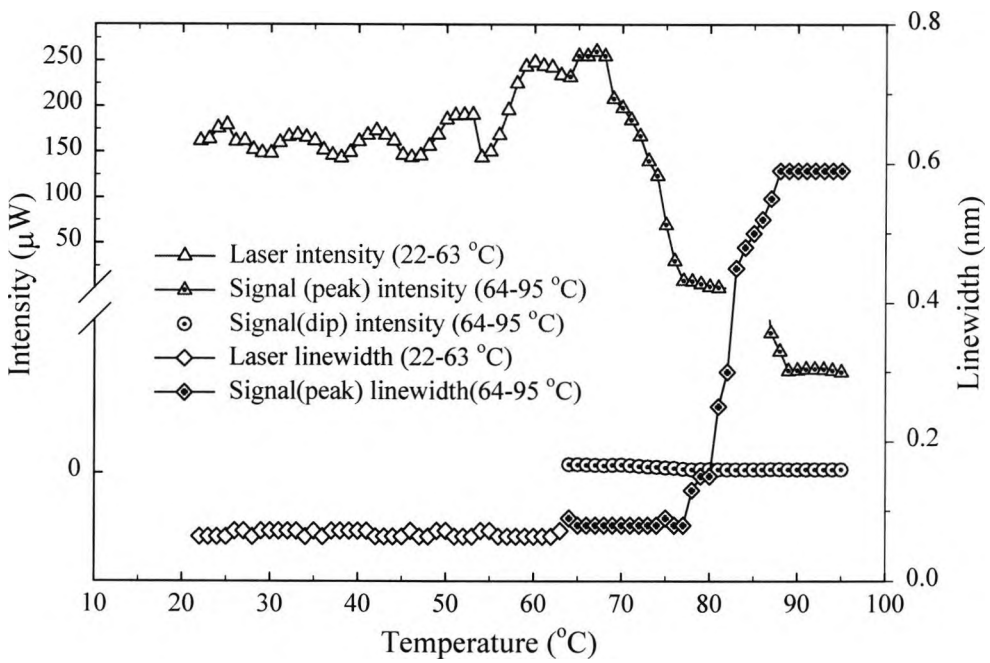

Fig. 7.7: Intensity and linewidth variation with temperature when the low reflectivity grating (LR_1) was placed in the oven for a fixed pump power of 16 mW.

With a further increase in temperature beyond which the transmission dip and the reflection peak were just separated, the peak intensity initially increases for a few degrees (Celsius), then drops down rapidly and finally becomes constant at a point where the laser action totally ceases. The dip in intensity was found to be almost constant over the temperature range from 64 °C to 95 °C and this is clearly seen from the figure. The intensity of the laser was much higher than the comparative intensities of the peak and dip signal, after the laser action totally ceased for the same fixed

pump power. Further, the linewidth of the laser (~ 0.09 nm) was found to be much narrower than the passive sensor linewidth (~ 0.59 nm) beyond the temperature at which the laser action totally ceased.

7.5.1.5 Output spectra

The output spectra of the laser based sensor system are shown in Fig. 7.8, at room temperature (~ 22 °C) and at 95 °C with a fixed pump power of 16 mW.

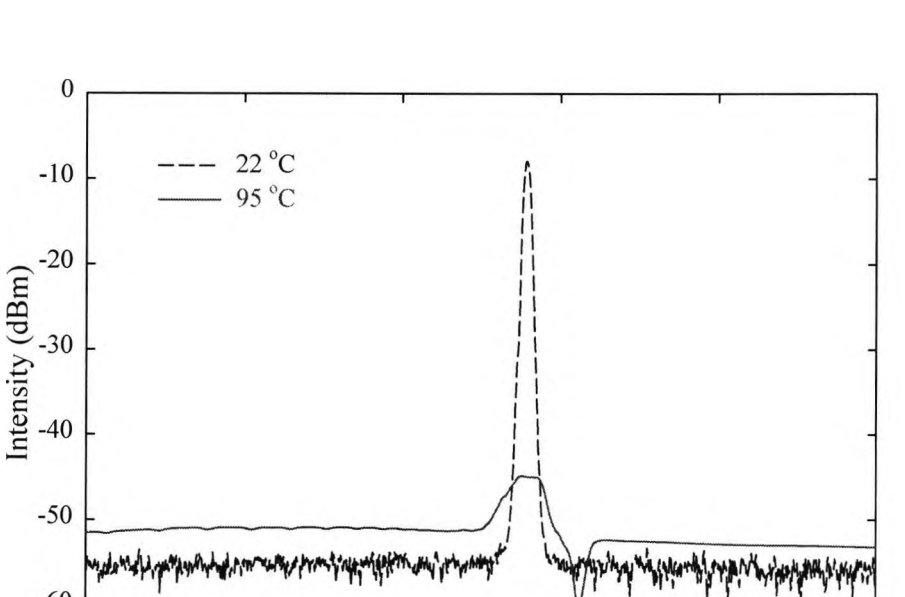

Fig. 7.8: Output spectra of the laser based sensor system at room temperature and at 95 °C when the low reflectivity grating (LR_1) was placed in the oven.

The figure clearly shows that at 22 °C, the signal-to-noise ratio (SNR) of the laser was measured to be ~ 46 dB with a linewidth of ~ 0.09 nm (measured using the OSA with a RBW of 0.1nm), whereas at 95 °C, the transmission dip and the reflection peak were totally separated, with the peak-to-dip intensity (PDI) value of ~ 15 dB, which is much lower than the SNR of the laser and the peak linewidth is much wider than the laser linewidth. At 95 °C, the reflection peak was found to overlap with the laser peak

at room temperature, as the high reflectivity grating (HR_1) was held at ambient temperature and the transmission dip moved towards the longer wavelength side of the spectrum, indicating that the low reflectivity grating (LR_1) responded to the temperature variation.

7.5.2. High reflectivity grating (HR_1 - reflectivity of 99.9 %) in oven

For this experiment, the high reflectivity grating (HR_1) was loosely placed in the oven and the low reflectivity grating (LR_1) was kept at ambient temperature, with the oven temperature being raised from room temperature to 95 °C, during which the temperature data were recorded using the OSA, with a RBW of 0.1 nm, as before. The stable operational range of the laser, the wavelength of which is determined by the Bragg wavelength of the low reflective grating as is seen in Chapter 3, may be expressed through Eq. (7.10) below:

$$HRT_{stable} = T_{room} + \frac{\frac{1}{2}\Delta\lambda_{HR} - \frac{1}{2}\Delta\lambda_{LR}}{S_{LT}}, \tag{7.10}$$

where HRT_{stable} is the stable operational range of the laser (~ 18 °C) above room temperature when the high reflectivity grating (HR_1) was heated. This temperature may be calculated using the linear sensitivity of the laser (6.67 pm/°C), when the low reflectivity grating (LR_1), responded to the temperature changes that was applied.

The unstable operational range of the laser may be expressed through Eq. (7.11) below:

$$HRT_{unstable} = \frac{\frac{1}{2}\Delta\lambda_{HR} + \frac{1}{2}\Delta\lambda_{LR}}{S_{LT}}, \tag{7.11}$$

Using Eq. (7.11), the unstable operational range ($HRT_{unstable}$) of the laser was found to be ~ 51 °C.

The maximum temperature for lasing (and thus the sensor operation) may be expressed through Eq. (7.12) below:

$$HRT_{total} = T_{room} + \frac{\Delta\lambda_{HR}}{S_{LT}}, \qquad (7.12)$$

where HRT_{total} is the temperature at which the laser action will cease when the high reflectivity grating (HR_1) is heated. Using Eq. (7.12), the temperature rise (above room temperature) that is required to quench the laser action totally is ~ 69 °C.

7.5.2.1. Wavelength response of the sensor

Fig. 7.9 shows the response of the laser-based sensor system when the high reflectivity grating (HR_1) was heated from room temperature to 95 °C. The experimental data indicate that from room temperature to 40 °C, the laser wavelength did show only negligible changes with temperature, and this agrees well with the temperature range predicted using Eq. (7.10).

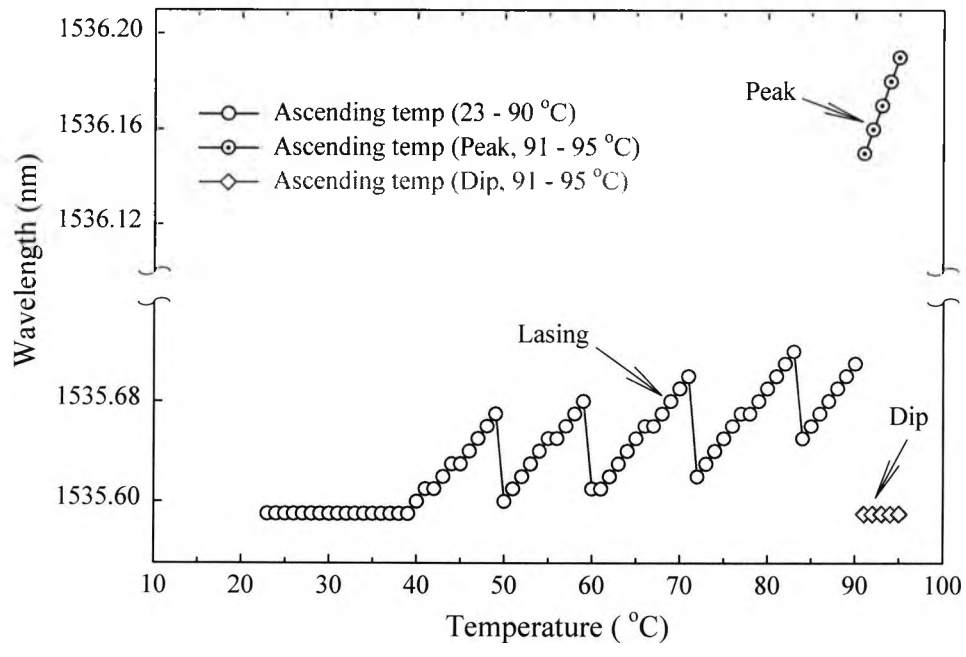

Fig. 7.9: Wavelength response of the laser-based sensor system with temperature, when the high reflectivity grating (HR_1) was placed in the oven and the low reflectivity grating was kept at ambient temperature.

Over the range from 41 to 90 °C, the laser demonstrated mode hopping, due to more rapid variation of its longitudinal mode than the Bragg wavelength of the grating [Kato *et al.* 1999; Hashizume and Nasu 2001]. The slope of the laser mode hopping profile corresponds to the temperature dependence of the longitudinal modes of the laser cavity and was found to lie in the region ~ 8.0 – 9.1 pm/ °C, which is ~ 28 % (on average) higher than the linear sensitivity of the laser of 6.67 pm/ °C. The mode hopping temperature region was ~ 9-11 °C. This unstable temperature range (50 ±1 °C) agrees well with the value predicted using Eq. (7.11). The small level of uncertainty (± 1°C) quoted arises from the variation of the room temperature, as the low reflectivity grating was kept at ambient temperature and also from the "smoothness" of the grating spectrum used, as mentioned earlier. At 91 °C, the reflection peak and the transmission dip were totally separated. At temperatures above 91 °C, the reflection peak continued to vary with temperature as the high reflectivity grating (HR_1) was placed in the oven and the transmission dip was found to remain constant at the Bragg wavelength of the low reflective grating (LR_1), as it was kept at ambient temperature. Thus the temperature required to quench the laser action agrees well with that calculated using Eq. (7.12).

7.5.2.2. Intensity and linewidth variation

Fig. 7.10 shows the intensity and the linewidth variation with temperature from room temperature to 95 °C, at a fixed pump power of 16 mW. The figure shows that the intensity remains almost constant from room temperature to 40 °C, where the laser wavelength showed negligible changes with temperature (see Fig. 7.9). With a further increase in temperature, the intensity varies with almost the same trend as the wavelength change over the temperature range from 41 °C to 90 °C, with a slope of ~ 8 μW/ °C from 40 °C to 71 °C and then showing a gradually decreasing trend from 72 °C to 90 °C. At 91 °C, the reflection peak and the transmission dip were totally separated and the intensity of both decreased to a level of a few nW, for the same fixed pump power. By contrast, there was no significant change in the linewidth observed from room temperature to 90 °C, beyond which the linewidth increases

significantly, remaining almost constant (~ 0.62 nm) and this corresponds to the temperature where the laser action totally ceases.

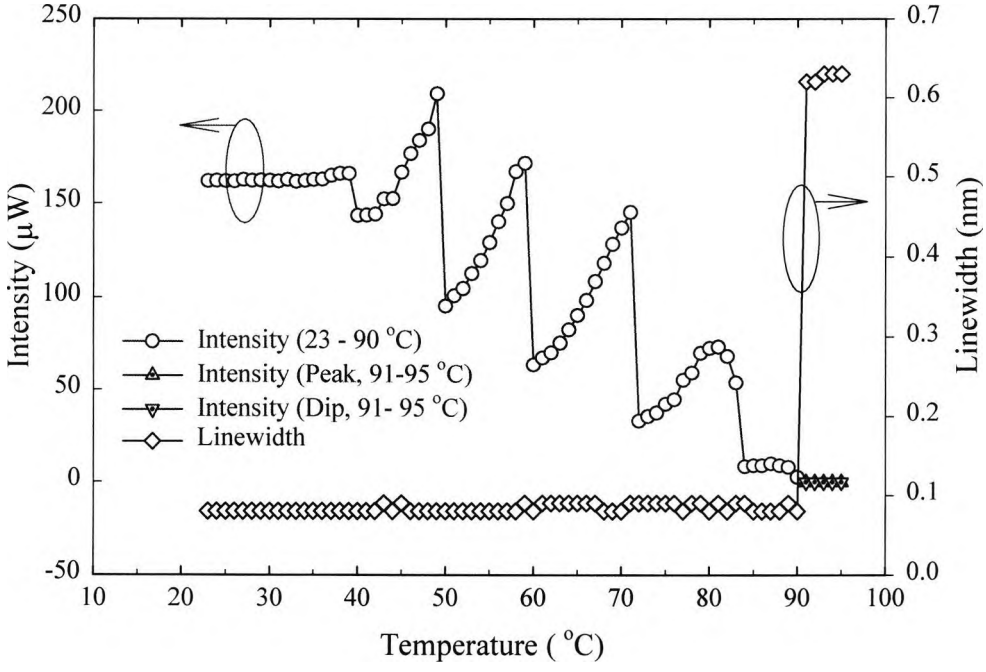

Fig. 7.10: Intensity and linewidth variation with temperature from room temperature to 95 °C when the high reflectivity grating (HR_1) was placed in the oven with a fixed pump power of 16mW.

7.5.2.3. Output spectra

Fig. 7.11 shows the output spectra of the laser-based sensor system at room temperature (~ 23 °C) and at 95 °C; with a fixed pump power of 16 mW. At room temperature, the signal-to-noise ratio (SNR) of the laser was found to be ~ 46 dB with a linewidth of ~ 0.09 nm (measured using the OSA as before) whereas at 95 °C, the reflection peak and the transmission dip were totally separated, with a dip-to-peak intensity (DPI) value of ~ 15 dB, which is much lower than the SNR of the laser. In addition, the peak width is much greater than the laser linewidth. By contrast, at 95 °C, the transmission dip corresponds to the laser peak at room temperature and the reflection peak was found to be on the longer wavelength side of the spectrum, as the

high reflectivity grating (HR_1) was placed in the oven and the low reflectivity grating (LR_1) was kept at ambient temperature. This is just the opposite of the case illustrated by the spectrum shown in Fig. 7.8, for the low reflectivity grating in oven.

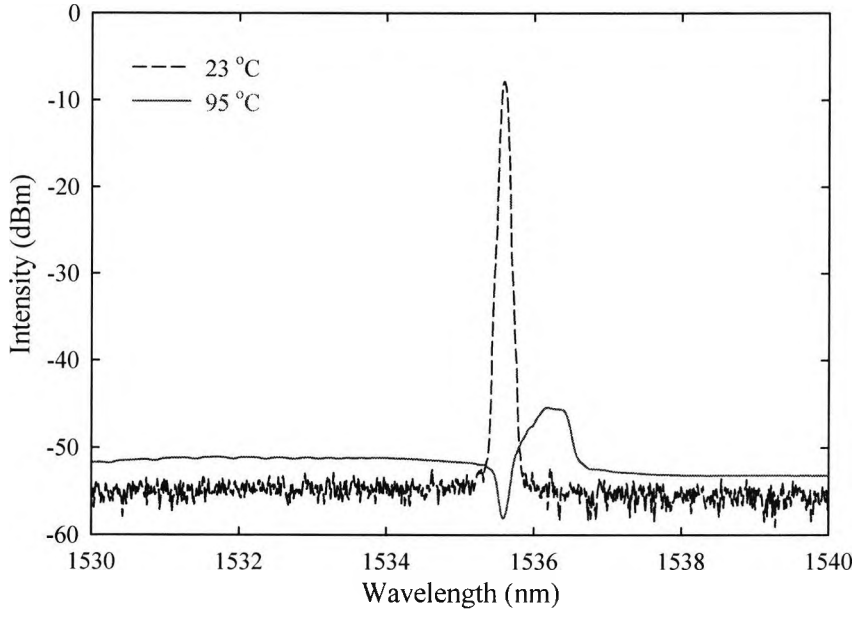

Fig. 7.11: Output spectra of the laser based sensor system at room temperature and at 95 °C when the high reflectivity grating (HR_1) was placed in the oven.

7.5.3. Laser sensor created with both gratings in oven

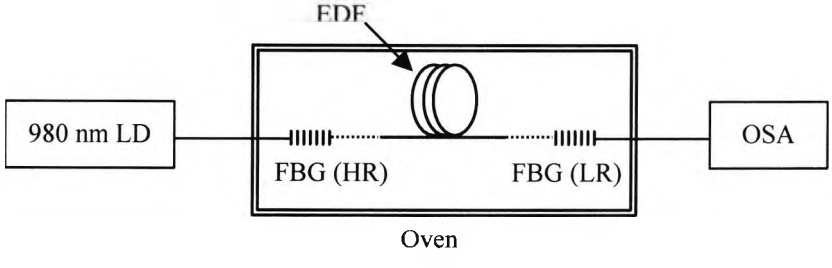

Fig. 7.12: Schematic of the experimental set-up of the laser probe with both the gratings in oven.

The sensor in this case comprised the whole length of the fibre laser, albeit with a very short cavity to minimise the spatial dimensions of the sensor probe itself and the

schematic of the experimental set-up is shown in Fig. 7.12. A similar wavelength-matched normal Bragg grating pair was created in B-Ge co-doped fibre having reflectivity of ~ 99.6 % with a FWHM bandwidth of 0.37 nm (FBG (HR)) and of ~ 86.6 % with a FWHM bandwidth of 0.25 nm (FBG (LR)) and their reflection spectra were shown in Fig. 7.13. The figure clearly shows that the Bragg wavelengths of both the gratings were matched at ~ 1535.34 nm. This was measured using the OSA with a RBW of 0.1 nm, at room temperature, after the gratings were annealed at 100 °C for the same period. These FBGs were fusion spliced to a short length of Er^{3+} fibre of 5.9 cm (Er 123: erbium-fibre details are given in Table 7.1) to form the laser cavity, and pumped by using a 980 nm laser diode with a fixed pump power of 18 mW. The laser output was monitored through the low reflectivity grating (LR) using the OSA with a RBW of 0.1 nm. For an Er^{3+} fibre length of ~ 5.9 cm, the cavity mode spacing was found to be 1.75 GHz or 14 pm (with n = 1.45 for silica fibre). As a result, the maximum number of longitudinal modes of the laser that would be possible is ~ 7, observable within the limited resolution bandwidth of 0.1 nm of the OSA used.

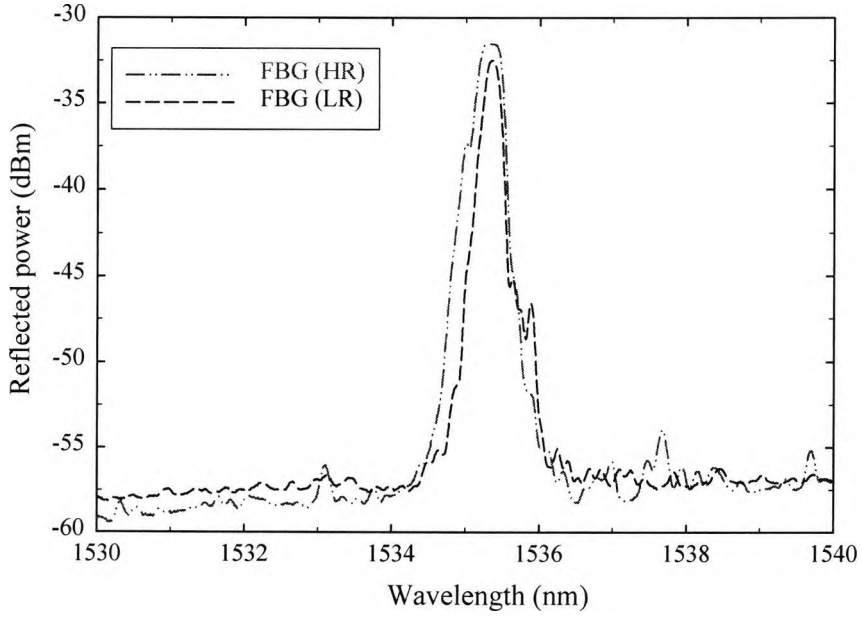

Fig. 7.13: Reflection spectra of both the high reflective (HR) and the low reflective (LR) Bragg gratings at room temperature after annealing.

7.5.3.1. Wavelength response of the laser

Fig. 7.14 shows the response of the laser wavelength with temperature, over the range from room temperature (~ 22 °C) to 95 °C. Initially, the oven temperature was raised in 1 °C steps from 22 °C to 40 °C, then in 5 °C steps from 40 °C to 95 °C, allowing a settling time of ~ 10 minutes at each temperature, before recording the data using the OSA. The thermal sensitivity was calculated using a linear fit to the experimental data (with a COD >0.999 and a SD of 0.0042) and was found to be 9.62 pm/ °C. The relationship of the laser wavelength, λ_L to the temperature, T can be expressed through the equation below:

$$\lambda_L(T) = 1535.12 + 9.62 \times 10^{-3} T, \qquad (7.13)$$

where T is the temperature applied (in degree Celsius) to the laser sensor. The figure clearly shows that the device responds linearly (even with a 1 °C step change) to the applied temperatures.

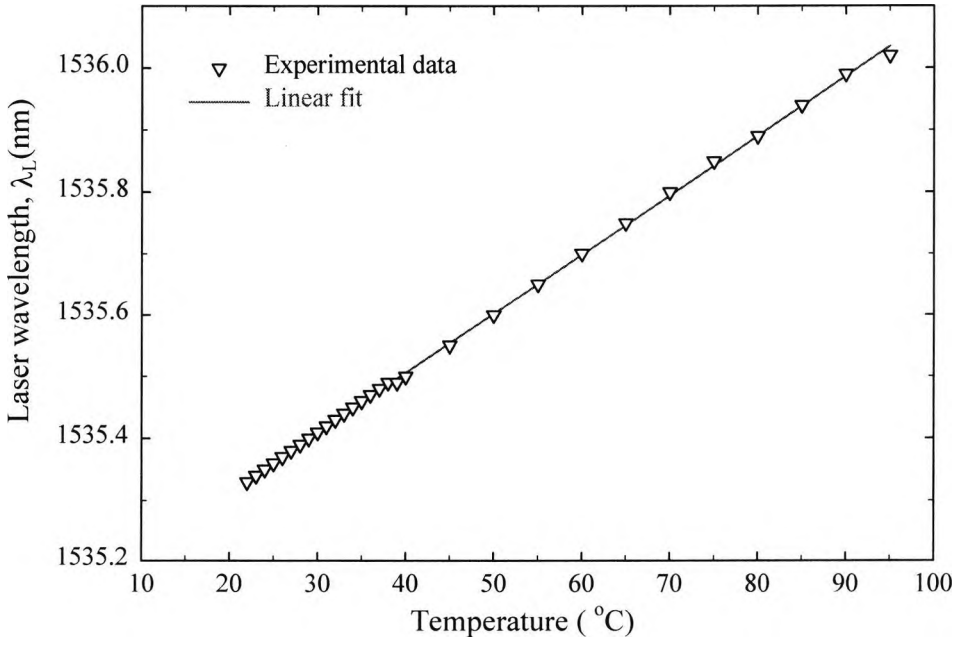

Fig. 7.14: Response of the laser wavelength with temperature from room temperature to 95 °C when the laser was placed in the oven.

The response was found to be consistent over several measurement cycles, with a repeatability of ± 0.01 nm, using the OSA with a RBW of 0.1 nm. This arrangement forms an ideal basis for a fibre laser temperature sensor over the above temperature range with a relatively short active probe length.

7.5.3.2. Output spectra of the laser

The output spectra of the laser were recorded with increasing temperature and are shown in Fig. 7.15. With increasing temperature, the laser wavelength shifted towards the longer wavelength side of the spectrum, arising from the fractional change in the grating period due to the thermal expansion coefficient of the fibre, along with the change in the fibre effective refractive index due to the thermo-optic coefficient effect, as discussed earlier by Eq. (7.8). The signal-to-noise ratio (SNR) of the active sensor was found to have decreased from 40 dB to 16 dB, for a temperature change of 22 °C to 95 °C, with a fixed pump power of 18 mW of 980 nm LD.

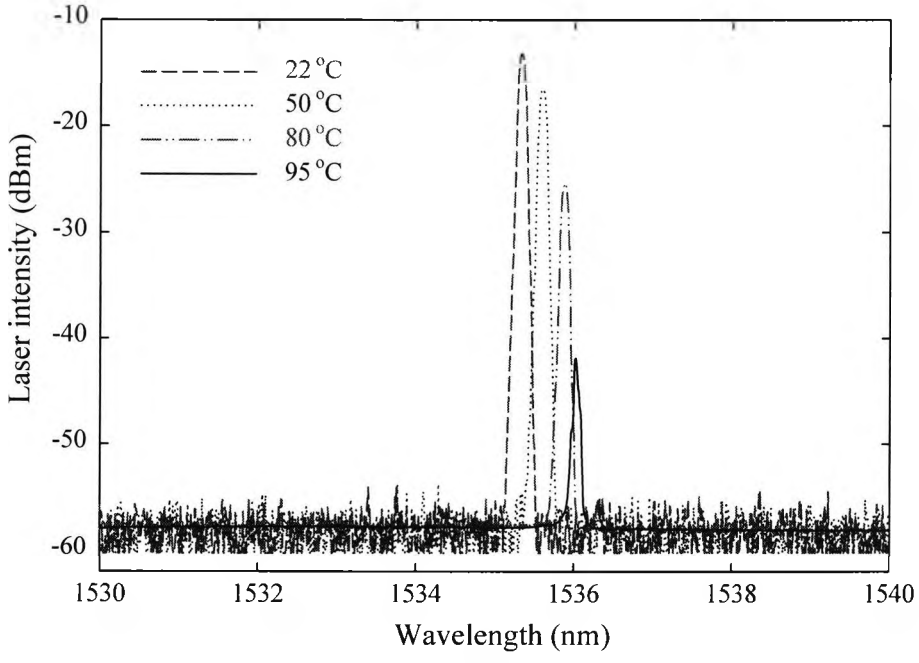

Fig. 7.15: Output spectra of the fibre laser at various temperatures from room temperature to 95 °C with a fixed pump power of 18 mW.

7.5.3.3. Intensity and linewidth variation of the laser

Fig. 7.16 shows the intensity and the linewidth variation of the laser over the temperature range from room temperature (~ 22 °C) to 95 °C, for the same fixed pump power. The laser intensity was found to decrease continuously with the increase in temperature. Zhang *et al.* [1998] have undertaken detailed investigations of the temperature characterisation of several different concentrations of erbium-doped fibre samples, and in a similar way the fluorescence lifetime of the Er^{3+} ions was found to decrease continuously with the increase in temperature (when excited using a 810 nm laser source, thus lowering the laser conversion efficiency).

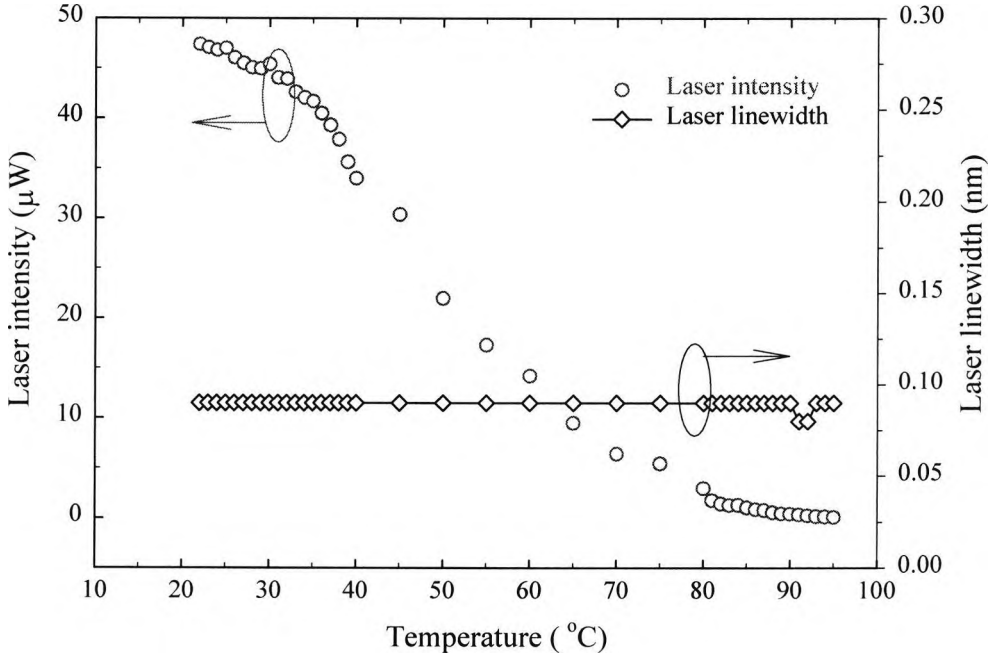

Fig. 7.16: The intensity and the linewidth variation of the laser from room temperature to 95 °C with a fixed pump power of 18 mW.

Imai and Hokazono [1997] and Pal *et al.* [2003] have also shown a continuous decrease in the fluorescence intensity seen from the erbium-doped fibre with increase in temperature. This scheme was used in the fluorescence intensity-based temperature sensing applications, when excited using 1480 nm or 980 nm pump sources. As a

result, the decrease in the SNR value of the laser is kept directly related to the fluorescence properties of the erbium-doped fibre used as the gain medium. However, the linewidth (~ 0.09 nm measured using the OSA) of the laser was found to be almost constant over the measured temperature range from 22 °C to 95 °C.

In all the experiments reported here, the applied temperature was limited to the range from room temperature to 95 °C (to ensure stability and reproducibility of the sensor system up to this temperature), since all the Bragg gratings were annealed at 100 °C prior to the experiment.

7.6. Summary

Laser-based sensor systems have been developed and discussed in details in Chapters 4, 5 and 6. They have been shown to be promising for wider range measurements applications (demonstrated for temperature in Chapters 4, 5; and extended for strain measurements in Chapter 6) where the laser cavity was formed using a normal Bragg grating and a chirped Bragg grating as optical feedback elements. In those studies, only the normal grating was allowed to respond to the temperature or the strain change and the chirped grating was kept at a fixed temperature. The operational range of the laser was determined by the optimum wavelength selection of the normal grating, the bandwidth of the chirped grating employed (over which the laser was measurand-tuned) and the temperature sustainability of the normal grating for temperature measurements, at elevated temperatures. Ball *et al.* [1993] have reported a simple wavelength-matched Bragg grating-based laser system for temperature and strain sensing applications as well as a continuously tuneable laser source [Ball and Morey 1992], where both gratings were kept in the same uniform state, irrespective of the temperature or strain variation. In this Chapter, when an individual Bragg grating was allowed to respond to the temperature variation in the laser configurations described, a very close relationship between the grating bandwidth and the temperature was obtained. The theoretically predicted temperature value agrees quite well with the temperature calibrated against conventional sensors in the experiments in both cases. The active element of the probe in this case is simply the grating itself.

When the low reflectivity grating (LR_1) was allowed to respond to temperature, the laser shows a very limited linear operational range, typically from room temperature to 55 °C, with a sensitivity of 6.67 pm/°C. On the other hand, when the high reflectivity grating (HR_1) was allowed to respond to temperature, the laser output remains stable from room temperature to 40 °C. An unstable operational range of the laser was found to lie between the linear (or stable) operational ranges of the temperature and the temperature at which the laser action totally ceases. At 90 (± 1) °C, the laser action totally ceases for the same fixed pump power. By controlling the full-width-half-maximum (FWHM) bandwidth of the Bragg gratings, the operational range of the laser could be designed to meet a different range of applications requirement.

In a similar way, when the short cavity length laser sensor (Fig. 7.12) was exposed to temperature variations, a linear response of the laser wavelength was observed over the temperature range from room temperature to 95 °C, showing a sensitivity of 9.62 pm/°C. The output power of the laser was observed to decrease continuously with the increase in temperature, which limits the signal-to-noise ratio (SNR) of the laser for high temperature monitoring applications. However, the output power of the system could be improved by employing an additional fibre amplification stage external to the probe; and with that the SNR of the active system, as reported by Ball and Morey [1994], but in doing so, creating a complex system overall.

For the characterisation of individual Bragg gratings acting as probes in a laser configuration, a relatively longer length (5 metres) of erbium-doped fibre with a lower dopant concentration (350-400 ppm of Er^{3+} ion) was chosen to achieve a higher level of pump power absorption along the length of fibre and at the same time to minimise the fluorescence lifetime quenching effect [Zhang *et al.* 1997]. By contrast, shorter length (~ 5.9 cm) of erbium-doped fibre with a higher dopant concentration (5000 ppm of Er^{3+} ion) was chosen to achieve a higher level of the fluorescence intensity when the whole laser itself formed the probe and was placed within the uniform temperature region (~10 cm) of the oven.

This research was carried out to impact on the optimum design of uniform wavelength-matched Bragg grating based-laser systems for sensor applications; examining two different configurations - one where both gratings are not to be exposed to the same measurand-state e.g. temperature and the other where the sensor probe is composed of the whole laser cavity, including both gratings. The high signal-to-noise ratio and the narrow linewidth in the laser signal, compared to a passive grating-based sensor scheme are important factors for the use of a laser-based sensor in dense wavelength division multiplexed (DWDM) applications (i.e. representing several different sensor channels).

The results reported in this Chapter have shown that the sensor, comprised of a short laser cavity *as a whole* forming the probe, offers superior performance over a wider range, as is seen by comparing the results shown in Fig. 7.14 with those in Fig.7.4 (the low reflectivity grating was allowed to respond to temperature and the high reflectivity grating kept at ambient temperature). In the following Chapter, the laser-based sensor concept will be further extended for a simple multiplexed sensor application using a wider bandwidth of the chirped grating and multiple Bragg gratings to form the laser cavities used.

7.7. References

- Ball, G.A. and Morey, W.W. (1992) Continuously tunable single-mode erbium fiber laser, *Opt. Lett.*, vol. 17, pp. 420-422.
- Ball, G.A., Morey, W.W. and Cheo, P.K. (1993) Single-and multipoint fiber-laser sensors, *IEEE Photon. Technol. Lett.*, vol. 5, pp. 267-270.
- Ball, G.A. and Morey, W.W. (1994) Compression tuned single-frequency Bragg grating fiber laser, *Opt. Lett.*, vol. 19, pp.1979-1981.
- Hashizume, N. and Nasu, H. (2001) Mode hopping control and lasing wavelength stabilization of fiber grating lasers, *Furukawa Rev.*, vol. 20, pp.7-10.
- Imai, Y. and Hokazono, T. (1997) Fluorescence-based temperature sensing using erbium-doped optical fibers with 1.48 μm pumping, *Opt. Rev.*, vol. 4, pp.117 –120.
- Kato, T., Takagi, T., Hamakawa, A., Iwai, K. and Sasaki, G. (1999) Fiber-grating semiconductor laser modules for dense-WDM systems, *IEICE Trans. Commun.*, no. E82-B, pp. 409-411.
- Kim, H.S., Kim, S.K. and Kim, B.Y. (1996) Longitudinal mode control in few-mode erbium-doped fiber lasers, *Opt. Lett.*, vol. 21, pp. 1144-1146.
- Limberger, H.J., Fonjallaz, P.-Y., Salathe, R.P. and Cochet, F. (1996) Compaction- and photoelastic-induced index changes in fiber Bragg gratings, Appl. Phys. Lett., vol. 68, pp. 3069-3071.
- Pal, S., Sun, T., Grattan, K.T.V., Wade, S.A., S.F. Collins, Baxter, G.W., Dussardier, B. and Monnom, G. (2003) Bragg grating performance in Er-Sn-doped germanosilicate fiber for simultaneous measurement of wide range temperature (to 500 °C) and strain, *Rev. Sci. Instrum.*, vol. 74, pp. 4858-4862.
- Wilson, J. and Hawkes, J.F.B. (1987) *Lasers: Principles and Applications*, Prentice Hall International Ltd, UK, pp. 1-34.
- Zhang, Z.Y., Grattan, K.T.V., Palmer, A.W., Meggitt, B.T. and Sun, T. (1998) Characterization of erbium-doped intrinsic optical fiber sensor probes at high temperatures, *Rev. Sci. Instrum.*, vol. 69, pp. 2924-2929.
- Zhang, Z.Y., Grattan, K.T.V., Palmer, A.W., Meggitt, B.T. and Sun, T. (1997) Fluorescence decay-time characteristics of erbium-doped optical fiber at elevated temperatures, *Rev. Sci. Instrum.*, vol. 68, pp. 2764-2766.

Chapter 8

Multiplexed fibre laser-based temperature sensor systems

8.1. Abstract

The single Bragg grating-based fibre laser approach has been developed in Chapters 4, 5 and 6. In this Chapter, this approach has been extended for parallel multiplexed temperature sensing applications. Multiple laser cavities were formed using a common broadband-chirped grating and several normal fibre Bragg gratings (FBGs) as optical feedback elements, used in conjunction with different lengths of erbium-doped fibres (EDFs) as the active gain media of the laser. To obtain simultaneous laser oscillations, the active gain media were externally pumped by using a 1480 nm laser diode, through a wavelength-matched multiple-splitter. Normal FBGs were used as the wavelength selective and the sensing elements of the laser system. Simultaneous laser oscillation at three different wavelengths through the output channels was obtained. As a result the temperature was measured over the range from room temperature (27 °C) to a maximum of 540 °C. The potential to develop the scheme more broadly as a quasi-distributed sensor scheme is discussed, followed by an overall summary of the Chapter.

8.2. Introduction

In many reported fibre Bragg grating (FBG)-based sensor schemes, the output power reflected from the narrow band FBG-based passive sensor systems is often quite weak, leading to a poor signal-to-noise ratio (SNR) and reducing the potential accuracy of the detection system, thereby creating limitations on the number of FBGs that may be interrogated for multi-sensor applications. Several multiplexed fibre laser-

based sensor systems have been developed for strain sensing applications [Kersey and Morey 1993a, Kersey and Morey 1993b; and Kim *et al.* 2001], but multiplexed fibre laser-based sensor systems for potential temperature sensing applications remain an ongoing challenge. Peng *et al.* [2003] have reported an FBG-based temperature sensor system using a fibre laser to measure the temperature over a short range from 0 to 40 °C. A Raman fibre laser probe has also been developed [Lee *et al.* 2004] for long-distance remote temperature sensing applications, typically reported for use over the range from 30 °C to 100 °C where the laser cavities were formed using two normal FBGs and a tuneable chirped grating in a serial configuration. In Chapters 4 and 5, fibre laser-based sensor systems were developed to measure temperature up to values as high as 500 °C (when 1000 με of strain was applied to the chirped grating in Chapter 5) in a single cavity configuration using a chirped grating and a normal type I or type IIA fibre Bragg gratings. In Chapter 6, a similar laser-based approach was used to measure the temperature up to 500 °C but extended to allow for strain measurement of 0-1200 με using a high temperature sustaining normal type I Bragg grating as the sensor head of the system. Alavie *et al.* [1993] have reported a serial multiplexed Bragg grating based fibre laser sensor system where each laser cavity was formed using a FBG and a broadband mirror, measuring the temperature over the range from 20 °C to 160 °C, with a sensitivity of 13.7 pm/°C.

In this Chapter, a multiplexed temperature sensor scheme has been developed and evaluated using a parallel pump-shared Bragg grating based fibre laser scheme. Multiple laser cavities were formed using a common broadband chirped fibre Bragg grating (CFBG) and several normal fibre Bragg gratings (FBGs) in conjunction with different erbium-doped fibres (EDFs) as the active gain media of the system. To obtain laser oscillation, the active gain media were externally pumped by using a 1480 nm laser diode (LD) through a 1480 nm 1×4 splitter and their outputs were monitored using an Optical Spectrum Analyser (OSA-HP86142A). The wavelength-selective and the sensing capacity of the FBGs over the spectrum of the common broadband chirped grating reflector and the splitter enhance the capability to configure a parallel multiplexed sensor configuration, thus allowing simultaneous multi-channel temperature information from several channels to be extracted, over the wider range

from 27 °C to 540 °C. This scheme also overcomes the limitations of the erbium-doped fibre lasers when used for strain sensing applications with multiple FBG-based sensor interrogation [Kersey and Morey 1993b, Yu *et al.* 2001] where the source of the system operates on a single wavelength by including a tuneable Fabry-Perot filter within the ring cavity.

8.3. Grating Fabrication

8.3.1. Normal Bragg gratings

Four different uniform fibre Bragg gratings were fabricated in germanium (Ge)-doped photosensitive fibre (fibre type: GF1, single mode fibre (SMF); cladding diameter: 125 μm, cut-off wavelength: 1.260 μm, supplier Nufern, Australia) using a KrF excimer laser as the ultra violet (UV) light source and using four different phase masks having different periods (details are summarised in Table 8.1) to inscribe the gratings associated with four different Bragg wavelengths. With laser energy of 12 mJ and a frequency of 200 Hz, it took less than three minutes (on average) of UV exposure to achieve the peak reflectivities of ~ 99 % of the Bragg gratings, with grating length of 6.5 mm each. Four different phase masks were used to achieve the Bragg wavelengths in the fibre ranging from ~ 1544 nm to 1558 nm with a wavelength difference of ~ 3.5 nm for each grating. However, the Bragg wavelength of each grating lies within the well-known fluorescence band of the erbium-doped fibre used as the gain medium of the laser. The transmission spectra of the grating profile were monitored online during their fabrication using the OSA, where the transmission spectrum of each grating is shown in *Section 8.4*. The detailed growth behaviour of the uniform gratings in this type of photosensitive fibres is given in Chapter 2.

Table 8.1: Specifications of different phase masks used to fabricate the uniform fibre Bragg gratings.

Phase masks	Period (nm)	Zero-order	Supplier
1	1066.4	2.8 %	O/E Land Inc., Canada
2	1069.9	0.18 %	O/E Land Inc., Canada
3	1073	2.05 %	O/E Land Inc., Canada
4	1076.6	1.35 %	O/E Land Inc., Canada

8.3.2. Chirped Gratings

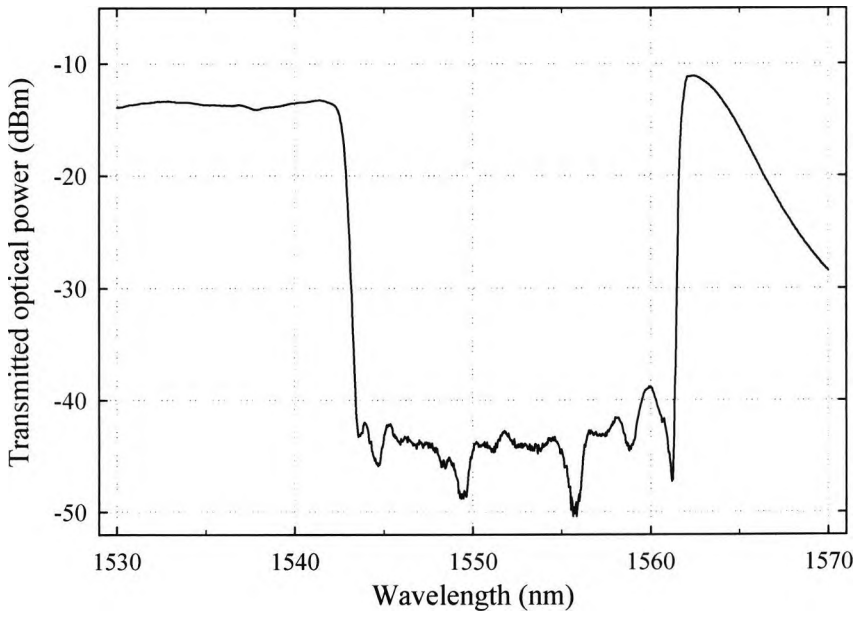

Fig. 8.1: Transmission spectrum of the chirped Bragg grating at room temperature.

For this scheme to be successful, it was essential to have a broadband reflector with a bandwidth large enough to cover the wavelength range of the above narrow band FBGs to be used. To achieve this, a broadband chirped grating was fabricated at Nanyang Technological University, Singapore, using a 100 mW continuous UV-laser emission through a scanning phase mask technique in hydrogen loaded boron-

germanium (B-Ge) co-doped fibre. The chirp rate of the phase mask is 2.25 nm/cm. The fibre was chosen due to its high photosensitivity and achieving a reflectivity of more than 99 % with a full-width-half-maximum (FWHM) bandwidth of ~ 20 nm with a centre wavelength of ~ 1552 nm. The transmission spectrum profile of the chirped grating used is shown in Fig. 8.1.

8.4. Annealing of the normal gratings

To ensure the stability and the wavelength reproducibility of the gratings, it was necessary to anneal them at a temperature higher than the maximum operating temperature of the sensor, since these gratings would form the active elements of the sensor probes.

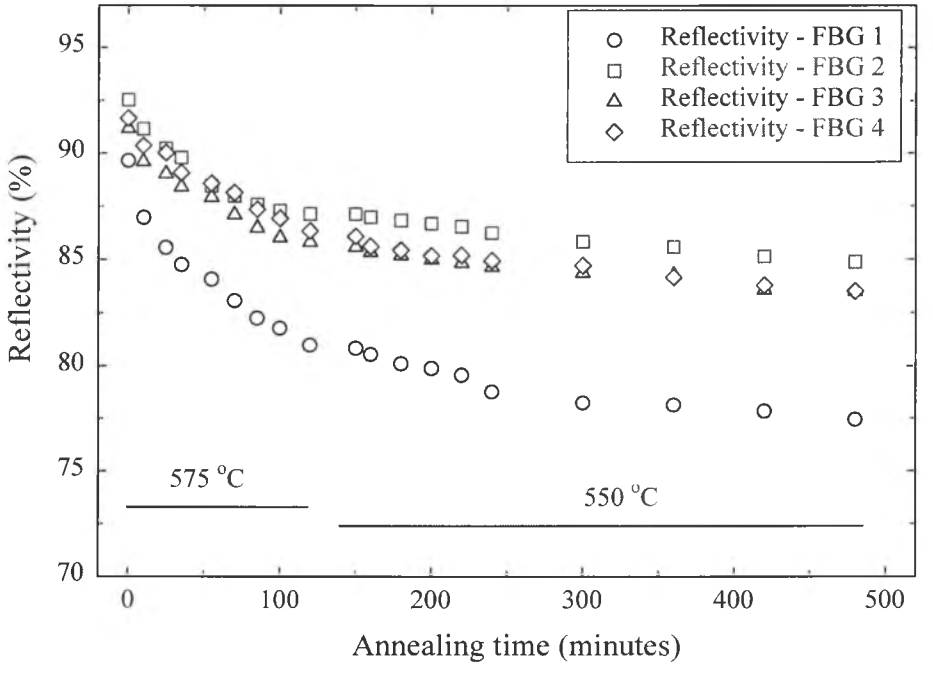

Fig. 8.2: Decay in the reflectivities of the normal Bragg gratings at an annealing temperature of 575 °C for two hours, followed by the temperature of 550 °C for six further hours.

To do so, all four normal gratings used were placed loosely in a well-calibrated oven (MTF 12/38/400) for annealing at appropriate temperatures. Initially this was done at 575 °C for two hours, followed by their being held at a temperature of 550 °C for six more hours to remove the transient, unstable characteristics of the gratings and thus to ensure reproducibility up to this temperature. During the annealing, by the time the oven temperature reached 575 °C (from room temperature), the gratings had already experienced an initial decay of their reflectivity from ~ 99 % to 90 %, this arising from the degradation of the UV induced refractive index modulation and their reflectivity values dropped to between ~ 81% (FBG1) and ~ 86% (FBG2 to FBG4) during the two hours that annealing was applied.

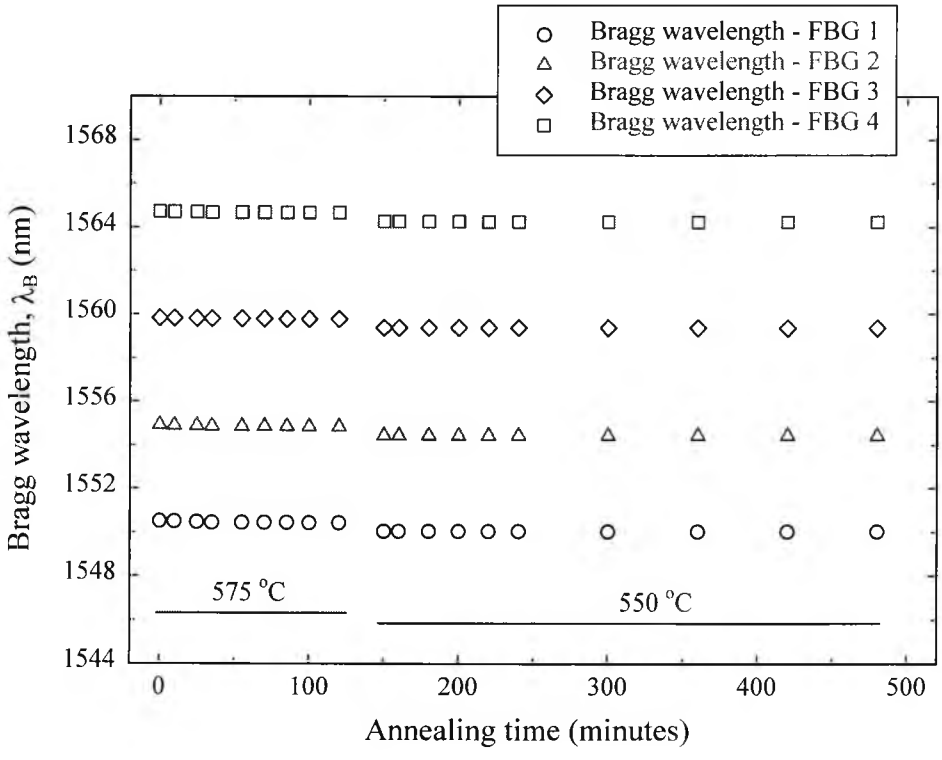

Fig. 8.3: Variation in the Bragg wavelengths of the normal Bragg gratings at temperature of 575 °C for two hours, followed by 550 °C for six further hours.

To retain the reflectivity values of around 80 % for all the gratings, the oven temperature was reduced to 550 °C and the gratings were annealed at this temperature for six hours. Blue shifts in the Bragg wavelengths were also observed, arising from

the degradation of the effective refractive index of the fibre core during the annealing [Pal *et al.* 2003]. Figs. 8.2 and 8.3 show the decay in the reflectivities and the variations of the Bragg wavelengths of the four uniform Bragg gratings during their annealing at temperatures of 575 °C and 550 °C respectively. The reflectivity of grating 1 (FBG1) remained at ~ 75 % with a Bragg wavelength of 1543.04 nm and the reflectivities of the other gratings were ~ 81 % (detailed results are summarised in Table 8.2), measured at room temperature after annealing. Fig. 8.4 shows the transmission spectra of the four normal Bragg gratings at room temperature before and after annealing.

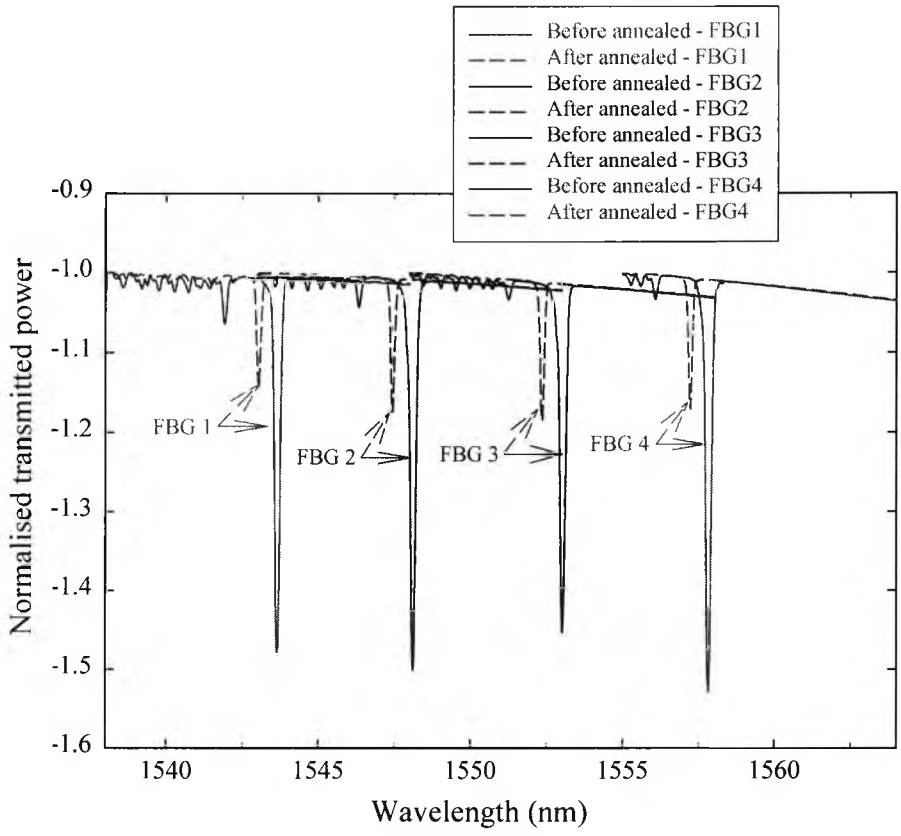

Fig. 8.4: Transmission spectra of the normal fibre Bragg gratings at room temperature before and after annealing.

Table 8.2: Characteristics of the normal fibre Bragg gratings at room temperature before and after annealing.

	Before annealing			After annealing		
Normal FBGs	Bragg wavelength (nm)	Reflectivity (%)	FWHM (nm)	Bragg wavelength (nm)	Reflectivity (%)	FWHM (nm)
FBG 1	1543.64	98.85	0.34	1543.04	74.87	0.20
FBG 2	1548.10	99.17	0.40	1547.44	81.30	0.21
FBG 3	1553.02	98.81	0.38	1552.36	81.52	0.20
FBG 4	1557.82	99.37	0.38	1557.23	80.86	0.20

8.5. Experimental Arrangement

Initially an experiment was performed using a single gain medium (EDF 1 of 5 meters length) being placed in front of the splitter and the normal FBGs were connected to each independent output port of the 1480 nm 1×4 splitter. The schematic of the experimental set-up is shown in Fig. 8.5.

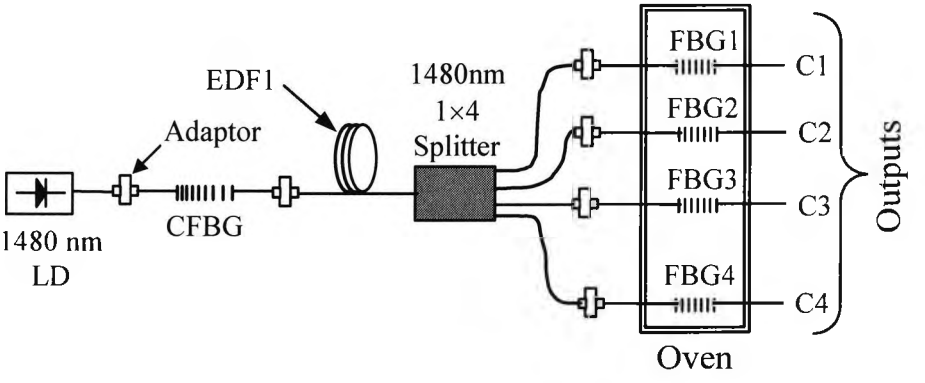

Fig. 8.5: Schematic of the experimental set-up for the parallel-multiplexed Bragg grating-based laser sensor system when a single gain medium was placed before the splitter. CFBG: chirped fibre Bragg grating, EDF: erbium-doped fibre and FBG: fibre Bragg grating.

Four different laser cavities were formed using the common broadband-chirped grating (as the rear reflector) and four thermally annealed, normal FBGs with a single erbium doped fibre (EDF) as the active shared-gain medium of the lasers. Detailed characteristics of the erbium-doped fibre (EDF1) are summarised in Tables 8.3. To obtain laser oscillation, light from a 1480 nm laser diode (LD) with the pump power of 60 mW was launched into the cavities through the common port of the 1480 nm 1×4 splitter and the outputs were monitored using the OSA.

The result showed that severe gain competition was observed among the possible lasing channels. Figs. 8.6 and 8.7 show the laser action seen for channels 1 and 2, observed separately from two different traces from the OSA. Fig. 8.8 shows the gain competition between channels 1 and 2 when the outputs from both channels (Channels 1 and 2) were plotted together in one graph. The gain competition arises from the homogeneous broadening nature of Er^{3+}-ions in the medium which limits the number of lasing modes (generally less than four) and their output power also fluctuates due to mode-competition [Kim *et al.* 2001].

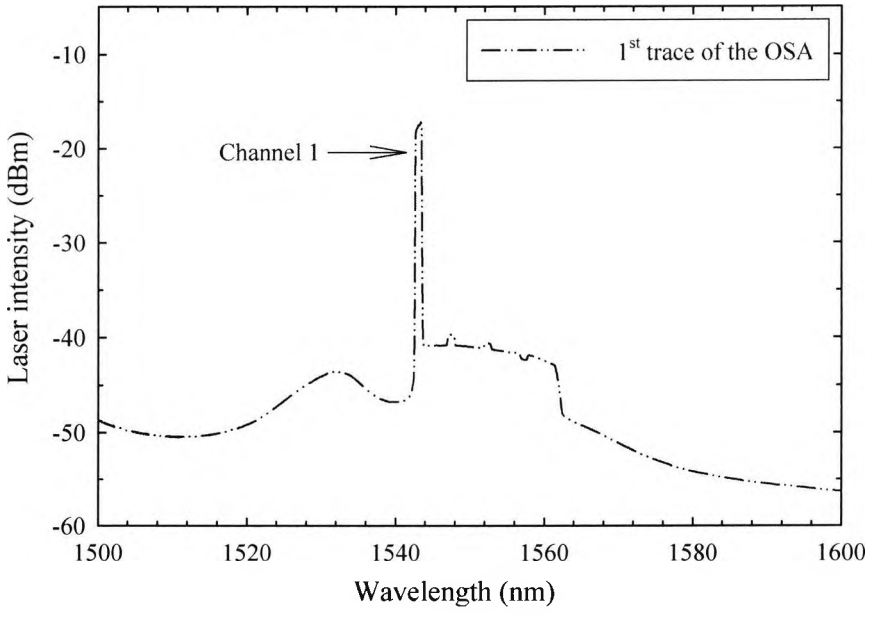

Fig. 8.6: Laser action from channel 1 when a single gain medium (EDF1, 5 metres) was placed before the splitter with a fixed pump power of 1480 nm LD.

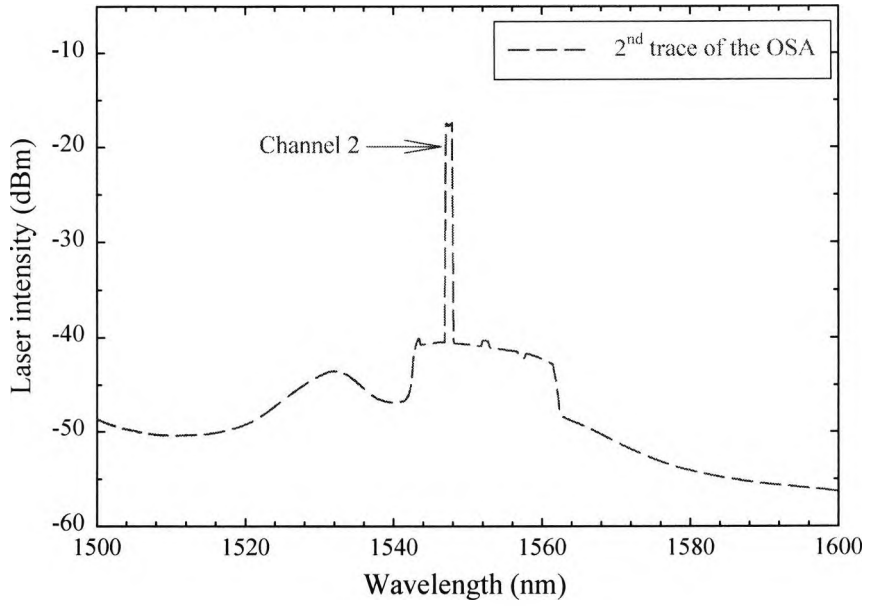

Fig. 8.7: Laser action from channel 2 when a single gain medium (EDF1, 5 metres) was placed before the splitter with a fixed pump power of 1480 nm LD.

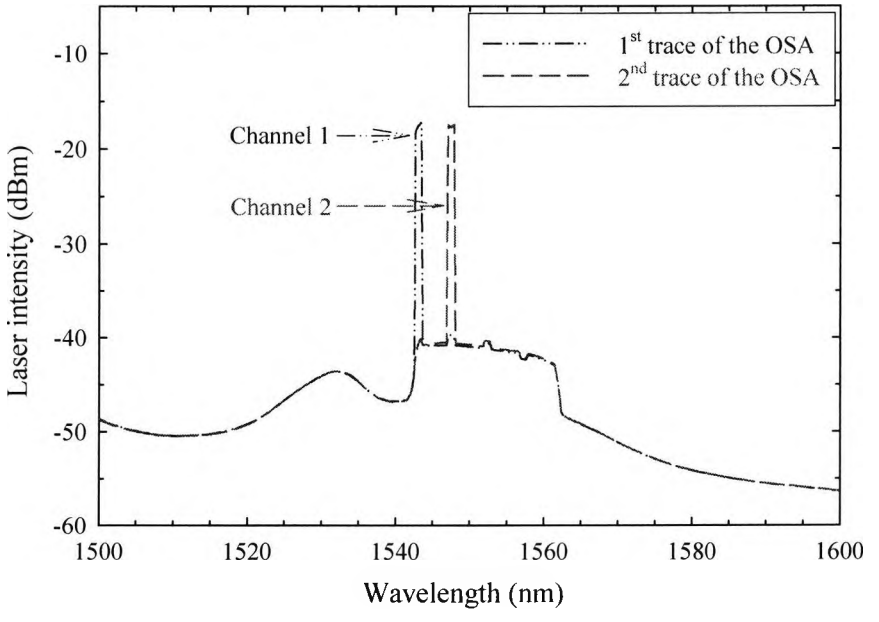

Fig. 8.8: Gain competition between two channels (channels 1 and 2) when a single gain medium (EDF1, 5 metres) was placed before the splitter with a fixed pump power of 1480 nm LD.

A sinusoidal phase-modulator [Zhou *et al.* 2003] or mode locking [Kersey and Morey 1993a] arrangements may be employed in front of the splitter to eliminate the gain competition using a single gain medium.

Table 8.3: Specifications of different erbium-doped fibres (EDFs) used in this work.

Types of EDFs used	Core dopant	Core diameter (μm)	Numerical aperture	Cut-off wavelength (μm)	Supplier
EDF 1	Er_2O_3 (350-400 ppm)+ Ge_2O_3+Al_2O_3	2.3	0.27	0.850	HighWave Optical Tech., France
EDF 2	Er_2O_3 (650-700 ppm)+ Ge_2O_3+Al_2O_3	3.0	0.26	1.0	HighWave Optical Tech., France
EDF 3	Er_2O_3 (3000 ppm)+ Ge_2O_3+Al_2O_3	3.4	0.18	0.895	Moritex Europe Ltd., Sweden

To avoid gain competition, different erbium-doped fibres (EDFs) were fusion-spliced to each independent output port of the 1480 nm 1×4 splitter as the active gain media of the lasers. The schematic of the experimental set-up is shown in Fig. 8.9.

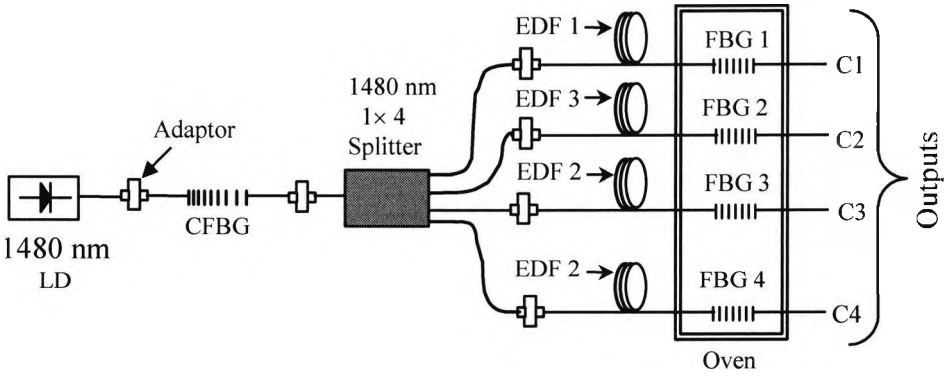

Fig. 8.9: Schematic of the experimental set-up for the parallel-multiplexed Bragg grating-based laser sensor system when a separate gain medium was placed across each channel after the splitter.

Thus four different laser cavities, each with independent-gain media were formed using the common broadband-chirped grating (as the rear reflector) and four thermally annealed, normal FBGs as optical feedback elements of the laser. Detailed characteristics of the erbium doped fibres and the different laser cavity configurations are summarised in Tables 8.3 and 8.4 respectively.

Table 8.4: Characteristics of different laser cavity configurations and lengths of erbium-doped fibres used in this work.

Laser Cavities	Chirped grating	Normal fibre Bragg gratings	Types of Er^{3+} doped fibres	Length of Er^{3+} doped fibres used	Outputs
Cavity 1	Common	FBG 1	EDF 1	12 metres	Channel 1 (C1)
Cavity 2		FBG 2	EDF 3	1 metre	Channel 2 (C2)
Cavity 3		FBG 3	EDF 2	7.5 metres	Channel 3 (C3)
Cavity 4		FBG 4	EDF 2	7.5 metres	Channel 4 (C4)

A longer length of erbium-doped fibre (EDF) was chosen for cavity 1 (EDF 1, 12 m) due to its relatively lower dopant concentration of erbium ions (350-400 ppm) to obtain a higher absorption of the pump power along the fibre length. A shorter length of EDF was used to create cavity 2 (EDF 3, 1 m), owing to its higher dopant concentration of erbium ions (3000 ppm) and two lengths of 7.5 metres of erbium doped fibre with an erbium ion concentration of 650-700 ppm (EDF 2) were used to form cavities 3 and 4 respectively. The input port of the 1480 nm 1×4 splitter was connected to the chirped Bragg grating (CFBG) and the output ports were connected to each cavity discussed above, through adaptors, where the gain media were fusion-spliced to four different normal fibre Bragg gratings (FBGs). The sensing gratings (FBG1 to FBG 4) were placed loosely in the centre of the tube oven (to avoid any axial strain effect which would affect the FBGs characteristic wavelengths) and the chirped grating was kept at ambient temperature. To obtain laser oscillation, light from a 1480 nm LD with the pump power of 70 mW was launched through the common port of the 1480 nm 1×4 splitter to split the pump power approximately

equally across the four channels, this giving ~ 17.5 mW per channel, and the outputs were monitored using the OSA.

8.6. Experimental results

8.6.1. Threshold level of the laser

When a separate gain medium and a normal FBG was connected to each independent output port of the 1480 nm 1×4 splitter, simultaneous laser oscillation at each of three output channels was obtained without gain competition. Fig. 8.10 shows the threshold levels of the lasers for channels 1, 3 and 4 respectively at various pump powers of the 1480 nm laser diode.

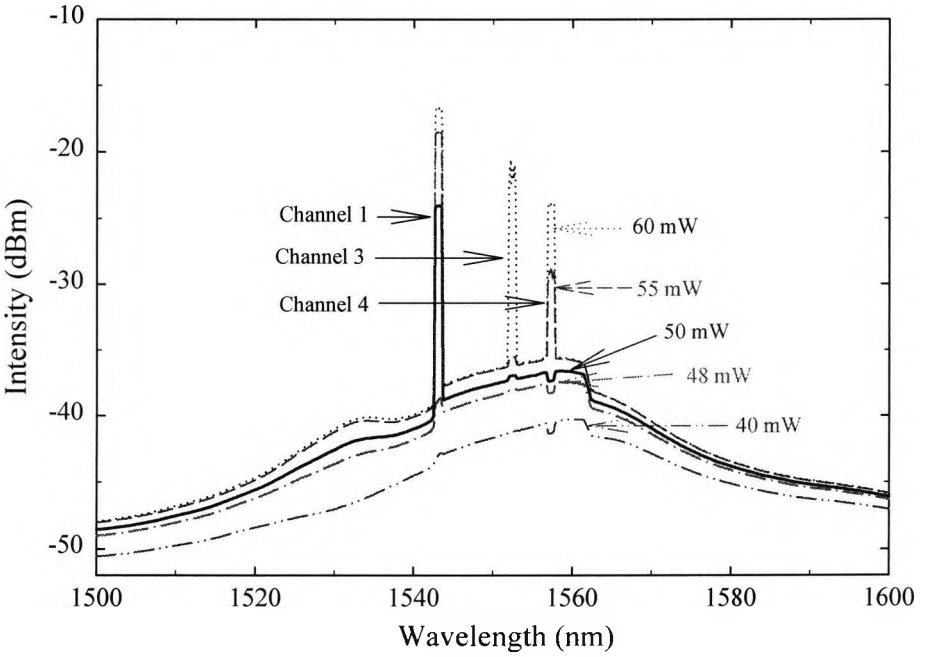

Fig. 8.10: Threshold level of the lasers for channels 1, 3 and 4 at various pump powers of the 1480 mn LD.

For a pump power of 48 mW, the spectra clearly show that the output of channel 1 was close to threshold for lasing and with a small increase in the pump power to 50 mW, lasing was observed. With a further increase in the pump power, the output

power level was easily improved. The next lasing output was observed for channels 4 and 3 with the pump power reaching ~ 55 and 60 mW respectively, whereas no lasing was observed for channel 2, even with the maximum pump power of 100 mW from the 1480 nm LD.

8.6.2. Output spectra

Fig. 8.11 shows such simultaneous laser oscillations at three different wavelengths corresponding to channels 1, 3 and 4 at temperatures of 100 °C and 300 °C respectively and Fig. 8.12 shows the laser outputs at two different wavelengths corresponding to channels 1 and 3 at a temperature of 540 °C, when the outputs were extracted through channel 4 with a fixed pump power of 70 mW at 1480 nm LD.

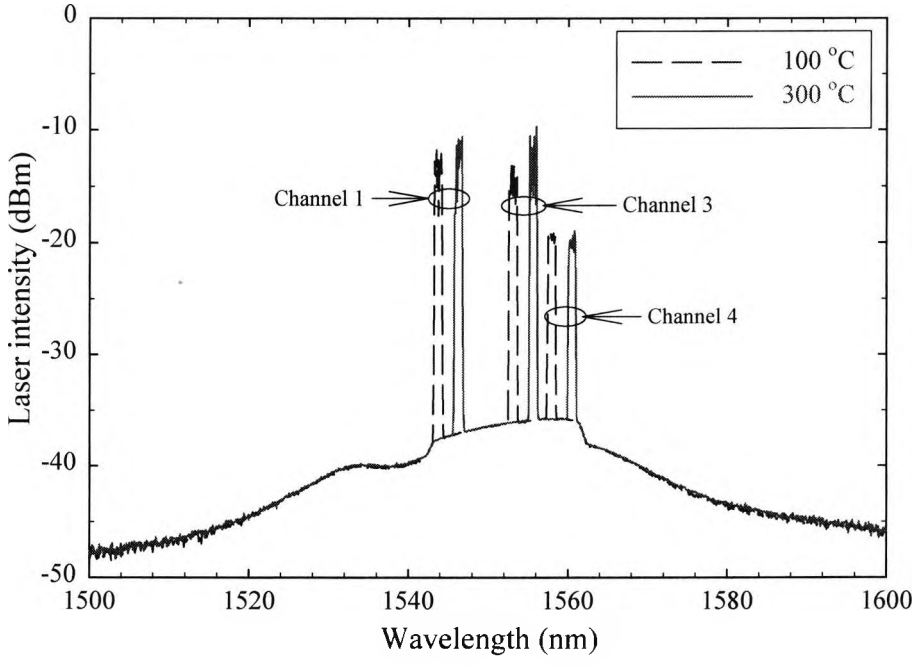

Fig. 8.11: Simultaneous laser oscillations at three different wavelengths for channels 1, 3 and 4 respectively at temperatures of 100 °C and 300 °C, with a fixed pump power of 70 mW of 1480 nm LD when the laser outputs were extracted through channel 4.

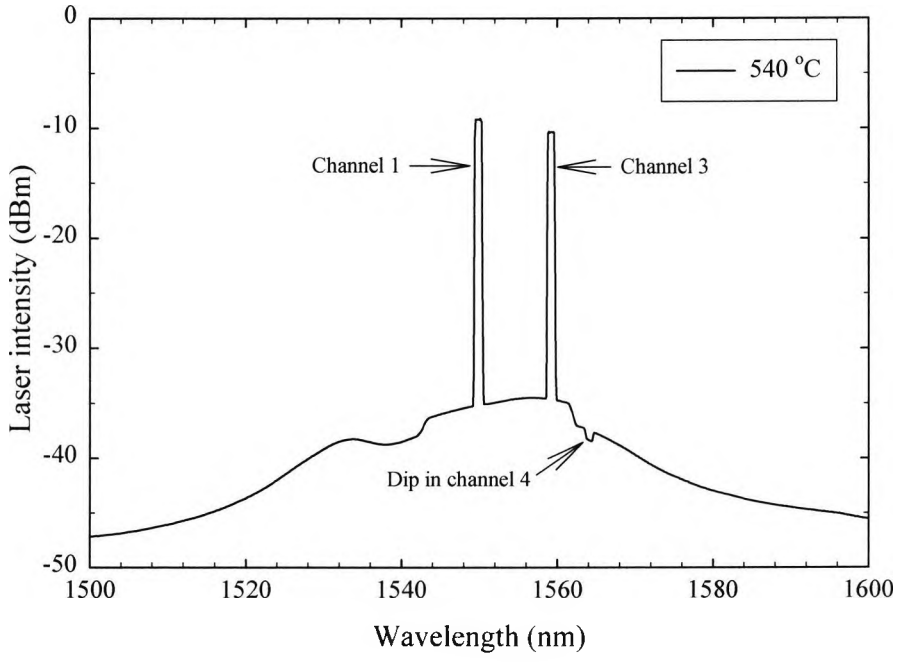

Fig. 8.12: Simultaneous laser oscillations at two different wavelengths for channels 1 and 3 at a temperature of 540 °C with a fixed pump power of 70 mW of 1480 nm LD when the laser outputs were extracted through channel 4.

At 540 °C, the Bragg wavelength of the normal grating used in channel 4 was found to lie outside the bandwidth range of the chirped grating, and as a result the channel simply became a passive sensor, showing small "dip" in the observed spectrum (Fig. 8.12).

Figs. 8.13 and 8.14 show the output spectra of the laser sensors operating at different temperatures over the range from 27 °C to 540 °C for channels 1 and 3 respectively with a fixed pump power of 17.5 mW per channel. For channel 4, the operational range of the laser was limited to a more restricted temperature range where temperature measurements extended only to 400 °C, beyond which the sensor simply became a passive sensor for the same fixed pump power. The output spectra of the channel 4 with different temperatures over the range from 27 °C to 540 °C are shown in Fig. 8.15. With increasing temperature, the laser wavelength shifted towards the

longer wavelength side of the spectrum, this arising from the fractional change in the grating period due to the thermal expansion coefficient of the fibre, along with the change in the fibre effective refractive index due to the thermo-optic coefficient effect, as described in Chapter 4.

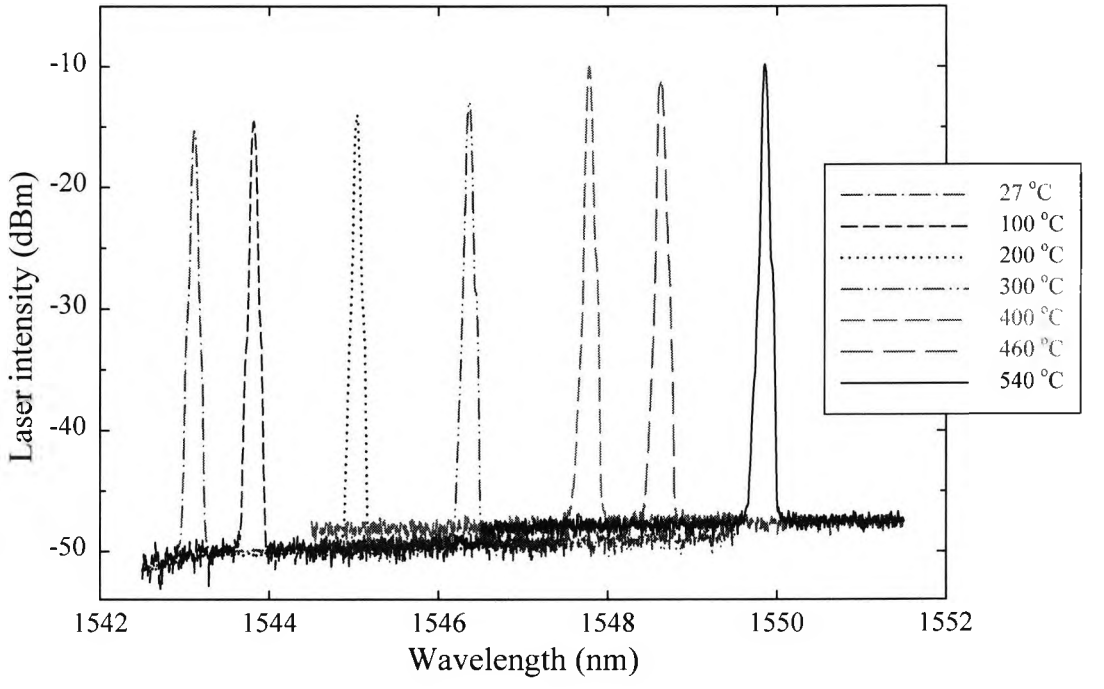

Fig. 8.13: Laser output spectra of channel 1 at different temperatures over the range from 27 °C to 540 °C, with a fixed pump power of 70 mW of 1480 nm LD.

The signal-to-noise ratio (SNR) of the laser was measured to be ~ 35 dB with a linewidth of ~0.07 nm, on average, over the maximum measured range of temperature from 27 °C to 540 °C (for channels 1 and 3 respectively), with an output power variation of less than ± 1.5 dB. This small variation may arise from the non-flat gain profile of the erbium-doped fibres used as the gain media of the lasers over a wide range of temperatures and also from the smooth spectrum profile of the chirped grating used compared to that of the chirped grating spectrum used in Chapter 6.

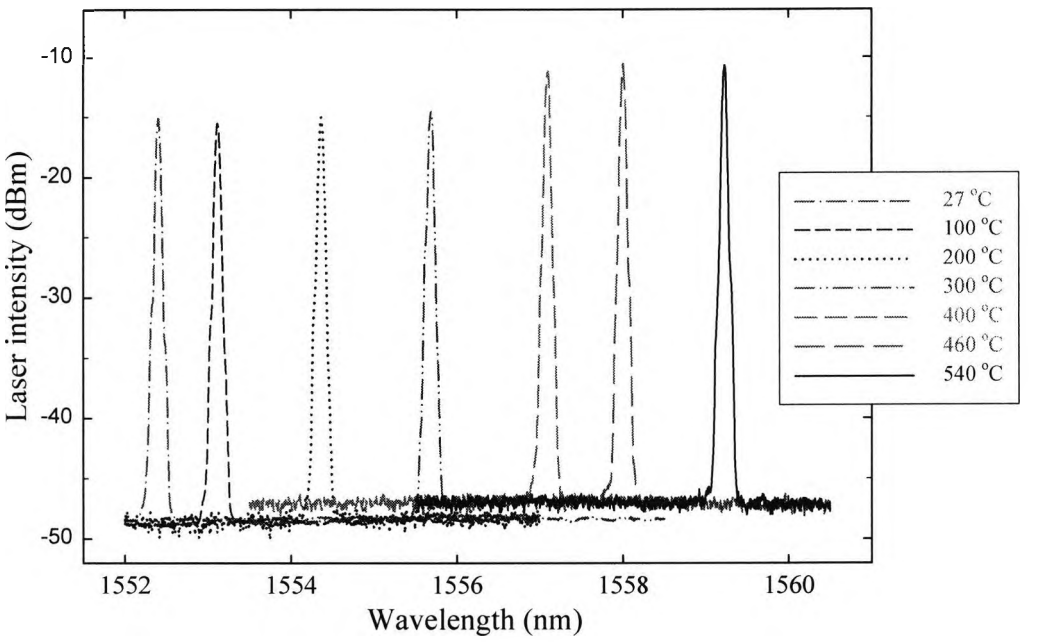

Fig. 8.14: Laser output spectra of channel 3 at different temperatures over the range from 27 °C to 540 °C, with a fixed pump power of 70 mW of 1480 nm LD.

For channel 4, the signal-to-noise ratio (SNR) value was measured to be ~ 26 dB over the temperature range from 27 °C to 380 °C, it then showing a decreasing trend to the situation where the final transition point of the laser was observed to be ~ 400 °C beyond which the channel simply became a passive sensor, with the amplitude of the signal dropped down to ~ 7 dB and then remained constant up to the temperature range of 540 °C for the same fixed pump power of 70 mW of 1480 nm LD.

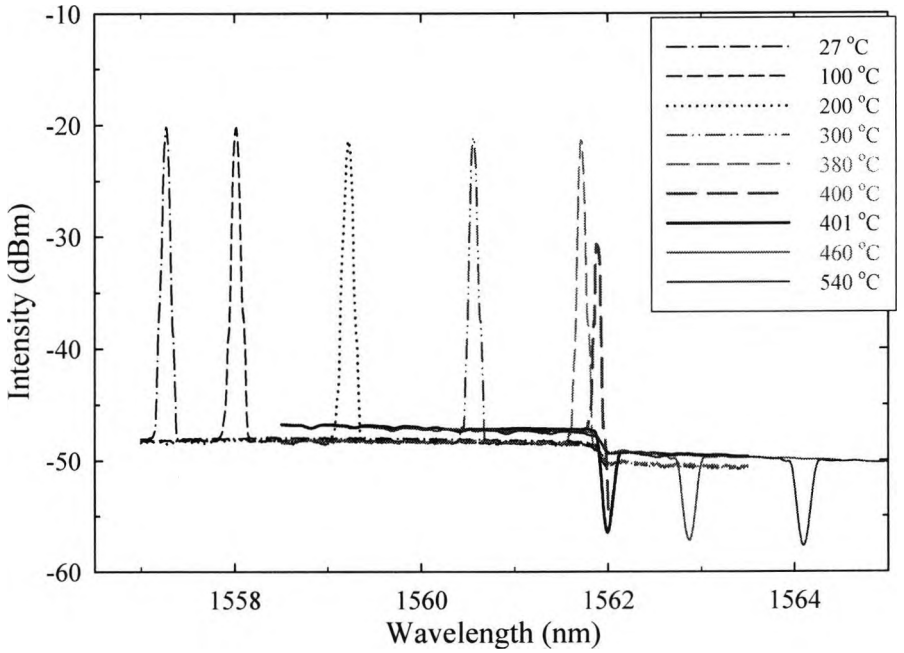

Fig. 8.15: Output spectra of channel 4 at different temperatures over the range from 27 °C to 540 °C, with a fixed pump power of 70 mW of 1480 nm LD.

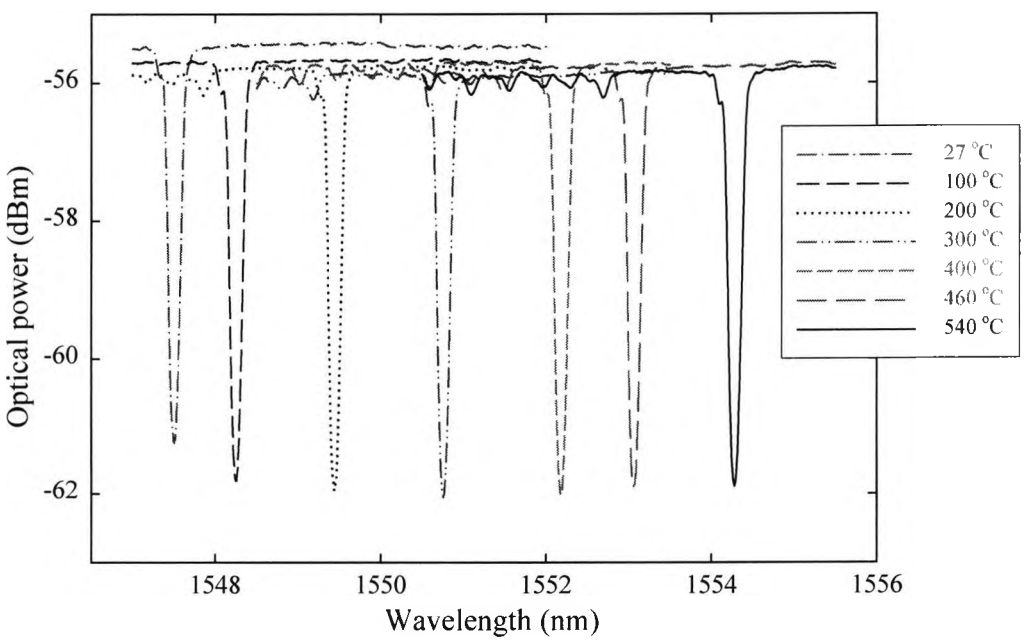

Fig. 8.16: Response of the Bragg wavelength in channel 2 with different temperatures over the range from 27 to 540°C, with a fixed pump power of 70mW of 1480nm LD.

For channel 2, the response of the Bragg wavelength with different temperatures from 27 °C to 540 °C is illustrated in Fig. 8.16, showing that the sensor was operating below the laser threshold level with the same fixed pump power of 70 mW of 1480 nm LD. The laser wavelengths for all the channels measured were consistent with the Bragg wavelengths of the FBGs used, owing to their narrow spectral width (~ 0.20 nm, on average), these being much narrower than that of the chirped grating bandwidth (~ 20 nm). The signal-to-noise ratio of channel 2 is about 6 dB on average, over the measured temperature ranges from 27 °C to 540 °C which is much lower then the SNR of the laser measured in other channels.

8.6.3. Sensor calibration

Fig. 8.17 shows the calibration of the laser wavelengths with temperature over the range from 27 °C to 540 °C for channels 1 and 3 and over the range from 27 °C to 400 °C for channel 4 respectively. The temperature was raised from room temperature to 540 °C, in incremental steps of 20 °C, allowing a settling time of ~ 15 minutes at each temperature to achieve thermal equilibrium between the oven temperature and the sensing gratings, before recording the data using the OSA. The laser wavelengths (λ_L) as a function of temperature (T) can be calibrated using both linear and nonlinear polynomial regressions fitting over the measured temperature ranges. Table 8.5 shows the comparison of the laser calibration for channels 1, 3 and 4 using both linear and nonlinear polynomial regressions fitting over the range from 27 °C to 540 °C (maximum).

For channel 1, the calibration of the laser wavelength (λ_L) as a function of temperature (T) can be expressed through the following equation below:

$$\lambda_L(T) = \begin{cases} 1542.479 + 0.01331T & \text{(Linear)} \\ 1542.771 + 1.03\times10^{-2}T + 5.314\times10^{-6}T^2 & \text{(2nd order)} \\ 1542.819 + 9.41\times10^{-3}T + 9.271\times10^{-6}T^2 - 4.681\times10^{-9}T^3 & \text{(3rd order)} \end{cases} \quad (8.1)$$

For channel 3, the calibration of the laser wavelength (λ_L) as a function of temperature (T) can be expressed through the following equation below:

$$\lambda_L(T) = \begin{cases} 1551.784 + 0.01338T & \text{(Linear)} \\ 1552.069 + 1.05\times10^{-2}T + 5.208\times10^{-6}T^2 & \text{(2nd order)} \\ 1552.116 + 9.56\times10^{-3}T + 9.083\times10^{-6}T^2 - 4.583\times10^{-9}T^3 & \text{(3rd order)} \end{cases} \quad (8.2)$$

For channel 4, the calibration of the laser wavelength (λ_L) as a function of temperature (T) can be expressed through the following equation below:

$$\lambda_L(T) = \begin{cases} 1556.762 + 0.0127T & \text{(Linear)} \\ 1556.938 + 1.034\times10^{-2}T + 5.583\times10^{-6}T^2 & \text{(2nd order)} \\ 1557.011 + 8.57\times10^{-3}T + 1.570\times10^{-5}T^2 - 1.589\times10^{-8}T^3 & \text{(3rd order)} \end{cases} \quad (8.3)$$

where T is the applied temperature (in degree Celsius) to the sensing gratings (FBGs).

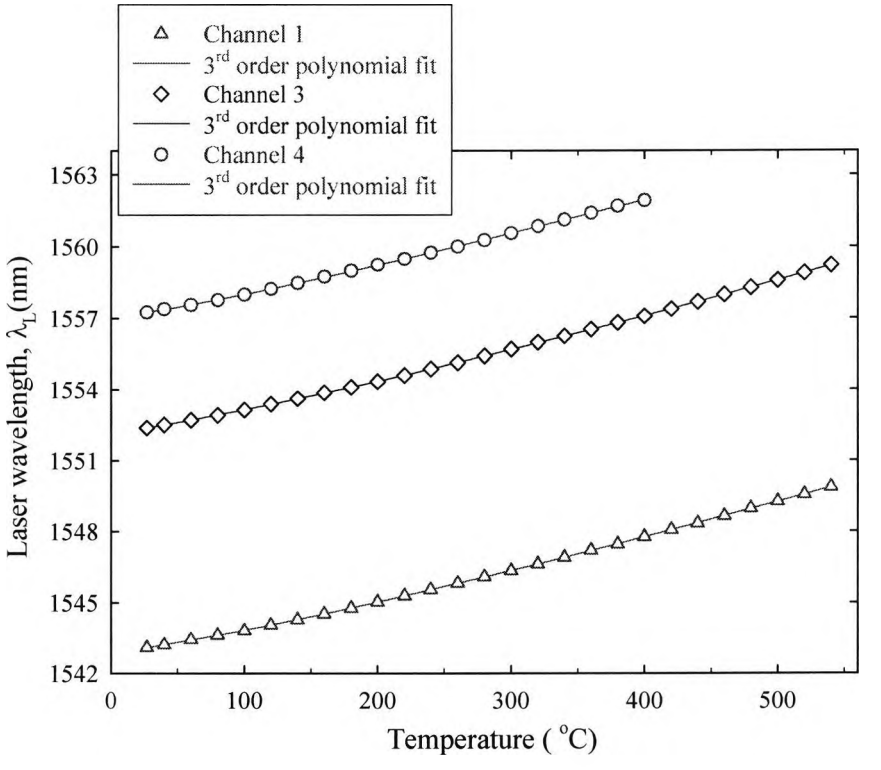

Fig. 8.17: Calibration of the laser wavelengths with temperatures over the range from 27 °C to 540 °C for channels 1 and 3; and from 27 °C to 400 °C for channel 4 respectively.

Table 8.5: Comparison of the laser calibration for channels 1, 3 and 4 using both linear and nonlinear polynomial regressions fitting over the range from 27 °C to 540 °C (maximum).

Parameters		Channel 1	Channel 3	Channel 4	Unit used
Temperature measurement range		27-540	27-540	27-400	°C
Thermal sensitivity with linear fit		13.31	13.38	12.70	pm/°C
Linear fit	Coefficient of determination (COD)	0.99693	0.99853	0.99777	-
	Standard deviation (SD)	0.11933	0.11708	0.07258	-
Thermal sensitivity with 2nd order polynomial fit		10.444 12.426 13.17	10.591 12.533 13.262	10.491 12.573 -	(27 °C) (400 °C) (540 °C)
2nd order polynomial fit	COD	0.99994	0.99994	0.9997	-
	SD	0.0167	0.01733	0.0252	-
Thermal sensitivity with 3rd order polynomial fit		9.657 12.369 13.051	9.802 12.459 13.128	8.982 12.307 -	(27 °C) (400 °C) (540 °C)
3rd order polynomial fit	COD	0.99998	0.99998	0.9999	-
	SD	0.00901	0.01053	0.01641	-
RMS error with linear fit		0.1148	0.1127	0.0689	(nm)
		8.63 8.63 8.63	8.42 8.42 8.42	5.43 5.43 -	(27 °C) (400 °C) (540 °C)
RMS error with 2nd order polynomial fit		0.018	0.0164	0.0233	(nm)
		1.723 1.449 1.367	1.549 1.309 1.237	2.22 1.853 -	(27 °C) (400 °C) (540 °C)
RMS error with 3rd order polynomial fit		0.008	0.0097	0.015	(nm)
		0.828 0.647 0.613	0.989 0.778 0.739	1.67 1.22 -	(27 °C) (400 °C) (540 °C)

Using a linear fitting, the sensitivity was found to be 13.13 pm/ °C, on average, across these channels, with a root mean square (RMS) error value of 0.099 nm in wavelength terms, this being equivalent to 7.5 °C in temperature. Using the polynomial fitting (3rd order), the temperature-dependent sensitivity was found to be 9.48 pm/°C and 12.38 pm/°C (on average) for channels 1, 3 and 4 respectively at 27 °C and 400 °C respectively with an RMS error of 0.011 nm or less than 2 °C, where the sensitivity at 400 °C was 31 % higher than that of the sensitivity at 27 °C.

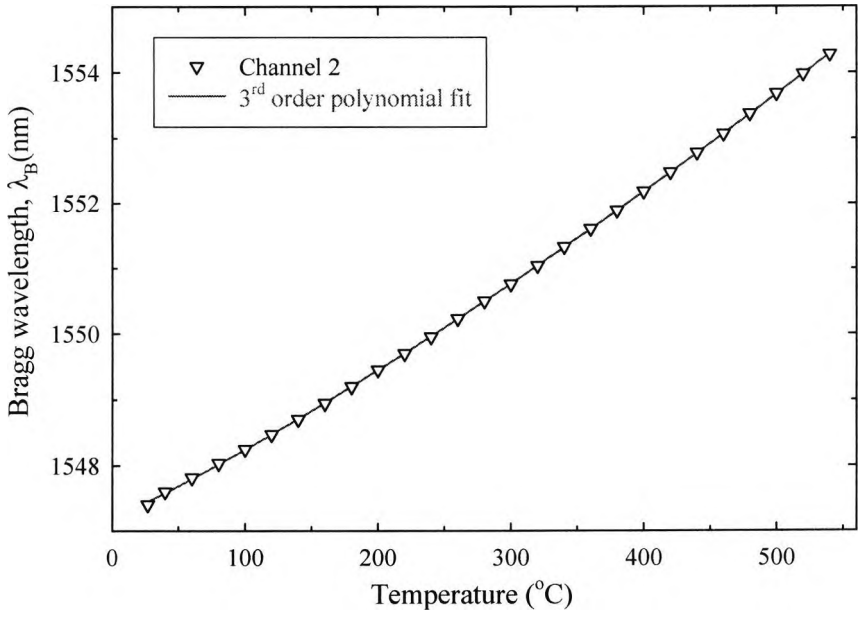

Fig. 8.18: Calibration of the Bragg wavelength with temperature over the range from 27 °C to 540 °C for channel 2 when its output was extracted using the same channel.

Fig. 8.18 shows the calibration of the Bragg wavelength with temperature over the range from 27 °C to 540 °C for channel 2 when its output was extracted through the same channel. Equally the response of the Bragg wavelength (λ_B) for channel 2 as a function of temperature (T) can be calibrated using both linear and nonlinear polynomial regressions fitting and this is expressed through the equation below:

$$\lambda_B(T) = \begin{cases} 1546.869 + 0.01338T & \text{(Linear)} \\ 1547.139 + 1.06\times10^{-2}T + 4.933\times10^{-6}T^2 & \text{(2nd order)} \\ 1547.174 + 9.96\times10^{-3}T + 7.732\times10^{-6}T^2 - 3.311\times10^{-9}T^3 & \text{(3rd order)} \end{cases} \quad (8.4)$$

Comparison of the Bragg wavelength calibration for channel 2 using both linear and nonlinear polynomial regressions fitting over the range from 27 °C to 540 °C is shown in Table 8.6.

Table 8.6: Comparison of the Bragg wavelength calibration for channel 2 using both linear and nonlinear polynomial regressions fitting over the range from 27 to 540 °C.

Parameters		Linear fitting	2nd order polynomial fitting	3rd order polynomial fitting	Unit used
Temperature range		27 – 540	27 – 540	27 – 540	°C
Sensitivity	27 °C	13.38	10.733	10.164	pm/°C
	400 °C	13.38	12.573	12.521	
	500 °C	13.38	13.264	13.168	
Coefficient of determination (COD)		0.99737	0.999947	0.999968	-
Standard deviation (SD)		0.111	0.0160	0.0127	-
Root mean square (RMS) error		0.107	0.015	0.012	nm
RMS error	27 °C	7.99	1.41	1.16	°C
	400 °C	7.99	1.21	0.938	
	540 °C	7.99	1.14	0.892	

Using a linear fitting, the sensitivity was found to be 13.38 pm/ °C, with an RMS error value of 0.107 nm (equivalent to 7.99 °C). Using the polynomial fitting (3rd order) to the experimental data, the temperature-dependent sensitivity was found to be 10.16 pm/°C and 12.52 pm/°C at 27 °C and 400 °C respectively, with an RMS error of 0.012 nm (equivalent to less than 2 °C in temperature).

For the calibration of the temperature measurement data in all the channels (active channels 1, 3 and 4; and passive channel 2) of the sensor, the non-linear regression coefficients showed an improvement in performance compared to that of the linear fitting. The non-linearity in the thermal sensitivity of the sensor over the wider measurement ranges of temperature mainly arises from the non-linear thermo-optic coefficient (ξ) of the silica glass fibre, as derived by Ghosh [1995]. The thermal sensitivity was found to be almost the same for all the channels since the normal Bragg gratings were fabricated in the Ge-doped photosensitive fibre using the same UV laser writing condition and were placed in the same oven for temperature characterisation. For channel 2, a laser-based response was not observed when monitoring through any of the other channels. Channel 2 was simply operating below the laser threshold level and a "flat-line" was observed when the outputs were extracted through any other channels (e.g. channel 4). This can easily be seen from Figs. 8.11 or 8.12. Interestingly, simultaneous laser action at three different wavelengths was easily observed through any of the output channels used.

The calibration of the multiple laser sensors was repeated with both increasing and decreasing temperature over which the sensor performance was found to be reproducible within the resolution bandwidth (RBW) of the OSA (0.06 nm) used, and with essentially no hysteresis being observed over what were repeatable cycles of measurement.

8.7. Summary

A key issue for multiplexed or multi-channel sensor systems is the maximum number of channels that can be interrogated in any sensor configuration. This depends on the bandwidth of the chirped grating, the temperature range required and the sensitivity of the system; the gain profile of the erbium-doped fibre used (~ 1525 nm to 1570 nm) and the total pump power. In this work, an FBG stabilised 1480 nm laser diode was chosen as the pump source, because of its ready availability with high pump power and at this pump wavelength, Er^{3+}-doped fibre is free from excited state absorption (ESA) [Digonnet 1993]. Ge-doped photosensitive fibre was chosen for the fabrication

of the normal FBGs because of their proven long lifetime at elevated temperatures [Pal *et al.* 2003] and also relatively higher level of photosensitivity for efficient writing of the gratings [Sun *et al.* 2001/2002]. In the present experiment, the laser outputs extracted through the sensing FBGs required elevated annealing temperatures (as high as 575 °C for two hours), followed by exposure of 550 °C for six more hours to retain the reflectivity values of ~ 81 %, following the annealing process. This reflectivity was high enough to form the laser cavities.

It was noted that when a single gain medium was used in front of the splitter, severe gain coupling was observed across the channels due to the homogeneous broadening nature of erbium ions in the medium. However, by placing a separate gain medium in each laser cavity, it was possible to obtain a simultaneous response from every output channel without gain competition, thus showing stable output power at each of the laser wavelengths with temperature. Although four normal FBGs were employed to the laser cavities, it was possible only in this preliminary report to obtain laser oscillations at three output channels (channels 1, 3 and 4 respectively), with channel 2 becoming a simple passive FBG sensor due to the threshold level difference among the channels. It is believed that with a lower dopant concentration of erbium-doped fibre (EDF 1: 350-400 ppm of Er^{3+} ions) as the gain medium, simultaneous laser operation at four output channels would be possible, but due to the limitations of the availability of such fibre for the present study, it was not possible in the work reported, but is the interest of future research-activity. A simultaneous response of the laser wavelengths at three output channels (channels 1, 3 and 4 respectively) was observed (through any of the output channels) which reduces the number of detection schemes required. By contrast, the response of the passive sensor (channel 2) was only observable through the same channel, thus requiring a separate detection scheme for every channel in such passive schemes. The signal strength was observed to be much higher for the lasing channels than the passive channels (channel 2 was operating below the laser threshold level and also channel 4 became a passive sensor beyond the temperature range of 400 °C) with the same fixed pump power. For the active sensor, an output power variation of less than ±1.5 dB obtained compared to that of the large power variation of the laser output in Chapter 6. This is due to the smooth spectrum profile of the chirped grating used to form the tunable cavity and

also utilising the fluorescence spectra of the erbium doped fibre over the 1552 nm wavelength region, when pumped using a 1480 nm LD.

For all the channels, experimental data were analysed using both linear and non-linear regression coefficients where the non-linear (3^{rd} order) temperature coefficients showed an improvement in fit to the data in the sensor calibration, leading to an RMS error of 0.015 nm (maximum) in wavelength, which is equivalent to 1.7 °C in temperature (considering the thermal sensitivity at 27 °C) compared to the linear fittings with an RMS error of 0.115 nm (maximum) (or 8.6 °C), over the wide measurement range.

The multiplexed sensor scheme can easily be employed for multipoint monitoring applications, as the outputs of each sensor are independent of each other, without gain competition, which further emphasises the reliability of the present network. However, a single pump source has enabled the excitation of simultaneous laser oscillation at different wavelength channels and the response was monitored using a single detection scheme (Optical Spectrum Analyser), which actually reduces the overall practical costs of the sensor systems demonstrated.

In conclusion, a novel approach based on a parallel multiplexed fibre laser sensor configuration has been reported for temperature sensing applications. The multiplexed laser-based sensor system offers both higher signal-to-noise ratio (SNR) and narrow linewidth over the conventional passive FBG sensor interrogations schemes. It is important to note that the sensor can be used to measure any parameter which responds to the narrowband Bragg grating e.g. temperature (as demonstrated), strain as measured in Chapter 6, humidity [Yeo *et al.* 2005] or chemical parameters [Cong *et al.* 2002] using coated FBGs. Indeed multi-channel probes responding to different parameters e.g. creating a combined temperature, humidity and strain sensor can be created with this scheme (where the temperature data can be used to correct for temperature effects in the other probes, if necessary) and is one of the interests of the future research in this field.

8.8. References

- Alavie, A.T., Karr, S.E., Othonos, A. and Measures, R.M. (1993) A Multiplexed Bragg grating fiber laser sensor system, *IEEE Photon. Technol. Lett.*, vol.5, pp.1112-1114.
- Cong, J., Zhang, X., Chen, K. and Xu, J. (2002) Fiber optic Bragg grating sensor based on hydrogels for measuring salinity, *Sensors and Actuators B*, vol. 87, pp. 487-490.
- Ghosh, G. (1995) Model for the thermo-optic coefficients of some standard optical glasses, *J. Non-Cryst. Solids*, vol. 189, pp. 191-196.
- Kersey, A.D. and Morey, W.W. (1993a) Multiplexed Bragg grating fibre-laser strain-sensor system with mode-locked interrogation, *Electron. Lett.*, vol.29, pp.112-114.
- Kersey, A.D. and Morey, W.W. (1993b) Multi-element Bragg-grating based fibre-laser strain-sensor, *Electron. Lett.*, vol.29, pp.964-966.
- Kim, S., Kwon, J., Kim, S. and Lee, B. (2001) Multiplexed strain sensor using fiber grating-tuned fiber laser with a semiconductor optical amplifier, *IEEE Photon. Technol. Lett.*, vol. 13, pp. 350-351.
- Lee, J.H., Kim, J., Han, Y.G., Kim, S.H. and Lee, S.B. (2004) Investigation of Raman fiber laser temperature probe based on fiber Bragg gratings for long-distance remote sensing applications, *Opt. Express*, vol. 12, pp. 1747-1752.
- Sun, T., Pal, S., Mandal, J. and Grattan, K.T.V. (Annual Report 2001/2002) Fibre Bragg grating fabrication using fluoride excimer laser for sensing and communication applications, *Central Laser Facility (CLF)*, Rutherford Appleton Laboratory, pp. 147-149.
- Pal, S., Mandal, J., Sun, T., Grattan, K.T.V., Fokine, M., Carlsson, F., Fonjallaz, P.Y., Wade, S.A. and Collins, S.F. (2003) Characteristics of potential fibre Bragg grating sensor-based devices at elevated temperatures, *Meas. Sci. Technol.*, vol.14, pp.1131-1136.
- Peng, P.C., Tseng, H.Y. and Chi, S. (2003) A simple fiber-Bragg-grating sensor system based on a linear-cavity fiber laser, *Microwave and Opt. Tech. Lett.*, vol. 37, pp. 15-17.

- Yeo, T.L., Sun, T., Grattan, K.T.V., Parry, D., Lade, R. and Powell, B.D. (2005) Polymer-coated fiber Bragg grating for relative humidity sensing, *IEEE Sensors Journal*, vol. 5, pp.1082-1089.
- Yu, Y., Lui, L., Tam, H. and Chung, W. (2001) Fiber-laser-based wavelength-division multiplexed fiber Bragg grating sensor system, *IEEE Photon. Technol. Lett.*, vol. 13, pp. 702-704.
- Zhou, K., Zhou, D., Dong, F. and Ngo, N.Q. (2003) Room temperature multiwavelength erbium-doped fiber ring laser employing sinusoidal phase-modulation feedback, *Opt. Lett.*, vol. 28, pp. 893-895.

Chapter 9

General conclusions and future work

9.1. Conclusions

This thesis covers the development and the characterisation of Bragg grating based-laser devices for high temperature sensor applications.

The detailed growth behaviour of both type I and type IIA fibre Bragg gratings (FBGs) in B-Ge co-doped and Ge-doped photosensitive fibres was studied in Chapter 2. The long-term temperature sustainability of the fabricated gratings was evaluated in terms of the decay in their reflectivity and the refractive index modulation, and their Bragg wavelengths variation with temperature. The work is seen as essential for the optimum selection of gratings for active sensor applications.

In Chapter 3, the optimisation of several wavelength-matched normal Bragg grating based fibre lasers was evaluated with consideration of different reflectivities of matched-pair Bragg gratings, different cavity configurations, dopant level of different erbium-doped fibres as the gain medium and the fibre length. The optimised results have been considered for sensor applications in subsequent chapters.

The new approach was developed on a *full-in-fibre* Bragg grating based laser probe for temperature sensing application for the first time to our knowledge in Chapter 4. The combination of a *chirped* Bragg grating and a normal Bragg grating was used to form the cavity feedback and enclosed a length of erbium doped fibre as the gain medium of the laser. The probe containing the normal grating (RB_1) was placed in oven for temperature measurement over the range from room temperature to 300 °C. The laser sensor was characterised by placing the chirped grating in oven and the

normal grating at ambient temperature; and the results obtained showed that the laser signal wavelength did not change with temperature variation under this configuration.

The type IIA Bragg grating was used as the sensing element of the laser system, in Chapter 5. Both the chirped grating and the normal grating were written into high germanium-erbium co-doped photosensitive fibre. The temperature was measured over the range from room temperature to 440 °C when the chirped grating was left unstrained and from 70 °C to 500 °C when it was strained. A significant improvement in the signal-to-noise ratio (SNR) and a narrow linewidth in the laser signal were obtained compared to those of the passive sensors.

In Chapter 6, the Bragg grating-based fibre laser system was used to measure the temperature up to 500 °C and the strain up to 1200 με. A high temperature sustainable normal type I grating was written into an Sb-Ge co-doped fibre and was used as the sensing element of the system. The fabrication of type IIA chirped grating was reported in the B-Ge co-doped fibre.

In Chapter 7, a detailed investigation into the output characteristics of a wavelength-matched normal Bragg gratings based fibre laser was studied, when each individual Bragg grating acting as the reflectors of the laser system, responds to temperature. An analytical model has been created for the first time reflecting the relationship between the grating bandwidth and the temperature under each operational condition. The output characteristics of a very short cavity length fibre laser were studied when placed in an oven for temperature measurement. The signal-to-noise ratio (SNR) of the laser was found to decrease continuously with increase in temperature.

The single Bragg grating-based fibre laser approach developed in Chapters 4, 5 and 6 has been extended for the parallel multiplexed temperature sensing applications in Chapter 8. Multiple laser cavities were formed using a common broadband-chirped grating and several normal fibre Bragg gratings (FBGs) as optical feedback elements used in conjunction with different lengths of erbium doped fibres (EDFs) as the gain media of the laser. When a single gain medium was placed in front of the splitter, severe gain-competition obtained across the laser channels. Simultaneous laser

oscillation at three different wavelengths was obtained without gain-competition when separate gain medium was placed across each channel after the splitter. The temperature was measured over the range from 27 °C to a maximum of 540 °C when normal FBGs were placed in the oven. Simultaneous multi-channel information through a single detection scheme will reduce the overall sensor cost for practical applications.

9.2. Recommendations for future work

The results obtained from several Bragg gratings-based fibre lasers for sensor applications have showed that laser-based devices offer significant improvement in the signal-to-noise ratio (SNR) and the narrow linewidth in the laser signal compared with those of the passive FBG sensors. This enhances the number of FBGs which may be interrogated for multiplexed applications with higher measurement resolution in the detection scheme.

In view of the work accomplished to date, the following further developments of the research are considered important and relevant:

- To extend the laser-based sensor scheme for the simultaneous measurements of temperature and strain; and their discrimination by employing an additional laser as reference.
- The multi-channel temperature-probe can be extended for measuring different parameters simultaneously, for example, creating a combined temperature, humidity and strain sensor scheme.
- The laser probe may be used for bio-medical applications where small diameter probes are required, for example, inserting in the human body for temperature profiling.

Finally, the work suggests that advanced optical fibre-laser sensors will find many other practical applications in the future.